2021

Silicon on insulator microdosimetry for radiation protection in space and aviation

Stefania Peracchi

SILICON ON INSULATOR MICRODOSIMETRY FOR RADIATION PROTECTION IN SPACE AND AVIATION

A Thesis Submitted in Fulfilment of
the Requirements for the Award of the Degree of

Doctor of Philosophy

From

University of Wollongong

By

Stefania Peracchi

BSc. (Physics Eng., Politecnico of Milan, Italy)
MSc. (Nuclear Eng., Politecnico of Milan, Italy)

Centre for Medical Radiation Physics
Faculty of Engineering and Information Sciences
School of Physics

2021

"What if I tell you that you are completely wrong?"

-cit from a believer.

Abstract

This thesis discusses the use of silicon on insulator microdosimeters for space and aviation applications.

International space agencies and private players like SpaceX announced to send astronauts to the Moon and Mars in the next decade.

Expanding the horizon of long-term space travel brings an inexhaustible amount of complexities, but the risks related to the astronaut's health must be taken into account as a priority. The harsh and abnormal conditions of the space environment, like the absence of gravity, isolation and confinement, cause effects on the body systems and behavior.

However, the biggest hazard of a human mission is invisible to the human eyes: cosmic radiation. The further we go from the Earth and its associated natural protection against radiation, such as atmosphere and magnetic field, the strongest the exposure to radiation becomes. Cancer risk increases, DNA mutations, damages to the central nervous system, cataracts, cognitive dysfunction, and in the worst-case even death, are effects associated with cosmic radiation.

Studies all around the world are constantly conducted in ground-based facilities, laboratories, as well as on the International Space Station, to evaluate human performances and develop countermeasures for a safer trip to space. Additionally, to reduce and monitor the radiation hazard, innovative spacecraft shielding and radiation detectors need to be discovered and made available for the next manned mission.

Even though on a lower level of risk, aircrew members and frequent passengers face the same issue of radiation exposure.

This thesis aims to develop a silicon-on-insulator microdosimeter that could address the two mentioned-above constraints: firstly to provide a portable detector capable of performing real-time measurements of the dose inside a spacecraft to alert astronauts in case of unacceptable level of radiation. Similarly, the device could be installed on-board aircraft to measure the dose that is used by airlines to monitor the exposure of their aircrew members.

Secondly, the microdosimeter is presented as a device that can be used to test innovative materials that could be more efficient for shielding of spacecraft and future habitats. The microdosimeter is capable to characterize the radiation field behind any shield of interest by measuring the quality of the radiation and evaluate the reduction in dose equivalent provided by the shielding material.

Several studies were performed to pursuit these thesis' goals including Monte Carlo simulation and experiments at international facilities accessing medical accelerators that provide ions and energies typical of the cosmic radiation environments.

The performances of the microdosimeter were evaluated to confirm its suitability for astronauts monitoring in space and aviation.

New materials and configurations for the shielding of future spacecraft and habitats were identified and studied.

A more detailed outline of each chapter of the thesis can be found in the section "Critical Overview".

Acknowledgments

Three years and half down under and plenty of people to thank all around the world.

A first thank to my adorable supervisors, Anatoly, Susanna, Linh and Dale, who have been my inspiring heroes and always pushed me to reach for the stars.

Thanks Anatoly, for welcoming me in your world and for all the times you asked me if I was happy here.

Thanks Susanna, for your Italian charisma that reminded me every day to keep my head up and never give up.

Thanks Linh, for your sweet words every time I felt down and lost.

Thanks Dale, for all the great laughs and unforgettable experiences shared together.

Grazie alla mia famiglia, che mi ha sempre accompagnata a quel gate in aereoporto con tanto orgoglio e che si è sempre fatta trovare a braccia aperte ad ogni mio ritorno. Grazie a loro che, non importa il fuso orario, hanno sempre risposto alle mie chiamate asciugandomi lacrime e condividendo vittorie. Grazie a loro che, ad ogni compleanno e Natale lontano, mi han fatto sentire a casa anche dietro ad uno schermo un po' sfuocato.

Un gros merci à ma deuxième famille à Paris, à qui est encore là et qui comme moi a trouvé une place ailleurs. À vous mes potes, que le dernier jour dans notre "ville de la lumière", pendant la fête de la musique, vous m'avez dit au revoir et jamais adieu.

Merci à toi ma chérie, qui m'as toujours rappelé que même la pire semaine ce n'est pas trop longue à supporter, et grâce à toi je suis arrivée au weekend ravie de te revoir.

Al mio panda preferito dall'altra parte del mondo a cui ho intasato la memoria del telefono con messaggi vocali infiniti, un amorevole grazie.

A tutti quegli amici storici in Italia che in ogni momento mi hanno supportato e sopportato anche a distanza, un abbraccio e un grazie enorme.

To my friends-colleagues who got lost in Tokyo with me, thanks for sharing the real fun of the Ph.D.

Thanks to him, that after all this time still keeps messing up the gender of Italian words and calling me "Bello".

Thanks to all those collaborators that put their experience into this project and helped me to successfully achieve my goals.

And then to them, my all crazy friends that I met in Australia, that saw the pain and the stress of this Ph.D on my face, lately. To those who still believe I will be an astronaut one day, to those I danced until the sunrise with, to those who held me up in the darkest days, to those who got sunburned at the beach with me in the sunny days, a huge thank from my heart.

I love you all.

Certification

I, Stefania Peracchi, declare that this thesis submitted in fulfilment of the requirements for the conferral of the degree Doctor of Philosophy, from the University of Wollongong, is wholly my own work unless otherwise referenced or acknowledged. This document has not been submitted for qualifications at any other academic institution.

Stefania Peracchi

10th February 2021

Preamble

The content of this thesis is the results of Monte Carlo simulations, experiments, data analysis and discussions performed by myself, Stefania Peracchi, with assistance from supervisors, colleagues and collaborators.

GEANT4 simulations presented in Chapter 2 are based on a code written by me under the supervision of Dr. David Bolst and Dr. Susanna Gualelli, and help of the PhD student James Vohradsky. Nevertheless, I carried out the simulation and data processing.

The charge collection characterization of detectors discussed in Chapter 3 was been performed under the supervision of Dr. Linh T. Tran and with the help of Dr. Zeljko Pastuovic in setting the beam at the accelerator.

The experimental data collected at HIMAC and discussed in Chapter 4 and Chapter 5 were part of an experimental campaign carried out between a few Ph.D. students, under the supervision of Dr. Linh T. Tran, with the assistance of the Japanese staff for running the beam. Similarly, regarding the data collected at PSI discussed in Chapter 6 and Chapter 7, I carried out the experiments with Dr. Linh T. Tran and the delivery of the beam was done by Dr. Serena Psoroulas, Dr. Martin Grossmann Handschin and Dr. David Meer. Nevertheless, I was the person performing all the data processing and analysis, which is presented in the thesis.

Publications

1. **S. Peracchi**, S Guatelli, L. T. Tran and A. B. Rosenfeld, “Simulation of cosmic radiation spectra for personal microdosimetry at the International Space Station's altitude”, *Journal of Physics: Conference Series,* Micro-Mini & Nano Dosimetry Conference 2018, 6–11 February 2018, vol 1154, Art. no. 012020, 2019.

2. **S. Peracchi**, J. Vohradsky, S. Guatelli, D. Bolst, L.T. Tran, D. A. Prokopovich, A. B. Rosenfeld, "Modelling of the Silicon-On-Insulator microdosimeter response within the International Space Station for astronauts' radiation protection," *Radiation Measurements*, vol. 128, Art. no. 106182, 2019.

3. **S. Peracchi,** L. T. Tran, B. James, D. Bolst, D. A. Prokopovich, J. A. Davis, S. Guatelli, M. Petasecca, M. L. F. Lerch, N. Matsufuji, A. Kok, M. Povoli, M. Jackson, and A. B. Rosenfeld, "A solid-state microdosimeter for dose and radiation quality monitoring for astronauts in space," *IEEE Transactions on Nuclear Science*, vol. 67, no. 1, pp. 169-174, 2020.

4. B. James, L. T. Tran, D. Bolst, **S. Peracchi**, J. A. Davis, D. A. Prokopovich, S. Guatelli, M. Petasecca, and M. Lerch, M. Povoli, A. Kok, M.-J. Goethem, M. Nancarrow, N. Matsufuji, M. Jackson, A. B. Rosenfeld, "SOI Thin

Microdosimeters for High LET Single-Event Upset Studies in Fe, O, Xe, and Cocktail Ion Beam Fields," *IEEE Transactions on Nuclear Science*, vol. 67, no. 1, pp. 146-153, 2020.

5. **S. Peracchi**, B. James, F. Pagani, V. Pan, J. Vohradsky, D. Bolst, D. A. Prokopovich, S. Guatelli, M. Petasecca, M. L. F. Lerch, S. H. Lee, T. Inaniwa, N. Matsufuji, M. Povoli, A. Kok, M. Jackson, T. Squire, A. B. Rosenfeld, and L. T. Tran, "Radiation shielding evaluation of spacecraft walls against heavy ions using microdosimetry," *IEEE Transactions on Nuclear Science*, pp. 1-1, 2020.

6. **S. Peracchi,** B. James, S. Psoroulas, M. Grossmann, D. Meer, D. Bolst, Z. Pastuovic, J. Vohradsky, S. Guatelli, D. A. Prokopovich, M. Petasecca, M. L. F. Lerch, M. Povoli, A. Kok, M. Jackson, A. B. Rosenfeld, and Linh T. Tran, "Modelling of protons spectra encountered in space using medical accelerator and its microdosimetric characterization", *Advances in Space Research*, vol. 67, no. 8, pp. 2534-2543, 2021.

7. V. A. Pan, F. Pagani, L. T. Tran, B. James, D. Bolst, **S. Peracchi**, J. Vohradsky, A. Pogossov, S. Guatelli, M. Petasecca, D. A. Prokopovich, D. Boardman, V. L. Perevertaylo, S. D. Chambers, A. G. Williams, S. Werczynski, N. Matsufuji, M. L. F. Lerch, M. Jackson and A. B. Rosenfeld, "Characterization of a Novel Large Area Microdosimeter System for Low Dose Rate Radiation Environments", *Nuclear Instruments and Methods in Physics Research Section A: Accelerators, Spectrometers, Detectors and Associated Equipment,* vol. 1002, art. no. 165238, 2021.

8. J. Vohradsky, L. T. Tran, L. Chartier, **S. Peracchi**, S. Guatelli, H. Kumada and A. B. Rosenfeld, "Activation study of experimental setup at Tokai

accelerator based iBNCT", 2020 (*submitted to Applied Radiation and Isotopes, currently under peer-review).*

9. J. Vohradsky, L. T. Tran, S. Guatelli, L. Chartier, C. Vandevoorde, E. Alexander de Kock, J. Nieto-Camero, D. Bolst, **S. Peracchi**, C. Hoglund, and A. B. Rosenfeld, "Response of SOI microdosimeter in fast neutron beams: experiments and Monte Carlo simulations", 2020 (*submitted to Physica Medica journal, currently under peer-review).*

10. J. Vohradsky, L. Chartier, L. T. Tran, A. Pogossov, S. Alnaghy, J. Paino, **S. Peracchi**, V. Pan, M. Povoli, A. Kok, and A. B. Rosenfeld, "Introduction and Implementation of the CMRP Radiodosimeter - A Novel Wireless Microdosimetry System", 2021 (to *submit to IEEE Transaction on Nuclear Science for peer-review).*

Conferences

1. **S. Peracchi**, S Guatelli, L. T. Tran and A. B. Rosenfeld, "Simulation of cosmic radiation spectra for personal microdosimetry at the International Space Station's altitude**".** *Oral presented by: S. Peracchi, at Mini-Micro-Nano-Dosimetry ad Innovative Technologies in Radiation Oncology (MMND-ITRO) Conference 2018, 6th–11th February 2018, Mooloolaba, Queensland, Australia.*

2. **S. Peracchi**, J. Vohradsky, S. Guatelli, D. Bolst, L. T. Tran, A. B. Rosenfeld, "GEANT4 simulation of the radiation environment within the International Space Station and the Silicon On Insulator microdosimeter response". *Oral presented by: S. Guatelli, at Third Geant4 International User Conference 2018, 29th-31st October 2018, Bordeaux, France.*

3. **S. Peracchi**, J. Vohradsky, S. Guatelli, D. Bolst, L. T. Tran, "Silicon-On-Insulator microdosimeter response within the International Space Station radiation environment". *Poster presented by: S. Peracchi, at 2018 IEEE Nuclear Science Symposium & Medical Imaging Conference, 10th-17th November 2018, Sydney, New South Wales, Australia.*

4. **S. Peracchi**, J. Vohradsky, S. Guatelli, D. Bols, L. T. Tran, and A. B. Rosenfeld, "Characterization of the hazardous radiation environment within

the International Space Station and dose evaluation on a 1 day-mission by using a novel SOI microdosimeter". *Oral presented by: S. Peracchi, at MedPhys2018 Student Research Symposium of the ACT/NSW Branch of the ACPSEM, 6th December 2018, Sydney, New South Wales, Australia.*

5. **S. Peracchi**, B. James, L. T. Tran, D. Bolst, D. A. Prokopovich, J. A. Davis, S. Guatelli, M. Petasecca, M. L. F. Lerch, N. Matsufuji, A. Kok, M. Povoli, M. Jackson and A. B. Rosenfeld, "A solid-state microdosimeter for dose and radiation quality monitoring for astronauts in space. *Poster presented by: S. Peracchi, at Nuclear & Space Radiation Effects Conference 2019, 7th-12th July 2019, San Antonio, Texas, USA.*

6. **S. Peracchi**, B. James, L. T. Tran, D. Bolst, D. A. Prokopovich, J. A. Davis, S. Guatelli, M. Petasecca, M. L. F. Lerch, N. Matsufuji, A. Kok, M. Povoli, M. Jackson and A. B. Rosenfeld, "A solid-state microdosimeter for dose and radiation quality monitoring for astronauts in space". *Poster presented by: L. T. Tran at 19th International Conference on Solid State Dosimetry, 15th-20th September 2019 Hiroshima, Japan.*

7. **S. Peracchi,** B. James, L. T. Tran, D. Bolst, D. A. Prokopovich, J. A. Davis, S. Guatelli, M. Petasecca, M. L. F. Lerch, N. Matsufuji, A. Kok, M. Povoli, M. Jackson and A. B. Rosenfeld, "A solid-state microdosimeter for dose and radiation quality monitoring for astronauts in space. *Oral presented by: L. T. Tran at ICRP 2019, 5th International Symposium on the System of Radiological Protection, 17th-21st November 2019 Adelaide, South Australia, Australia.*

8. **S. Peracchi**, B. James, L. T. Tran, D. Bolst, D. A. Prokopovich, J. A. Davis, S. Guatelli, M. Petasecca, M. L. F. Lerch, N. Matsufuji, A. Kok, M. Povoli, M. Jackson and A. B. Rosenfeld, "A solid-state microdosimeter for dose and

radiation quality monitoring for astronauts in space. *Poster presented by: S. Peracchi, at ANSTO User Meeting 2019, 2nd-3rd December 2019, Sydney, New South Wales, Australia.*

9. **S. Peracchi**, J. Vohradsky, S. Guatelli, D. Bolst, L. T. Tran, A. B. Rosenfeld, "GEANT4-based microdosimetry for astronauts' radiation protection". *Oral presented by: S. Peracchi, at the 4th GEANT4 School & Monte Carlo Workshop for Radiotherapy, Imaging and Radiation Protection, 2nd-8th December, 2019, Wollongong, New South Wales, Australia.*

10. S. Guatelli, **S. Peracchi** et al., "Radiation protection of astronauts in missions to Mars". *Public outreach presented by: S. Guatelli at Science at the Local, 28th June 2020, Sydney, New South Wales, Australia.*

11. **S. Peracchi,** B. James, S. Psoroulas, M. Grossmann, D. Meer, Z. Pastuovich, D. Bolst, S. Guatelli, D. A. Prokopovich, . Petasecca, M. L. F. Lerch, M. Povoli, A. Kok, M.Jackson, A. B. Rosenfeld, and L. T. Tran, "Modeling of protons spectra encountered in space using a medical accelerator and its microdosimetric characterization". *Oral presented by: S. Peracchi, at the 2020 Virtual IEEE Nuclear Science Symposium & Medical Imaging Conference, 31st October-7th November 2020, Boston, USA.*

12. **S. Peracchi,** B. James, F. Pagani, V. Pan, J. Vohradsky, D. Bolst, D. A. Prokopovich, S. Guatelli, M. Petasecca, M. L. F. Lerch, S. H. Lee, T. Inaniwa, N. Matsufuji, M. Povoli, A. Kok, M. Jackson, T. Squire, A. B. Rosenfeld, and L. T. Tran "Radiation shielding evaluation of spacecraft walls against heavy ion beams using microdosimetry". *Oral presented by: S. Peracchi, at the Virtual Nuclear & Space Radiation Effects Conference 2020, 1st-4th December 2020, Santa Fe, New Mexico, USA.*

13. **S. Peracchi,** B. James, S. Psoroulas, M. Grossmann, D. Meer, Z. Pastuovich, D. Bolst, S. Guatelli, D. A. Prokopovich, Petasecca, M. L. F. Lerch, M. Povoli, A. Kok, M.Jackson, A. B. Rosenfeld, and L. T. Tran, "Modeling of protons spectra encountered in space using a medical accelerator and its microdosimetric characterization". *Oral presented by: S. Peracchi, at the Virtual MedPhys2020 Student Research Symposium of the ACT/NSW Branch of the ACPSEM, 15th December 2020, Sydney, New South Wales, Australia.*

14. **S. Peracchi,** J. Vohradsky, S. Guatelli, D. Bolst, L. T. Tran, D. A. Prokopovich, and A. B. Rosenfeld, "GEANT4-based microdosimetry for astronauts' radiation protection". *Oral presented online by: S. Peracchi, at 43rd COSPAR Scientific Assembly 2020, 28th January–4th February 2020, Sydney, New South Wales, Australia.*

15. **S. Peracchi**, L. T. Tran, B. James, D. Bolst, D. A. Prokopovich, S. Guatelli, M. Petasecca, M. L. F. Lerch, M. Povoli, A. Kok, , N. Matsufuji, M. Jackson, and A. B. Rosenfeld, "Shielding verification in radiation space environment with biologically relevant dosimetry". Or*al presented by: A. B. Rosenfeld, at 43rd COSPAR Scientific Assembly 2020, 28th January–4th February 2020, Sydney, New South Wales, Australia.*

16. L. T. Tran, **S. Peracchi**, D. Bolst , B. James, S. Psoroulas, M. Grossmann, D. Meer, D. A. Prokopovich, S. Guatelli, M. Petasecca, M. L. F. Lerch, M. Povoli, A. Kok, M. Jackson, and A. B. Rosenfeld, "Shielding verification in radiation space environment with biologically relevant dosimetry". *Oral presented by: L. T. Tran, at 43rd COSPAR Scientific Assembly 2020, 28th January–4th February 2020, Sydney, New South Wales, Australia.*

Awards

1. **International Postgraduate Tuition Award** to attend Ph.D. degree, from the University of Wollongong, 2017, Australia.

2. **Matching Scholarship**, from the University of Wollongong, 2017, Australia.

3. 2018 IEEE NSS MIC **Trainee grant** at IEEE Nuclear Science Symposium and Medical Imaging (NSS/MIC) 2018, Sydney, Australia.

4. **Paul-Phelps Continuing Education Grant**, Nuclear and Space Radiation Effects (NSREC) Conference, 2020, USA.

5. **People's Choice Award**, 2020 Virtual 3 Minutes Thesis Asia-Pacific Competition, University of Queensland, 2020, Australia.

6. Virtual 2020 IEEE NSS MIC **Trainee Grant** at IEEE Nuclear Science Symposium and Medical Imaging (NSS/MIC) 2020.

Media and press

Australian Press

- https://www.uow.edu.au/media/2020/three-minute-thesis-winner-helping-to-make-space-travel-safer.php?fbclid=IwAR2IxN7r7J3lrJhr1cXMfNSVmH-jpvAWH2ZLKj9TCC1vWU5DM7IA1Fd2zEM
- https://news.eis.uow.edu.au/complex-research-you-have-3mins/
- https://www.illawarramercury.com.au/story/6885574/uows-own-cosmic-ray-detector-wins-for-cutting-long-story-short/?fbclid=IwAR2IxN7r7J3lrJhr1cXMfNSVmH-jpvAWH2ZLKj9TCC1vWU5DM7IA1Fd2zEM
- https://innovationcampus.com.au/three-minute-thesis-winner-helping-to-make-space-travel-safer/
- https://www.ansto.gov.au/news/experiments-carried-out-on-antarctic-flight
- https://www.uow.edu.au/media/2018/antarctica-flight-the-living-laboratory-for-radiation-sensor-testing.php
- http://getstem.com.au/experiments-carried-antarctic-flight/
- https://universe.uow.edu.au/research/stefania-peracchi-to-compete-in-3mt-asia-pacific-final/
- https://universe.uow.edu.au/research/uow-3mt-winner-through-to-final-eight-in-asia-pacific-finals/
- https://www.uow.edu.au/media/2020/uow-physics-student-wins-peoples-choice-award-at-asia-pacific-3mt-finals.php?fbclid=IwAR3Oug_KmFeUcW3nZeowGy_JYLbPI9muvLTPyRKlIIOjPJEfBhnQmwbFzGI

- https://www.acgr.edu.au/impact-blog/winners-of-the-2020-asia-pacific-3mt-final/'
- "UOW physics student named People's Choice", *The Illawarra Mercury newspaper*, issued the 3rd October, NSW, Australia.
- https://www.uow.edu.au/the-stand/2020/stefanias-journey-to-outer-space.php

International Press

- https://www.ecodibergamo.it/stories/premium/Cronaca/dallaustralia-al-polo-sudmisura-le-particelle-cosmiche_1369804_11/?fbclid=IwAR2IxN7r7J3lrJhr1cXMfNSVmH-jpvAWH2ZLKj9TCC1vWU5DM7IA1Fd2zEM
- https://socialbg.it/stefania-peracchi-di-villa-di-serio-incanta-laustralia-con-la-sua-ingegneria/?fbclid=IwAR2IxN7r7J3lrJhr1cXMfNSVmH-jpvAWH2ZLKj9TCC1vWU5DM7IA1Fd2zEM
- "L'Australia premia l'ingegno nucleare di Stefania Peracchi", L'eco di Bergamo newspaper, issued the 14th October 2020, Bergamo, Italy.

Radio

- https://www.abc.net.au/radio/illawarra/programs/breakfast/breakfast/12552580
- https://www.abc.net.au/radio/illawarra/programs/drive/drive/12706362
- https://www.sbs.com.au/language/italian/audio/dall-italia-all-australia-dalla-luna-a-marte-il-viaggio-dell-italiana-che-studia-le-radiazioni-cosmiche?fbclid=IwAR16l_3wQdvzicFsr0TYCUyTvxREEMXPxWr0u8lcNATjzkoyqHq_HjsH0ts
- https://www.sbs.com.au/language/italian/audio/il-mio-viaggio-da-milano-all-australia-fino-a-marte

Table of Contents

List of Figures

List of Tables

Glossary of Acronyms

ADC ..... Analogue to Digital Converter
ALARA ..... As Low As Reasonably Achievable
AMS ..... Accelerator Mass Spectrometry
ANSTO ..... Australia's Nuclear Science and Technology Organization
CCE ..... Charge collection efficiency
CERF ..... CERN-EU high-energy Reference Field
CMEs ..... Coronal Mass Ejections
CMRP ..... Centre for Medical Radiation Physics
CRAND ..... Cosmic Ray Albedo Neutrons Decay
DAQ ..... Data Acquisition system
DIL ..... Dual in line, Dual In Line
DRIE ..... Deep reactive ion etching
EHPs ..... Electron-hole pairs
EPCARD European Program Package for the Calculation of Aviation Route Doses
EVA ..... Extravehicular activity
FLC ..... Four-Leaf Collimator
GCRs ..... Galactic Cosmic Rays
GEANT4 ..... Geometry And Tracking
GEO ..... Geomagnetic Earth Orbit
HEO ..... High Earth Orbit
HIMAC ..... Heavy Ion Medical Accelerator in Chiba
HZE ..... High atomic number (Z) and energy (E)
IBA ..... Ion Beam Analysis
IBICC ..... Ion Beam Induced Charge

ICRP International Commission on Radiological Protection, International Commission for Radiological Protection
ICRU..... International Commission on Radiation Units and Measurements
IGE ..... International Geostationary Electron
ISS..... International Space Station
JISCARD ... Japanese Internet System for the Calculation of Aviation Route Doses
LEO ..... Low Earth Orbit, Low Earth Orbit
LET..... Linear Energy Transfer
MEO ..... Medium Earth Orbit
NASA-SEE..... NASA Space Environment and Effects
ONERA..... Office National d' Etudes et de Recherches Aérospatiales
OOF ..... Out-of-field
OPAL..... Open-pool Australian light-water reactor
PCAIRE..... Predictive Code for Aircrew Radiation Exposure
PCB ..... Printed Circuit Board
PMMA ..... PolyMethylMethAcrylate
POLE..... Particle ONERA-LANL Environment
QST..... Quantum and Science Technology
RBE ..... Relative Biological Effectiveness
SAA..... South Atlantic Anomaly
SEM ..... Scanning Electron Microscope
SEU ..... Single Event Upset
SIEVERT Systeme d'Information et d'Evaluation par Vol de l'Exposition au Rayonnement cosmique dans les Transports aeriens
SOI..... Silicon-on-insulator
SPENVIS ..... Space Environment Information System
SPEs..... Solar Particles Events
SV ..... Sensitive Volume
TEPC..... Tissue Equivalent Proportional Counter
TLD ..... Thermoluminescent dosimeter

Critical Overview

This thesis presents the microdosimetry approach to radiation protection in space and aviation. In particular, the use of silicon on insulator (SOI) microdosimeters has been investigated for future space and air crew radiation monitoring, as well as for characterization of the radiation field typical encountered at the International Space Station (ISS) altitude and in deep space.

The thesis begins with Chapter 1 where an overview of the radiation sources in space (i.e. Galactic Cosmic Rays (GCRs), Solar Particle Events (SPEs), and trapped particles in the Van Allen Belts) and the natural shielding provided by the Earth atmosphere and magnetic field is presented. Then, the regulations adopted by international organizations to protect humans in space and aviation are discussed in terms of dose limits. Microdosimetry is a very effective approach to quantify the radiation effects due to the exposure to a mixed radiation field such as the one found in space. Thus, this chapter will conclude with a description of the development of SOI microdosimeters.

As a first step in understanding the performances of the SOI microdosimeter in space, in Chapter 2, the radiation environments encountered at the ISS was modeled by simulating the particles' fluxes coming from the three main sources of cosmic radiation with GEANT4. The Columbus module of the ISS was modeled and the SOI microdosimeter was placed inside it to simulate its response in a one-day mission.

After the simulation gave promising results with an overall agreement with existing experimental measurements, Chapter 3 presented the characterization and

calibration of the latest designs of the 3D SOI “Mushroom” microdosimeters. For this purpose, the charge collection efficiency study by using the ion-based induced charge (IBIC) technique at the accelerator situated at the Australian Nuclear Science and Technology Organization (ANSTO) facility was performed.

The next step of the thesis was to conduct experiments with radiation sources that could mimic at least partially the particles encountered in space and previously simulated in Chapter 2. Hence, Chapter 4 showed the first experimental campaign conducted at the Heavy Ion Medical Accelerator in Chiba (HIMAC), where the SOI microdosimeter was tested against heavy ion beams of oxygen and iron, as an example of medium and high LET GCRs. The scenario of the microdosimeter inside and outside the Columbus module in space was reproduced by using aluminum slabs representing the shielding wall of the spacecraft.

Chapter 5 follows the research theme of Chapter 4 as it was decided to investigate in more depth the shielding efficiency of the whole structure of the Columbus module wall, by irradiating it with carbon, neon, silicon heavy ions with different energies. Additionally, innovative materials with expected better shielding properties than aluminum were used to evaluate a possible dose reduction inside the spacecraft.

Nevertheless, the main component of the radiation environment in space consists of protons. Thus, to achieve a more complete overview of the response of the microdosimeter, it was tested with proton beams. Usually, ground-based facilities provide monoenergetic beams to mimic particles in space. However, it would be preferable to have poly-energetic beams that represent better the complexity of the radiation field in space. In Chapter 6, a methodology to use a medical accelerator to mimic and deliver a spectrum of protons typical of space was introduced. For this purpose, the fluences of GCR, SPE, and Trapped protons simulated in Chapter 2 were used to program the treatment planning system that delivered the proton beam. The experiments were carried out at the Paul Scherrer Institute (PSI), in Switzerland. The SOI “Mushroom” microdosimeter previously tested at HIMAC was irradiated with spectral fluences in the energy range of 70 - 230 MeV and its response was studied.

Chapter 7 shows a similar study to the one discussed in Chapter 5, where the Columbus shielding structure was irradiated with mono-energetic heavy ion beams but this time with the spectra of protons in the wider energy range (70 – 230 MeV) modeled in Chapter 6. The gantry was rotated, from 0° to 180°, around the microdosimeter to perform irradiations that could mimic an isotropic exposure in space, and studied the angular dependence of the microdosimeter response.

Finally, Chapter 8 is dedicated to the conclusions of this thesis and provides recommendations to develop further this research project.

Chapter 1

Literature review

In this chapter, the topic overview will be explained in detail, starting from a description of radiation sources in space, and natural existing shielding to protect humans. Then, the regulation for radiation protection in space and aviation will be discussed based on publications adopted by International associations.

Moreover, the theory of microdosimetry will be explained to underline the main quantities used for investigating the quality of the radiation environment in space and aviation in terms of energy deposition in a target of the dimension of biological cells, and dose.

Finally, an overview of silicon on insulator microdosimeters since their first generation will be discussed to provide details about detectors used during experimental studies of interest for this thesis. Additionally, it is included a comparison with the already existing tissue proportional counter used to investigate measures and countermeasures in the field of radiation protection in space and aviation.

1.1 Space Radiation

1.1.1 Radiation sources

The space radiation environment is a complex and mixed field that pervades the Universe and has attracted the attention of many scientists all around the world for many centuries. The first observed interaction of radiation coming from the outer space with Earth is dated in 1859, when R. C. Carrington, an English astronomer, realized that a massive solar eruption interfered with telegraph systems which failed all around Europe and America [1]. After Antoine Henri Becquerel and Marie and Pierre Curie discovered radioactivity, later in 1912, physicist Victor Frank Hess undertook a series of balloon experiments that led to the discovery of cosmic radiation, and consequently him to win the Nobel prize [2]. He found that the level of radiation rose with altitude due to the presence of ionizing radiation coming from the Sun. This discovery was proved by the physicist Robert Andrews Millikan, who confirmed the extraterrestrial origin of such radiation and gave it the name of "cosmic rays" defining them "the birth cries of atoms being born in interstellar space" [3].

The interest in this mysterious source of radiation speeded up among the scientific community, which eventually was able to assign origin and characteristic.

Three main sources of cosmic rays are nowadays recognized as responsible for the eventually harmful exposure of humans to radiation while traveling to space: the Galactic Cosmic Rays, Solar Particle Events and trapped charged particles in the Van Allen Belts.

Galactic Cosmic Rays

Galactic Cosmic Rays (GCRs) originate from sources beyond the solar system, such as supernova explosions of stars in deep space, and move through space at nearly the speed of light. Their distribution throughout space is considered isotropic.

The GCR spectrum consists of two components: the leptonic one, essentially 2% of solitary electrons and positrons, and the baryonic one, 98% of the particles, approximately 87% protons, 12% alpha particles, and 1% nuclei of heavier ions, called HZE ions for their high atomic number Z and their high energy E [4]. Figure 1.1 shows the relative abundance of HZE typical of GCRs.

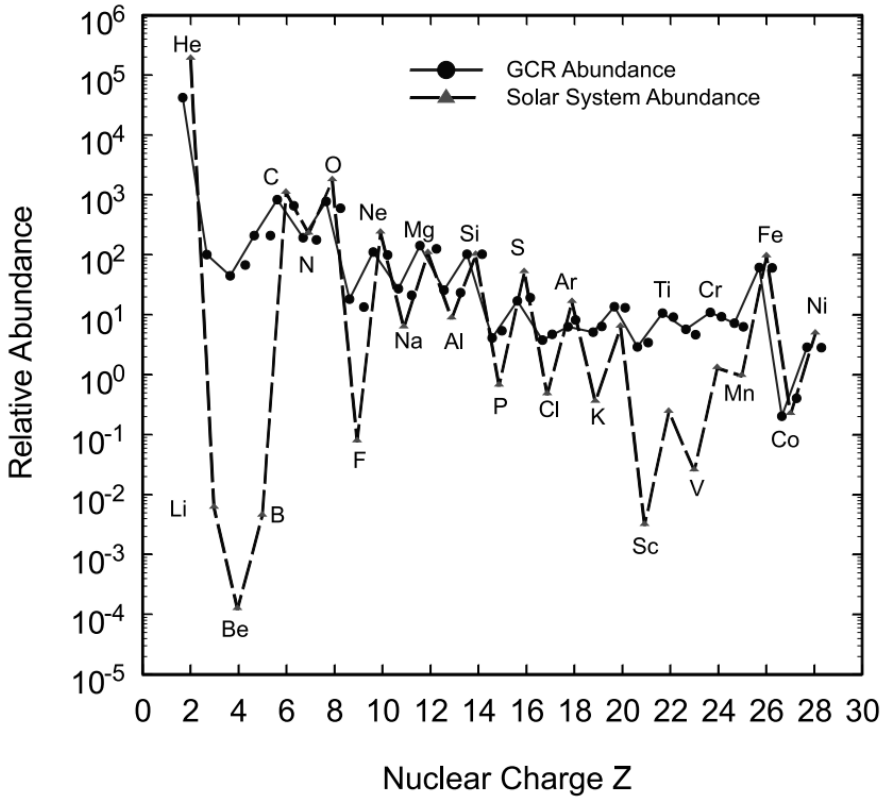

Figure 1.1. Image courtesy of (G. Horneck, 1994) [5]: the relative abundance of GCR ions is shown from He to Ni. Nuclei with nuclear charge Z >28 are characterized by an abundance lower than the scale of this plot, thus are not shown. As a comparison, the solar system abundances for these same elements are shown.

Despite the HZE ions are less abundant, they possess significantly higher linear energy transfer with a greater potential for radiation-induced damages. The problem of the potential hazard posed by HZE was discovered when the astronauts of the Apollo 11 mission returning from the Moon, reported visualization of light flashes after some period of dark adaptation. These light flashes were eventually associated with HZE penetrating the spacecraft structure and the astronaut's eyes, interacting

directly with the retina or indirectly via Cerenkov interaction in the vitreous fluid of the eye [5].

The complexity of the GCRs radiation field is identified by its wide energy spectrum from several eV up to 10^{12} MeV, and fluctuable intensity of the flux depending on several factors related to the natural shielding of the solar magnetic field and associated solar activity [6]. A more detailed explanation of the correlation between the GCRs modulation and those factors will be presented in section 1.1.2. However, Figure 1.2 shows an example of fluxes for the most abundant GCRs, and how the solar activity anti-correlates to the GCRs intensity. The energy peak of the fluence for these ions is at ~1 GeV/u in case of solar maximum condition, whereas the peak shift at ~400 MeV/u for solar minimum condition but with higher fluence intensity.

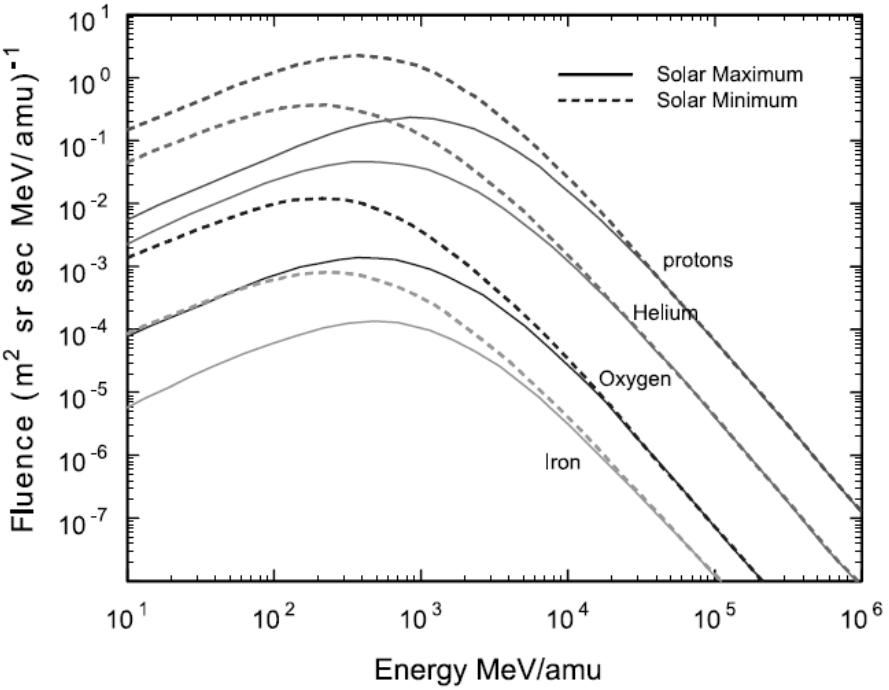

Figure 1.2. Image courtesy of (E. R. Benton et al., 2001)[6]: the effect of the minimum and maximum phases in the solar cycle on the energy spectrum for GCRs as protons, helium, oxygen and iron, encountered in LEO.

Solar Particle Events

In the early 1940s, Solar Particles Events (SPEs) were first observed. They consist of protons, electrons and HZE ions with energy ranging from a few tens of keV to GeV, and are associated with impulsive emission events from the sun, such as solar flares or the shockwaves associated with coronal mass ejections (CMEs) [7].

A solar flare refers to a sudden burst of X-ray emitted due to the high fluxes of electrons trapped in a coronal loop that accelerate along magnetic lines exiting and reconnecting to the Sun's surface (see Figure 1.3a). When a solar flare is characterized by low intensity and low energy particle fluxes, its presence can be observed only when the radiation is emitted along an open magnetic field's line that connects to the Earth or to a spacecraft.

Nevertheless, the most intense SPEs, also with the highest energies, follow CME-driven shocks of plasma: the gradual event is due to an erupting filament with no accompanying flare. The ejected material is a magnetized plasma dominated by protons and electrons but carrying also alpha particles typically of the corona material. The flux of particles is generally one or three orders of magnitude greater than that in impulsive events, with a smooth and extended time profile coming from continuous acceleration at the moving CME shock (see Figure 1.3b).

There is an important implication with respect to these events' effects: the direct injection of solar flares affects only a narrow regime in space, whereas the shock fronts driven by CMEs can extend over large angles of propagation and thus can fill them with high fluxes of particles. In particular, the very big and fast events produce highly relativistic particles accelerated to energies of several tens of MeV within $5 \div 10$ solar radii, which means the 5% of the Sun-Earth distance, and can reach Earth in a few hours. This makes prediction and warning of SPE events quite challenging, if not impossible with current technology [8]. Figure 1.4 shows an example of the integral fluence of some intense SPE recorded in the second half of the 20^{th} century.

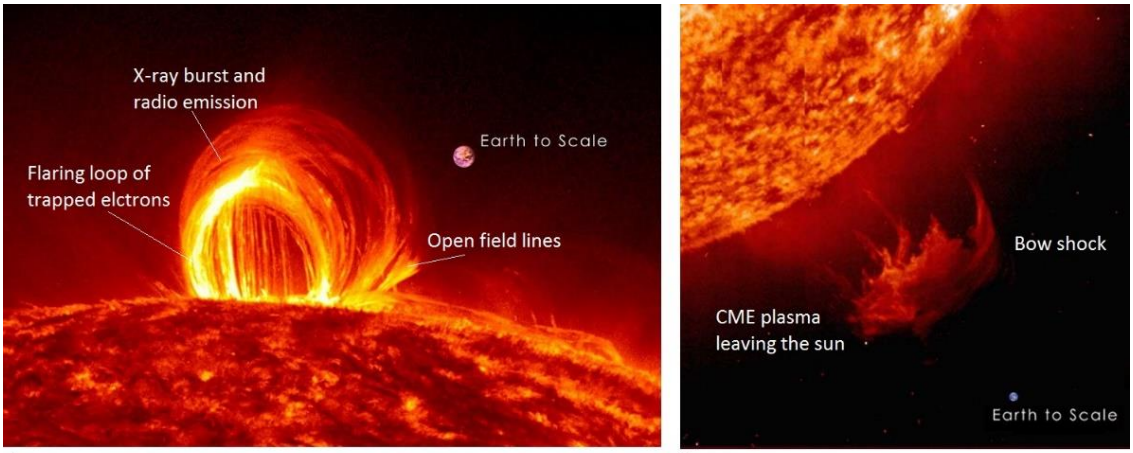

Figure 1.3. Image courtesy of NASA: a) Solar flare associated with trapped electrons accelerating along a magnetic field's line and reconnecting to the corona inducing bursts of X-ray; b) Shock wave propagating towards the Earth associated to the ejection of plasma during a CME.

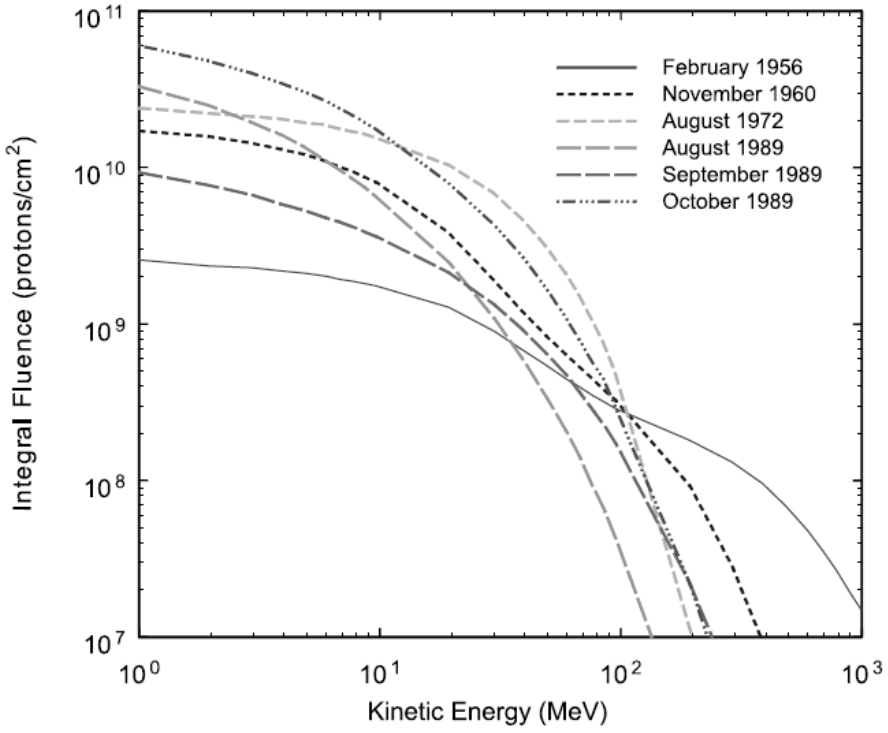

Figure 1.4. Image courtesy of (E. R. Benton et al., 2001) [6]: the fluence of protons recorded for some SPE events occurring from 1956 to 1989.

Trapped radiation in the Van Allen Belts

The geomagnetic field works as a trap for charged particles coming from outer space or the sun. These particles have a complex motion made of three periodic components: the gyration around a magnetic field line, the propagation along the field line with magnetic mirroring at the end-points, and the longitudinal drift (west for positive particles, east for electrons). This results in two stable belts of trapped radiation around Earth, called Van Allen belts, from James van Allen who headed their discovery with the first U.S. satellite Explorer 1 in 1958. The belts extend from an altitude of about 1,000 to 65,000 kilometers above the surface of the Earth [6]. In this region, the radiation levels vary, distinguishing an inner belt and an outer belt (see Figure 1.5).

The outer belt, extending from 13,000 to 60,000 km above the Earth's surface, consists mainly of electrons with a maximum energy of 10 MeV. The belt is mostly produced by the inward radial diffusion and local acceleration due to the transfer of energy from whistler-mode plasma waves to radiation belt electrons. The trapped particle population contains also various ions, most of them in the form of protons, but also alpha particles and oxygen ions similar to those in the ionosphere but much more energetic. The outer belt's electrons are also constantly removed by collisions with atmospheric neutrals, losses to the magnetopause, and the outward radial diffusion. The electrons here have a high flux and at the outer edge, close to the magnetopause, where geomagnetic field lines open into the geomagnetic "tail", fluxes of energetic electrons can drop to the low interplanetary levels within about 100 km, a decrease by a factor of 1000 [6, 9].

Typically up to 6,000 km above the Earth's surface, the inner belt is inhabited by electrons in the range of hundreds of keV and with fluxes one order magnitude less intense than in the outer belt, and high-energy protons exceeding hundreds MeV (see Figure 1.6). It is believed that proton energies exceeding 50 MeV in the lower belts at lower altitudes are the result of the beta decay of neutrons created by cosmic ray collisions with nuclei of the upper atmosphere and then backscattered into space. This phenomenon is known as the Cosmic Ray Albedo Neutrons Decay

(CRAND). The source of lower energy protons is believed to be proton diffusion due to changes in the magnetic field during geomagnetic storms [10].

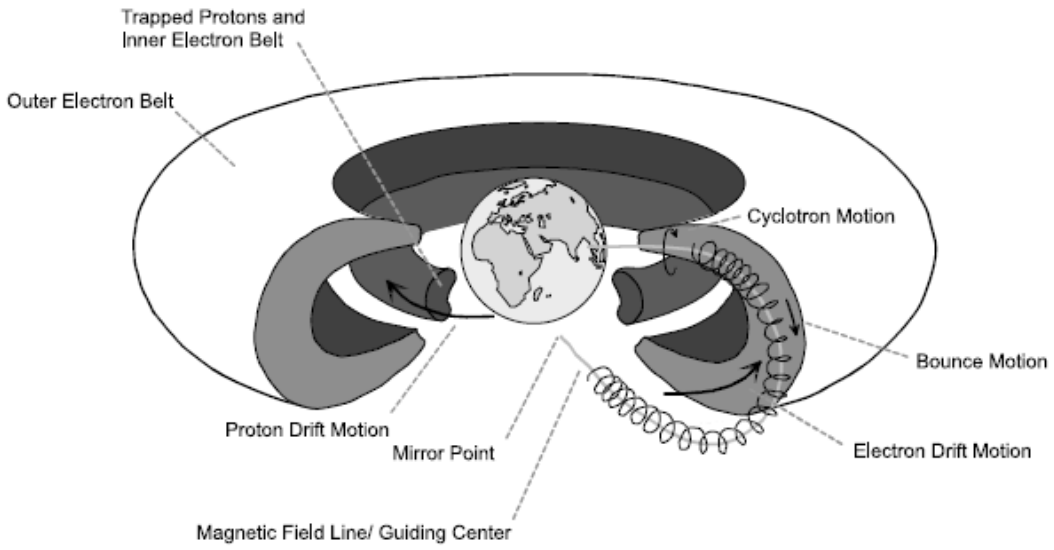

Figure 1.5 Image courtesy of (E. R. Benton et al., 2001) [6]: the motion of trapped particles in the Van Allen Belts.

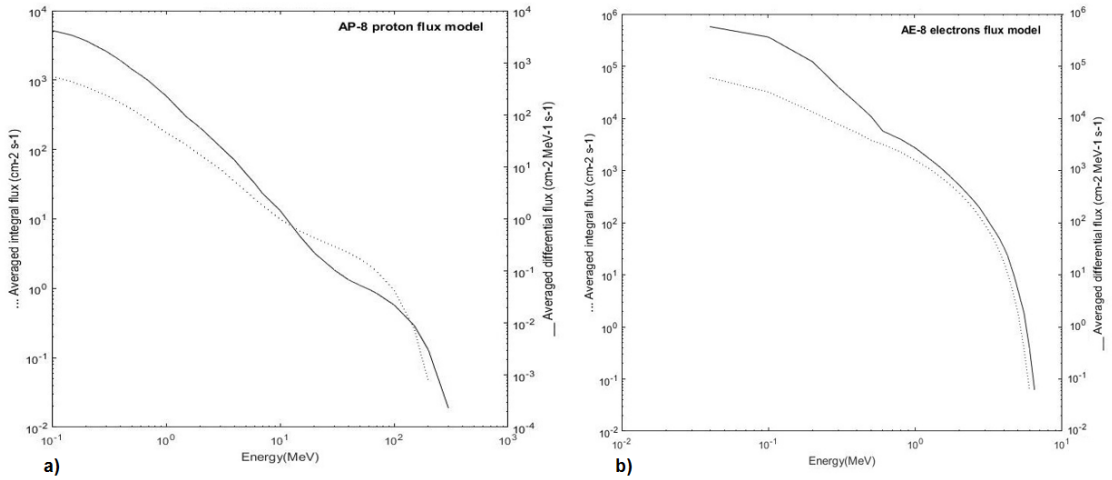

Figure 1.6. a) Protons and b) electrons fluxes in the inner Van Allen Belt simulated with SPENVIS by using AP-8/AE-8 models (for more details see section 1.4.1).

The inner belt is characterized by a very interesting feature: the axis joining the north and south poles is tilted 11° from the rotational axis of the Earth, inducing a 500 km offset of the belts' geomagnetic center compared to the Earth's geometric center. Consequently, the inner Van Allen belt makes its closest approach to the surface of the Brazilian coast in a region called the South Atlantic Anomaly (SAA). The inner boundary may go down to roughly 200 km above the Earth's surface, causing a disruption of the particles fluxes, which become more intense (see Figure 1.7) [9].

The intensity of trapped particles fluxes is subject to large fluctuations at times of increased solar activity. At solar maximum the greater insolation leads to expansion of the upper atmosphere and enhances trapped proton losses at low altitudes. Therefore, the radiation hazard associated with trapped particles is less at solar maximum, as explained before for GCRs.

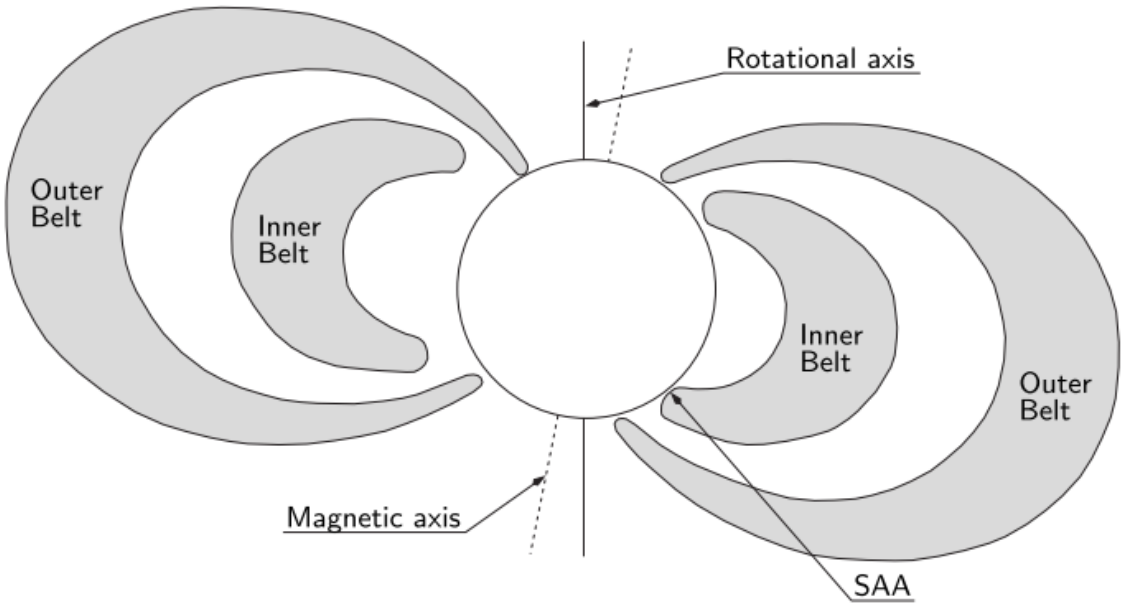

Figure 1.7. Image courtesy of NASA: The South Atlantic Anomaly closest approach to Earth's surface.

1.1.2 Radiation shielding in the Earth environment

Protection against cosmic radiation is provided naturally by three elements in our solar system. The strength of the natural shielding can be described from an Earth's point of view, considering different orbits. Three main orbits are classified based on the distance from the Earth's surface: the Low Earth Orbit (LEO) extends up to 2,000 km altitude, the Medium Earth Orbit (MEO) covers the range from 2,000 to 36,000 km altitude, where eventually the Geomagnetic Earth Orbit (GEO), also called geostationary orbit is found at 36,000 km, and finally the High Earth Orbit (HEO) above 36,000 km altitude. However, considering further manned explorations with destination the Moon, or Mars, the extremely big distance from the surface of the Earth makes this classification no longer valid.

The first element providing shielding to incoming cosmic rays once humans leave the Earth is the Earth's atmosphere itself, which consists of a number of layers with distinguishable properties. Three-quarters of the atmospheric mass reside within the first layer called troposphere, whose thickness varies between 17 km at the equator and 7 km at the poles. The second layer called stratosphere, from 20 to 50 km, includes the ozone layer where ultraviolet rays are absorbed and from 50 to 85 km most meteors burn up in the mesosphere. Above 85 km altitude extends the thermosphere till the base of the exosphere at 690 km. Within this layer exist areas where high-energy ultraviolet radiation causes photoionization and photo-dissociation of atoms and molecules, generating ions, reason why take the name of ionosphere. The ionosphere represents a big catalyzer for incoming radiation as does not absorb them but ionizes them causing interference with communication signals and satellites, as well as can prematurely decay spacecraft orbits and expose astronauts to radiation-borne health risks. Finally, the exosphere is the uppermost region of Earth's atmosphere which gradually fades into the vacuum of space, merging with the planet's magnetosphere [11].

The interaction of cosmic rays with atoms and molecules in the atmosphere has two opposite effects: the absorption of low energy radiation, but also the fragmentation of high-energy particles into secondary particles of lower energy

through spallation processes, which initiate a cascade (see Figure 1.8). These two effects neutralise each other the closer we go to the Earth's surface. The mass thickness of the air above a given altitude is called atmospheric depth, and is proportional to the air pressure at that point. It decreases approximately exponentially as altitude increases. At sea level, the atmosphere provides around 1000 g/cm^2 shielding: the dense layer of atoms and molecules induces many more collisions with incoming particles, which are eventually absorbed by the atmosphere or reach the ground with extremely low energy, making life safe on our planet. Astronauts leaving the Earth's surface find themselves travelling through a less dense atmosphere, which has a reduced efficiency in absorbing cosmic rays and consequently are exposed to high level or ionizing radiation. An intermediate scenario refers to aviation: the ambient radiation increases by approximately 15% for each increase of 600 m in altitude, depending on latitude [12, 13]. Immediately above a commercial flight altitude, at 19 km altitude, which corresponds an atmospheric depth of 58 g/cm^2, the primary proton flux is reduced to about half of the outer-space incident flux, the alpha particle flux to about a quarter, and the heavy ion flux to about 3% or less, depending on the mass of the ion. However, as already said, a particles cascade of lighter nuclei, protons, neutrons, charged and neutral pions, kaon and barions, is initiated. Further interactions can produce electron-positron pairs, giving rise to an electromagnetic cascade of electrons, positrons and photons (see Figure 1.8).

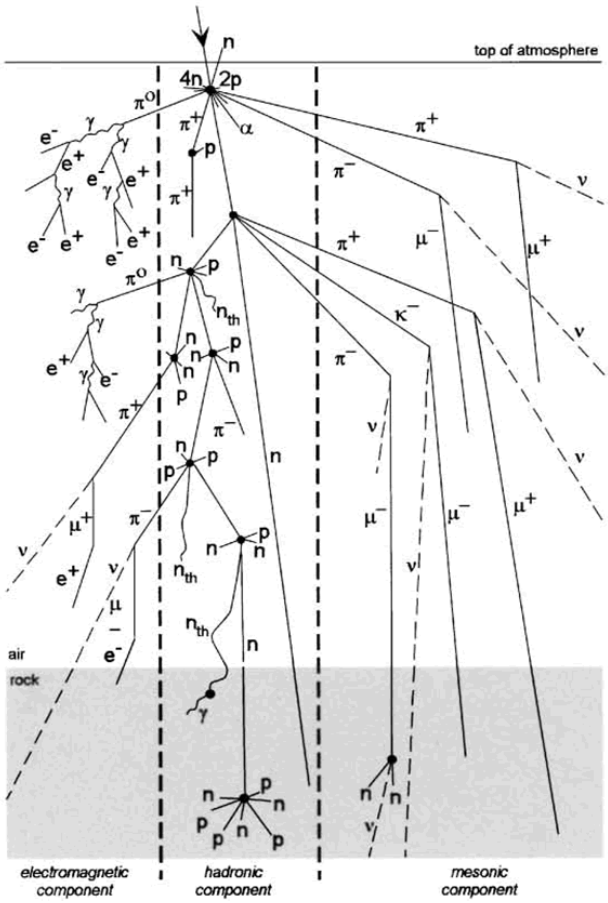

Figure 1.8. Image courtesy of (P. H. Blard, 2006) [14]: example of a particle cascade induced by a neutron collision within the atmosphere.

As mention before, the outermost layer of the atmosphere merges with the magnetosphere, which is identified as the region where the geomagnetic field of the Earth (geomagnetic field) dominates over the interplanetary space one. The joint work of currents generated by the geomagnetic field provides a complex and asymmetrical shield from incoming charged cosmic particles from outer space as it deflects them acting together with the solar wind, a stream of charged particles emitted from the sun. Due to the dipolar nature of the geomagnetic field and its inclination of 11° from the Earth's rotational axis, shielding varies depending on the geographic position. The vertical cut-off rigidity R is the quantity that describes the momentum of a vertically incident particle and its resistance to deflection by a static magnetic field. It is defined as the product of the magnetic field B expressed in Tesla and the gyroradius ρ of the particle due to this field expressed in (Kg m s-

[1] C^{-1} T^{-1}), or the product of the particle momentum p in GeV c^{-1}, and q is its charge in C [15].

$$R = B\rho = p/q \tag{1.1}$$

The action of the static magnetic field perpendicular to the velocity vector of the particle, causes a perpendicular force to both velocity and field, defining a plane through which the particle moves. The units for the vertical rigidity are Tm or GV. At equatorial latitudes the geomagnetic field is almost parallel to the Earth's surface, thus vertically incident particles with rigidity less than 15 GV are reflected back into space. Around the magnetic poles, where the geomagnetic field is nearly vertical, the vertical cut-off rigidity approaches zero and the maximum number of primary cosmic rays can reach the atmosphere [16] (see Figure 1.9). As a result, cosmic radiation levels are higher in polar regions and decline towards the equator. However, the geomagnetic field fades with distance from the Earth, thus provides shielding from cosmic radiation in LEO, partially in MEO and completely absent in GEO/HEO.

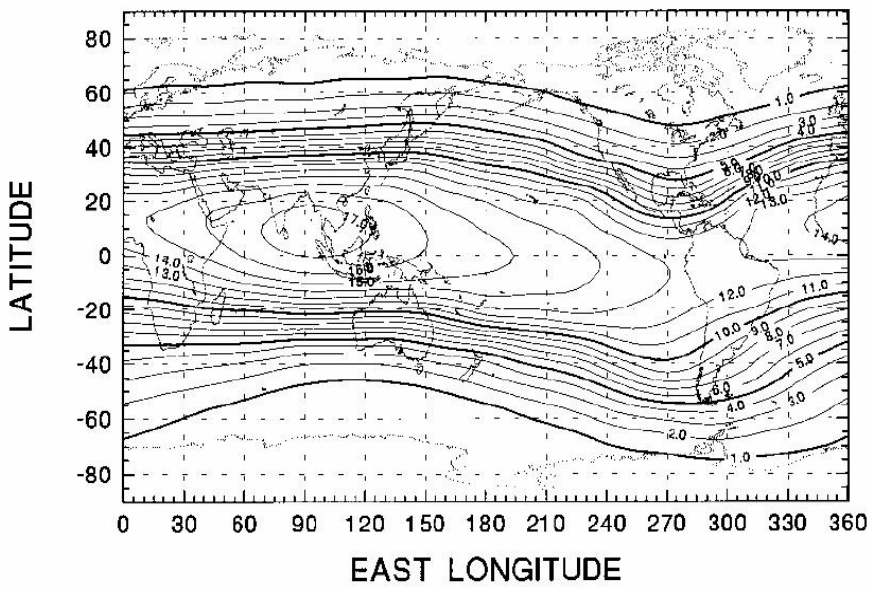

Figure 1.9. Image courtesy of (D. F. Smart et al., 2007) [16]: iso-rigidity contours for vertical cut-off rigidities depending on latitude and longitude.

Finally, the Sun's activity influences the intensity of the flux of cosmic radiation on a cyclic base. The Sun has an electromagnetic field with a basic dipole component that reverses direction every 11 years identifying a solar cycle. In each cycle, the strength of the magnetic field of the Sun varies and produces sunspots. Sunspots correspond to a concentration of magnetic field fluxes where emissions of plasma occur and particles are carried in space with their own convoluted electromagnetic field (solar wind). The population of sunspots quickly rises in what is called the solar maximum phase of the solar cycle, producing a more intense solar wind, and more slowly falls during the solar minimum phase of it. During a solar maximum, the Sun's greater electromagnetic field deflects charged particles of cosmic radiation outward through the solar system in a joint action performed by the more intense solar wind that scatters away more efficiently cosmic radiation particles. The result is a reduction of the particle fluxes of GCRs in the inner solar system during solar maxima and conversely, GCRs fluxes are more intense while in solar minima (see Figure 1.10) [17-19].

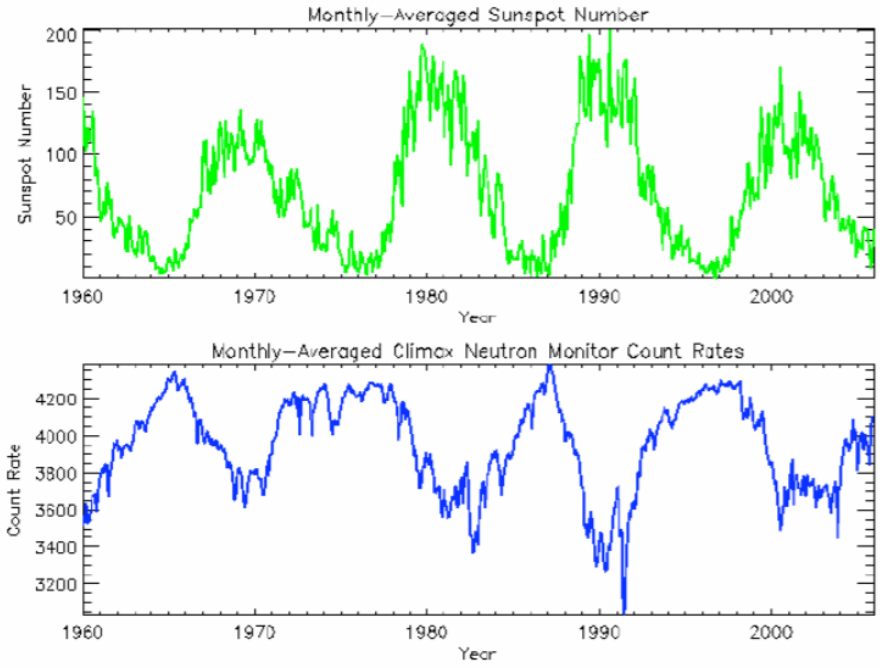

Figure 1.10. Image courtesy of National Research Council [18]: anti-correlation between solar cycle modulation characterized by minimum and maximum phases of sunspots appearance, and local incident GCR flux indicated by the neutron counts recorded by the Climax monitor, Colorado (USA).

However, recent studies showed an interesting quite activity of the Sun during the last cycles that led to a prolonged solar minimum phase between cycle 23 and 24 [20]. The unexpected decrease in the interplanetary magnetic field's strength resulted in a very weak modulation, and consequently shielding, of GCRs. Fluxes of GCRs reached the highest level of the last 25 years causing a consistent variation in the prediction of the dose rates. Events like that need to be taken into account for astronauts' radiation protection as they might vary considerably the exposure during permanence in space and decrease the number of days safely spent by an individual.

The shielding of GCR relies on the natural modulation related to the Sun activity, whereas SPE are unpredictable and shielding can only occur through artificial barriers. GCR energy peaks are around tenth of GeV/u making the spacecraft shielding inefficient to stop energetic heavy ions, or inducing fragmentation of even more hazardous particles form a radiobiological point of view. SPEs instead, have lower energies but higher intensities thus are more likely to be stopped by implemented physical shields and pose a hazard for more exposed area of the spacecraft of during Extra Vehicular Activities.

1.2 Radiation protection in space and aviation

The International Commission for Radiological Protection (ICRP) has noted a convention to distinguish different kinds of exposure that a person can incur during a lifetime. Since 1990, in the Publication 60 [21] three definitions have been used: occupational, medical and public exposure.

Occupational exposure refers to any kind of exposure to radiation incurred at work as the result of situations that can reasonably be regarded as being the responsibility of the operating management. Exposure to natural sources as potassium-40 in the body, cosmic rays at ground level, and radionuclides in the earth's crust are all outside any reasonable scope of control. However, whenever a worker is particularly exposed to such natural sources, more than the public, the

person must be included in the occupational exposed workers' definition. Four particular classes of workers are considered to be monitored under practical guidance:

- workers in workplaces where radon needs particular attention;
- workers dealing with storage of materials not usually radioactive but that contain significant traces of natural radionuclides;
- workers attending aircraft flight;
- workers attending space flights.

The Commission states that: “medical exposure is confined to exposures incurred by individuals as part of their own medical diagnosis or treatment and to exposures (other than occupational) incurred knowingly and willingly by individuals helping in the support and comfort of patients undergoing diagnosis or treatment” [21]. Finally, the public exposure encompasses all exposures other than occupational and medical.

For this thesis purposes, from now on we will focus on occupationally exposed workers in the space and aviation industry. To control the exposure, dose limits are needed: for this reason, the Commission established for a particular set of practices, a level of dose above which the consequences for an individual are considered unacceptable. Generally, the term “unacceptable” associates with all consequences linked to a variation of the average mortality for a particular category of workers in that particular environment. The probability of an attributable fatal cancer and the average period of life lost if the attributable fatality occurs is also a parameter to define dose limits age and sex-dependent. The dose limit is usually defined on an annual base over a working lifetime of 47 years, based on models that take into account environmental, metabolic and dosimetric factors.

1.2.1 Air crew

Considering that the number of frequent passengers will continue to increase and aircraft technology will enable planes to fly during more time and at higher altitudes, aircraft crew and passengers' cosmic radiation exposures are bound to increase in the future. The basic protection strategy recommended by the ICRP

implies following the requirement of maintaining the exposure as low as reasonably achievable (ALARA principle).

However, limits in term of dose need to be defined, as the assessment of the total collective annual effective dose of aircraft crew in the world is estimated to be 70–80% of all recorded occupational doses worldwide [22]. Each country contributes differently according to their aviation industry, respecting the dose limit fixed by the ICRP in a range of 5 to 10 mSv/year. An example of average and maximum annual dose recorded by some European countries is shown in Figure 1.11: Germany recorded the highest maximum effective dose of 7 mSv, and all the other countries' average dose varies between 1 and 2.5 mSv. Around the same period of time, the average effective dose for aircraft crew in the USA is comparable and was estimated to be 3.1 mSv for 2006, In Japan, the annual crew doses were evaluated for the year 2007: 1.7 mSv on average and 3.8 mSv at maximum for pilots, and 2.2 mSv on average and 4.2 mSv at maximum for cabin attendants [23].

According to data recorded in 2009, Germany was the country with the largest number of flight personnel: 66% of the total of occupationally exposed workers in Germany. In Figure 1.12, an interesting comparison is made in terms of a number of workers exposed to a particular dose interval in aviation and in the nuclear industry in Germany. The distribution of individuals exposed to radiation in aviation is relatively uniform along a range of dose up to 5 mSv. In comparison, the underlying exposure conditions in the nuclear industry are typically much more variable than those in aviation. Thus the number of nuclear workers exposed to the level of radiation typical of aviation is extremely lower.

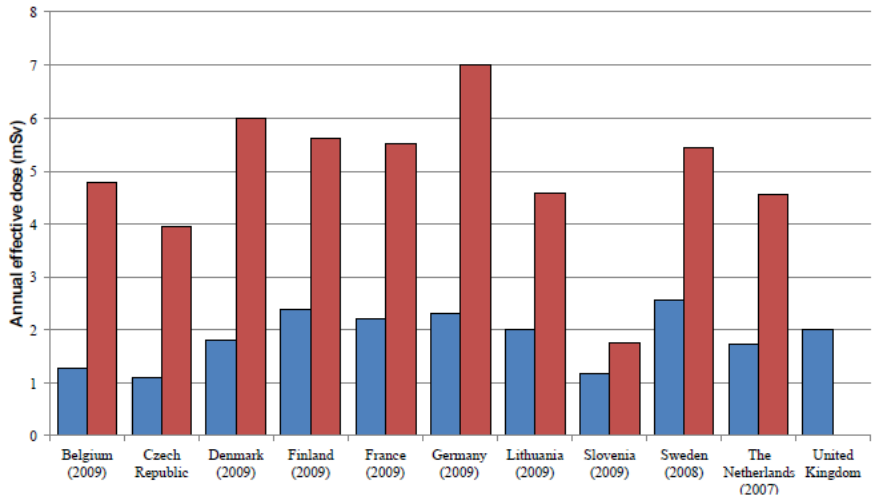

Figure 1.11. Courtesy of ICRP Publication 132 [23]: average (blue) and maximum (red) annual effective dose for crew members in some European countries.

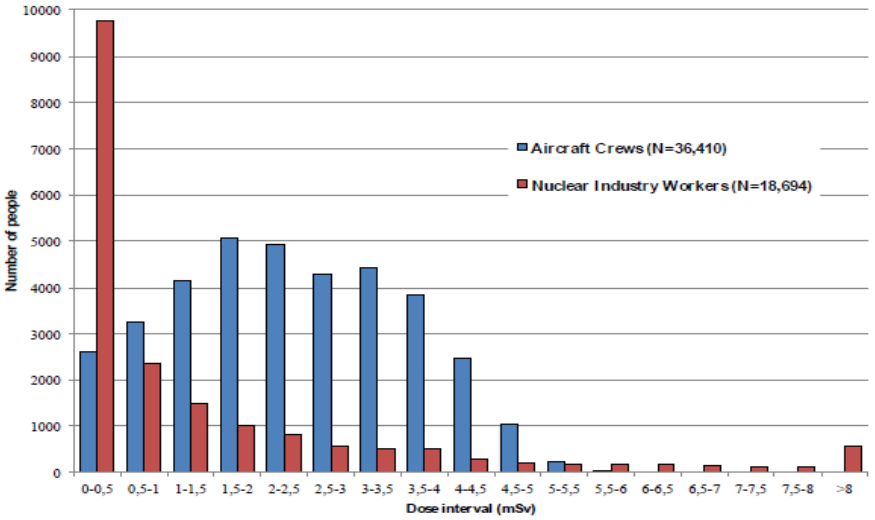

Figure 1.12. Courtesy of ICRP Publication 132 [23]: distribution of dose received in 2009 in Germany by aircrew and the one received by nuclear industry workers. N is the total number of people exposed.

Different approaches are nowadays adopted by federal organizations to regulate the exposure to cosmic radiation in aviation. The majority of airline companies conduct measurements onboard their fleet by using radiation detection, mostly TEPC to directly measure both the absorbed dose in tissue and the radiation quality in terms of linear energy transfer [24, 25]. Other devices have been also used

on-board aircraft to collect data for research purposes such as Liulin-type spectrometers, Thermoluminescent dosimeter (TLD), track detector as the plastic CR39, Bonner spheres and other types of radiation detectors [26-32]. The characterization of devices before measurements could be taken on-board is usually performed in ground-based facilities that provide a radiation field similar to the cosmic one at commercial flight altitude. For example, since 1992 the CERN-EU high-energy Reference Field (CERF) [33] represented the reference facility for the calibration and intercomparison of detectors in wide energy broad neutron fields typical of aviation [34-36].

However, experimental data are often compared with estimated dose values obtained from a calculation using computer codes that use specific parameters related to flight routes. For example, the latest CARI-7 program from the United States Federal Aviation Administration calculates the effective dose from GCRs based on an anthropomorphic phantom [37]. The European Program Package for the Calculation of Aviation Route Doses (EPCARD) developed by the Helmholtz Zentrum Munchen is used by European organization for the assessment of the effective dose or the ambient dose equivalent and to determine the contribution of the different field components [38]. A program that runs on the Microsoft Excel platform is provided available in Japan is the Japanese Internet System for the Calculation of Aviation Route Doses (JISCARD) for the total effective dose and ambient dose equivalent along a flight path [39]. Also, the semi-empirical Canadian code PCAIRE, Predictive Code for Aircrew Radiation Exposure is a well-recognized code that has been validated against measurements performed on-board on several routes [40]. Finally, the SIEVERT, Systeme d'Information et d'Evaluation par Vol de l'Exposition au Rayonnement cosmique dans les Transports aeriens, is a computerized system for flight assessment of exposure to cosmic radiation in air transport adopted in France to assist airlines in applying the European directive about radiation protection of aircrew members [41]. Many other computer programs and systems are used and a detailed comparison can be found in [42].

1.2.2 Space crew

Individual doses in space are generally higher than in usual exposure situations on Earth, thus, deterministic effects in specific organs, e.g. lens of the eye or skin, cannot be ignored. For comparison, in aviation the average annual dose equivalent that interests a pilot is approximately 5 mSv, whereas if we consider future mission to Mars, that level of dose would be the daily dose equivalent for an astronaut.

The measurement or assessment of doses is fundamental to the practice of radiological protection, but for this particular situation, computer modeling and simulation of the dose, particle fluence, LET distributions are needed in addition [43]. Computational models used to estimate the risk from radiation in space use data from survivors of atomic bombs, as exposed to the highest level of radiation ever measured and available documented follow-up studies on a huge variety of people. Two factors are mainly considered to assess the risk: the quality factor Q of the radiation field that compares the effectiveness of galactic heavy ions with gamma rays and the effective dose. So far, epidemiological studies suggest that the lowest dose value of ionizing radiation at which good evidence of increased cancer risks in human exists is approximately 10 - 50 mSv for acute exposure and around 50 - 100 mSv for prolonged exposure [44]. The ICRP recommends limiting the exposure to 20 mSv annually over 5 years, with a maximum of 50 mSv in any 1 year for occupationally exposed workers. However, for astronauts, the whole body dose is estimated to be 1 - 2 mSv per day during interplanetary travels, and 0.5 - 1 mSv per day on the planet's surface. Hence, a 6 months mission is about 80 mSv, but a Mars mission of almost three years will most likely exceed 1 Sv. An example of risk assessment for future missions to the Moon and Mars is presented in Table 1.1, as the outcome of a study from (F. A. Cucinotta and M. Durante, 2006). The individual dose for astronauts was calculated considering the body inside a spacecraft (5 g cm^{-2} aluminum thick) in solar minimum condition, alias, the maximum intensity of GCRs. Usually, the maximum level of risk acceptable for astronauts is set at 3% fatal risk, meaning the risk of mortality for cancer, but other risks for degenerative diseases causing uncertainties can preclude the conducting of a mission [45].

Table 1.1. Reproduced from (F. A. Cucinotta et al., 2006) [45]: example of radiation risk assessment for men and women during lunar and Martian missions.

	Absorbed dose (Gy)*	Effective dose (Sv)	Fatal risk, % (95% CI)	
			Men (age 40 years)	Women (age 40 years)
Lunar mission (180days)	0.06	0.17	0.68% (0.2-2.4)	0.82%(0.24-3.0)
Mars orbit (600days)	0.37	1.03	4.0%(1.0-13.5)	4.9%(1.4-16.2)
Mars exploration (1000days)	0.42	1.07	4.2%(1.3-13.6)	5.1%(1.6-16.4)

Calculations are at solar minimum, where GCR dose is highest behind 5 g/cm^2 aluminum shield. *Mean for tissues known to be sensitive to radiation and at risk of cancer including lung, colon, stomach, bladder, bone marrow, and breast and ovaries in women. Competing causes of death are included in calculations because they decrease risk probabilities if high (i.e.,>5%).

Table 1.2. Reproduced from (Y. F. Ali et al., 2020) [44]: limits on effective dose adopted by NASA and JAXA for 1-year mission.

Agency	Personal traits				
	Gender	Age			
		30	40	50	60
NASA	M	0.78	0.88	1.00	1.17
	F	0.60	0.70	0.82	0.98
JAXA	M	0.60	1.00	1.20	1.20
	F	0.60	0.90	1.10	1.10

Limit values are estimated not to exceed a 3% Risk of Exposure Induced Death (REID) from fatal cancers at a 95% confidence level. Dose limits are expressed in Sv.

The peculiar situation in space requires special recommendations to be issued regarding accumulative dose limits for astronauts to prevent deterministic effects induced by radiation. Each national space agency adopts different limits obtained through different methodologies (computing simulation, measurements, epidemiological studies, etc) [46]: for example, the Chinese Space Agency (CSA), the European Space Agency (ESA) and the Russian Federal Space Agency (RFSA) agree on a single career dose limit of 1 Sv for all genders and ages [47], while NASA

and the Japanese Aerospace Exploration Agency (JAXA) use different limits [44], summarized in Table 1.2.

A solution to reduce the uncertainties in risk assessment is to perform calculations and experiments at a molecular level. The study of the interaction of radiation with cells inducing damages in the DNA chain is essential to improve the understanding of cancer occurrence and then identify potential deterministic effects post-exposure: the probability of chain breaks, chromosomal alterations, repairs, are related to the LET of particles, which varies along the particle's track itself. Depending on the type of particles and interaction with matters, tracks can be more or less densely concentrated: the ionization process along the track produces delta electrons, which can laterally spread. These electrons extend over a larger region, deposit energy, and induce radiobiological effects further from the incoming particle's track. This increment of ionization density is typical of HZE ions as can be observed in Figure 1.13b: the heavier the ion, the higher the ionization density. This reflects in Figure 1.13a: the human nuclei exposed to silicon and iron ions present a clear dense track where each green dot represents a DNA double strand break. The very high LET of these particles reduce the spacing between the DNA breaks and consequently reduce the probability of repair. Whereas, sparsely ionizing radiation as gamma rays are uniformly distributed in the nucleus [48].

The relative biological effectiveness (RBE) depends on the type of particles, energy and of course type of tissue, so eventually depends on the more or less dose rate. RBE factors can be used for the evaluation of either cancer risks, hereditary risk, or any other harmful deterministic effect [49].

Finally, to pursuit with coherence the need of expanding the knowledge about cancer risk assessment in space and aviation, a micro-scaled approach is recommended, such as microdosimetry. Reason why in the next section it will be discussed the theory of microdosimetry followed by the overview of instrumentation used in space and aviation starting from the standard gold instrument tissue proportional counter to the new silicon on insulator microdosimeters used for this thesis.

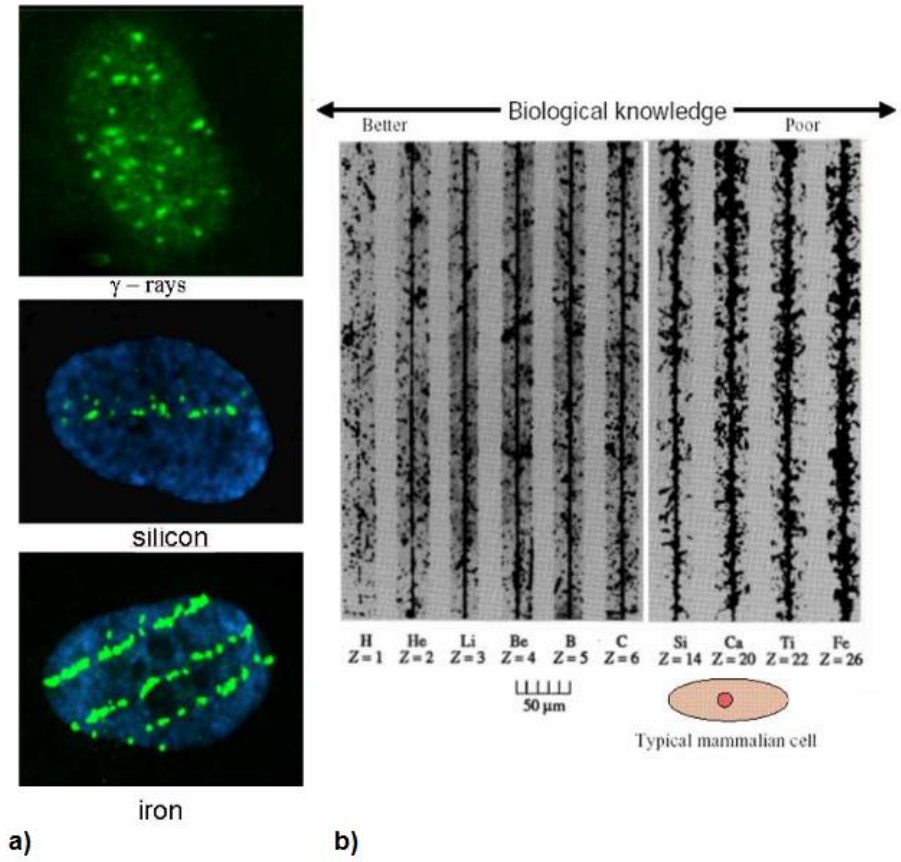

Figure 1.13. Image courtesy of (F. A. Cucinotta et al., 2019)[48]: a) track structure of gamma rays, silicon ion and iron ions crossing a nucleus of human fibroblast, and b) tracks of different ions, form protons to iron, in nuclear emulsions show the increase of ionization density along the track due to higher production of delta electrons.

1.3 Microdosimetry

1.3.1 Theoretical approach

The radiation protection of astronauts and aircrew members in terms of effects induced on human health is challenging requiring an approach at a cellular level as already discussed in the previous section 1.2.2.

The effectiveness of energy transfer by ionizing radiation to atoms inside the human body is unique due to its highly concentrate ejection of electrons and nuclear constituents all along the track of the charged particles. The distribution of the energy deposited in a target and the consequent level of biological induced effect varies between different types of ionizing radiations. Even though the quantity *absorbed dose,* defined as the mean energy $d\bar{\varepsilon}$ deposited in a macroscopic target of volume of mass dm is the standard dosimetric quantity to describe the overall amount of radiation dose, it does not give information about microscopic interaction of radiation with biological cells and effects induced in the target as the human one. Thus, the macroscopic quantity absorbed dose is defined as following and expressed in Gray, (Gy), obtained from J/kg:

$$D = \frac{d\bar{\varepsilon}}{dm} \tag{1.2}$$

Nevertheless, in the last century, microdosimetry was founded by H. H. Rossi to aim the measurement and quantification of the spatial and temporal distribution of the energy deposited in the matter through a system of new concepts and physical quantities that bring together dosimetry and radiobiology [50]. Firstly, the regional microdosimetry was based on the concept of specified dimension sites in which the energy is deposited regardless of its microscopic distribution. Secondly, the termed structural microdosimetry originated by A. M. Kellerer, included the description of the pattern of energy deposited by secondary radiations in branches of the primary particle track, and related effects. Radiation effects depend on changes or alterations of the matter pattern where discrete ionization interactions occur, in the so-called transfer points. The number and location of those points influence the probability of an effect to happen. For this reason, microdosimetry employs the concept of *energy deposition event*, meaning the production of statistically correlated transfer points. Thus, the energy deposited in an event ε is the sum of all energies deposited by the charged particles and its secondaries in a delimited region called *site* of mass m.

The microdosimetric quantity *specific energy*, z (Gy), is then the quotient of ε by m:

$$z = \frac{\varepsilon}{m} \tag{1.3}$$

Additionally, another stochastic quantity called *lineal energy* y (keV/µm) is defined as the energy imparted a single event ε divided by the *mean chord length* $\bar{l}$, meaning the average length of randomly oriented chords in a volume exposed to an isotropic field of infinite straight lines:

$$y = \frac{\varepsilon}{\bar{l}} \tag{1.4}$$

that for a convex body of volume V and surface S is given by the Cauchy's:

$$\bar{l} = \frac{4V}{S} \tag{1.5}$$

Because microdosimetry is a stochastic approach, the probability distribution of quantities must be defined. The probability that the lineal energy y produced by an event in the interval $[y,\ y + dy]$ is $f(y)dy$, where $f(y)$ is the *frequency distribution* leading to the formulation of the *frequency-mean lineal energy* $\bar{y}_F$:

$$\bar{y}_F = \int_0^\infty y\, f(y)dy \tag{1.6}$$

Using the same approach, the *dose distribution* $d(y)$ and the *dose-mean lineal energy* $\bar{y}_D$ can be determined by:

$$d(y) = \frac{1}{\bar{y}_F}\, y\, f(y)dy \tag{1.7}$$

$$\bar{y}_D = \int_0^\infty y\, d(y) dy \tag{1.8}$$

The dose-mean lineal energy can also be expressed as:

$$\bar{y}_D = \frac{1}{\bar{y}_F} \int_0^\infty y^2\, f(y) dy \tag{1.9}$$

All the microdosimetric quantities are stated in the International Commission on Radiation Units and Measurements (ICRU) report 36, 1983 [51].

The somewhat similar non-stochastic quantity *Lineal Energy Transfer (LET)* is not simply the same as the lineal energy y, because the LET defined as dE/dx represents the mean energy dE lost in an electronic collision by a charged particle traversing a distance dx, hence it includes the energy transferred to delta radiations. However, to exclude the kinetic energies of these electrons, we need to fix a cut-off Δ and consequently consider the *restricted linear energy transfer* L_Δ. Also, the lineal energy y is subject to geometric cut-off: the energy ε is the one deposited in the selected site during the event, but the statistic of particle belonging to that event is influenced by the size of the site. If the size is too big, some particles may not entirely traverse the volume, and if it is too small, the concept of particle track becomes vague. Microdosimetry usually adopts a spherical volume of 1 µm diameter size. So, in the most extreme simplified case, where we assume that the track of the particle is rectilinear, equal to the site's dimensions, and the energy loss is continuous and confined to the track, the LET can only characterize the mean energy deposited in traversals. It excludes the possibility of a track curvature due to delta electrons and underestimates the energy deposit. Finally, of great importance in microdosimetry is the process of straggling: charged particles lose energy discontinuously and in small sites comparable to the DNA molecule the fluctuation in energy deposited can be extreme.

Nevertheless, a quantity able to weight absorbed doses by their biological effect is needed and the ICRU [52] defined the *dose equivalent* H by:

$$H = \bar{Q} * D \tag{1.10}$$

where the $\bar{Q}$ is the average q*uality factor* and D is the absorbed dose. The quality factor is dimensionless but to avoid confusion between absorbed dose and dose equivalent, it was established a different name for units of H, which is expressed in Sievert (Sv). The definition of the quality factor Q reflects the relative biological effectiveness of different types of radiation and it is usually given as a function of the unrestricted LET as follow:

$$\bar{Q} = \frac{1}{D} \int_{LET=0}^{\infty} Q(LET)\, D_{LET}\, dL \tag{1.11}$$

where D is the absorbed dose, D_{LET} is the distribution of D in unrestricted LET, and $Q(LET)$ is the quality factor as a function of the LET. By definition of LET, the integration is performed over D_{LET} due to all charged particles, excluding their secondary electrons [43]. Particularly the latest Publication 60 of the International Commission on Radiological Protection (ICRP) stated a well-defined dependence of Q to the LET shown below [21]:

Table 1.3. The ICRP Publication 60 definition of the quality factor Q depending on the LET.

LET (keV/µm)	Q
< 10	1
$10 \div 100$	$0.32\, LET - 2.2$
> 100	$300/\sqrt{LET}$

The ICRU in the Publication 40 defined the quality factor dependent on the lineal energy y, linearly increasing also for LET<10 keV/µm as following:

$$Q(y) = \frac{a_1}{y}\left[1 - e^{(-a_2\, y^2 - a_3\, y^3)}\right] \tag{1.12}$$

where $a_1 = 5510$ keV/µm, $a_2 = 5 \cdot 10^{-5}$ µm^2/keV^2 and $a_3 = 2 \cdot 10^{-7}$ µm^3/keV^3.

However, due to the evidences obtained during radiobiological experiments, the ICRP in a joint task with the ICRU recommended the use of the quality factor dependent on the lineal energy in 1 µm sites, expressed by the formula [53]:

$$Q(y) = 0.3y \left[1 + \left(\frac{y}{137}\right)^5\right]^{-0.4} \tag{1.13}$$

which can be also be approximated in dependence of LET, by entering into the function $Q(y)$ the argument [53]:

$$y = \frac{9}{8} LET + 0.75 \tag{1.14}$$

This definition is recognized by (Kellerer and Hahn, 1988) and shown in Figure 1.14. Although this formulation tries to correlate the notions of LET and lineal energy to cover most possible scenarios, it considers the contribution of energy deposit by delta electrons, but not the effect of straggling or nuclear spallation. For example, the resulting difference between Q(y) and Q(LET) is 5% for the determination of the dose equivalents from secondary neutrons in proton therapy [54]. However, the main advantage in choosing y, rather than LET, is that y can be directly measured, unlike LET needs to be mathematically calculated.

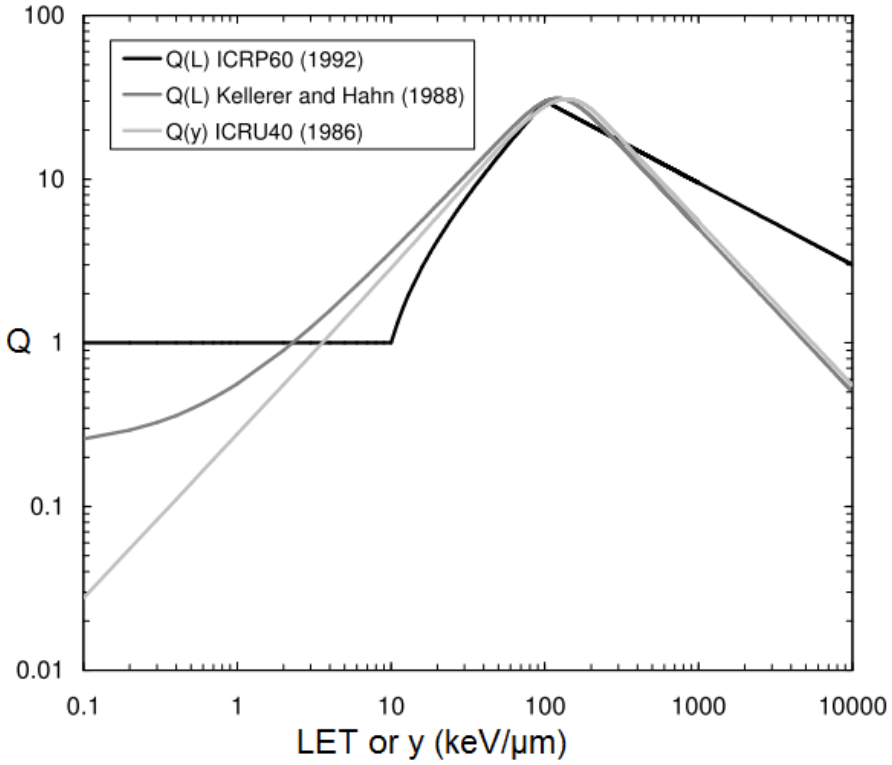

Figure 1.14. Three main definitions of the quality factor Q depending on the LET or the lineal energy y.

Microdosimetry aims to investigate radiation effects in sites comparable to biological cells, thus the effect of Auger electrons emitted from atomic nuclei bound or DNA need to be determined with microdosimetric techniques and quantities which do not average the absorbed dose over the entire mass of the site, regardless the nature of the radiations. Therefore, microdosimetry is a powerful tool to be used for radiation protection purposes thanks to its capability to measure the dose equivalent for any arbitrary single or mixed radiation field, without preliminary knowledge of the field composition, by means of the type of particles and energy. The radiation environment in space and aviation fall into the type of field just cited with the additional feature to be time-varying and compositions as affected by uncontrollable natural events.

In experimental microdosimetry, the microdosimetric spectrum is usually presented in log scale because of the wide range of y and its distribution $f(y)$ value in realistic fields. The graphical display of the spectrum can be presented as:

$$\int_{y_1}^{y_2} f(y)dy = \int_{y_1}^{y_2} [\, yf(y)]\, dlog(y) \tag{1.15}$$

As a consequence, measuring the microdosimetric spectra, the dose equivalent is derived in its logarithmic form:

$$H = D \int Q(y)\, y^2\, f(y)\, d(\log(y)) \tag{1.16}$$

The dose equivalent assumes a particular definition in case of individual monitoring of humans exposed to a radiation field. In fact, the *personal dose equivalent Hp(d),* is defined as the dose equivalent in soft tissue at an appropriate depth *d*, below a specified point on the human body, where the individual dosimeter in worn. Usually, the assessment of the dose equivalent is performed at a tissue equivalent depth of 10 mm for the body and 0.07 mm for the dose to the skin.

As for this thesis purposes, the dose is measured in silicon by a silicon on insulator detector. However, for personal monitoring of humans, tissue conversion factors need to be used to convert the dose in silicon to the dose in tissue-equivalent. Thus the practical definition of the *personal dose equivalent* at a depth d in tissue becomes:

$$Hp(d) = \bar{Q} * (D_{si} * \mathrm{cf}) = \bar{Q} * D_{TE} \tag{1.17}$$

where the *conversion factor cf* applied to the *absorbed dose in silicon* D_{si}, give the corresponding *absorbed dose in tissue-equivalent* D_{TE}.

The conversion factor varies according to the type of radiation and energy and will be mentioned in each of the following studies when necessary.

However, for radiation protection purposes in space, another quantity is often used to describe the overall amount of dose for the whole body, weighting each organ contribution. The *effective dose* E is defined as:

$$E = \sum_T w_T \sum_R w_R * D_{T,R} = \sum_T w_T * H_T \tag{1.18}$$

where H_T, the equivalent dose in an organ or tissue T, is weighted by the weight factor for the organ or tissue w_T, or $D_{T,R}$, the mean absorbed dose in an organ or tissue T from radiation of type R, is weighted by the radiation weighted factor w_R and the organ or tissue factor w_T. The sum is always performed overall organs and tissues, which are considered to be sensitive to the induction of stochastic effect. The units for the effective dose is Sv.

1.3.2 Experimental Microdosimetry

Tissue Equivalent Proportional Counters

The standard gold for microdosimetry is the Tissue Equivalent Proportional Counter (TEPC). The first proportional counter developed by H. Rossi, has a spherical air cavity called sensitive volume (SV) of 2.5 cm diameter filled with low-density gas, typically propane at a pressure of 17 Torr [55], to enhance the gas multiplication up to 10^4. This allows the equivalency to a 1 µm diameter tissue-equivalent SV. The device sees the anode sitting along the internal diameter of the chamber and a bias is applied between the anode and the chamber wall (see Figure 1.15). The multiplication region is limited to the narrow space around the wire and has a radius of the order of a few times ten mean free paths for ionizations. The thinner is the wire, the larger is the electrical field and independent from the geometrical shape of the SV.

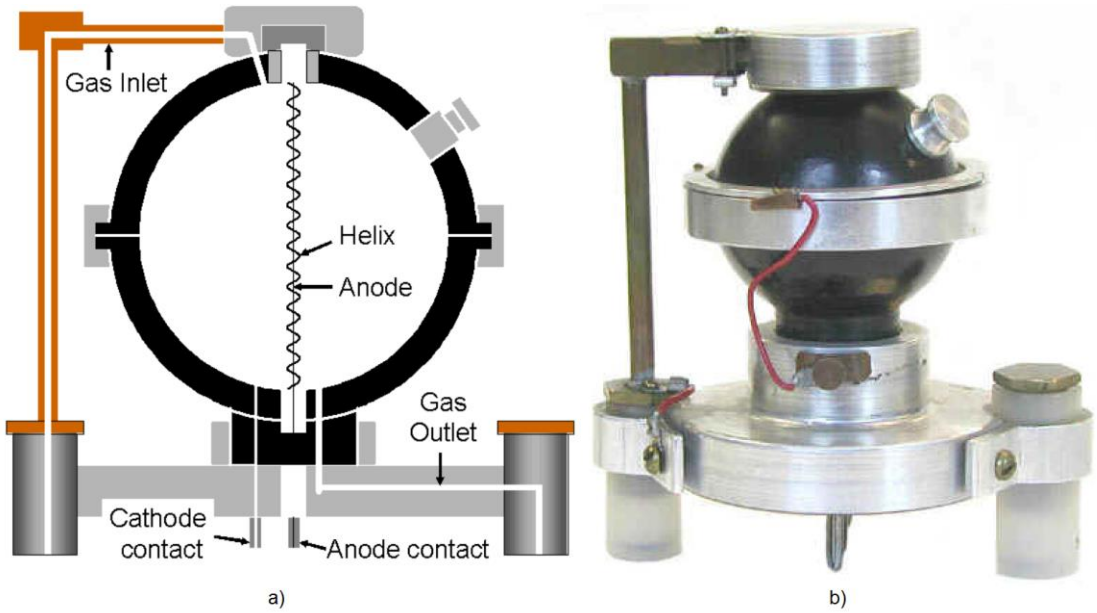

Figure 1.15. a) Schematic of the Rossi Proportional Counter; b) Realistic photo of the typical TEPC.

Nevertheless, the TEPC has several limitations for experimental measurements: firstly, it is bulky and large dimensions make it not always easy to carry, as for example on an airplane or spacecraft, as well as reduce the spatial resolution. It also required high voltage to operate and the filling gas needs to be maintained at low pressure to assure tissue-equivalency. TEPCs suffer also wall effects caused by the scattering of primary and secondary particles, which may cause distortion of the real microdosimetric spectrum. There are different wall effects: the V-effect occurs when a difference between the density of the wall and the cavity induces an increase in nuclear collisions in the wall. Then there are two delta rays effects caused by direct or indirect events: during direct events, the primary charged particles trajectory crosses the cavity and delta electrons created in the wall deposit energy in the cavity; while during indirect events the trajectory of the primary passes outside the cavity but if sufficiently close to the wall interface, delta electrons can penetrate it and deposit energy. Otherwise, if the trajectory is far from the wall surface, delta electrons will be stopped within the wall before reaching the cavity [56].

Silicon on insulator microdosimeters

In the '90s, the Center for Medical Radiation Physics (CMRP), University of Wollongong, started using a new approach for microdosimetry measurements using silicon semiconductor detectors to address the limitations of the TEPC. The silicon microdosimeter operates using a p-n junction characterized by a depletion region, where the electric field exists for collecting electron-hole pairs created by ionizing radiation. However, charge collection does not occur simply via drift in the depletion region, but also diffusion from outside and the funneling phenomenon associated with the injection of high carrier concentration into the device, contribute significantly. This results in a poor definition of the sensitive volume, which can be improved by confining the depletion region to geometrical constrains of the small SV. Based on this concept, the CMRP invented the silicon-on-insulator (SOI) microdosimeter technology. A silicon microdosimeter consists of an array of micron-sized silicon SVs to mimic an array of biological cells. SVs are fabricated as reverse-biased p-n junctions on a bonded SOI wafer of different thicknesses (2, 5, 10 µm) isolated from beneath by a thin layer of SiO_2. Each device has a maximum of 6 arrays, designed has odd and even and can be connected in parallel or readout independently by separate charge-sensitive preamplifiers. This dual-channel readout improves the RBE identification for different high energy ions of the same LET but with different track structure of delta electrons typical for space application [57]. The first generation of SOI was characterized by 2D 30 x 30 µm planar SV as shown in Figure 1.16 and mounted on a Dual In Line (DIL) package. [57, 58]. Preliminary charge collection efficiency (CCE) studies showed diffusion outside the SVs and crosstalk between neighboring SVs, leading to the conclusion that bigger spacing and a guard ring were needed to prevent charge collection outside the designated areas.

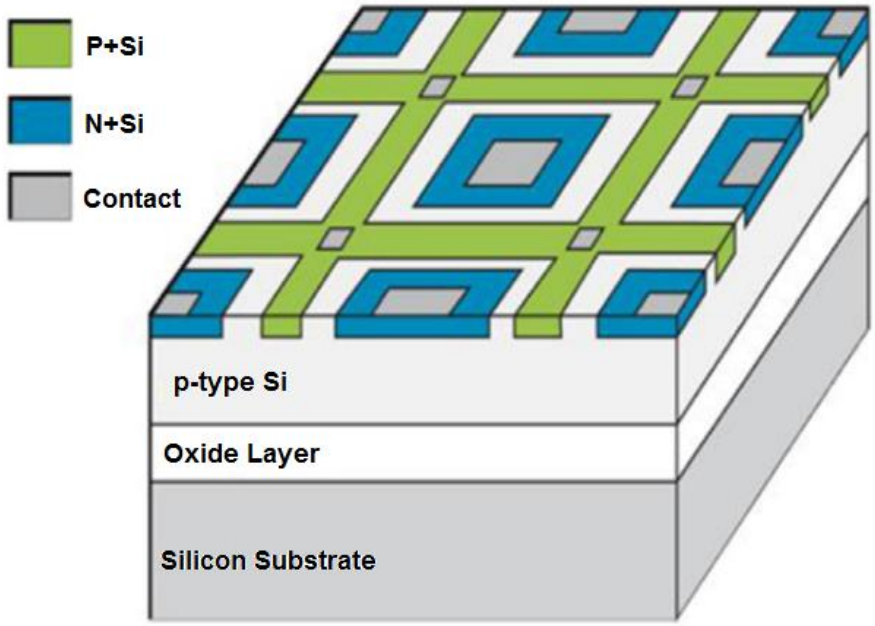

Figure 1.16. The first generation of the SOI microdosimeter developed at the CMRP [57].

The second and third generations were implemented with cylindrical SV that reduced the chord length variance and with a large area of 4 x 4 mm^2. Investigations in mixed radiation fields typical of space, avionics, and hadron therapy showed that SOI microdosimeters match the microdosimetric spectra of conventional TEPC [59, 60]. However, the charge collection sharing between adjacent SVs was still an issue.

The solution of freestanding-on-silicon oxide 3D SVs seemed to be the one to pursuit: with the third generation of SOI called "bridge", it was made an essential step forward. The device was fabricated on a high resistivity n-type SOI active layer and a low resistivity supporting wafer. The large area of 4.1 x 3.6 mm^2 is segmented into three sections to reduce the noise by minimizing the capacitance of each one. The surroundings of the SV were fully etched to a depth of 10 µm with the deep reactive ion etching (DRIE) technique, giving parallelepiped SVs of 30 x 30 x 10 µm dimension connected on top by a bridge, here where the name comes from, to support the aluminum connection (seeFigure 1.17). The DRIE technique is based on the "Bosch process" that sees energetic plasma ions such as sulfur hexafluoride etching the wafer in a nearly vertical direction, followed by a commonly used passivation layer C_4F_8 deposition to protect the vertical sidewalls. With a total of

4248 diodes on a high resistivity n-type active layer 10 µm thick, and low resistivity supporting wafer passivated with SiO_2, the "bridge" showed a 100% charge collection efficiency in the square regions of the 3D SV. Unfortunately, some charge collection was observed in the bridge tunnel due to the high resistivity of the n-SOI silicon.

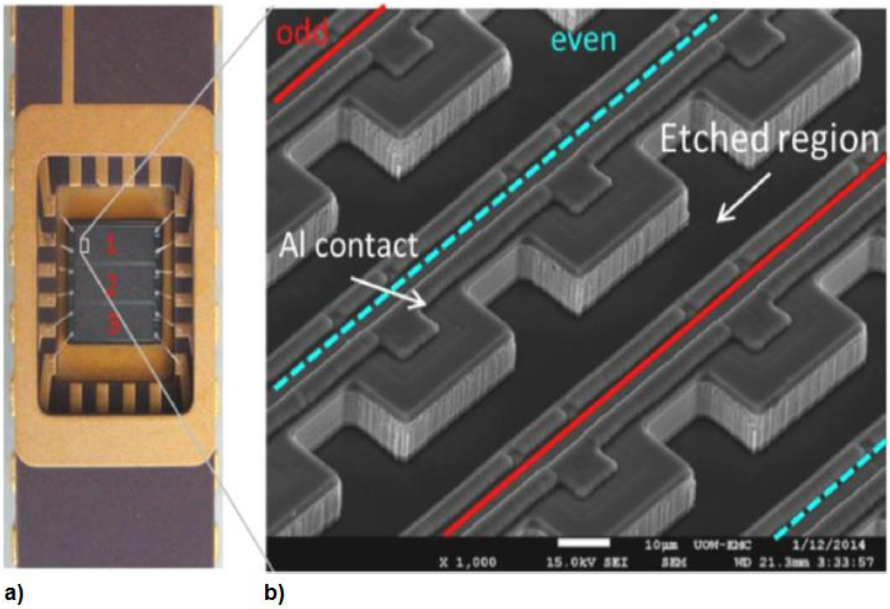

Figure 1.17. a) The SOI "bridge" microdosimeter mounted on a dual-in-line package; b) a SEM image of a part of array of SVs.

The final freestanding design was achieved with the fifth generation of the 3D microdosimeter, which was named "Mushroom". Thanks to well-estalished collaboration with the SINTEF MiNalab, Oslo, Norway, different design of the microdosimeter were fabricated with full 3D cylindrical SVs. The first proposed design shown in Figure 1.18 included the substitution of the silicon support wafer with PolyMethylMethAcrylate (PMMA), in which SVs would have been fully embedded to improve the tissue equivalency of the device. The SV of 10 µm height and 18 µm diameter consists in a n^+ electrode surrounded by a ring p^+ electrode produced using DRIE, followed by polysilicon deposition and doping [57].

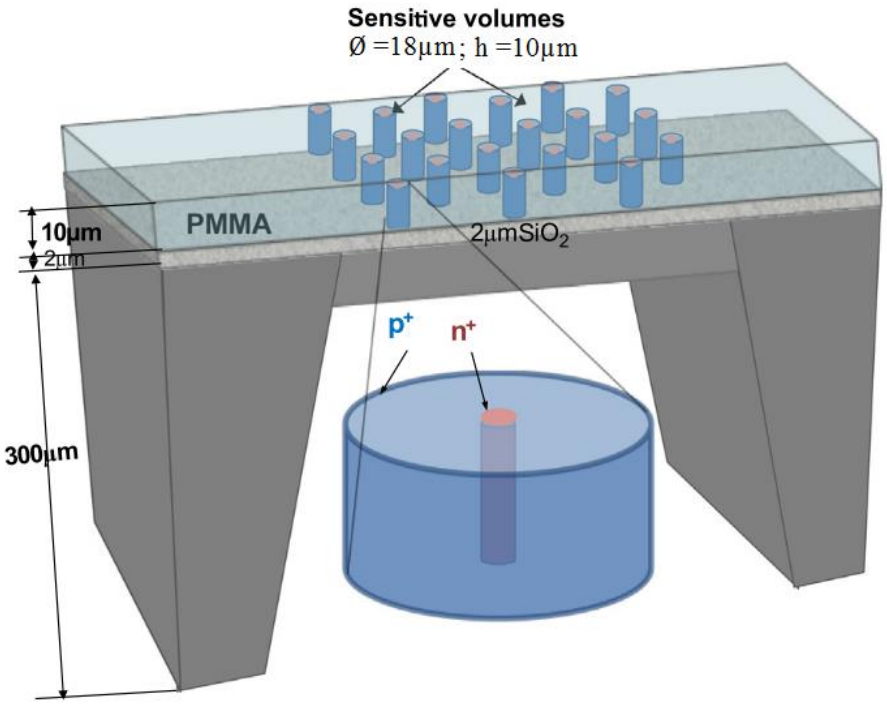

Figure 1.18. Proposed design of the 3D "Mushroom" microdosimeter with cylindrical SVs embedded in PMMA [57].

Figure 1.19 shows the following two designs with different structure of the SVs [61]: the trenched planar 3D structure consists of 3D cylindrical SVs with a planar n^+ core produced by ion implantation (planar technology) surrounded by a complete p^+ doped trench filled with polysilicon (see Figure 1.19a,c). The second structure of the "Mushroom" microdosimeter is called trenched 3D, which also consists of 3D cylindrical SVs with a core column of air and n^+ doping in the inner core walls of the SV center (see Figure 1.19b,d). To avoid the possibility of charge generated outside the SV from being collected, each SV is surrounded by a trench of air with p^+ doping on the outer wall. In this structure, the p+ trench and n+ column of the SV are not filled with polysilicon, therefore the trench cannot be a closed cylinder. In order to electrically connect SVs in an array, two half-moon trenches were made leaving some silicon to allow passage for the metal contacting the inner n+ electrode. Outer Al buses were connected to p+ outer electrodes of 3D SVs. Scanning Electron Microscope (SEM) images clearly showing the structure of the fabricated microdosimeter are shown in Figure 1.19c,d. Both structures have

SVs with diameters of 18 µm or 30 µm, fabricated on a high resistivity p-type SOI with a 5 or 10 µm thick active layer bonded to a low resistivity supporting wafer and 2 µm silicon oxides in between.

During the studies discussed in this thesis, the SOI "Mushroom" microdosimeters designs shown in Figure 1.19 were used and details about the SV dimensions will be mentioned in each chapter.

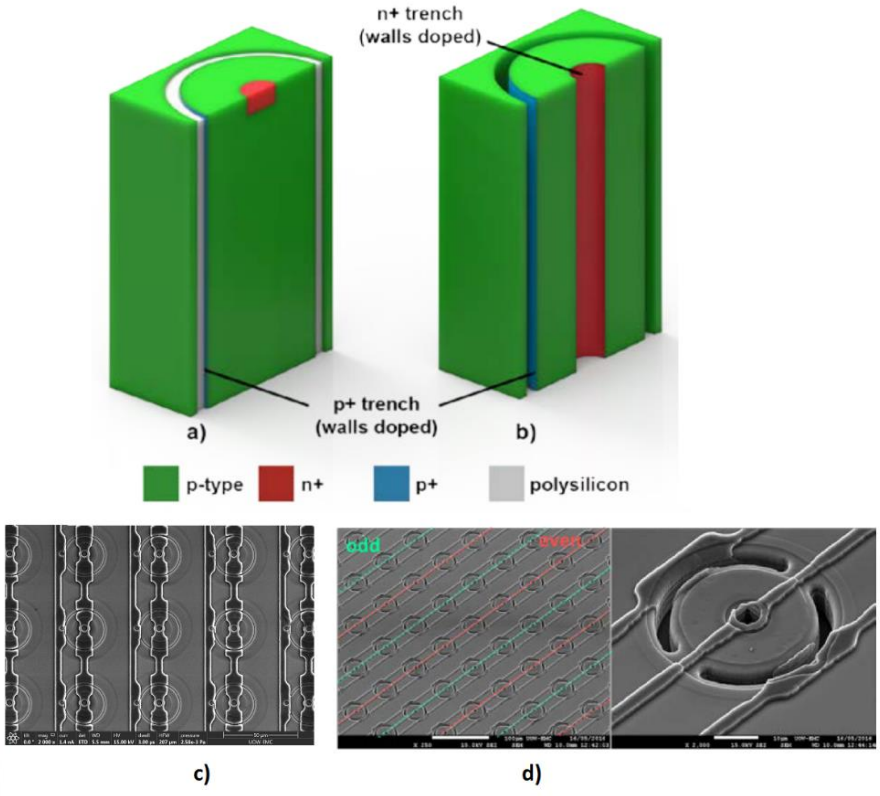

Figure 1.19. a) Simplified schema illustrating the SV geometry of a trenched planar structure, and b) trenched 3D structure; c) Scanning electron microscope (SEM) image of the "Mushroom" filled with polysilicon and d) "Mushroom" filled with air.

The SOI microdosimeters are always mounted on a 2 mm DIL package which is plugged at the end of a printed circuit board (PCB). The resulting low noise spectroscopy-based readout electronics is called MicroPlus probe (or μ^+ probe) shown in Figure 1.20[62]. The probe is then usually connected to a preamplifier and

a shaping amplifier that eventually send the signal to a Multi Channel Analizer (MCA) to process the signal through a software on a laptop.

During the discussion of this thesis, it will be used the term MicroPlus probe to identify the electronics including the connected SOI microdosimeter.

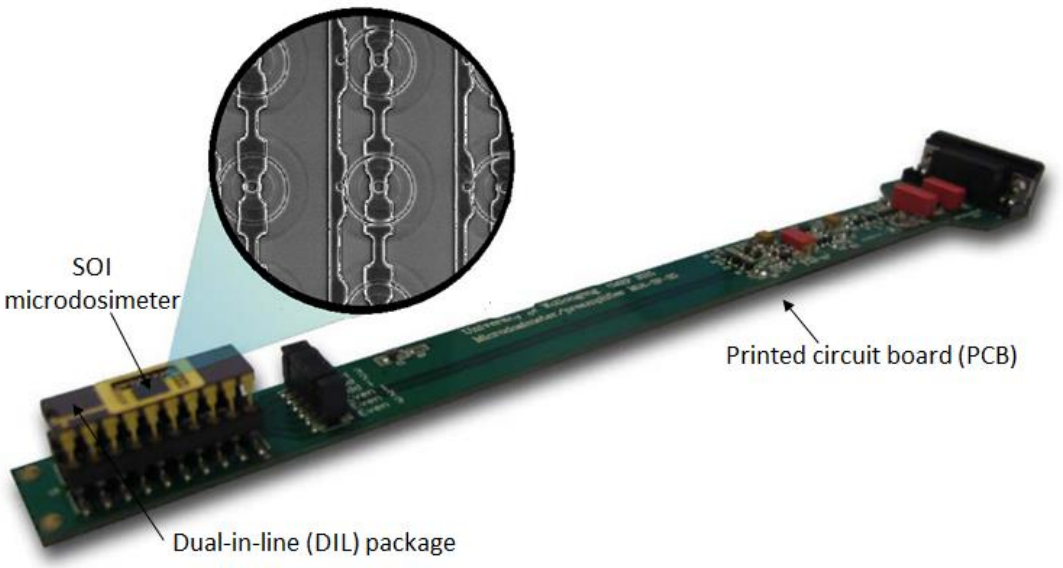

Figure 1.20. Image reproduced from (L. Chartier et al., 2017) [62]: MicroPlus probe, the microdosimetric probe with the SOI "Mushroom" microdosimeter connected at the left end. A zoomed-in Scanning Electron Microscope (SEM) image shows a top view of SVs array of the microdosimeter.

Chapter 2

Modeling of Low Earth Orbit radiation environment

In this chapter, results published in the paper from S. Peracchi et al., "Modelling of the Silicon-On-Insulator microdosimeter response within 1 the International Space Station for astronauts' radiation protection," Radiation Measurements, vol. 128, 2019 [63], are presented and discussed.

As the first author of this Elsevier article, I retain the right to include it in the thesis, provided it is not published commercially. Permission is not required, and the article is reproduced from the journal Radiation Measurements. The link to the version of record on ScienceDirect with the Creative Commons CC-BY-NC-ND license for author manuscript can be found at DOI: 10.1016/j.radmeas.2019.106182

For the first time the response of the 3D "Mushroom" microdosimeter was investigated in the radiation environment encountered inside and outside the Columbus module of the ISS, by using SPENVIS and GEANT4 simulations. Tissue-equivalent microdosimetric spectra of GCRs, SPEs, and trapped protons were obtained to estimate the dose equivalent delivered to the astronauts.

2.1 Introduction

Astronauts are exposed to high energy cosmic radiation, which may have harmful health effects. As already discussed in details in section 1.1.1, at the altitude of the International Space Station (ISS), there are three main radiation sources. Galactic Cosmic Rays (GCRs) are a constant component of the radiation field made up of approximately 87% protons, 12% helium nuclei and 1% heavy ions (e.g. C, O, Si, Fe) with a wide energy range, up to hundreds of GeV/n. Solar Particle Events (SPEs) mainly consist of protons emitted by the Sun during periods of intense activity, with energies up to hundreds of MeV [64]. Because of the Earth magnetic field, protons and electrons are trapped in the Van Allen Belts.

Recent research predicts that the cosmic rays exposure during long space missions outside the Earth's magnetosphere, as to Mars, can double the cancer risk [65]. It is therefore paramount to characterize cosmic radiation and its effects on astronauts' health. A powerful approach to determine the effect of space radiation in astronauts is microdosimetry [50]. Tissue Equivalent Proportional Counters (TEPCs) are currently the standard for experimental microdosimetry. TEPCs have a large spherical volume suitable for low particles fluxes and filled with tissue-equivalent gas. Nevertheless, TEPCs have relatively large dimensions which reduce the spatial resolution and introduce wall effects. In addition, the system complexity requires a high voltage supply [58].

The 3D sensitive volumes (SVs) "Mushroom" microdosimeter is investigated in this study [9], with the intent to characterize, for the first time, its response in the radiation environment typical of the ISS. Here, I report the results emerging from the characterization of the radiation environment inside and outside the Columbus module of the ISS, and the microdosimetric response of the 3D "Mushroom", by means of Monte Carlo simulations.

An accurate knowledge of the nature of the radiation environment in space and aviation is of utmost importance for protection of humans. Simulation tools are nowadays the key to investigate aspects that are not accessible in reality by human, like particles fluxes in space. The capability of simulating cosmic rays transport

from the outer space till though the Earth's atmosphere allows to better quantify and eventually predict scenarios which are not fully replicable in ground-base experimental facilities.

Researchers have access to several software and online tools to perform space radiation studies, from particles propagation in space to shielding efficiency of spacrafts designs. In the following sections, the two main simulation tools used for this thesis purposes are introduced: the Space Environment Information System (SPENVIS) and the Geometry And Tracking Monte Carlo toolkit (GEANT4).

2.1.1 SPENVIS: Space Environment Information System

The Space Environment Information System (SPENVIS) is an online instrument created to facilitate the use of models of the spatial environment in a consistent and structured way, developed by a consortium led by the Royal Belgian Institute for Space Aeronomy for ESA's Space Environments and Effects Section through its General Support Technology Programme. The SPENVIS allows rapid analysis able to produce reliable results used by space engineers to plan mission in all its aspects.

At the hearth of SPENVIS is the project concept: a project is defined firstly by an input set of points regarding a spacecraft trajectory (the orbit generator tool) or a set of geographical coordinates (the coordinate grid generator tool). The first choice regards the planet of departure of the mission, or simply the one whose environment wants to be studied: Mercury, Earth, Mars, Jupiter are the available ones. Secondly, for example in case of a spacecraft trajectory, the type of orbit selected and the number of segments which constitute it, allow the transition from planet to planet, or simply the orbit around one. Information about altitude parameters and durations of the mission are required, and the final orbit is graphically represented as a function of these parameters.

Once the project is defined, the user has access to the following packages, all based on standard models internationally recognized:

- radiation sources and effects;
- spacecraft charging, meaning superficial and internal deep dielectric charging, solar array potentials;
- atmosphere and ionosphere with world maps and profiles of atmospheric and ionospheric constituents and parameters, and additional estimation of atomic oxygen erosion effects on exposed surfaces on low altitude spacecraft;
- magnetic field calculation in terms of strength and vector components, coordinates over spacecraft trajectories, and visualization of magnetic drift shells;
- meteoroid and debris fluxes;
- GEANT4 tools including models for shields investigation, and microdosimetry;
- integrated access to the European Cooperation on Space Standards (ECSS) on space environment and effects.

Typically, output results from a SPENVIS model run can be downloaded by the user in the form of reports and data files and as a variety of plot types lots in different graphics formats [66].

In this work, it was largely used the first package to model the radiation environment on Low Earth Orbit (LEO), where the International Space Station (ISS) currently orbits. For a space trajectory, a suite of radiation source models are available including GCR, long and short-term SPE and trapped particles in the Van Allen Belts. For each source, the magnetic shielding is normally set to its quiet state, meaning all field directions are considered without stormy events. The ability of a particle to penetrate the magnetosphere is determined uniquely by its momentum divided by its charge. The resulting quantity called geomagnetic cutoff rigidity represents the threshold below which no charged particle can penetrate the magnetosphere to a specific point from a specific direction [67]. As the geomagnetic cutoff depends on the particle's arrival direction, its transmission is averaged over all arrival directions. For a given location and rigidity, the integrated solid angle from where particles with this rigidity can reach the location, divided by $4pi$, is called the attenuation or exposure factor. SPENVIS provides the attenuation factor for each particle's energy is averaged over the spacecraft orbit and then multiplied with the interplanetary particles fluence provided by the source models. However, in the attenuation factor calculation it is taken into account the physical presence

of the Earth that covers part of the solid angle from which particles can arrive at a given location. The geomagnetic cut-off is often altered during magnetic storms, allowing particles with lower energy to penetrate points in the magnetosphere that they normally would not [15]. Therefore, the user can change the default option of a quiet magnetosphere into a disturbed one.

GCR radiation models

There are four main models for GCR and they all predict fluxes for protons and heavier ions from helium to uranium, in the near-Earth space beyond the Earth's magnetosphere.

- **The ISO-15390 model:** it is based on the semi-empirical GCR models of the Moscow State University (MSU), and published in the International Standard ISO Draft 15390 [68]. It is the standard for estimating the radiation impact of galactic cosmic rays on hardware and on biological and other objects when in space. The model accounts for a 22-years solar cycle, which induces variations in the GCR particles fluxes, and in the large-scale heliospheric magnetic field. The solar activity is characterized by the average of Wolf (sunspot) numbers on a period time of 12 months.
- **The Nymmik et al. (1996) model:** this model from Nymmik et al. (1996) is basically the same as the ISO model except that it estimate an increase of the ion flux for energies below 10 MeV/u.
- **The CREME96 (Sol. Min.) model:** implemented in SPENVIS is for the solar-minimum GCR environment and corresponds with the GCR maximum last observed in 1986-87. This model is based on the model of Nymmik [69] and includes anomalies fluxes for He, N, O and Ne ions around 10 MeV/u derived from results obtained by the NASA's very first small explorer SAMPEX.
- **The CREME86 models: t**he four CREME86 models are part of the original CREME96 models explained above and marked by the four interplanetary weather indices M = 1, 2, 3 and 4. The weather index M=1 gives the best approximation to the galactic cosmic ray flux at the given date and is also included, whereas the M=2 and M=4 models includes the

additional fully-ionized and singly-ionized anomalous component, respectively. Index M=3 gives the worst-case of galactic cosmic ray level, whose fluxes are so severe that they have only a 10% chance of being exceeded by actual fluxes at any moment.

SPE radiation models

SPE are difficult to predict with exact occurrence, intensity and duration, hence they are a big obstacle for both short and long-term missions planning, particularly if costly design and humans are threatened by such occasional high-level radiation events. To evaluate the accumulated dose over a mission lifetime, the solar protons fluence must be estimate with long-term models, but as for any form of long-term forecasting, the statistical interpretation of data based on past observation is crucial. Because in situ SPE observation has been only started since the early says of space age by satellites, the inaccuracy of a model is dependent on the size of data used, thus three models have been formulated for long-term solar particles fluences.

- **The King model: t**his model was the standard model for a long time and it based only on data obtained during the active years of solar cycle (1966-1972). King observed that the number of events and their frequency were lower in this cycle compared to the previous one, so predicted a linear decreasing dependency of proton fluence. This turn out to be false as the following year the solar activity increased (see Figure 2.1), and King decided to based his model only on measurements taken during cycle 20 as representative of cycle 21. King classified some anomalously events, as the great proton event occurred in August 1972, which accounted 70% of the total fluence be above 10 MeV. Such event would have been potentially lethal for an astronauts flying through [70].
- **The JPL model:** Feynman and colleagues addressed the questionable assumptions made by Kin, constructing the JPL-85 model based on in-situ SPE detection during solar cycle 20 and 21 [71]. Solar cycle 19, was also taken into account even though data were collected with detectors flown on rockets and balloons, and not during in-situ measurements. However, the difference in methods for data collection implied a non-uniform data set, ad

led to the formulation of the JPL-91 model. The model is based on continuous record of daily average fluxes of protons with energy above thresholds of 1, 4, 10, 30 and 60 MeV, during the actual 7 active years of the cycle. In fact, Feynman observed that the high fluence usually begins 2.5 years prior to the reference date of the maximum and ends 4.5 years after this date (see Figure 2.1). The fluence thresholds corresponding to the energies listed above are 10, 5, 1, 1, and 1 (in cm^{-2} s^{-1} sr^{-1}). As the model is represented by a probability of exceeding a given fluence during a mission, the confidence level is located at 95%, meaning that only the 5% of missions identical to the one considered will have fluences larger than that determined for the 95% confidence level.

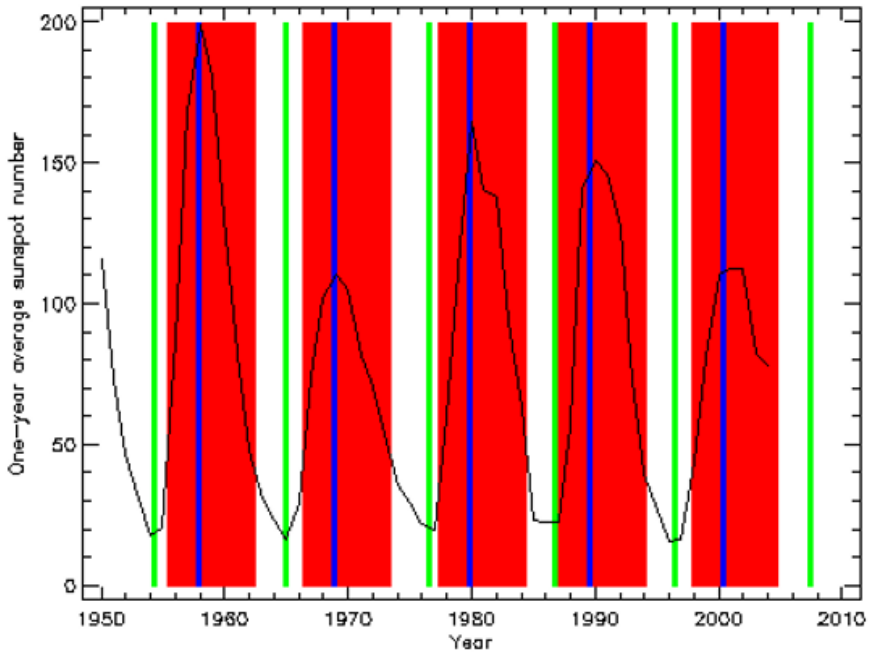

Figure 2.1. Mean number of sunspot averaged on one year. The blue and green vertical lines indicate the date of solar maximum and minimum, respectively; the red areas show the solar active phase lasting 7 years, defined by Feynman [71] for the JPL models.

Lately, an update of the JPL91 model has been suggested by Rosenqvist and colleagues [72], using a complete set of solar proton events from January 1974

to May 2002. However, the JPL-91 model has been recommended for mission planning [73].

- **The ESP models: e**ven though the JPL models are very useful for predicting events fluences, they still have an incomplete set of data, due to limitations in the solar active phase considered and thresholds adopted. For these reasons, the ESP models were developed in the NASA Space Environment and Effects (SEE) framework by Xapsos and colleagues [74]. These extremely complex models are retrieved with the maximum entropy theory method [75] for generating a probability distribution when the data are incomplete, resulting in the least biased distribution in case of missing information. As output the user can select two scenarios: the cumulative fluence over a mission or the worst-event fluence along it.

However, short-term models are necessary to forecast SPE fluxes during any extravehicular activity (EVA) and to evaluate single event upset (SEU) rates. Actually, all models are derived from models used for long-term prediction of GCR. For example, the CREME86 model can be used for short term SPE simply subtracting the component of cosmic rays (M=1) resulting in only solar protons fluences. Similarly, in the CREME96, three episodes of SPE recorded have been implemented, and finally the ESP Xapsos model the energy range have been slightly varied to fit particle fluxes in the short term.

Van Allen Belts radiation models

Due to their large energy coverage, trapped particles in the Van Allen Belts cause a variety of effects in spacecraft, components and biological systems. SPENVIS gathers implemented specific models for both electron and proton fluxes.

- **The AP-8/ AE-8 models: t**he old NASA AP-8 and AE-8 radiation belt models [76] are still the de facto standards for engineering applications because so far they are the only models that completely cover the region of the radiation belts, and have a wide energy range for both protons and electrons. The omnidirectional integral fluxes span in the energy range of 0.04 to 7 MeV for electrons (AE-8) and 0.1 to 400 MeV for protons (AP-8).

Both models comes in two versions for solar minimum and solar maximum, and assess spectra for all altitudes and orbital inclinations. However, it seems to underestimate the high-energy fluxes at low altitudes, because of the extrapolation applied in that range due to little data. An updated version of these models, AP-9 and AE-9, is currently under evaluation.

- **The CRRESPRO and CRRESELE models: t**wo omnidirectional models have been developed by the Air Force Research Laboratory thanks to results sent by the satellite CRRES: the CRRESPRO for protons [77], and the CRRESELE for electrons [78]. The satellite flew in a low-inclination geosyncronous transfer orbit during solar maximum condition in 1990-1991. It is not suitable for studying the radiation environment inside the ISSI because it is best suitable for orbits above 1000 km altitude.
- **The PBS97 model: t**his model is specifically made for trapped protons at altitudes below 600 km, based on measurements performed in solar minimum conditions in the years 1994-1995 by the Proton/Electron Telescope on-board the SAMPEX satellite [79]. The energy range of this model spans from 18.5 to 500 MeV, which extends the high-energy limit of the AP-8 model but cuts of the low-energy compositions. Also, the PBS97 is a directional model whose fluxes require to be multiplied by a factor $4pi$ to obtain a full omnidirectional model for radiation effects purposes.
- **The ONERA/DESP models POLE V1, V2 and IGE-2006:** two models for geostationary electron environment have been developed at the Office National d' Etudes et de Recherches Aérospatiales (ONERA): the Particle ONERA-LANL Environment (POLE) [80] and the International Geostationary Electron model (IGE) [81]. Radiation monitors installed on-board Geosynchronous Equatorial Orbit (GEO) American and Japanese satellites, recorded data for more than 2 solar cycles from which models were created.

2.1.2 GEANT4: Geometry and Tracking Monte Carlo

As mentioned in the section above, in this study SPENVIS has been used to generate the particles fluxes to use as input in an ad-hoc GEANT4 simulation, which was developed as part of this PhD project and described in the following chapters.

The Geometry And Tracking Monte Carlo toolkit (GEANT4) is a simulation software tool to model the interaction of particles with matter, developed by more than 100 collaborators all around the world. It is the only free open-source Monte Carlo code for research in radiation physics spanning from eV scale up to high-energy physics. GEANT4 provides modelling capability of complex experiments in all aspects, starting from the set-up geometry, the definition of all materials involved, the generation and tracking of particles through every interaction they undergo, till the response of nuclear instrumentation, generation and storage of data set, all accompanied by the visualization of the above listed features at different level of details. The user is able to take decision from the initial problem definition right through to the production of results and graphics for publication. To this end, GEANT4 is rich in models and build-in commands, which are constantly updated by the experienced collaborators, making this tool one of the largest radiation physics Monte Carlo codes in terms of affluence size and scope [82].

The functionality of GEANT4 is extensively described in the GEANT4 Application Developer Manual [83] and GEANT4 Physics Reference Manual [84].

Physics models

The interaction between particles and materials is ruled by complex physics models including electromagnetic, hadronic, radioactive decay, optical, transportation, and so on. The physics processes are classified into categories to which different classes of models belong, according to type of particles and energies.

The electromagnetic processes in an energy range from 100 eV to TeV include ionization, bremsstrahlung, multiple scattering, Compton and Rayleigh scattering,

photo-electric effect, annihilation, pair conversion, synchrotron and transition radiation, scintillation, refraction, reflection, absorption and Cherenkov effect. Between several packages, the mostly used in this study is the *GEANT4 Standard Electromagnetic* Package that handles interaction down to 1 keV. This package is commonly used for High Energy Physics experiments as those one in the space field, whereas the *GEANT4 Electromagnetic Low Energy* Package is more appropriate for low energy studies, i.e. medical applications. Is it important to mention that the production of secondary particles in a given material, as δ-rays, is modeled based on a threshold, called "cut", in relation to the range of the particle: if the actual range is bigger than the cut, further secondary particles are generated and tracked, otherwise their energy is considered to be deposited locally. During simulations performed as part of this thesis, the cut was set as a compromise between the desired statistical uncertainty affecting the simulation results and the simulation execution times.

The GEANT4 hadronic physics models describe processes as elastic and inelastic scattering, neutron fission and neutron capture from thermal energies up to TeV scale. To describe the intra-nuclear cascade of hadrons at high energies, the Binary or the Bertini models can be used, while the nuclear de-excitation and the high precision neutron interactions up to 20 MeV are described in the Evaporation models. Ion hadronic interactions can be described with the alternative physics models Binary Cascade, Wilson Abrasion, or the Quantum Molecular Dynamic (QMD) model.

2.2 Materials and Methods

The study subject of this section was performed by means of SPENVIS and GEANT4, discussed just above [9]. In order to reduce the execution times involved with the project, the simulation study consisted of two parts. The first one intended to characterize the radiation environment inside the Columbus ISS module. The

second one modelled the response of a 3D “Mushroom” device when exposed to the radiation environment calculated by the first study.

2.2.1 Simulations models adopted

The first goal of this study was to accurately characterize the radiation environment outside and inside the ISS, in the Low Earth Orbit. The SPENVIS online software tool [85] was adopted to obtain the cosmic radiation spectra of the four main radiation sources outside the ISS. A mission of two days was considered with an orbit at 408 km apogee and 401 km perigee, with ISS’s inclination of 51.6°, and 3D visualized as shown in Figure 2.2.

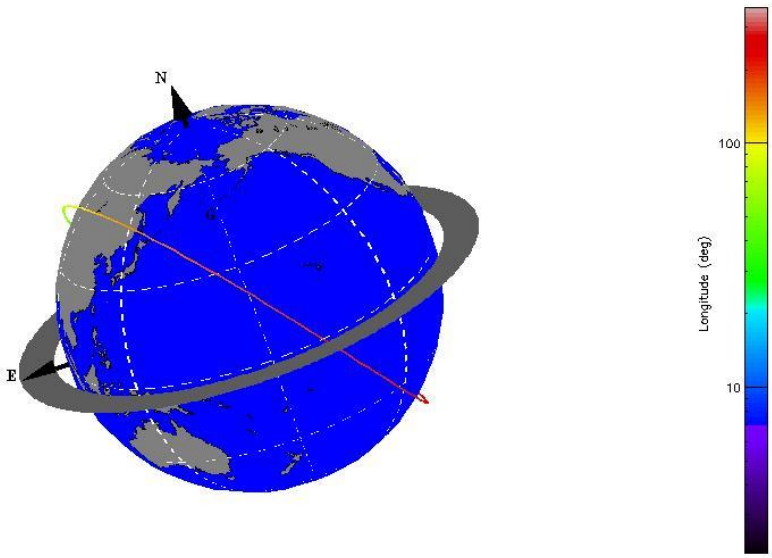

Figure 2.2. 3D visualization of the ISS orbit during the simulated mission with SPENVIS.

Between the variety of SPENVIS’ models presented in section 2.1.1, the following ones were selected to describe the radiation field surrounding the ISS according to raccomendation for mission planning:

- the NASA AP8/AE8 models for trapped protons and electrons, with an energy range up to 400 MeV and 7 MeV, respectively;
- the CREME96 model for GCRs, particularly protons and helium nuclei with a maximum kinetic energy of 100GeV/n; the energy spectra are for a solar minimum, corresponding to the worst case scenario for the GCRs;
- the JPL-91 model for SPE protons with kinetic energy up to 500 MeV.

It is well known that the region of the South Atlantic Anomaly presents an anisotropy regarding the trapped particles flux. Several approaches can be adopted due to the existence of several models used to mimic the radiation environments of trapped particles. We decided to use the AP8/AE8 model as it is the NASA de facto standard for mission planning. It is one of the models considering an isotropic flux together with the PSB97 and the CRRESPRO models. An advance extension of the AP8/AE8 model, based on the Badhwar & Konradi 1990 model called UP [86], allows taking into account the anisotropy. Nevertheless, in a previously published study the difference in using the above-cited different models was investigated and it was concluded that dose rates due to incident anisotropic trapped particles are lower, or equal to those of omnidirectional models and the AP8/AE8 model is the more favorably comparable to experimental data between all isotropic models [9].

To adopt the most conservative approach possible, we considered models for solar minimum conditions, which represent the worst-case scenario for radiation exposure of humans in terms of dose rate: the solar cycle lasts 11 years and is characterized by phases of maximum and minimum intensity. It is well known that the GCRs flux is anti-correlated to the solar activity [87].

Figure 2.3 shows the differential fluxes of particles derived by the preliminary run of the above-mentioned models in SPENVIS along the ISS orbital mission. Together with the most abundant GCRs protons and helium ions, other ions fluxes as carbon, oxygen, silicon and iron ones are shown to provide an understanding of the decreasing order of magnitude of fluxes for less abundant ions in space.

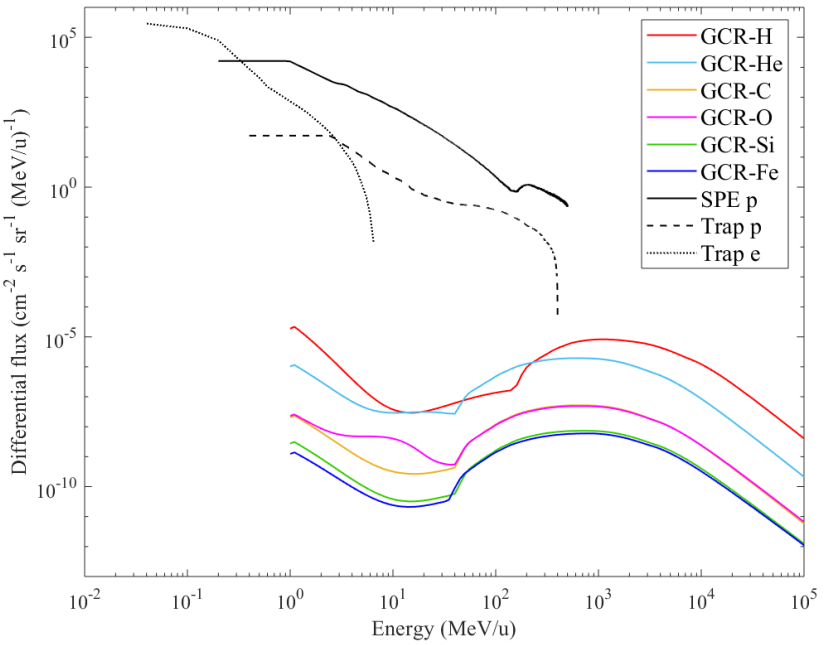

Figure 2.3. Differential fluxes of particles at the ISS altitude along the orbit modeled by using SPENVIS, outside the Columbus module.

In the GEANT4 simulation, the radiation field was modeled by means of the General Particle Source (GPS), as emerging from a sphere S_1 with radius R_1= 1 km, towards the ISS. The European laboratory Columbus was modelled in the simulation at the center of S_1 (see Figure 2.4a-b). The direction of the incident radiation was modeled with a cosine distribution. This configuration of generation of primary particles is appropriate to model the isotropic radiation field typical of outer space when the radius of S_1 is significantly larger than the size of the ISS like in our simulation study [9]. In order to reduce the execution times of the simulation, particles were modeled emerging from a cone with a half-aperture angle θ_{max}, which is the maximum angle that subtends the entire Columbus (see the grey area in Figure 2.4a-b).

The Columbus module was modeled as a cylinder with sizes 5 m in diameter and 8 m in height, set in the center of the S_1. Based on specifications of the real Columbus' structure and materials [88], the walls of the cylinder were modeled as a multilayer of different materials (e.g. Aluminum, Kevlar and Nextel) and thicknesses (see Figure 2.4c).

GEANT4 10.4 was used and the following Physics constructors were adopted to model all physics interactions: G4EmStandardPhysics_option3, G4HadronPhysicsQGSP_BIC_HP, G4HadronElasticPhysicsHP, G4EmExtraPhysics, G4StoppingPhysics, G4IonBinaryCascadePhysics, G4RadioactiveDecayPhysics, and G4DecayPhysics.

The kinetic energy spectra of all primary and secondary particles produced within the multilayer were retrieved as output of the simulation when reaching the inner habitat of the Columbus, as shown in Figure 2.4c. Due to simulating a cone source with a half-aperture angle of θ_{max}, to obtain the real counts C_r of the particles reaching the inner habitat of the Columbus, the simulation results C_s were scaled based on the formula [89]:

$$C_r = C_s * \frac{N_r}{N_s} \tag{2.1}$$

where N_s is the number of simulated events. N_r is the number of real events expected, calculated by the formula:

$$N_r = \phi * 4\,\pi^2 * R_1{}^2 * \sin^2\theta_{max} \tag{2.2}$$

where ϕ is the total energy integrated flux of incident particles simulated by SPENVIS in outer space.

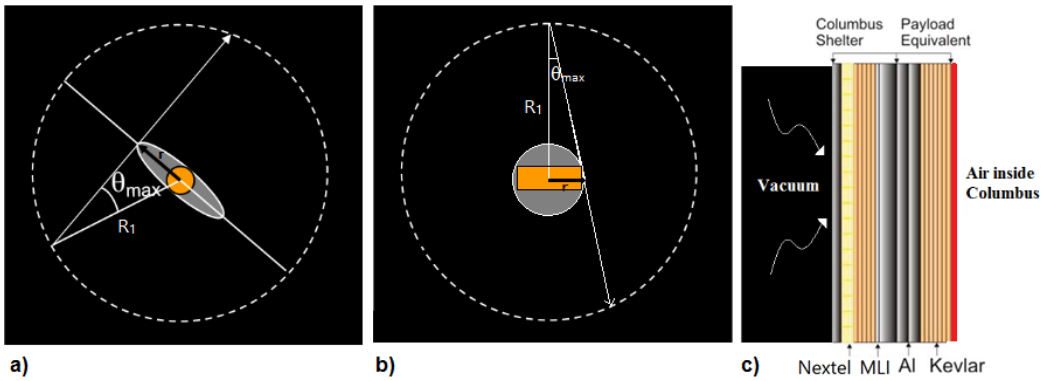

Figure 2.4. GEANT4 simulation geometry with the radiation sources generated from random points on the sphere S1 (dashed line), directed towards the Columbus module (orange area in its a) frontal and b) lateral view. c) GEANT4 model of the Columbus multilayer: the red line represents the surface where the output radiation flux is retrieved [87].

2.2.2 The 3D "Mushroom" microdosimeter

The energy spectra of particles recorded after the Columbus wall in the simulation study described in 2.2.1 were then used to model the radiation field inside the Columbus. For completeness, for each source of GCR protons, GCR helium ions, SPE and trapped protons, a Phase Space file was created including all primary and secondary particles produced by interaction with shielding materials of Columbus, while propagating through it. The particles were generated as emerging from a sphere S_2 with radius R_2 equal to the radius of the innermost cylinder volume (astronauts' habitat) of the Columbus. They were generated with an isotropic distribution inside the Columbus by means of a cosine distribution of the direction. The microdosimeter is set in the center of the sphere S_2, which corresponds also to the center of the Columbus. We adopted the same biasing method of the angular distribution (analogously to the first part of the study), to increase the number of particles interacting with the microdosimeter.

Figure 2.5 shows the GEANT4 model of the simulated 3D "Mushroom" detector. The design of the 3D "Mushroom" microdosimeter corresponds to the one shown in Figure 1.19b. The SV has dimensions of 30 µm in diameter and 10 µm in height. The 2500 SVs are embedded in PolyMethylMethAcryl (PMMA) and placed on a 0.85 µm thick SiO_2 deposited above 300 µm support wafer. [90-92].

To represent the scenario of an astronaut inside the Columbus module, we considered the microdosimeter surrounded by a PMMA sphere of 10 mm radius. This particular thickness was chosen to evaluate the operational quantity for individual monitoring, the personal dose equivalent $Hp(10)$, at a depth of 10 mm below a specified point on the human body indicated by the position where the dosimeter is usually worn. This quantity is state in the ICRP Publication 123, as necessary for the assessment of the protection quantity effective dose in space [43].

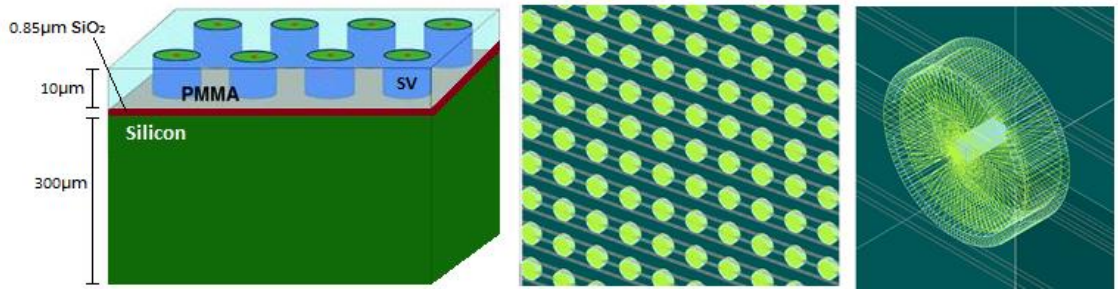

Figure 2.5. From the left: the 3D "Mushroom" microdosimeter design; the GEANT4 SVs array; the zoomed view of a SV.

The output of the simulation is the frequency of the energy deposition ε of each single event occurring in the silicon SVs of the microdosimeter. The lineal energy y was then calculated following the equation (1.4) listed in section1.3.1. The mean chord length of the SV, $\bar{l}$, was the calculated by the Cauchy's formula in isotropic fields (see equation (1.5) in section 1.3.1).

Through the analysis of the measured silicon microdosimetric response of the the "Mushroom" microdosimeter, the absorbed dose in tissue-equivalent, D_{TE}, was obtained converting the measured absorbed dose in silicon by applying a conversion factor of 0.58 resulting from tissue equivalency studies for mixed fields [59, 93].

Finally, the personal dose equivalent 10 mm deep in the body of an astronaut, $Hp(10)$, was calculated as the product between the mean quality factor of the mixed field and the absorbed dose in tissue-equivalent (see equation (1.17) in section 1.3.1). As a consequence of the direct measurement of the lineal energy y, the quality factor depending on y $Q(y)$ was derived based on the equation (1.12) stated by the ICRU Report 40 in section 1.3.1 [52].

In the Report 40, the liaison group of ICRP and ICRU recommends to increase the quality factors for densely ionizing radiations, such as neutrons, but also to assign quality factors less than unity to sparsely ionizing radiations, such as X rays or fast electrons. Despite newer definitions of the quality factor as a function of LET, our choice of adopting the definition of Q in function of y was due to the fact that the SOI microdosimeter can directly measure the lineal energy y for each single event occurring in the SV. Compared to the ICRP-60 definition of $Q(LET)$ approximated to 1 for $LET<10$ keV/μm [21], SOI microdosimters allow lineal energy

measurements as low as 0.15 keV/µm [61] leading to a direct measurement of $Q(y)<1$ at low y, according to equation (1.12). This experimental threshold was adopted in the simulation.

Additionally, the interest of this study was also in evaluating the daily dose to astronauts in order to compare it to the dose rate measured during experimental campaigns on the ISS reported in the literature.

For each radiation source (GCR, SPE and trapped radiation), $2 \cdot 10^9$ primary particles ($N_{simulated}$) were simulated. Integrating the initial differential flux ϕ_i inside the Columbus over all energies E_i, we could estimate N_{1day}, the real number of incident particles entering the Columbus in 24 hours, as follow:

$$N_{1\ day} = \left(\sum_{All\ energies} \phi_i * E_i \right) * S_{columbus} * 2\pi * 86400 \tag{2.3}$$

where the total integrated flux was multiplied by the surface of the Columbus module $S_{Columbus}$, 86400 seconds in a day and 2π, assuming that only half of the Columbus module of the ISS is facing the incoming cosmic field from outer space, because the other half is facing the Earth.

The dose simulated was normalized per incident particles and then scaled for the number of particles expected in 1 day:

$$Dose_{1\ day} = Dose_{simulated} * \frac{N_{1\ day}}{N_{simulated}} \tag{2.4}$$

2.3 Results and Discussion

2.3.1 The radiation environment outside and inside the ISS

The energy spectra of the radiation environment outside the Columbus, modeled with SPENVIS, are shown in Figure 2.6 (green lines), with their corresponding spectra modeled inside the Columbus with Geant4 (solid lines). As expected, incident GCR protons and helium nuclei with energy above 10 GeV/n are not stopped by the multilayer wall and they reach the inside of the spacecraft where astronauts live and work. Particles with energy above 1 GeV/u are slowed down during the propagation through the multilayer, with a reduction of one order of magnitude to the differential flux, while protons below 5 MeV are fully absorbed. It can be observed that the space radiation produces high fluxes of secondary neutrons from spallation reactions and a non-negligible flux of nuclear products with energy of hundreds of MeV/n.

Similar results were obtained for SPE and trapped protons. After the Columbus' wall, the majority of protons have energies above 100 MeV, while the initial abundance of low-energy protons has been fully stopped by the shielding wall. However, the residual tail at low-energy refers to the high-energy primary protons, which slowed down in energy, as well as secondaries generated by scattering, accompanied by a significant production of secondary low energy neutrons (red solid lines).

Because of their low energy (up to 7 MeV), all trapped electrons are stopped during the propagation through the Columbus' wall. Hence, we decided not to present the spectrum, as negligible.

All spectra in Figure 2.6 also show that the main secondary particles' components are protons, helium nuclei and neutrons. In addition, other secondary particles, like gamma rays, electrons and nuclear fragments produced during the propagation through the wall, were detected in low abundance. For each source of

GCR protons, GCR helium ions, SPE and trapped protons, a Phase Space file was created including all primary and secondary particles, and used as input to represent the radiation environment incident on the microdosimeter for the simulation of its response.

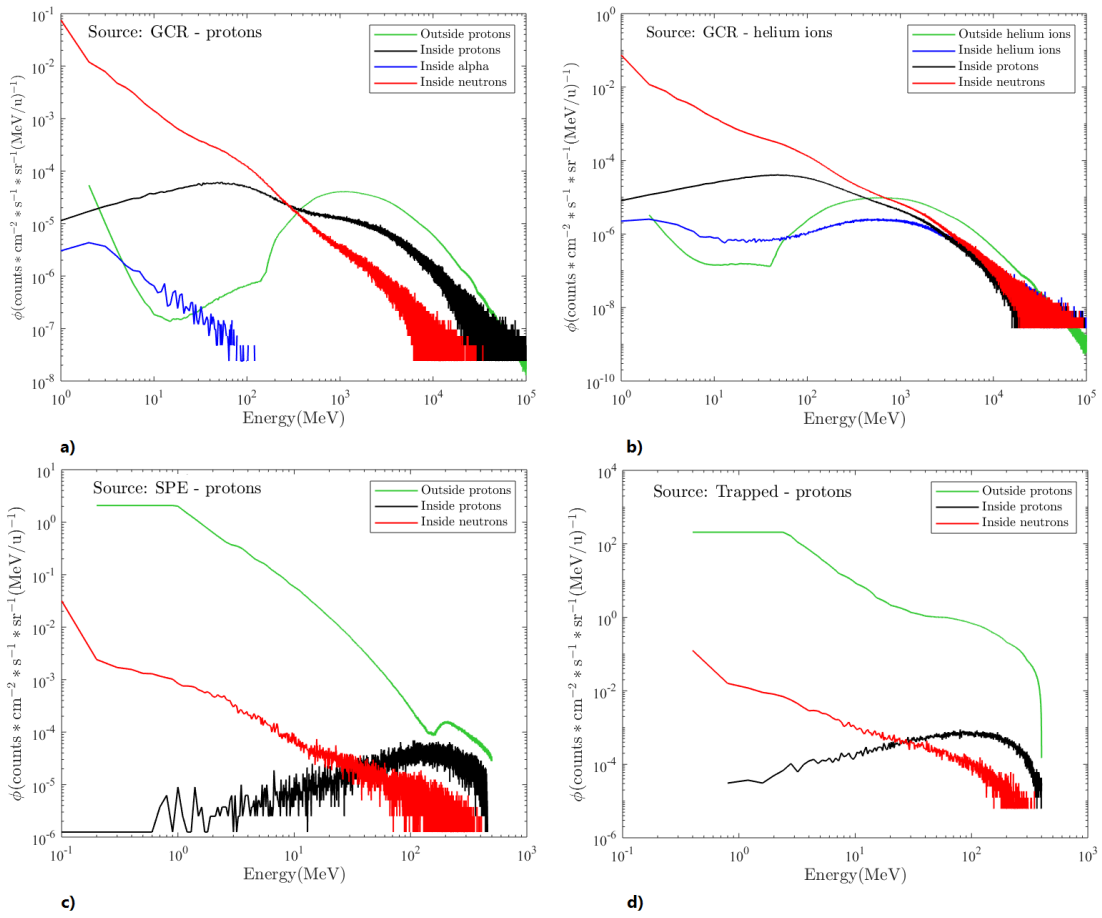

Figure 2.6. Simulated spectra inside the ISS behind the multilayer wall for main sources: a) GCR protons, b) GCR alpha, c) SPE protons and d) Trapped protons. The green lines represent the radiation spectra outside the ISS obtained from SPENVIS and used as input to the simulation. The solid lines are particles inside the ISS: the blue lines represent helium nuclei, the black lines are protons and the red lines are secondary neutrons.

2.3.2 **The response of the microdosimeter**

We simulated the response of one 3D "Mushroom" microdosimeter: this decision was made in order to be able to evaluate which is the number of

microdosimeters to have an acceptable counts statistics during a 1day mission in space. In fact, the small dimensions of the sensitive area allow the design optimization of the device, connecting in parallel multiple microdosimeters assuring a low noise induce by the electronic, which eventually can be removed by setting very low thresholds in the read-out system.

The MCA spectra in Figure 2.7 show the frequency of energy deposition events for the 7 most abundant particle species recorded by the microdosimeter. From the zoom of the spectra up to 6 MeV we can definitely identify an abundance of particles depositing energy up to 3 MeV. The total number of counts per day detected is in a range of $10^5 \div 10^7$, with the exception of protons that are above 10^8 counts/day. However, we found that helium nuclei mainly produced by protons deposit energy up to 6.4 MeV and ^{12}C ions up to 7.3 MeV. Several other heavier ions as ^{13}C, ^{14}N, ^{22}Na, ^{24}Mg, ^{26}Al, ^{27}Si, generated mostly by interaction with the materials of the Columbus' wall but also with the microdosimeter itself have a lower rate around $10^2 \div 10^3$ counts/day. These high-LET particles contribute to relevant energy depositions in the SVs of the microdosimeter up to 13.3 MeV. This promising result confirms the importance of including in simulation models also fragments with lower abundance in space, which eventually bring a higher contribution to the dose to astronauts.

Finally, considering the small area of the SOI microdosimeter, we can say that the statistics obtained from our simulation was good to represent the particles scenario encountered inside the ISS. Surely, the microdosimeter will be tested in facilities providing such particles and energies, to evaluate the noise contribution due to the electronics.

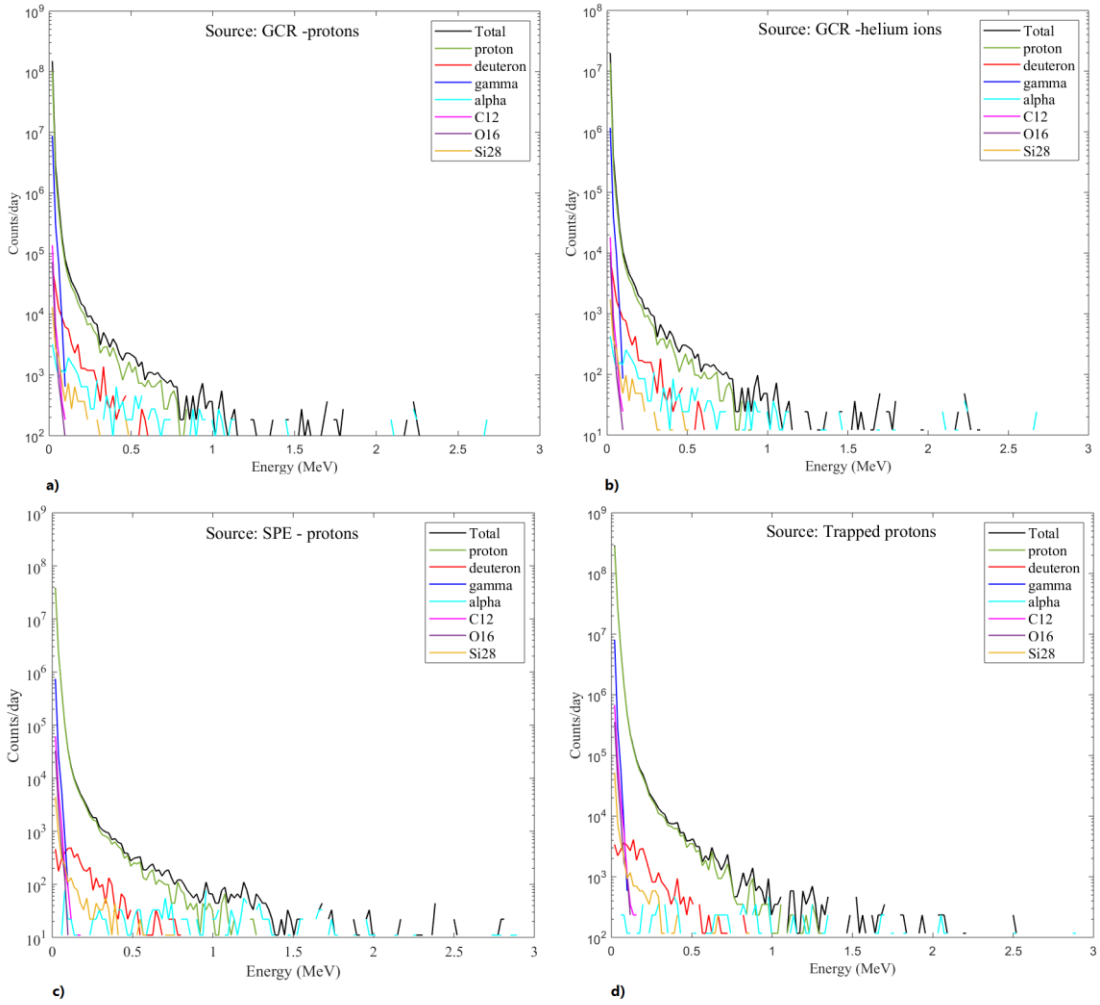

Figure 2.7. Zoom up to 6 MeV of simulated energy spectra with 1024 channels, representing counts recorded in a 1day mission by the microdosimeter. Four sources were distinguished: a) GCR protons, b) GCR helium nuclei, c) SPE protons, d) Trapped protons.

Figure 2.8 shows the simulated tissue equivalent microdosimetric spectra obtained with the "3D Mushroom" microdosimeter irradiated with the simulated radiation field inside the Columbus module. The simulations consisted of $2 \cdot 10^9$ primary particles shot for Phase Space file of each radiation source (GCR, SPE and trapped protons, and GCR helium ions). The areas of the microdosimetric spectra are normalized to 1. As expected, both the radiation incident on the ISS and the secondary particles affect the response of the microdosimeter. Protons are mainly responsible for the response corresponding to lineal energies spanning from 0.1 keV/µm to tens of keV/µm. Secondary particles such as electrons, gamma rays,

pions, muons are predominant at low lineal energies up to a few keV/µm. It is interesting to see the dose contribution from secondaries produced by GCR protons. A significant peak of secondary helium nuclei around 100 keV/µm originated by GCR protons, accompanied by a few relevant ^{12}C, ^{16}O and ^{28}Si ions with lineal energy up to 25 keV/µm with a few exceptions up to 158 keV/µm (Figure 2.8a).

In Figure 2.8b, microdosimetric spectra from the GCR alpha source show the peak of primary helium nuclei that traverse the Columbus' wall, slowing down in energy due to the interaction and production of secondaries. Again, the production of heavy ions such as ^{12}C, ^{16}O and ^{28}Si, dominates in the range of lineal energies up to 50 keV/µm with a few ions reaching lineal energy up to 890 keV/µm.

Because of their similar energy range, SPE and trapped protons induce a similar response in the microdosimeter (see Figure 2.8c-d). In both cases, the proton peak is covering the range of lineal energies 0.1 ÷ 10 keV/ µm. Secondary heavy ions as ^{12}C, ^{16}O, ^{28}Si contribute to the microdosimeter response from low lineal energies up to ~ 150 keV/µm.

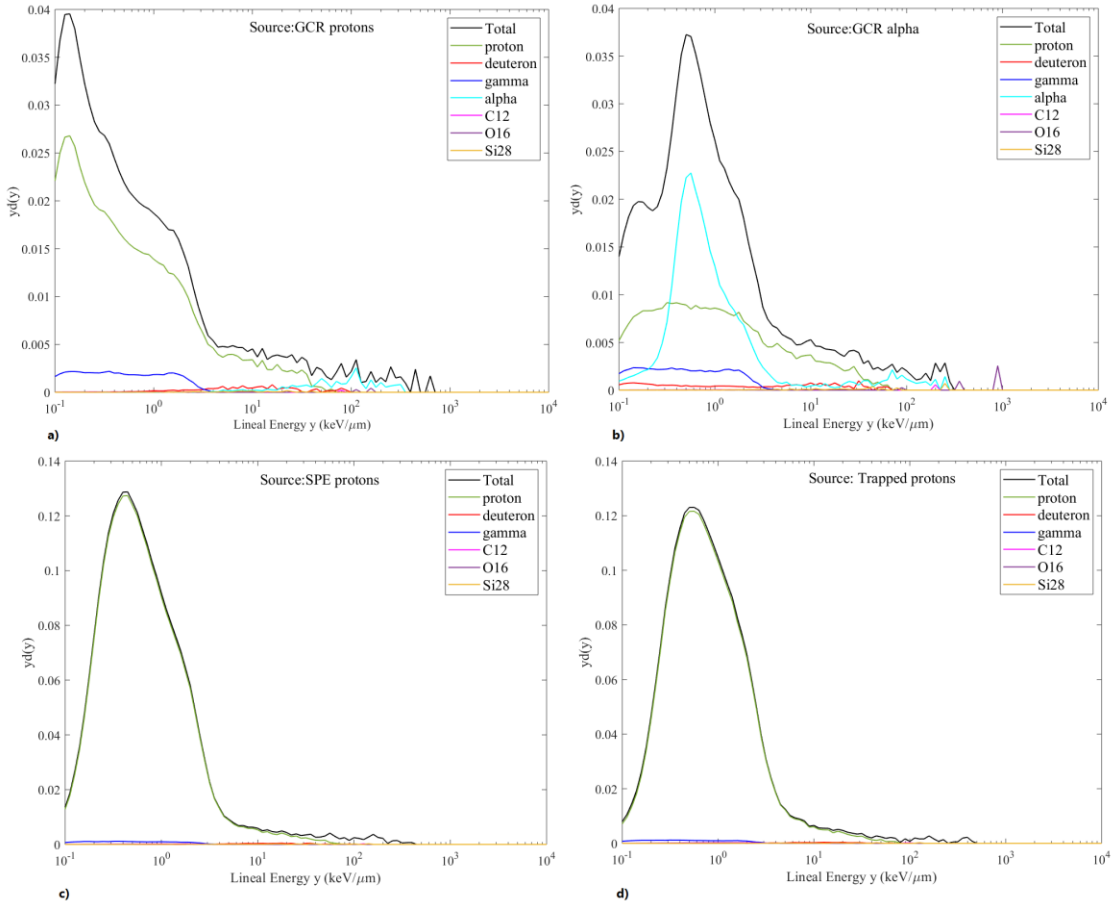

Figure 2.8. Simulated tissue equivalent microdosimetric spectra as a response of the 3D "Mushroom" with main radiation sources: a) GCR protons, b) GCR helium nuclei, c) SPE protons, d) Trapped protons. Secondary particles as electrons, pions, muons were detected at low lineal energies. However, their spectra have not been shown in this figure not to overload the graph.

Table 2.1 shows the values of absorbed dose in tissue equivalent D_{TE}, mean quality factor $\bar{Q}$ and the corresponding dose equivalent $Hp(10)$ calculated for 1-day mission as explained above. Observing the microdosimetric spectra in Figure 2.8c-d for SPE and trapped protons sources, the $\bar{Q}$ value is lower than 1 because of the predominant contribution to the dose coming from protons with lineal energies below 1 keV/µm. This is possible due to the definition of $Q(y)$ in equation (1.12, allowing quality factor below 1 for lineal energy below 10 keV/ µm. On the contrary, for GCR sources the $\bar{Q}$ value is higher due to low LET protons of high energy that produce target fragments with higher LET.

Results in terms of dose agree with experimental measurements performed at the ISS's altitude in previous experimental campaigns [94, 95]. The highest contribution in terms of dose is due to the trapped protons' source because of the proximity of the inner Van Allen Belt to the ISS's orbit. Moreover, the real-time ISS's orbit calculated by SPENVIS has a quick pass closer to the South Atlantic Anomaly, a region in South America where the inner belt is closer to the Earth's surface, and to the ISS's orbit too, because of the magnetic axis offset of our planet. The 550 µGy/day of dose deriving from the trapped protons source matches with 567 µGy/day measured and published in [95]. The 327 µSv/day of total absorbed dose from GCRs obtained from our simulation respects the value of dose 360 µSv/day for maximum GCRs intensity [95]. Finally, we have not recorded intense SPE events during the day modelled with SPENVIS thus the dose of 42 µGy/day is in the range of doses recorded and published in [95].

According to the choice of adopting a quality factor definition in term of y stated in the ICRU-40, it is clearly justified the result of $\bar{Q}$ <1 for SPE and trapped protons considered as sparsely ionizing radiation sources. Moreover, for completeness and for a direct comaprison to $\bar{Q}$ value measured onboard the ISS, a calculation of *Q(LET)* based on ICRP-60 has been done with the knowledge of the microdosimetric spectra. Assuming that y is equal to the *LET*, we obtained a value of $\bar{Q}$ equal to 1.31 and 1.30 for SPE and trapped protons respectively, which is in agreement with the literature showing a value of $\bar{Q}$ equal to 1.3 for both sources [95]. This evidence confirms that currently used SOI microdosimeters are capable to measure accurately the quantity y and its distribution in a mixed radiation environment as the one really encountered at the ISS altitude. Nevertheless, depeding on the adopted definition of $\bar{Q}$, results can be different for sparsely ionizing radiation. Newer definitions of the quality factor do not invalidate the one stated in ICRU-40, used in this paper. Additionally, (*A. M. Kellerer and K. Hahn, 1988*) suggested that the option between LET as the reference parameter and the microdosimetric variable, y, may not necessitate an exclusive choice [53].

Table 2.1. Dose in tissue-equivalent $D_{TE}$and Dose Equivalent $Hp(10)$ resulting from the simulation of the microdosimeter embedded in a sphere of 10mm radius of PMMA. Results are within an error range of $\pm 1\%$.

Source 2π	Number of particles in 1 day	$\bar{Q}$	D_{TE} (μGy/day)	$Hp(10)$ (μSv/day)
GCR protons	$1.83 \cdot 10^{11}$	1.41	190	267
GCR alpha	$2.43 \cdot 10^{10}$	1.52	39	60
SPE protons	$2.21 \cdot 10^{10}$	0.73	42	31
Trapped protons	$2.34 \cdot 10^{11}$	0.69	550	378

2.4 Conclusions

A GEANT4 model was implemented to reproduce the radiation environment encountered at the International Space Station altitude. The three main sources of cosmic radiation, GCR, SPE and Trapped particle in the Van Allen Belts, were considered and particles fluxes were preliminarily obtained by simulating a realistic orbit with the online tool SPENVIS. The shielding structure of the Columbus module docked at the ISS was selected, reproduced in GEANT4 and isotropically exposed to simulated fluxed. As outcome of the simulation, the resulting mixed field of primary and secondary charged particles reaching the inside habitat of the Columbus was retrieved.

The response of the 3D SOI "Mushroom" microdosimeter placed in the centre of the Columbus was investigated when exposed to the simulated radiation field. The simulated microdosimetric spectra of GCRs, SPEs, and trapped protons show an evident contribution from protons at low energies, followed by other secondary particles as electrons, gamma rays, helium nuclei, muons. Although the abundance of heavy ions is smaller than protons' one, heavy ions as C, O, Si, Fe make large contributions to dose, especially because of their high lineal energy.

However, according to radiation protection purposes, the interest of this study led to the evaluation the absorbed dose and dose equivalent to an astronaut. The doses and were calculated for a daily mission in space, as well as the quality factor for each radiation source. The good agreement found with data in the literature

demonstrates that our GEANT4 model is adequate for simulating the radiation environment at the ISS altitude. Moreover, the 3D SOI "Mushroom" microdosimeter gave an interesting response for the first time. Considering the simulation of a 1 day mission the counts statistic shows a minimum value of 10^2 counts/channel for each source, at predominant energies. Additionally, the total number of counts spans from 10^3 counts for less frequent particles to 10^8 for protons, each day. This number of counts shows that in principle the "Mushroom" microdosimeter can be used for space radiation protection.

In summary, the favourable agreement between the simulated performance of the microdosimeter in the ISS radiation environment against the literature makes the SOI microdosimeter an advantageous candidate as an alternative to the standard TEPC for dose monitoring in space thanks also to its small dimensions and portability, low voltage supply needed and accuracy in characterizing the field.

It should be noted that for high-energy proton field which is part of the spectrum of GCR protons field, the current size of the sensitive volumes in the SOI microdosimeter will provide smaller $\overline{y_D}$ in comparison with 1 µm diameter SV of TEPC adopted in the Q(y) dependence.

In order to better quantify the accuracy of the model used for this study for application in the astronauts' radiation protection filed, GEANT4 results discussed in this chapter will be compared with experimental measurements performed at different international irradiation facilities. In particular, the microdosimeter's response against the heavy ions component of the cosmic field will be presented in Chapter 4 and Chapter 5, where irradiations performed at the Heavy Ions Medical Accelerator in Chiba (Japan) will be discussed. Additionally, the shielding structure of the Columbus simulated by GEANT4 in this study, will be investigated against heavy ions typical of GCRS.

Whereas, the characterization of the protons field's component will be discussed in Chapter 6 and Chapter 7, as result of irradiations of the "Mushroom" microdosimeter at the proton therapy centre Paul Scherrer Institute (Switzerland). In fact, the energy spectra of GCRs, SPEs and trapped protons simulated and discussed in this chapter were used to program the treatment planning system of

the medical accelerator in order to irradiate the microdosimeter with a realistic fluence spectrum of protons.

Chapter 3

Charge collection characterization of the SOI microdosimeters

In this chapter, the charge collection efficiency study of the latest designs of the 3D "Mushroom" microdosimeter suitable for radiation environments with low flux rate, as the cosmic one, is presented. The Ion Beam Induced Charge collection (IBIC) technique was used for this purpose, by accessing the accelerator facility of the Australia's Nuclear Science and Technology Organization. IBIC is extremely powerful technique for detector characterization before performing any kind of experiments. It allows one to evaluate the full depletion voltage of the device and to see any possible damages in the arrays of SVs shown in via the median energy maps.

3.1 Introduction

3.1.1 ANSTO: Australia's Nuclear Science and Technology Organisation

The Australian Nuclear Science and Technology Organization (ANSTO) is a statutory body of the Australian government formed in the 1987 as the national nuclear organization for nuclear expertise. Five research facilities operates such as the Open-pool Australian light-water reactor (OPAL), the Centre for Accelerator Sciences, The Australian Centre for Neutron Scattering, the Cyclotron facility and the Australian Synchrotron. For this thesis purposes, I was granted access to the Centre for Accelerator Sciences facility, which is as a world-leading centre for accelerator mass spectrometry (AMS) and accelerator-based ion beam analysis (IBA) techniques. Four tandem accelerator systems belong to the facility, but only one, the 6 MV SIRIUS accelerator, was used during experiments involving the Ion Beam Induced Charge (IBIC) technique of interest of this thesis.

3.1.2 The 6 MV SIRIUS accelerator

The SIRIUS is built around a 6 MV Pelletron tandem accelerator where three different line sources inject beams of negative ions with energies up to 90 keV. In Figure 3.1, the schematic of the SIRIUS accelerator is presented: on the top left corner the three sources enter the Pelletron. Firstly, the MC SNIC cesium sputtering ion source (S1) for ions from H to U, secondly the direct extraction duoplasmatron ion source (S3) produces a H-beam, and finally the radio-frequency ion source with a rubidium vapour charge exchange chamber, Alphatross (S4) for He-beam production. The low energy ions entering the Pelletron are positively charged undergoing charge stripping either by gases (He and Ar) or by foils at the positive

terminal. In fact, the accelerator has two equipotential Van De Graff sections, where firstly negative ions are accelerated through a potential difference towards the centre, then the low pressure gas strips electrons from the ions till its positive charge is reached and the finally accelerated till the exit. The exiting ions, as can be seen in Figure 3.1, are directed in two high-energy beamlines, the AMS for mass spectroscopy (beamlines A2-A5) and the IBA for ion beam analysis (B5-B7). A more detailed description of the accelerator and its component along the beamlines can be found elsewhere [96].

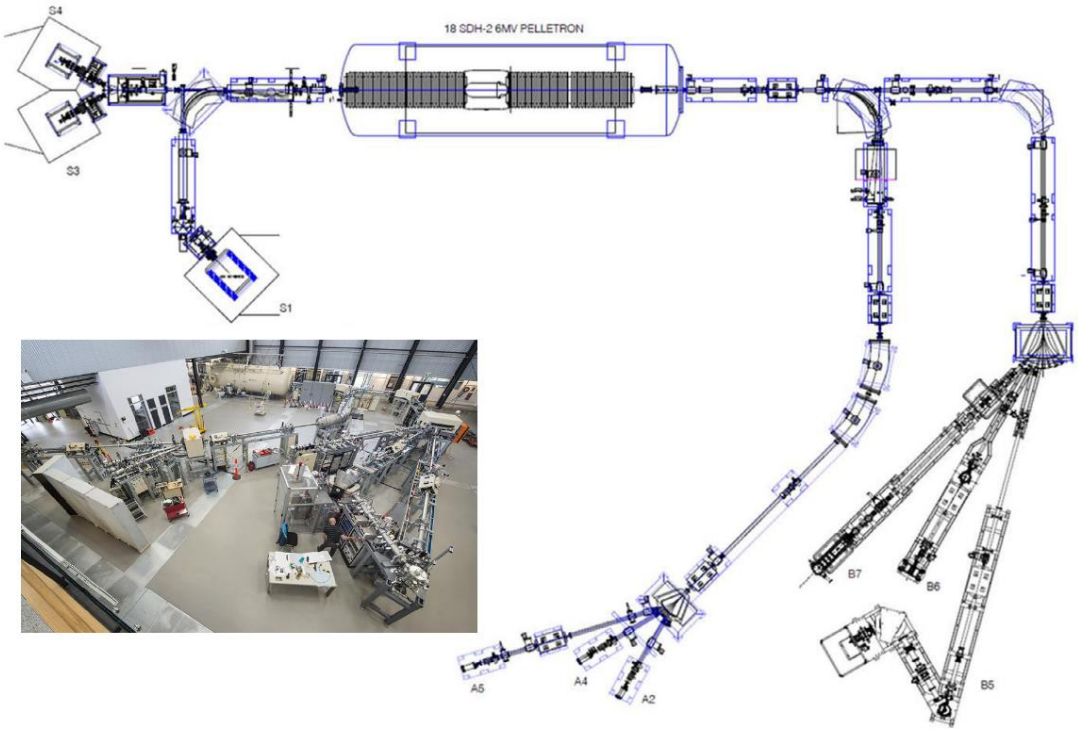

Figure 3.1. Picture and sketch courtesy of (Z. Pastuovic et al., 2016) [96]: floor layout of the SIRIUS accelerator system. Two branches for injection of low energy ions (IBA with the DEDIS-S3 and Alphatross-S4 ion sources, and AMS/IBA shared with the MC SNICS-S1 source), and two branches for high energy ion beam analysis (the AMS with A2, A4 and A5 beamlines and the IBA with B5, B6 and B7 beamlines) are shown on the low energy (left) side and high energy (right) side of the NEC 18SHD-2 6 MV Pelletron accelerator (middle). Inset shows a photo of the 6 MV system.

Particular focus will be put on the IBA beamline as it was used for experiments discussed in this chapter. A series of magnets and slits deflect and focus the ion

beam which reaches a switching magnet that allows the analyzed beam to be focused onto object slits in three custom built IBA beamlines: the dual beam surface engineering end-station (B5), the dual chamber beamline for channeling and NRA (B6), and the ion microprobe (B7).

The beamline B7 is the one hosting the ion microprobe and the control system designed by the Oxford Microbeams Ltd, and usually used for IBIC measurements. The microprobe arrangement allows the focus of high-energy heavy ion beams, high ion currents in small spot sizes, and scan widths 1000 times larger than the spot sizes. An aluminum girder isolated from ground vibration by a massive concrete block, holds a series of arrangements to control, collimate and direct the beam to a vacuum chamber hosts the target (see Figure 3.2). The end-station of the microprobe includes different components such as: the sample holder, the piezoelectric SmarAct XYZR micro-manipulator, the Infinity tele-ZOOM microscope, an high resolution camera, and detectors [96]. The target chamber is pumped down to produce a vacuum to prevent energy attenuation and scattering of the ion beam.

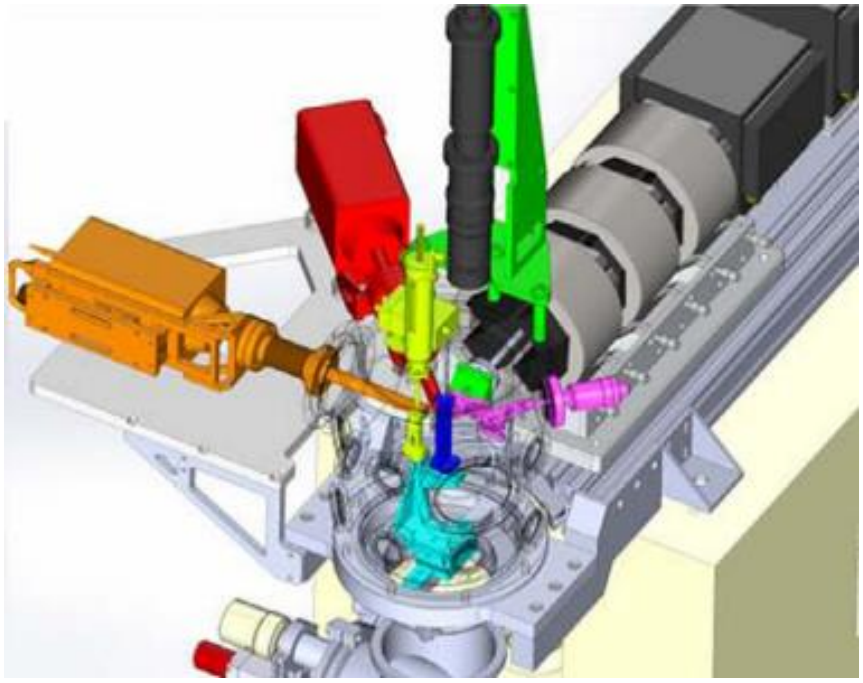

Figure 3.2. Image courtesy of (Z. Pastuovic et al., 2016) [96]: the end-station of the B7 beamline hosting the stainless steel vacuum chamber (shown transparently) with components: photon detectors (orange and red), particle detectors (yellow and magenta), micromanipulators (cyan), and sample holders (blue).

3.1.3 Ion Beam Induced Charge technique

The Ion Beam Induced Charge (IBIC) technique is a scanning microscopy technique to measure and image the transport properties of semiconductor materials and devices, by using finely focused MeV ion beams as probes focused down to submicrometer spots.

The interaction of ions of energy of MeV with matter is mostly characterized by the ion energy loss in collisions with the atomic electrons, whereas the interaction with the atomic nuclei is less frequent. The emitted electrons, called delta rays, subsequently lose their energy through the interaction with the orbital atomic electrons. Thus, in a semiconductor, the overall significant effect is the production of many electron-hole pairs (EHPs), that leads to the production of a measurable charge pulse from each incident ion. The resulting pulse height spectrum is distributed around a main peak, whose position is proportional to the charged measured at the electrode. The ratio of this charge measured at the signal peak and the charge generated by ionization is called the charge collection efficiency (CCE) [97]. By using the IBICC technique, the charge collection properties of a detector can be studied under different biases. The angular dependence of the CCE can also be investigated.

3.2 Material and Methods

3.2.1 Experimental data acquisition set-up

The detector is mounted on an aluminum stick inserted vertically in the vacuum chamber and its position is refined by a x, y, and z manipulator. A video camera is available to help aligning the sample and focusing the image. The Data Acquisition (DAQ) system consists of software installed in Windows, a scanning

amplifier, four 8192 channel Analogue to Digital Converters (ADCs), and a current integrator connected to the sample holder.

For the experimental IBIC measurements that will be discussed in this chapter, the microbeam used was a 5.5 MeV He^{2+} ions beam, scanned over the surface of the microdosimeters. The spot linear size of the microbeam is approximately 1 µm. For a single energy deposition event occurring in the microdosimeter, the beam position (X,Y) and energy deposited was recorded and used to create median energy maps, allowing the charge collection in the device to be observed visually and to correlate the energy distribution to the spatial distribution [98] [99]. Energy deposited in the microdosimeter was measured using a low noise in-house built MicroPlus probe. The signal is processed by a dual timing ADC to process the spectrum of the scan.

In order to determine the dimensions of the IBIC images, spatial calibration was performed by scanning a copper grid and the energy of each transmitted ion was measured using a surface barrier detector behind the grid.

The energy deposition of the ion beam to the microdosimeter was calibrated using a calibrated fully depleted 300 µm thick planar silicon Hamamatsu PIN photodiode with 100% charge collection efficiency (CCE) in response to 5.5 MeV He^{2+} ions beam [100].

3.2.2 Microdosimeters under investigation

The radiation environment in space is characterized by a 4π isotropic exposure and by a low flux rate, thus new detectors need to consider a large detection area and free standing 3D SVs. Thus, the latest design of the 3D trenched planar "Mushroom" microdosimeter for space application is similar to the one described in section 1.3.2, however it has larger number of SVs. With respect to the previous design of the "Mushroom", whose array area was 2 x 2 mm^2, the array area of the new design for low-dose rate environments in space application was increased to 10 x 10 mm^2. Keeping the same pitch of 50 µm between SVs, many more SVs were added to the array. The CCE of two microdosimeters was investigated: while the SV's diameter of both of them was 18 µm, the SV's height was 5.16 µm for the first

detector and 10.25 µm for the second one. The microdosimeter active layer (i.e the SOI wafer thickness) is guaranteed by wafer manufacturer within ± 0.5 µm. The polysilicon region was etched on the surface of the device to achieve a better planarization [101], and to allow a more robust metal connection between the SVs as seen in Figure 3.3b. Additionally, Figure 3.4 shows two SEM images of the cross-section of SVs with dimensions of 5 µm and 10 µm thick designs obtained by electron microscopy. These images was performed by the team led by Prof. Elena Pereloma at the Australian Institute for Innovative Materials, University of Wollongong.

The performance of these devices was studied under different biases with a possibility to operate these devices in passive mode for space application. Thus, the microdosimeter was biased at voltages of 0, 1, 2, 5 and 10 V and results were compared.

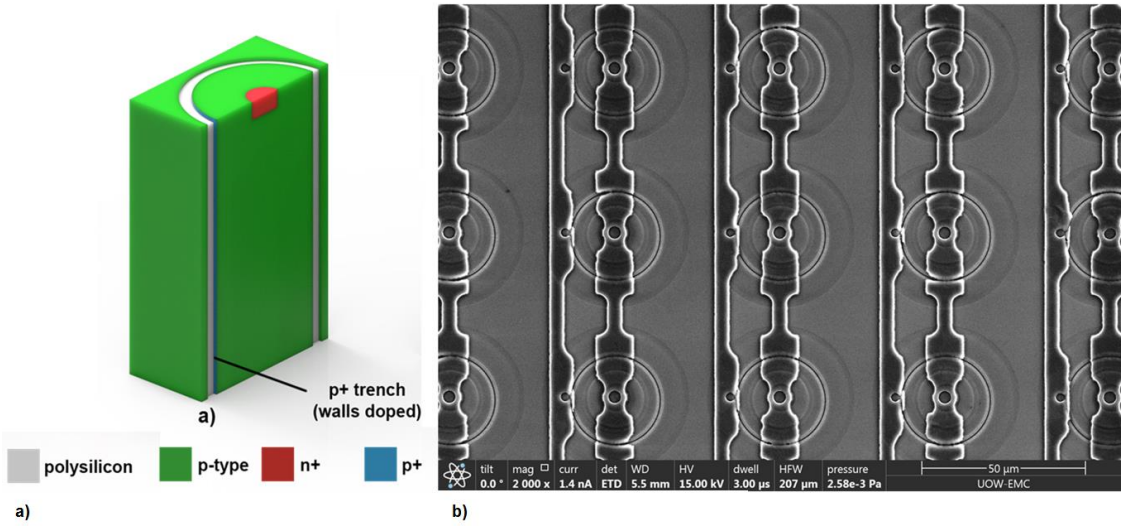

Figure 3.3. a) Simplified schematics illustrating the SV geometry of a trenched planar structure of the new SOI "Mushroom" microdosimeter, and b) the SEM image of the SVs array of the microdosimeter.

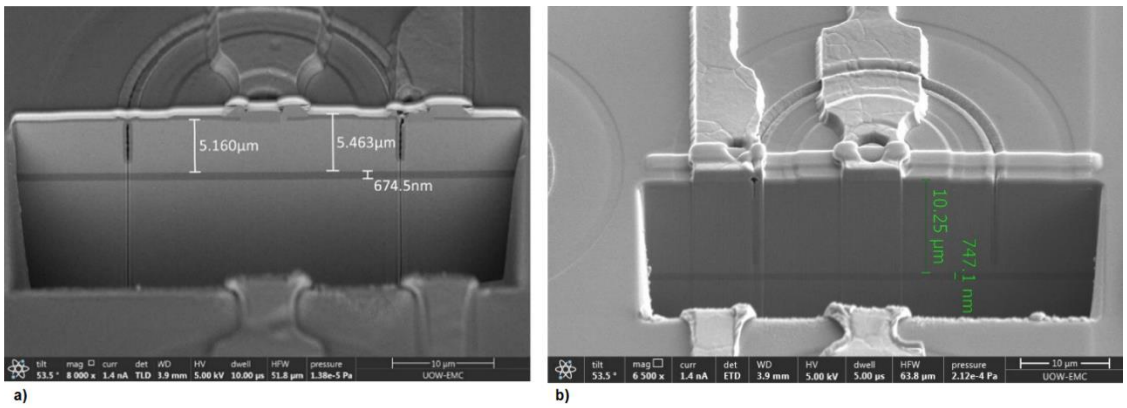

Figure 3.4. Images courtesy of the Electron Microscopy Centre, Australian Institute for Innovative Materials at University of Wollongong: the cross-sectional SEM images of the 18 µm diameter SV for the "Mushroom" a) 5.16 µm thick, b) 10.25 µm thick.

3.2.3 GEANT4 simulation

GEANT4 simulation were performed to evaluate the energy deposition in the two "Mushroom" microdosimeters, 5 and 10 µm thick. The microdosimeters were modeled following details described in the previous section 3.2.2, and irradiated with a normal incident beam of 5.5 MeV He^{2+}. The spectrum of energy deposited in the SVs of the microdosimeters was stored as output of the simulation.

The GEANT4 version and the physics lists adopted for this simulation are the same used for modeling the "Mushroom" microdosimeter's response in LEO environment (see section 2.2.1 of Chapter 2).

3.3 Results and Discussion

Figure 3.5 shows the MCA spectra obtained when raster scanning the 10 µm SVs thick "Mushroom" microdosimeter with 5.5 MeV He^{2+} ions, when different biases were applied. In all spectra, it can be observed an energy peak in the range of 1330 - 1450 keV, which resembles the peak simulated with GEANT4 where the expected energy deposition in 10-µm-thin "Mushroom" microdosimeters is 1470 keV.

The detector is completely depleted with a 97% CCE at 10 V, whereas at 0 V the CCE achieved is 90%. The difference in the simulated value and the measured one can also be attributed to the fact that the thickness of the SV can vary of ± 0.5 µm. The corresponding charge collection can be visualized in the median energy maps in Figure 3.6: in each map there are two rows with four SVs collecting charge individually. The visible dots outside the SVs correspond to some events occurring because of the noise in the electronics, but not related to meaningful charge collection outside the SV.

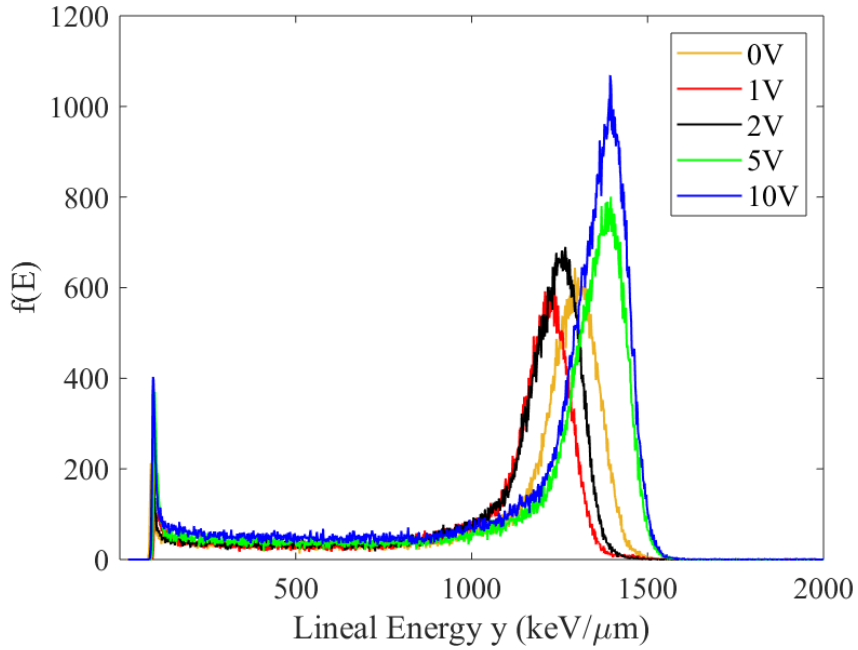

Figure 3.5. MCA spectrum obtained from 18 µm diameter and 10 µm thick "Mushroom" microdosimeter irradiated with 5.5 MeV He^{2+} ions, when different bias of 0, 1, 2, 5, and 10 V were applied.

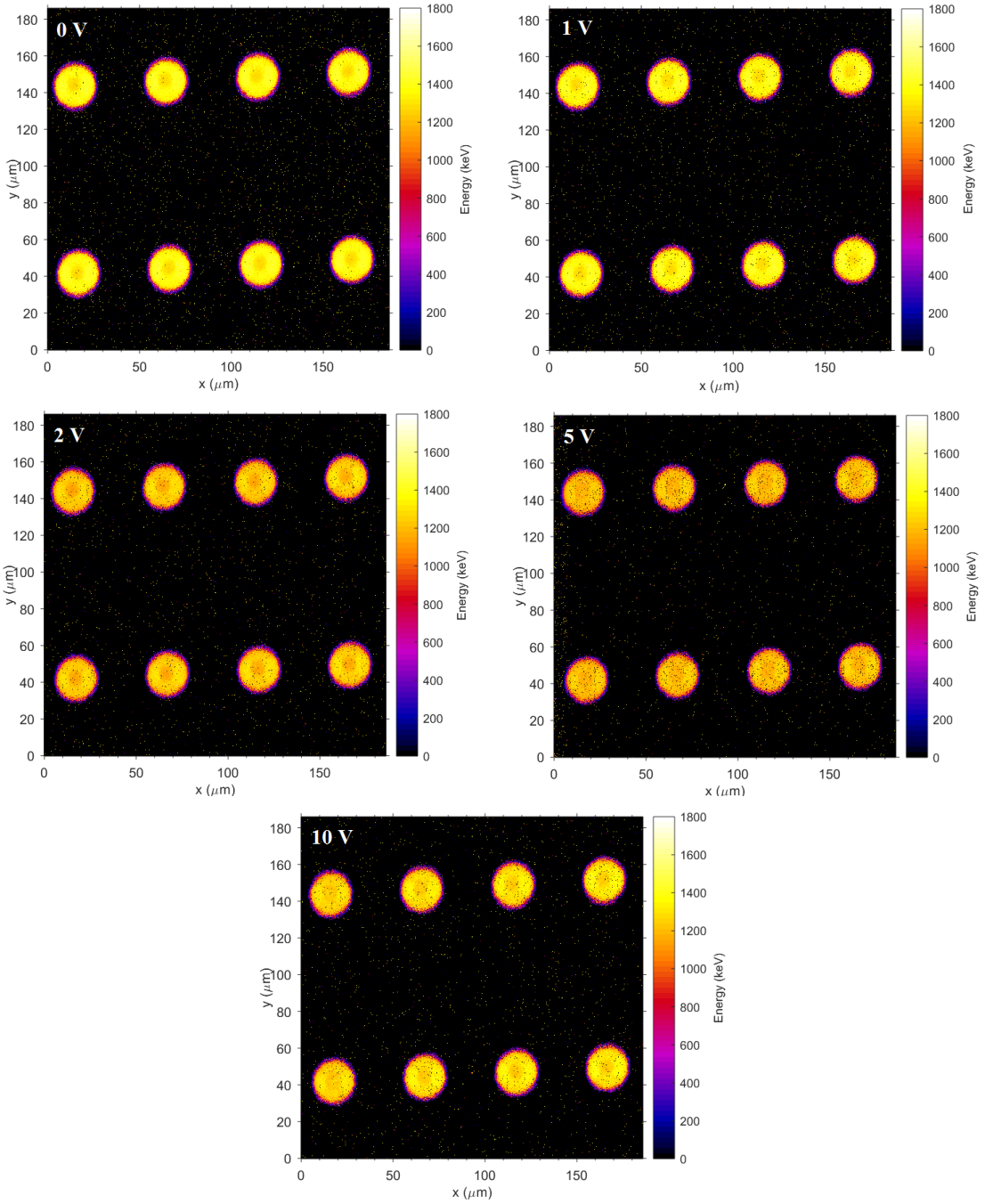

Figure 3.6. Zoomed energy map of 8 SVs of the "Mushroom" microdosimeter irradiated with 5.5 MeV He^{2+} ions, when different bias of 0, 1, 2, 5, and 10 V was applied. Each SV has dimension of 18 µm diameter and 10.25 µm thickness.

An additional irradiation was performed limiting the raster scanning area to only one SV to facilitate the distinction of different areas and layers in the SV.

The SV has a very well defined volume shape with uniform charge collection in the p-type sensitive area (yellow area) with a distinct n^+ core of events depositing energy approximately of 1200 keV. The outermost trenched region filled with polysilicon and with a p^+ doped wall is characterized by events at lower energy up to 700 keV. Figure 3.7b-c shows an evident difference in the median energy map at the core level: a 10 V bias applied enhances the charge collection in the sensitive area, thus the core appears vaguer.

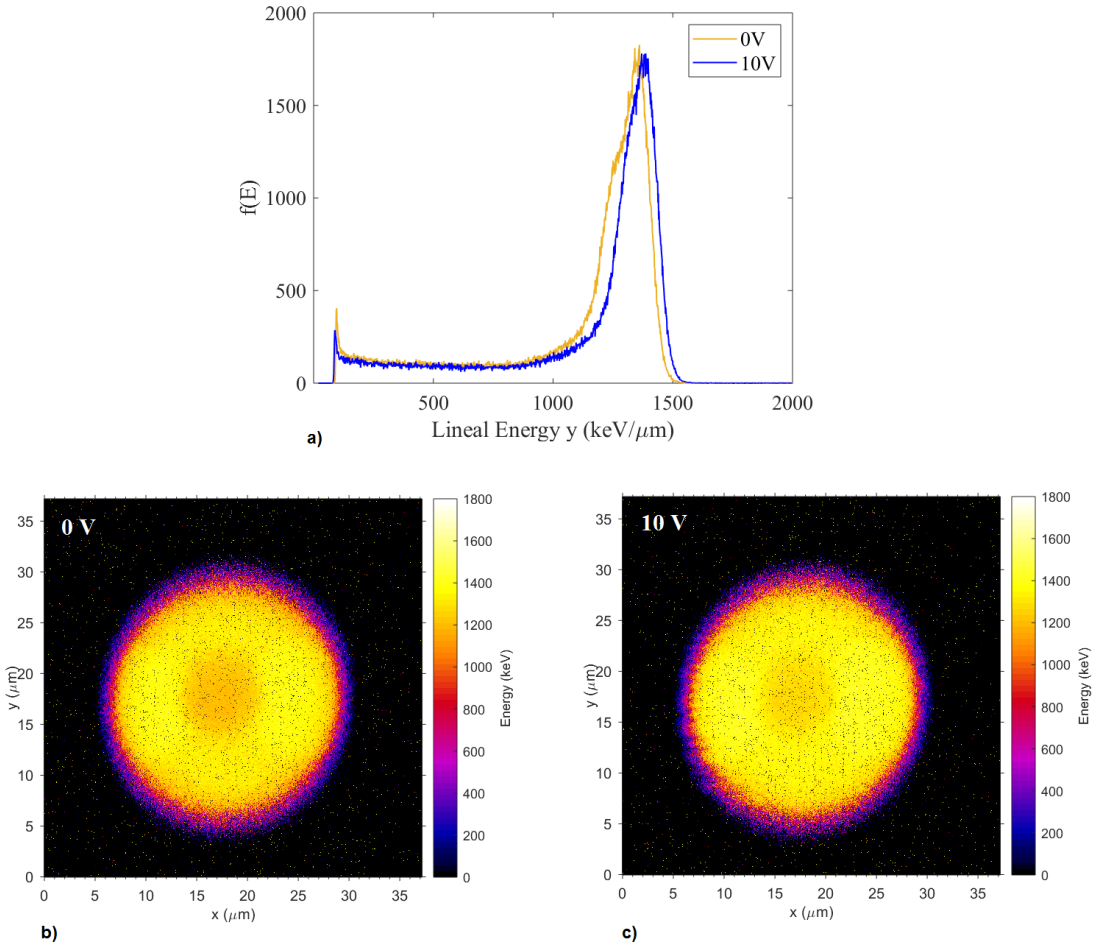

Figure 3.7. a) MCA spectrum obtained from 18 µm diameter and 10.25 µm thick "Mushroom" microdosimeter irradiated with 5.5 MeV He^{2+} ions, and corresponding median energy map illustrating the spatial distribution of energy deposited in a single SV when b) the detector was biased at voltage of 0 V and c) at 10 V.

In Figure 3.8, the MCA spectra for irradiations of the "Mushroom" microdosimeter with SVs 5 µm thick are reported. From GEANT4 simulations, the energy deposited in the peak is expected to be 732 keV. The main peak matches the simulated value, confirming the CCE increasing from 98% to 100%, for 0 and 10 V respectively. However, the spectra are characterized by two "shoulders" in the energy range of 400 – 650 keV putting in evidence the deficit of collected charge in the planar core. This is also confirmed in Figure 3.9, where the median energy maps are characterized by well-defined SVs with a visible core with a more orange appearance. Results agree with a previous study performed by using IBIC technique in [101], where the latest designs of the "Mushroom" where irradiated with 3 MeV He^{2+} ions.

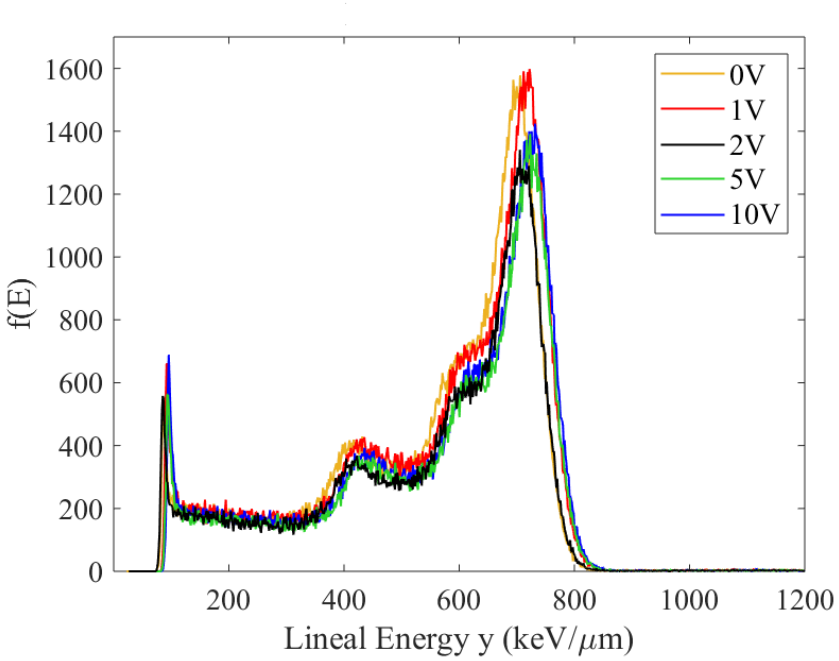

Figure 3.8. MCA spectrum obtained from 18 µm diameter and 5.16 µm thick "Mushroom" microdosimeter irradiated with 5.5 MeV He^{2+} ions, when different bias of 0, 1, 2, 5, and 10 V was applied.

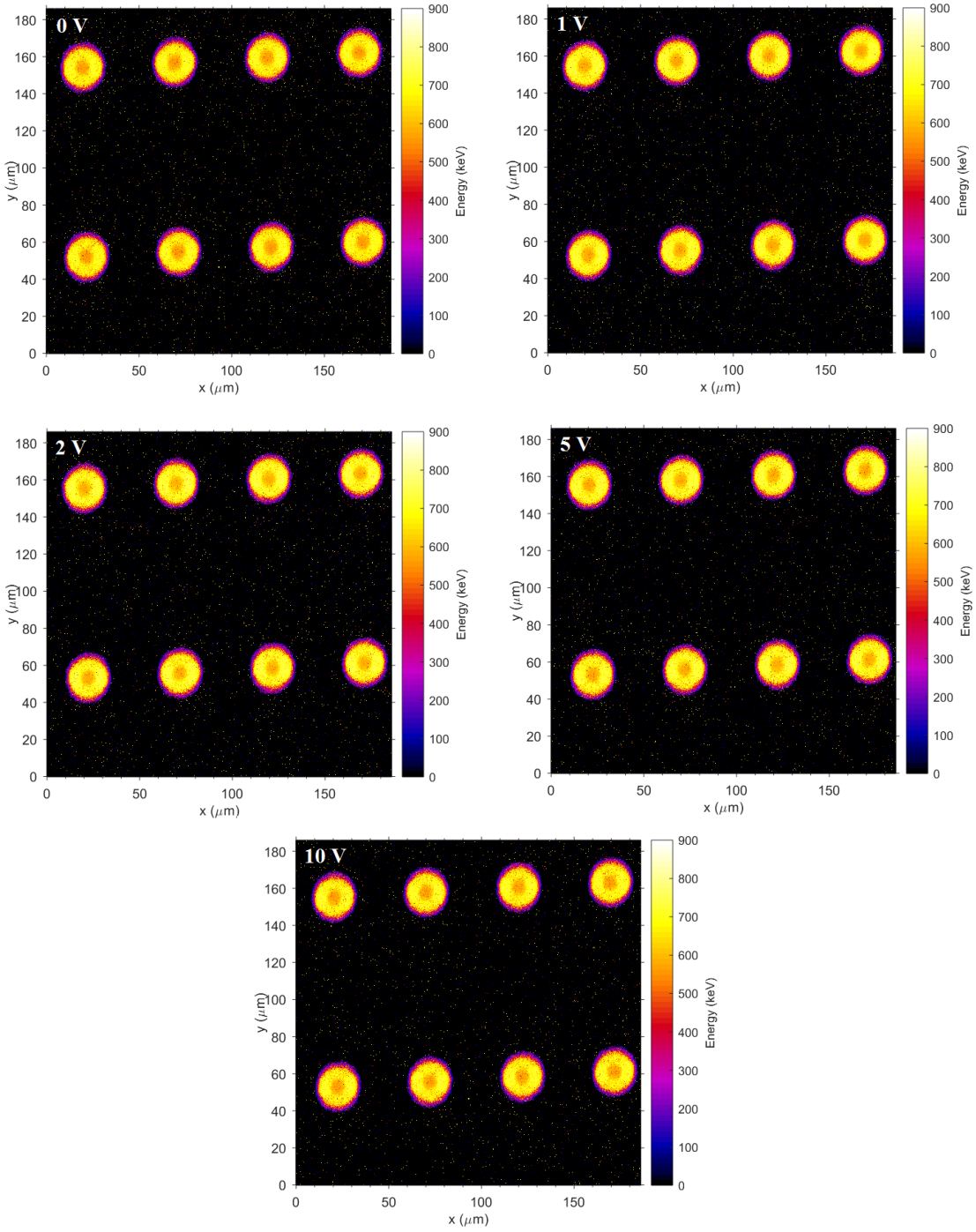

Figure 3.9. Zoomed energy map of 8 SVs of the "Mushroom" microdosimeter irradiated with 5.5 MeV He^{2+} ions, when different bias of 0, 1, 2, 5, and 10 V was applied. Each SV has dimension of 18 µm diameter and 5.16 µm height.

3.4 Conclusions

The charge collection of the large area "Mushroom" microdosimeter for space application were studied using the IBIC technique. The microdosimeters have cylindrical SVs with diameter of 18 µm and with either 5 or 10 µm height. The large area of 10 x 10 mm^2, corresponding to a sensitive area of 5 x 5 mm^2 when pitch of 50 µm between SVs is considered, makes this new design suitable for radiation environments characterized by a low radiation flux rate such as in space.

The microdosimeters were connected to the low noise MicroPlus probe and exposed to a 5.5 MeV He^{2+} ions scanning beam: the energy spectra together with corresponding mean energy maps were obtained to visualize the charge collection in the SV.

The uniform charge collection and a well-defined volume shape visualized in the mean-energy map reflect in a high CCE reaching full depletion of the device. Despite the n^+ planar core happened to be characterized by slightly lower energy events for lower voltages applied, the main peak of energy deposited match the expected value simulated with GEANT4.

Nevertheless, the charge is well collected inside the SV region, and only a few visible dots are seen in the region between SVs which relate to electronics noise and not to charge diffusion or collection outside the sensitive area.

In conclusion, the new large area microdosimeter geometry was demonstrate to be suitable for radiation environment characterized by low flux rate of particles, thus for application in space. The microdosimeter will be used in following studies presented in this thesis where its response will be characterized in heavy ions and proton field.

Chapter 4

Microdosimetric measurements in heavy ions accelerator beam lines

In this chapter, results obtained in an experimental campaign performed at the Heavy Ions Medical Accelerator in Chiba, Japan, are discussed and included in the publication presented at the Nuclear & Space Radiation Effects Conference 2019 [102].

As first author of the article "S. Peracchi, et al., A solid-state microdosimeter for dose and radiation quality monitoring for astronauts in space, IEEE Trans. Nucl. Sci., vol. 67, no. 1, pp. 169-174, January 2020", I retain the right to include it in the thesis. After consultation with the IEEE TNS journal, the article is reproduced in this chapter from the original source found through the DOI: 10.1109/TNS.2019.2943597.

This study shows the response of the SOI "Mushroom" microdosimeter with 3D sensitive volumes to 400 MeV/u ^{16}O and 500 MeV/u ^{56}Fe ions mimicking the Galactic Cosmic Rays outside and inside the International Space Station (ISS). The average quality factor $\bar{Q}$ and the dose equivalent ($Hp(10)$) of the radiation field were obtained experimentally in different set-ups, and the results were compared with GEANT4 simulations. In particular, scenarios of an astronaut inside and outside the spacecraft, as well as dose evaluation at different depths in the human body were considered.

4.1 Introduction

In this study, the SOI "Mushroom" microdosimeter whose charge collection efficiency was investigated in Chapter 2, was used to characterize the heavy ions component of the galactic cosmic rays field encountered at the ISS altitude.

Irradiations were carried out at the Heavy Ions Medical Accelerator in Chiba (HIMAC) with two types of ions: ^{16}O ions as representatives of the most abundant species of HZE after alpha particles, and ^{56}Fe ions as the heaviest ion's type with abundance similar to oxygen ions. The relative abundance was discussed in section 1.1.1 when the HZE component of GCR was introduced.

Moreover, the use of a reproduced sample of the shielding wall of the Columbus module docked at the ISS allowed the evaluation of the quality factor and the dose equivalent inside and outside the spacecraft.

Three types of measurements were done: the measurements of the dose equivalent below a specified point in an astronaut's body freely floating in inside and outside the spacecraft. The dose 0.07 mm deep below the skin ($Hp(0.07)$) and the dose at 10 mm depth in the body ($Hp(10)$) [50] were measured considering tissue-equivalent converters around the microdosimeter to reproduce the human body.

A Monte Carlo simulation using GEANT4 was developed to have a deeper insight in the experimental measurements.

Secondly, measurements at different depths in a water phantom were done to evaluate the variation of the dose equivalent and the quality factor resulting from the secondary radiation field produced while primary ions propagate through the body of an astronaut and interact with nuclei.

Finally, out-of-field measurements were carried out using the water phantom to characterize the secondary radiation field generated by primary ions propagating through the body, and scattering at wider angles causing a potential exposure of nearby organs.

4.1.1 The HIMAC facility

In 1957, the initially named National Institute for Radiobiological Science, whose name was changed in 2017 into National Institute for Quantum and Radiological Science and Technology (QST) was established as a radiation research institute and hospital in Japan, with a focus on radiological science. Since 1975, the QST treated, with fast neutrons and protons, patients afflicted by cancer in several part of the body such as those in the abdominal area, prostate, eye, bone and soft tissue, head and neck, lung, gynecological region, etc. Then, after extensive study of different ions for optimal physical and biological advantages, carbon ions were selected. In 1993, the Heavy Ion Medical Accelerator in Chiba (HIMAC) was launched, becoming the world's first heavy ion accelerator complex dedicated to medical uses. The HIMAC accelerator was then immediately used for carbon ion radiotherapy, and became a leading center in the world treating more than 7000 patients [103].

The HIMAC building schematic is shown in Figure 4.1. It houses the synchrotron which includes the ion sources, followed by the linear accelerator that can accelerate ions up to 6 MeV/u. The main part of the accelerator, which accelerates ions to the 73% of the speed of light, consists in dual synchrotron rings, ejecting particles in the horizontal and vertical high-energy transport beam lines that end in three rooms (A, B, and C) for patients' treatment. The need to adapt therapies to the changes in size, shape and location of tumors, led to the planning of a new particle therapy facility provided with a rotational gantry.

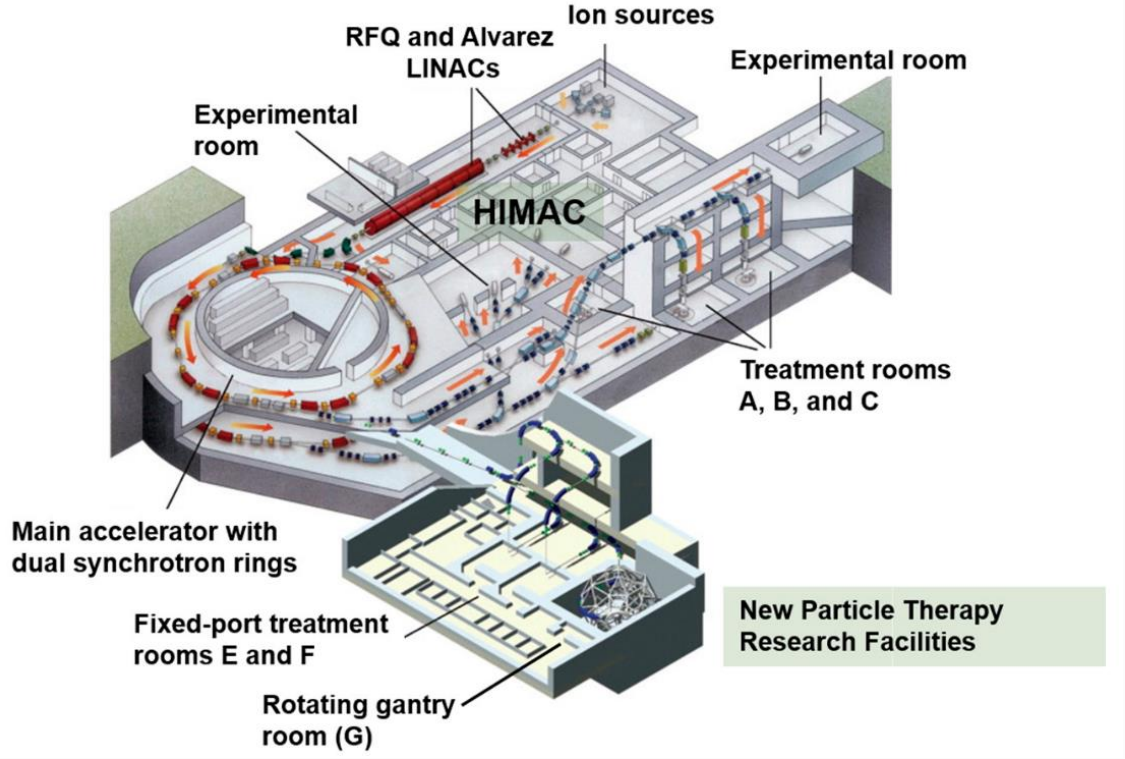

Figure 4.1. Image courtesy of (O. Mohamad, et al., 2018) [103]: Schematic view of the HIMAC building at the NIRS.

The HIMAC is also home of researchers coming from all around the world to conduct experiments related to nuclear physics, and many other field involving the use of radiation. The HIMAC Biological exposure room is the one assigned for such purposes, thanks also to the possibility of deliver a beam of different types of ions (from He to Ar) and energies. This room has a 250 cm thick concrete wall though which the tube containing the beam goes. As shown in Figure 4.2, once the beam enters the exposure room, two cylindrical wobbler magnets shape it, before reaching a series of scatterers, usually Tantalum and Lead. Collimators, vacuum shutter, filters and the aluminum four-leaf collimator (FLC) are then used to collimate and reduce the neutron contribution of the beam. At this point, optional PMMA shifter of different water-equivalent thicknesses can be inserted along the beam to shift the range of particles, according to the study that wants to be performed. Finally, the beam can then be further collimated and shaped by an X-Y collimator positioned

140 mm before the isocenter, where researchers usually set up their instrumentation [104, 105].

The experimental campaigns presented in this chapter were performed in the biological beamline. The experimental set-up adopted in the study of this thesis will be presented in details in the methods section.

Figure 4.2. Photo of the HIMAC BIO exposure room with modelled components of the beam line (on top, not in scale) [104].

4.2 Materials and Methods

Irradiations were carried out at the Heavy Ions Medical Accelerator in Chiba (HIMAC) using a passive scattering beam of 400 MeV/u ^{16}O and 500 MeV/u ^{56}Fe, inside the BIO exposure room described in section 4.1.1. For the ^{16}O ion beam a 0.910 mm thick tantalum scatterer was used, while for the ^{56}Fe ion beam a

combination of a 0.215 mm thick tantalum scatter and a 1.60 mm thick lead scatterer were used. A field size of 5 × 5 cm^2 was produced using a 5 cm thick X-Y brass collimator placed at 140 mm upstream of the isocenter.

As final assessment of the beam before starting any experimental irradiation, a compulsory measurement of the physical dose was performed to evaluate the position of the Bragg peak for 400 MeV/u ^{16}O and 500 MeV/u ^{56}Fe ions in water equivalent thickness. For this purpose, the PMMA range shifters (see Figure 4.2) were sequentially inserted along the beam line to achieve water-equivalent depths of interest to which the dose was evaluated. An ionization chamber was used to measure the dose.

4.2.1 The SOI "Mushroom" microdosimeter

The SOI microdosimeter used in this experiment is the "Mushroom" model which was previously studied in Chapter 2 and whose response was simulate inside the ISS in Chapter 2. As a reminder, the microdosimeter design consists of a matrix of 400 cylindrical silicon SVs with dimensions of a biological cell. Each SV has a n^+ planar electrode surrounded by p^+ trench electrode filled with polysilicon [61, 92]. The SV has dimensions of 18 µm in diameter and 10 µm in height and the distance between two adjacent SVs is 50 µm (pitch) (see Figure 3.3).

The energy deposited by particles inside the SVs is experimentally measured by the microdosimeter on an event-by-event basis by primary and secondary particles. The energy deposited was divided by the average chord length $\bar{l}$, which in our case was 10 µm, to finally obtain the lineal energy y. From the measured frequency distribution $f(y)$ and the dose lineal energy distribution $d(y)$ as described in details in sections 1.3.1, the microdosimetric spectra $yd(y)\ vs\ y$ in logarithmic scale was derived. Through the analysis of the microdosimetric spectra, the average quality factor $\bar{Q}$ of the radiation field of interest was calculated. $\bar{Q}$ can be calculated with the equations provided by the ICRP Publication 60 [106], shown in Table I, in section 1.3.1. The quality factor definition depends on the LET, which refers to the unrestricted linear energy transfer. However,

in this study the lineal energy y is used to calculate Q, instead of LET. Particularly, the LET and y will not differ significantly except for relatively low LET radiation with an energy of ~100 MeV or higher. This approximation is accepted especially when the energy of ions is decreasing and LET increasing with more relevant increase of the RBE. At these energies of protons, the range of delta electrons in water is much larger than the size of the sensitive volume.

Additionally, for astronauts' individual monitoring, we evaluate the personal dose equivalent $Hp(0.07)$ and $Hp(10)$ at the depth of 0.07 mm and 10 mm, respectively, in the human body. To reproduce the human body condition for these two quantities calculation, we used two Poly(methyl methacrylate) (PMMA) converters 0.07 mm and 10 mm thick as an approximation of the ICRU human tissue [107] during the measurements in the free air geometry, which were placed on top of the SVs. The value of the personal dose equivalent in tissue was calculated multiplying the average quality factor $\bar{Q}$ by the absorbed dose in silicon deposited in the microdosimeter and by a tissue-equivalent conversion factor of 0.58 obtained from tissue equivalency studies in mixed radiation fields of secondary charged particles as in ion therapy and space [59, 93, 108], according to the equation (1.17).

Finally, we normalized the dose equivalent $Hp(d)$ per unit absorbed dose in water (per Gy) delivered at the Bragg Peak (BP). The value of absorbed dose in water was derived by a preliminary measurement of the Bragg curve. This normalization was applied to all dose calculations for the irradiations with iron and oxygen ions.

4.2.2 Irradiation of the microdosimeter in free air geometry

The SOI microdosimeter was connected to a low noise MicroPlus probe as shown in Figure 4.3b.

A free air geometry was implemented by placing the MicroPlus probe with the "Mushroom" microdosimeter along the central axis of the beam, as shown in Figure 4.3 [62]. Two PMMA converters of 0.07 mm and 10 mm thick were put in front of

the probe to reproduce the scenario for the personal dose equivalent $Hp(0.07)$ and $Hp(10)$ estimation, respectively.

Because the aim was to mimic the radiation environment outside and inside the ISS, the spacecraft's wall was modeled with two aluminum slabs corresponding to the ISS wall's specification [88, 109]: the first slab of 7.3 mm thickness represents the real aluminum pressurized shell of the ISS. The thicker slab of 35.95 mm includes an additional layer corresponding to the so-called "Internal Out-fitting". This is the equivalent areal mass of aluminum accounting for several devices and structures non homogeneously distributed inside the habitable volume of the ISS, which provide a further barrier and source of additional secondaries to particle's radiation.

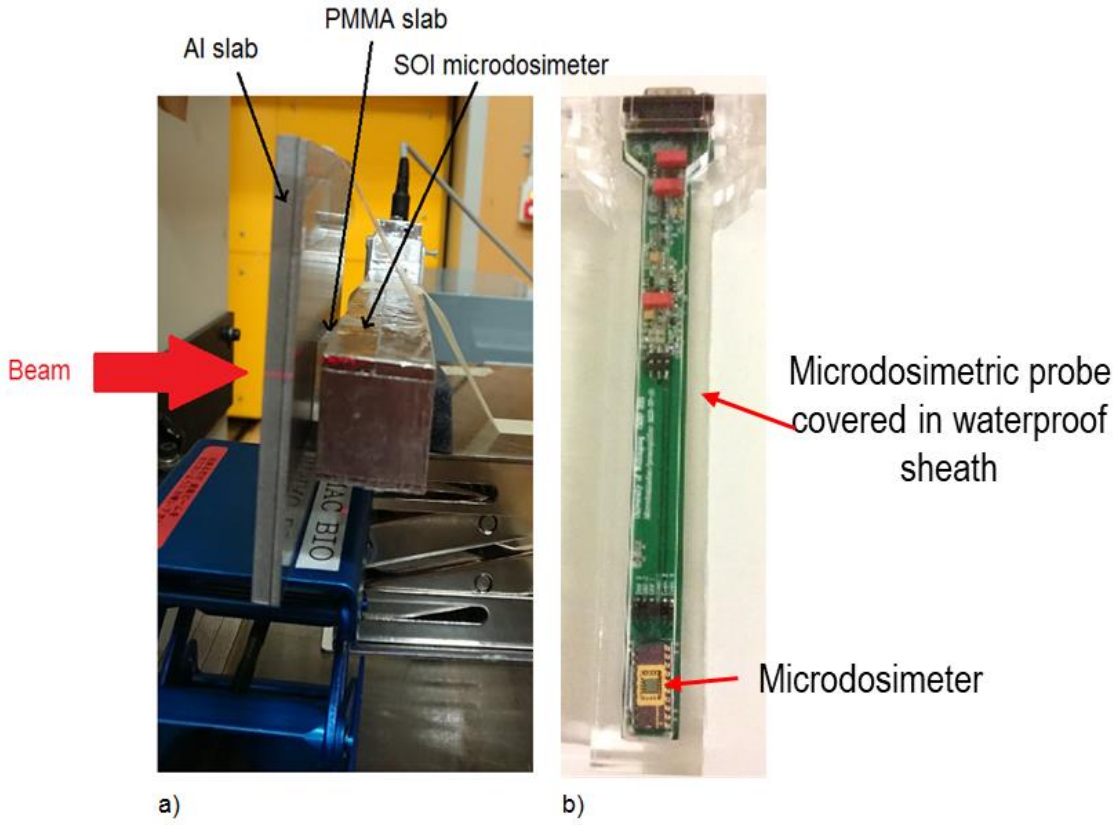

Figure 4.3. a) Free air geometry setup inside the irradiation room at HIMAC. b) MicroPlus probe inserted into a waterproof sheath with SOI "Mushroom" microdosimeter connected at the end of the PCB.

4.2.3 Irradiation of the microdosimeter inside a water phantom geometry

In-field measurements

To mimic different positions in an astronaut's body, the microdosimetric response was measured setting the microdosimeter in different positions in a water phantom, which represented the astronaut's body. Thus, in our study we approximated the human body as made of water, with density 1 g cm^{-3}. The $\bar{Q}$ and Hp values were then estimated.

The position of the MicroPlus probe in a water phantom was controlled remotely using an X-Y motion stage developed in house (Figure 4.4) [62]. The μ^+ probe was moved along the Y-axis in the beam's central axis with the beam incident on the top of the cylindrical SVs of the microdosimeter. Due to mechanical constraints, the minimum water equivalent depth achievable in the water phantom was 11.17 mm, referred to as the "entrance depth".

This study compares the microdosimetric spectra measured inside (with Al wall) and outside (no Al wall) of the spacecraft for an astronaut. In particularly, we used a 35.95 mm Al slab for oxygen ions measurements and only a thin 7.3 mm Al slab for iron ions, because the 35.95 mm thick Al slab would have stopped the primary iron beam, before reaching the water phantom.

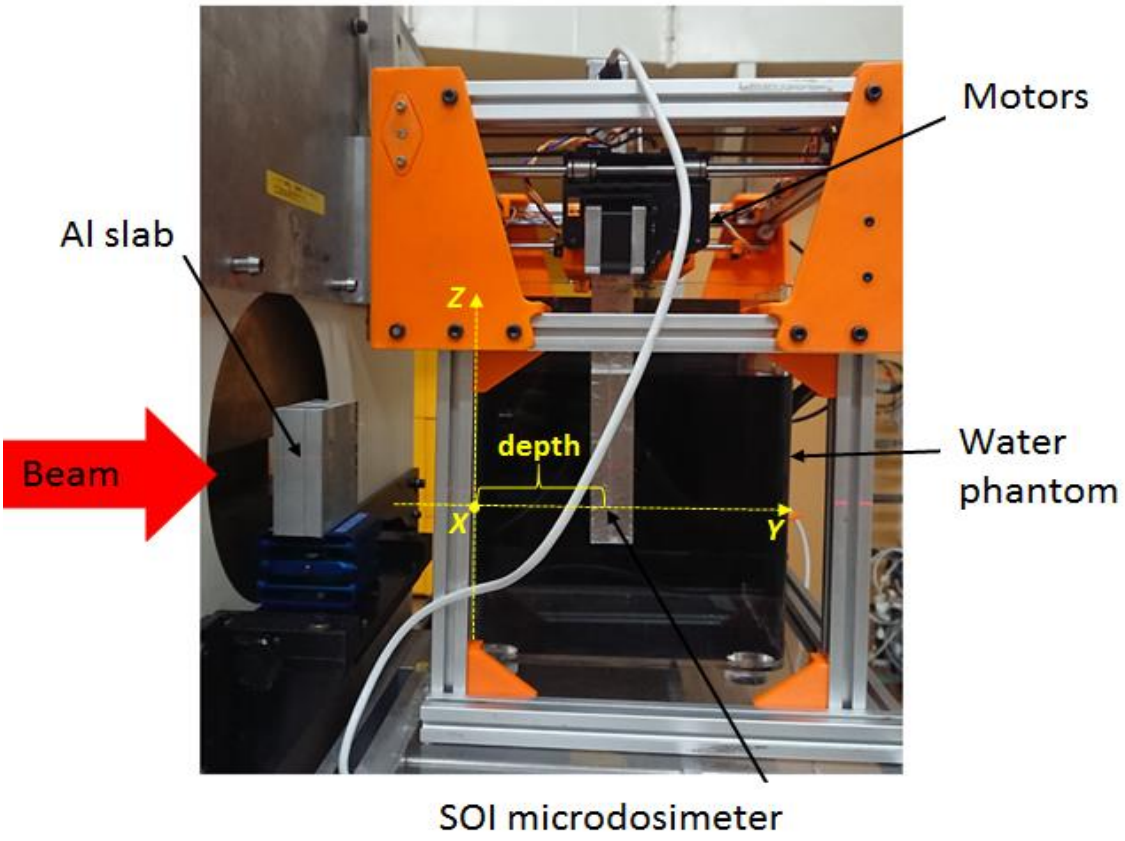

Figure 4.4. Water phantom geometry setup inside the irradiation room at HIMAC, with 35.95mm thick Al slab for the particular case of oxygen ions.

Out-of-field measurements

When GCRs pass through the human body then induce interactions with the tissues, this process consequently generates a field of secondary particles, like high energy neutrons that spread out from the direction of the primary incident ion. These secondary particles can cause exposure of nearby organs or tissues and pose even more severe hazard. Measurements outside or the primary radiation field is called "out-of-field" measurements in order to investigate the radiation level in this region.

As part of the study, three lateral positions out-of-field (OOF) have been considered, particularly on a beam field size of 5 x 5 cm^2, the SOI microdosimeter

was placed at 2.5, 3.5 and 5.5 cm laterally from the beam central axis as shown in Figure 4.5. Due to the sensitive area of the detector of 1 x 1 mm^2, for the measurement performed at 2.5 cm, the microdosimeter was exactly at the edge of the field facing the beam, and half of the active area of the detector was inside the primary ions beam. For 400 MeV/u ^{16}O ions, the microdosimetric spectra of the mixed radiation field including the primaries and secondaries, were measured and the quality factor and the dose equivalent were obtained. The MicroPlus probe was placed in the water phantom at entrance depth (20 mm) and before the BP (180 mm) (the BP for 400 MeV/u Oxygen ion was 186.1 mm) and moved laterally to the edge of the field for OOF measurements. Finally, the measurements were repeated for two scenarios: "no wall" and "with Al wall" where "no wall" represents the situation of an astronauts performing an extra vehicular activity in free space, and "with Al wall" represents the astronauts inside the spacecraft behind the aluminum shielding wall.

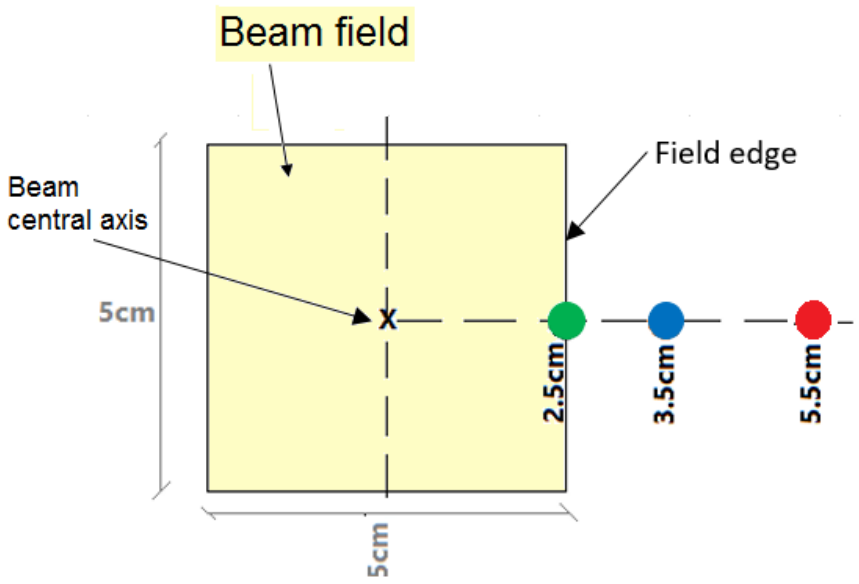

Figure 4.5. Schematic of the "out-of-field" irradiation positions of interest, considering a beam field size of 5 x 5 cm^2.

4.2.4 GEANT4 simulation validation

A GEANT4 simulation was developed based on the passive biological beamline model at HIMAC, validated through experimental measurements by (Bolst et al., 2019) [104]. The model reproduces the exact set up used during experiments, discussed in section 4.2.2. The specifications of materials constituting the spacecraft's wall were the same used for the simulation discussed in Chapter 2.

The GEANT4 version 10.02.p3 was adopted with the following physics list: *G4StandardOption3* to describe electromagnetic interactions, *Binary Intranuclear Cascade (BIC)* for hadronic interactions and *G4HadronElasticPhysicsHP* for elastic scattering of hadrons.

The simulation measured the energy deposition per single event occurring in the SV of the microdosimeters and consequently, the microdosimetric spectrum of the mixed field is retrieved as output for comparison with the experimental one. Through the analysis of the spectrum, the average quality factor and the dose equivalent are calculated using the same mathematical method described in section 4.2.1.

4.3 Results and Discussion

The measurement of the physical dose was performed to evaluate the position of the Bragg peak for 400 MeV/u ^{16}O and 500 MeV/u ^{56}Fe ions in water equivalent thickness. Figure 4.6 shows the relative energy deposition curve, where the dose was normalized to 1 in correspondence of the Bragg peak. Incident iron ions resulted to have a range of 73.1 mm in water, whereas lighter oxygen ions have a Bragg peak at 186.1 mm deep in water.

The knowledge of the dose at the Bragg peak in water allows the normalization of the dose equivalent detected by the SOI microdosimeter during experiments, as explained in section 4.2.1.

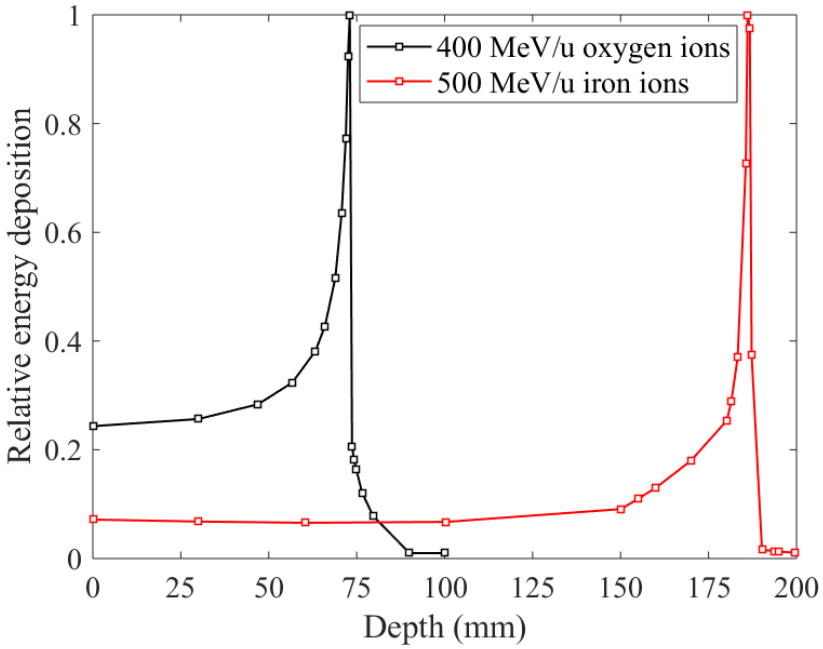

Figure 4.6. Relative energy deposition in water for 400 MeV/u ^{16}O and 500 MeV/u ^{56}Fe ions, preliminarily measured at the HIMAC BIO exposure room. The Bragg Peak was observed to be at 73.04 mm depth for iron ions and 186.1 mm depth for oxygen ions.

4.3.1 Free air geometry measurements

Figure 4.7 shows tissue-equivalent microdosimetric spectra measured with the 3D "Mushroom" SOI microdosimeter and their derived Q average value ($\bar{Q}$) for 500 MeV/u ^{56}Fe ions. The introduction of the 7.3 mm wall does not significantly change the microdosimetric spectra measured behind 0.07 mm and 10 mm of PMMA, which is dominated by primary ^{56}Fe ions. The corresponding $\bar{Q}$ values without/with 7.3 mm of Al wall were 23.38 and 22.69, respectively with the 0.07 mm PMMA converter and 22.97 and 22.10, respectively with the 10 mm PMMA converter. For an Al wall thickness of 35.95 mm, the primary ^{56}Fe ions are fully stopped, and the radiation field inside of the spacecraft is determined by the secondary fragments and neutrons originated in the Al wall. As can be seen, the microdosimetric spectra obtained with the thick Al wall is broader in comparison with the lineal energy spectrum from the thin Al wall. This is due to the contribution of secondary particles generated inside the Al wall from the primary beam, producing lower $\bar{Q}$

values of 14.63 and 17.35 with two PMMA converters of 0.07 mm and 10 mm, respectively. The values of $Hp(0.07)$ and $Hp(10)$ were calculated based on the microdosimetric spectra and are shown in Table 4.1. When the thick wall of Al was placed in front of the microdosimeter, ^{56}Fe ions are fully absorbed, the dose equivalent values dropped dramatically. The personal dose equivalent at the skin $Hp(0.07)$ was calculated to be three times higher than the dose at 10 mm depth in tissue. It can be noted while personal dose equivalent at depth 10 mm was reduced in comparison to the dose equivalent at depth 0.07 mm, the $\bar{Q}$ is increased essentially owing to modification of secondary particles' spectrum along the depth in the phantom. Microdosimetric spectra measured with the "Mushroom" microdosimeter reveal to be themselves very sensitive to these changes with depth in water.

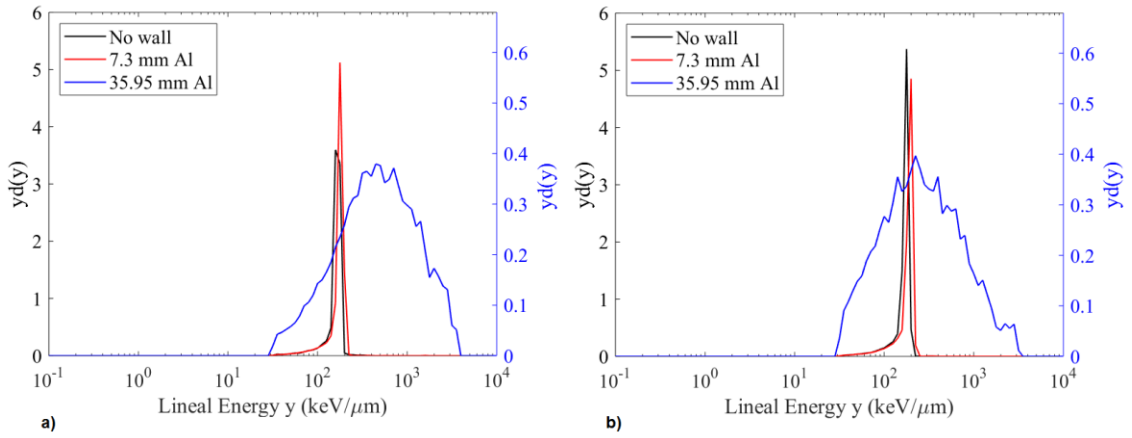

Figure 4.7. Microdosimetric spectra obtained during 500 MeV/u ^{56}Fe irradiations in free air with two PMMA converters of a) 0.07 mm thickness, and b) 10 mm thickness.

Similarly, Figure 4.8 shows tissue-equivalent microdosimetric spectra measured with the 3D SOI "Mushroom" microdosimeter for 400 MeV/u ^{16}O ions. In this case, the oxygen ions can penetrate the thick wall of 35.95 mm without being fully stopped, due to the higher range in water of 400 MeV/u ^{16}O ions compared to 500 MeV/u ^{56}Fe ions (as in Figure 4.7). When considering the 35.95 mm thick aluminum wall, the $\bar{Q}$ increases from 3.82 to 4.66, with 0.07 mm thick PMMA and from 3.84 to 4.83 with 10 mm thick PMMA converter. Derived Hp(0.07) and Hp(10)

are also increased and show how harmful the field of ^{16}O ions is, particularly it is worse inside the spacecraft for this particular energy of the incident ion, which is not stopped in the wall, reducing the energy of the O ions and increasing higher LET after passing through the Al wall and converter.

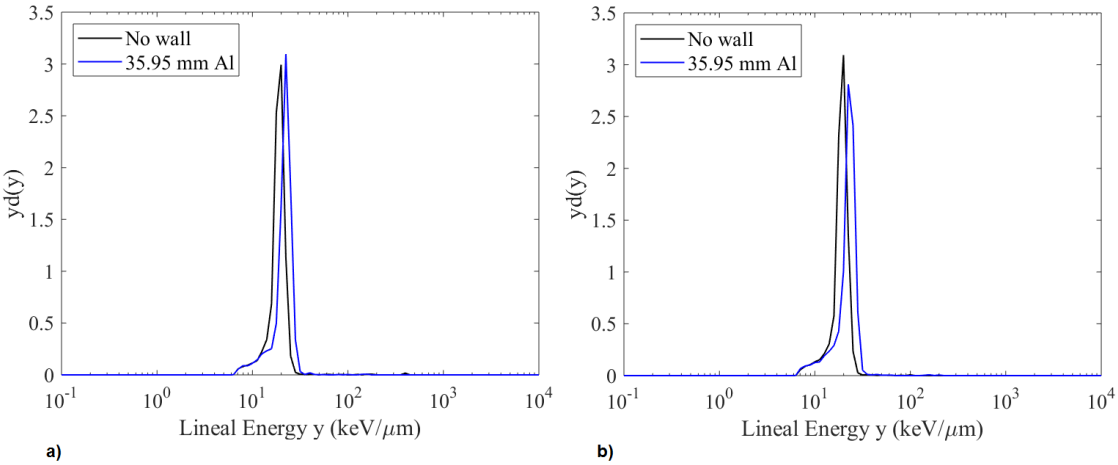

Figure 4.8. Microdosimetric spectra obtained during 400MeV/u ^{16}O irradiations in free air with two PMMA converters of a) 0.07 mm thickness, and b) 10 mm thickness.

Table 4.1. Dose equivalent calculated based on microdosimetric spectra for measurements in free air. Results are within an error range of $\pm$ 1%.

500 MeV/u ^{56}Fe				
	$\bar{Q}$	$Hp(0.07)$ (Sv/Gy)	$\bar{Q}$	$Hp(10)$ (Sv/Gy)
No Al	23.38	1.99	22.97	1.93
7.3mm Al	22.69	1.97	22.10	1.92
35.95mm Al	14.63	0.43	17.35	0.13
400 MeV/u ^{16}O				
	$\bar{Q}$	$Hp(0.07)$ (Sv/Gy)	$\bar{Q}$	$Hp(10)$ (Sv/Gy)
No Al	3.82	0.47	3.84	0.45
35.95mm Al	4.66	0.54	4.83	0.56

GEANT4 simulations in free air geometry provide a good agreement with the experimental results in terms of $\bar{Q}$ (Table 4.2). For all simulations results we adopted the error obtained for measurements with the thick aluminum wall (35.95

mm). In addition, an example of comparison of the experiment and simulation microdosimetric spectra is shown in Figure 4.9. Experimental and simulated peaks match accurately and the tail at low-energy is well represented by the simulation.

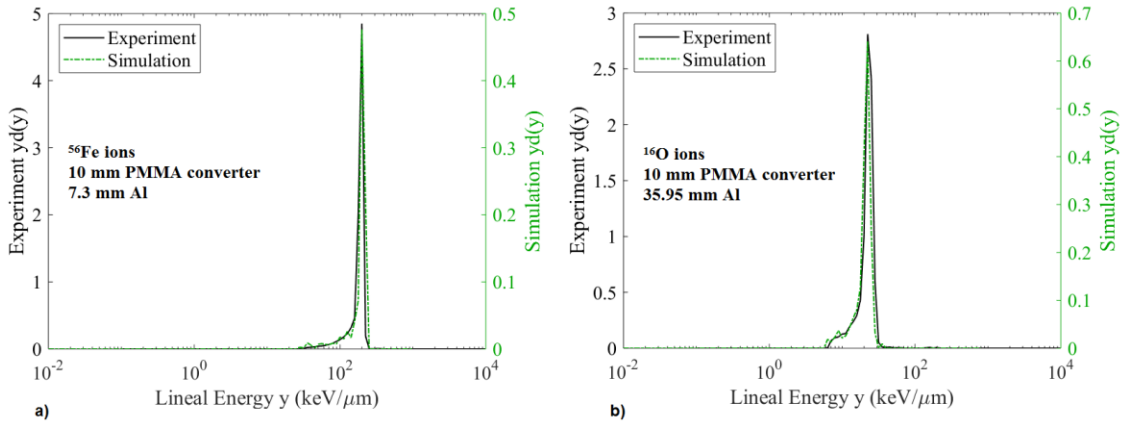

Figure 4.9. Example of microdosimetric spectra comparison from experiments and GEANT4 simulation: a) 500MeV/u ^{56}Fe irradiations in free air with 10 mm thick PMMA converter and Al wall of 7.3 mm thickness; b) 400MeV/u ^{16}O irradiations in free air with 10 mm thick PMMA converter and Al wall of 35.95 mm thickness.

Table 4.2. $\bar{Q}$ values obtained from experiment and simulation in free air geometry with 10mm PMMA converter.

500 MeV/u ^{56}Fe		
	$\bar{Q}$ Experiments	$\bar{Q}$ Simulation
No Al	22.97 ± 0.14	21.08 ± 1.28
7.3mm Al	22.10 ± 0.14	20.51 ± 1.28
35.95 Al	17.35 ± 0.18	16.32 ± 1.28
400 MeV/u ^{16}O		
	$\bar{Q}$ Experiments	$\bar{Q}$ Simulation
No Al	3.84 ± 0.04	3.78 ± 0.23
35.95 Al	4.83 ± 0.05	4.48 ± 0.23

4.3.2 Water phantom measurements

Figure 4.10 shows the trend of $\bar{Q}$ at different depths in water obtained during the irradiation with 400 MeV/u ^{16}O. When no Al wall is considered (outside of the spacecraft scenario), the LET of oxygen ions entering the water phantom is 19.38 keV/µm, according to equations in Table 1.3 the $\bar{Q}$ value increases along depths in the body until 184 mm, corresponding to the BP position. The astronaut's body will be exposed mostly to primary oxygen ions until they stop at the BP and consequently, the dose will be due to fragments and other secondary particles produced downstream of the BP. Nevertheless, with the presence of the aluminum wall 35.95 mm thick, the ^{16}O ions have a range of 90 mm in water. For organs at the depths less than 110 mm the $\bar{Q}$ values are higher if the astronaut is inside the spacecraft, representing a more harmful situation for the space crew, depending on organs' depth.

When comparing the two scenarios, we can observe that oxygen ions are more harmful at deeper depths in the body if the astronaut was outside the spacecraft because of the increasing trend of $\bar{Q}$. If the astronaut was inside the spacecraft, the shielding of the wall would cause a shift of the Bragg Peak to a more superficial depth, causing a higher $\bar{Q}$ at the entrance of the body. Figure 4.11 shows the same ascendant trend was observed for the dose equivalent H (Table 4.3): at 90 mm depth in the body, the dose behind the spacecraft's wall is almost 100 higher per Gy delivered at the BP in water than considering an astronaut outside the spacecraft.

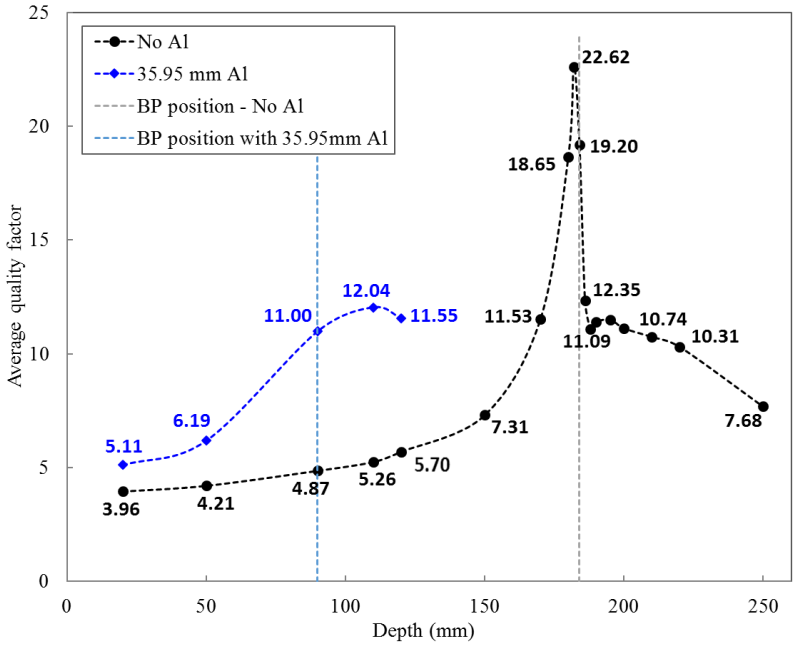

Figure 4.10. Quality factor $\bar{Q}$ at same depths in water with and without Al wall, obtained with SOI microdosimeter in response to 400 MeV/u ^{16}O ions. Vertical dashed lines show the Brag Peak position at 90 mm depth in water and 184 mm depth in water, respectively with 35.95 mm Al wall and without.

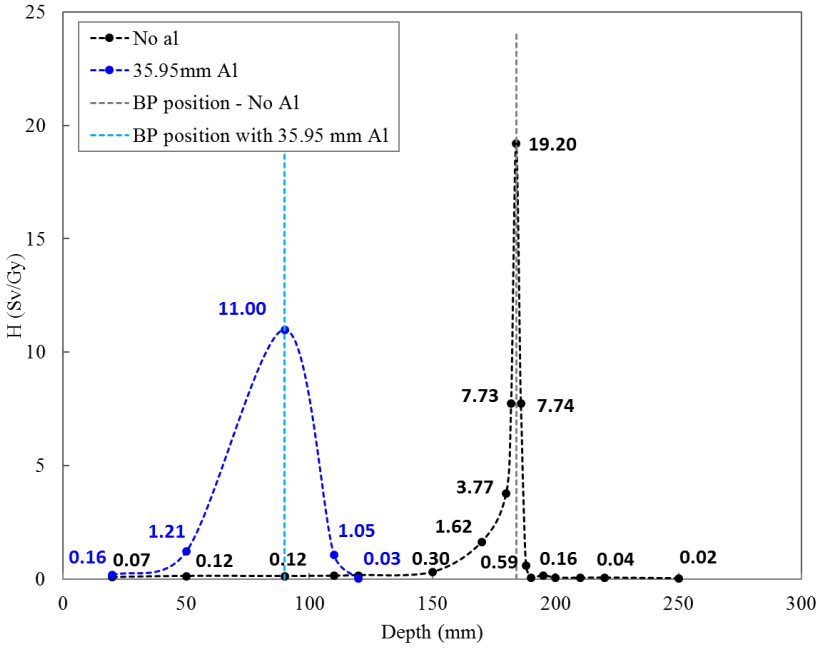

Figure 4.11. Dose equivalent H at same depths in water with and without Al wall, obtained with SOI microdosimeter in response to 400 MeV/u ^{16}O ions. Vertical dashed lines show the Brag Peak position at 90 mm depth in water and 184 mm depth in water, respectively with 35.95 mm Al wall and without.

Table 4.3. Dose equivalent and average quality factor calculated based on the microdosimetric spectra for oxygen ions measurements in water with and without the aluminum wall. Errors were within a range of ± 2%.

400 MeV/u ^{16}O				
	No Al		35.95 mm Al	
Depth (mm)	$\bar{Q}$	H (Sv/Gy)	$\bar{Q}$	H (Sv/Gy)
20	3.96	0.07	5.11	0.16
50	4.21	0.12	6.19	1.21
90	4.87	0.12	11.00	11.00
110	5.26	0.13	12.04	1.05
120	5.70	0.16	11.55	0.03
150	7.31	0.30		
170	11.53	1.62		
180	18.65	3.77		
182	22.62	7.73		
184	19.20	19.20		
186	12.35	7.74		
188	11.09	0.59		
190	11.40	0.06		
195	11.51	0.16		
200	11.12	0.05		
210	10.74	0.04		
220	10.31	0.05		
250	7.68	0.02		

The same measurement was carried out with 500 MeV/u ^{56}Fe ions for an Al wall thickness of 7.3 mm and the corresponding $\bar{Q}$ trend is shown in Figure 4.12. In contrast to the oxygen ions, when no Al wall is considered (outside of the spacecraft scenario), $\bar{Q}$ decreases with depths until 75 mm, corresponding to the BP position. According to the definition of quality factor in Table 1.3, this behavior can be explained by the high *LET* of primary iron ions entering the water phantom being 167.98 keV/µm and further increasing with depth, which is much higher than the *LET* of 19.38 keV/µm at the entrance depth observed for oxygen ions. Therefore, $\bar{Q}$ is decreasing with depth upstream of the BP according to the quality factor's behaviour for *LET* >100 keV/µm as in Table 1.3. Downstream of the BP, where

the radiation field is due to fragmented primary iron ions and neutrons with lower *LET*, $\bar{Q}$ increases for *LET* <100 keV/µm.

Nevertheless, the dose equivalent *H* per Gy delivered at the BP in water increases with depth, because the absorbed dose is growing faster with depth compared to the decrease of $\bar{Q}$. Similarly, $\bar{Q}$ values behind the Al wall of 7.3 mm thickness (inside the spacecraft scenario) decrease faster at the BP position shifted at 57.3 mm depth in water. The change of *H* values with depth in astronauts, per Gy delivered at the BP in water, is presented in Figure 4.13 and Table 4.4. Values are higher at the same depth in astronauts in comparison to the dose equivalent outside of the spacecraft but this difference is not so compared to ^{16}O ions.

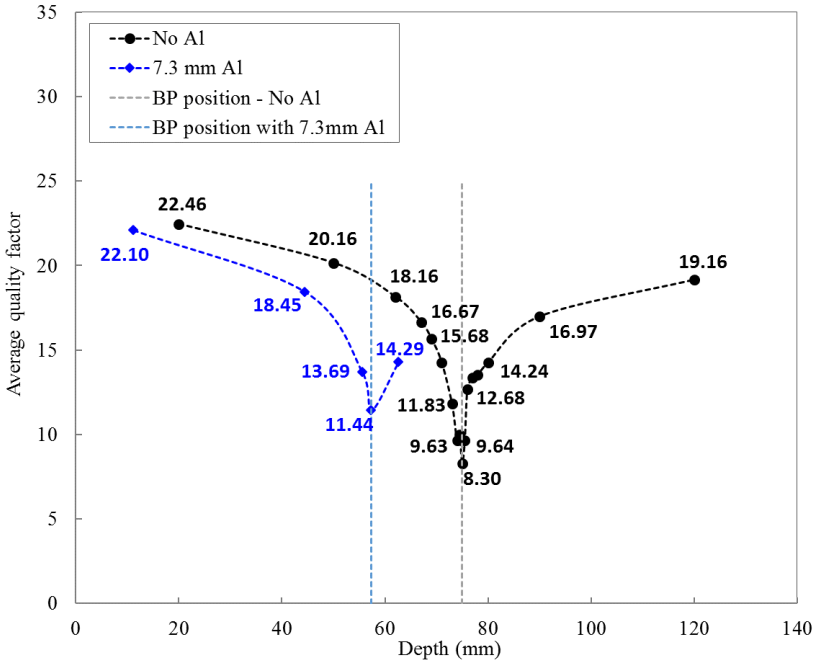

Figure 4.12. Quality factor Q at the same depths in water with and without 7.3mm Al wall, obtained with SOI microdosimeter in response to 500 MeV/u ^{56}Fe ions. Vertical dashed lines show the Brag Peak position at 57.3 mm depth in water and 75 mm depth in water, respectively with and without 7.3 mm Al wall.

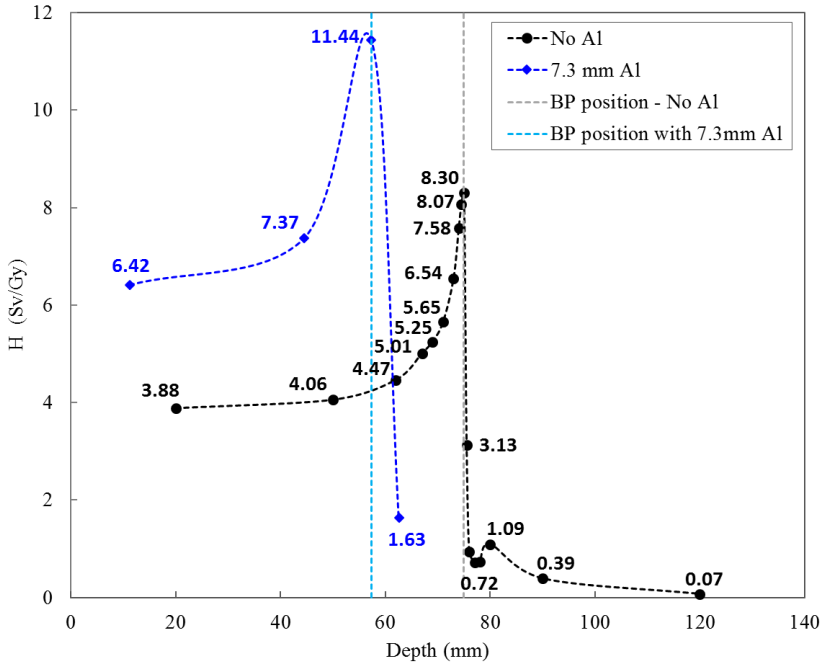

Figure 4.13. Dose equivalent H at the same depths in water with and without 7.3mm Al wall, obtained with SOI microdosimeter in response to 500 MeV/u ^{56}Fe ions. Vertical dashed lines show the Brag Peak position at 57.3 mm depth in water and 75 mm depth in water, respectively with and without 7.3 mm Al wall.

Table 4.4. Dose equivalent and average quality factor calculated based on the microdosimetric spectra for iron ions measurements in water with and without the aluminum wall. Errors were within a range of $\pm$ 2%.

500 MeV/u ^{56}Fe					
	No Al			35.95 mm Al	
Depth (mm)	$\bar{Q}$	$H\ (Sv/Gy)$	Depth (mm)	$\bar{Q}$	$H\ (Sv/Gy)$
20	22.46	3.88	11.17	22.10	6.42
50	20.16	4.06	44.46	18.45	7.37
62	18.16	4.47	55.58	13.69	5.01
67	16.67	5.01	57.33	11.44	11.44
69	15.68	5.25	62.6	14.29	1.63
71	14.28	5.65			
73	11.83	6.54			
74	9.63	7.58			
74.5	9.98	8.07			
75	8.30	8.30			
75.5	9.64	3.13			
76	12.68	0.94			
77	13.35	0.72			
78	13.51	0.73			
80	14.24	1.09			
90	16.97	0.39			
120	19.16	0.07			

4.3.3 Out of field measurements

Results from the out-of-field measurements for ^{16}O ions at two depths of interest in the water phantom are presented in Figure 4.14 and Figure 4.15. A visible predominant peak is observed when the detector is laterally displaced 2.5 cm from the central axis. Clearly this position represents a particular case where the microdosimeter is facing the beam at the edge of the field 5 x 5 cm^2 wide. In fact, half of the SVs that constitute the device are still in field and obviously are reached by primary oxygen ions propagating through the water phantom. In both cases, at

the entrance depth and immediately before the Bragg peak depth, the only difference concerning the two scenarios, with and without the spacecraft wall, is observed to be a shift of the peak to higher lineal energy when the 35.95 mm thick aluminum wall is used in front of the water phantom. The reason of the shift have been already discussed in the previous section 4.3.2: mainly, oxygen ions interact with the aluminum wall, loosing energy and consequently they reach the microdosimeter with lower kinetic energy which corresponds to a higher lineal energy.

It is interesting to observe the microdosimetric spectra for the fully out-of-field measurements at 3.5 cm and 5.5 cm lateral positions. In Figure 4.14 corresponding to depth in water of 20 mm, spectra are mostly constituted by low-LET particles as recoil protons induced by neutrons, generated by the interaction of energetic primary oxygen ions within the first 20 mm of water. There is no evidence of a distinct peak of primary ions, as they propagate straight through the phantom without reaching any SV of the microdosimeter, but a tail at higher lineal energy is present due to low energy secondaries with high LET. As the device is moved further from the edge of the field, the $\bar{Q}$ increases while the dose equivalent H tends to be almost constant due to the convoluted effect of the absorbed dose which is decreasing laterally.

However, in Figure 4.15 spectra have been measured at depth of 180 mm in the water phantom, immediately before the occurrence of the full energy deposition in the corresponding Bragg peak. The same considerations about the production of secondaries particles discussed for the previous case in Figure 4.14 can be applied now. The concentration of low-LET fragments in this case is higher, due to deeper in the water phantom: in fact approaching the Bragg peak, primary oxygen ions have already reduced their energy, and increased the number of lower energy fragments with higher LET scattering outside the field and hitting the microdosimeter displaced laterally. On the contrary, in Table 4.5 the values of $\bar{Q}$ and H decrease while the microdosimeter is moved away from the edge of the field. The abundance of low-LET secondaries particles makes the average quality factor decreasing according to formula stated by the ICRP60 (see Table 1.3), where for LET (and/or y) decreasing below 100 keV/µm, the Q(LET) decreases as well.

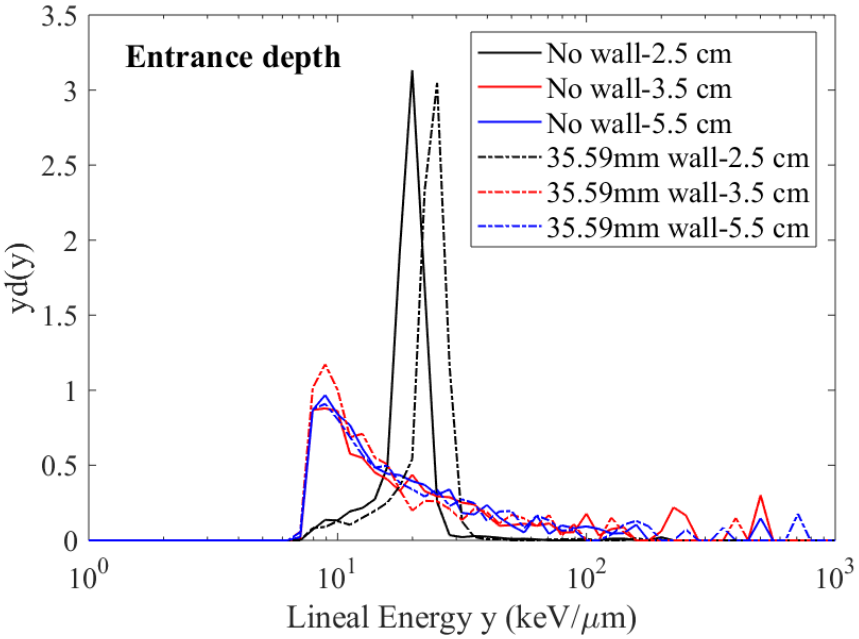

Figure 4.14. Microdosimetric spectra obtained for out-of-field measurements for oxygen ions placing the microdosimeter at 20 mm depth in the water phantom, and laterally displaced it of 2.5, 3.5 and 5.5 cm from the central axis. Two scenarios are compared: without the spacecraft wall ("No wall") and with the 35.95 mm thick slab of aluminum wall.

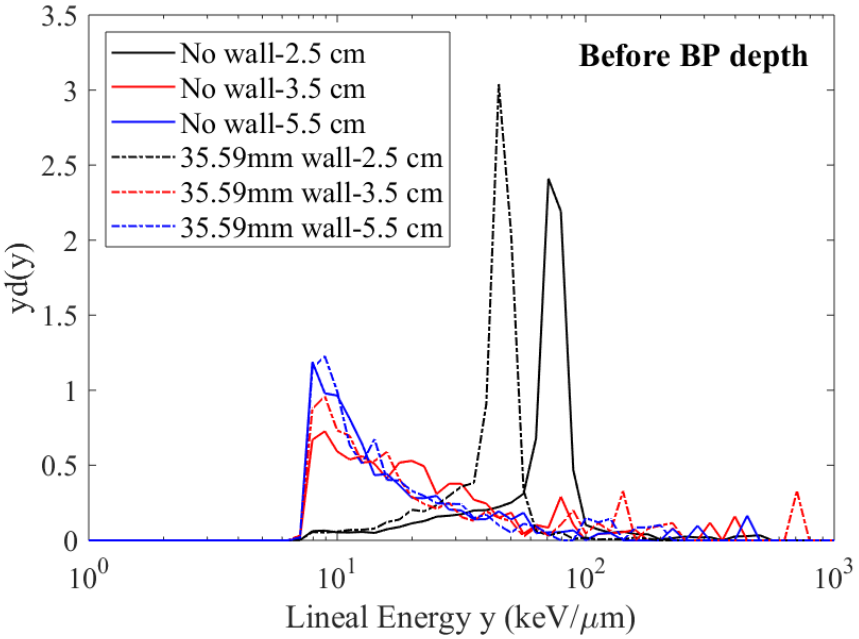

Figure 4.15. Microdosimetric spectra obtained for oxygen ions out-of-field measurements placing the microdosimeter at a depth of 180 mm (i.e. before the Bragg peak) in the water phantom, and laterally displaced it of 2.5, 3.5 and 5.5 cm from the central axis. Two scenarios are compared: without the spacecraft wall ("No wall") and with the 35.95 mm thick slab of aluminum wall.

Table 4.5. Measured averaged quality factor and dose equivalent for irradiation at out-of-field positions in water with and without the 35.95 mm thick aluminum wall. Errors were within a range of $\pm$ 2%.

400 MeV/u ^{16}O					
		No wall		35.95 mm wall	
	Lateral	$\bar{Q}$	$H\ (Sv/Gy)$	$\bar{Q}$	$H\ (Sv/Gy)$
Entrance depth	2.5cm	4.08	0.08	5.22	0.17
	3.5cm	6.35	0.12	4.84	0.16
	5.5cm	5.30	0.10	5.71	0.18
Before BP depth	2.5cm	18.12	3.61	11.02	11.02
	3.5cm	6.33	1.26	6.55	6.55
	5.5cm	4.57	0.91	5.07	5.07

4.4 Conclusions

The response of an SOI "Mushroom" microdosimeter was investigated with high-energy ions at HIMAC (Japan) typical for GCR. Two irradiations were carried out with 400 MeV/u ^{16}O ions and 500 MeV/u ^{56}Fe ions, in a free air geometry and in a water phantom with and without the presence of aluminum slabs representing the wall of a spacecraft. Two PMMA converters of 0.07 mm and 10 mm thick were put in front of the probe to mimic conditions for measurements of the dose equivalent $Hp(0.07)$ and $Hp(10)$. The aim was to study the hazard posed by heavy ions inside and outside a spacecraft to evaluate the effects of the wall's shielding material. Results including dose equivalent normalized to an absorbed dose in a BP and $\bar{Q}$ were obtained using the tissue-equivalent microdosimetric spectra obtained with "Mushroom" microdosimeter. Oxygen ions became more harmful once they reached the inside of the spacecraft due to the high LET ions and secondaries produced while propagating through the 35.95 mm Al and either 0.07 or 10 mm PMMA. On the contrary, iron ions are totally stopped by the 35.95 mm thick wall resulting in a lower $\bar{Q}$ and dose equivalent at depth of 0.07 mm and 10 mm in

PMMA. If the wall thickness is reduced to 7.3 mm of Al, representing only the outer shell of the spacecraft and the "Internal Out-fitting" (devices made of aluminum inside the spacecraft) is not considered, iron ions propagate through the Al without being stopped or incurring significant fragmentation. Hence, the $\bar{Q}$ and $Hp(0.07)$ and $Hp(10)$ remained almost unvaried.

The $\bar{Q}$ values at different depths within the body of an astronaut were investigated with and without the presence of the aluminum wall (35.95 mm thick for oxygen irradiation and 7.3 mm thickness for iron irradiation), representing the two scenarios encountered in space, inside and outside the spacecraft. Due to the low y of 19.38 keV/µm at the entrance depth of the water phantom, the $\bar{Q}$ value corresponding to oxygen ions is increasing with depth in a body according to the equations listed in Table 1.3. Conversely, iron ions see a decrease of $\bar{Q}$ along depths of the human body because of the higher y at the entrance depth of the water phantom (167.98 keV/µm), and its further increase after the BP due to lower LET fragments than primary ^{56}Fe ions. The presence of the shielding wall caused a shift of the Bragg Peak to more shallow depths in the water phantom, resulting in a more harmful exposure of superficial organs of the astronaut's body as in the case of oxygen and iron ions considered in this study. For two scenarios (inside and outside the spacecraft), the same organs of the astronaut body will have essentially different dose equivalent exposure that also depends on energy spectra and type of ions that is difficult to predict accurately during space missions. Additionally, the SOI "Mushroom" microdosimeter due to its small size will be useful for in anthropomorphic phantom studies inside a spacecraft.

Therefore, for wide energy ranges of GCR ions, the Al wall does not always reduce the radiation hazard inside the spacecraft. While stopping lower energy ions, the wall can attenuate the energy of primary ions and produce secondary particles. Particularly, the dose equivalent can increase at shallow depth but can be reduced (or increased further) deeper in the body of an astronaut.

Measurements out-of-field showed the presence of low-LET secondary particles as recoil protons induced by neutrons scattered away from the beam central axis, further the primary beam of ions propagates in the water phantom. The dose equivalent measured at later positions at the entrance of the water phantom is

similar to the one measured in-field on the beam central axis. This confirms there are also secondary particles of high LET that deposit a not considerable amount of energy in nearby tissue but they have a higher quality factor. On the contrary, when approaching the Brag peak's depth, the primary ions reduced already the energy, interacting with water and scattering more low-LET secondaries. Thus the quality factor reduced and the dose equivalent too.

In conclusion, microdosimetry is a useful approach for evaluating the quality factor of a mixed radiation field typical of space radiation, without knowing the composition of the mixed charged particles field behind the shielding wall. Such measurements are currently available on the ISS using the conventional Tissue Equivalent Proportional Counter (TEPC), which is bulky, requires a high voltage supply and cannot be used as a personal dosimeter for astronauts [110]. Portable and low power devices are preferable since an astronaut's location inside the ISS changes and the composition and dose rate of the radiation field is not predictable.

This study confirms that the portable microdosimetric probe with SOI "Mushroom" microdosimeter is suitable for quantifying the quality of the radiation field in space in terms of $\bar{Q}$, as well as evaluating the efficiency of shielding materials in terms of $Hp(d)$. Results for scenarios of astronauts inside the spacecraft have been validated with Geant4 simulations, confirming the feasibility of using SOI microdosimeter for space application. While the dose to astronauts during deep space mission, like planned to Mars (about 360 days round trip), is expected to be 1 - 3Gy [111-113], the radiation damage to silicon devices is not an issue especially for SOI devices [92], making the microdosimeter "Mushroom" an attractive choice for personal dosimeters for astronauts.

The next chapter will presented a more detailed investigation of the shielding properties of all materials constituting the wall of the Columbus. Highly hydrogenated materials with expected better shielding efficiency were studied as alternative to aluminum for design of spacecrafts or habitats in future manned missions to more hazardous radiation environments as the Lunar or the Martian one.

Chapter 5

Experimental characterization of the shielding properties of innovative materials

As a consequence of the doubts brought up in Chapter 4 about the shielding efficiency of aluminum, in this chapter it will be presented the study of shielding efficiency of innovative materials for the design of future spacecrafts against heavy ions of different types and energies obtained at the Heavy Ions Medical Accelerator in Chiba, Japan. The quality factor, Q, and the normalized dose equivalent, H, derived from microdosimetric measurements behind different spacecraft wall configurations and materials such as Carbon Fiber, Polyoxymethylene, and Perspex with the same areal density compared to currently used aluminum were investigated.

The results have been presented at the Nuclear & Space Radiation Effects Conference 2020 and published on the IEEE Transaction on Nuclear Sciences journal as: "S. Peracchi et al., Radiation shielding evaluation of spacecraft walls against heavy ions using microdosimetry, IEEE Trans. Nucl. Sci., 2020" [114]. As I am the first author, the journal gave the permission to reproduce the article in this thesis referring to the original source found at DOI: 10.1109/TNS.2020.3032946.

5.1 Introduction

Radiation effects induced on astronauts by cosmic rays entering the spacecraft are an extremely important issue especially for long manned missions in space. As mentionned in the introduction of Chapter 4, Galactic Cosmic Rays (GCRs) consists of 1% of heavy ions which have the capability of penetrating the spacecraft-shell inducing major radiobiological effects on humans. The hadronic interaction of particles with shielding materials leads to fragmentation of primary ions into secondary radiation with higher LET, which deposit energy via ionization in the astronaut.

The composition of the spacecraft's shield must address multidisciplinary requirements, including protection from debris and thermal insulation. Although current materials are adopted for their excellent mechanical properties, they might not be efficient in shielding of cosmic rays, especially when the radiation environment becomes more hazardous during solar flares. Adding extra high-density materials for radiation protection purposes to spacecraft is not an option due to weight restrictions. Alternatively, one can study existing shielding materials properties and potentially, replace existing shielding materials with innovative ones with better shielding properties. Another option could be to optimize the arrangement of the shell design, according to the influence that the order of materials can cause on the final particles flux.

In this work, experiments in heavy ion beams with and without a multiple layers wall (also called multilayer) mimicking the realistic ISS wall were carried out. The 3D "Mushroom" SOI microdosimeter descried in section 1.3.2 was set after the mimicked wall to measure the energy deposition distribution due to the radiation field emerging from the multilayer. The mixed charged particles field resulting from selected incoming heavy ions, typical of GCRs, hitting the shielding structure of the Columbus module docked on the ISS was characterized in terms of microdosimetric spectra, $\bar{Q}$ and $Hp(10)$. Also, referring to the literature [115], alternative materials such as Perspex, Polyoxymethylene, and Carbon Fiber, were considered in this study. Irradiations were carried out at the Heavy Ions Medical

Accelerator in Chiba (HIMAC), Japan, with some of the GCRs ions present is space, such as 400 MeV/u ^{20}Ne, 180, 230 and 490 MeV/u ^{28}Si, and 290 MeV/u ^{12}C ions.

5.2 Materials and Methods

In this study, two SOI "Mushroom" microdosimeters were used: the difference is in the dimension of the sensitive volumes (SVs) as the first microdosimeter had SVs 5 µm thick and 30 µm in diameter, whereas in the second design the SVs were 10 µm thick with a 18 µm diameter. In both cases, the SV structure was the same as presented in Figure 3.3 in section 1.3.2. The second one's SVs were 10 µm thick and 18 µm in diameter.

The SOI microdosimeters were covered by 10 mm thick PMMA slab which is considered a suitable substitution for water and consequently a good approximation of the human body for astronauts radiation dose monitoring. [116]. The average quality factor $\bar{Q}$ of the radiation field and the dose equivalent at 10 mm depth in the body of an astronaut, $Hp(10)$, where calculated as explained in section 4.2.1 of Chapter 4.

Before starting any experimental irradiation, by using a ionization chamber, the preliminary measurement of the Bragg curve was performed for each of the above-cited ions and energies considered in this study. The PMMA range shifters shown in Figure 4.2 were sequentially inserted along the beam line to achieve water-equivalent depths of interest to which the dose was evaluated.

5.2.1 Spacecraft shielding properties

The multi-layer structure of the spacecraft wall was implemented to reflect several factors such as mechanical and thermal properties along with radiation protection which is paramount to protect astronauts living in harsh environments.

Aluminum alloy 2219 is primarily used as an outer shell to fragment high velocity projectiles, as well as being used as a main infrastructural material. An

intermediate bumper is usually made of Kevlar® and Nextel®, which are well-known materials for their excellent resistance and absorption properties against meteoroids and debris impacts. Kevlar® (polyp-phenylene terephthalamide) is an organic fiber (patented by DuPont) composed of C (50%), H (35%), N (7%), and O (7%), and when used in a spacecraft shell is usually impregnated with 38% mass content of Epoxy. Nextel is a complex woven ceramic fiber manufactured by 3M Corporation. The composition by weight fraction is Al_2O_3 (62%), SiO_2 (24%), and B_2O_3 (14%). Finally, a thermal passive system called Multi-Layer Insulation (MLI) composed of layers of Mylar, Dacron, Teflon-coated fiber-glass woven cloth and Kapton may be used followed by another layer of Aluminum alloy 2219 [117].

In this work, we studied the realistic shielding configuration of the Columbus module docked at the ISS described in Table 5.1 [88, 109]. This shielding configuration was selected in our study as the result of a series of successful hypervelocity tests performed by Thales Alenia Space Italia and collaborators [88, 118]. This multilayer shield is also a countermeasure for cosmic radiation exposure. Despite the pressurized shell of the Columbus module representing the main structural shield, an extra payload needs to be taken into account for radiation protection. In fact, a great number of devices and structures are located inside the habitable volume of the Columbus with no influence on the structure's resistance of the spacecraft but effect astronauts' shielding. The majority of them are composed of aluminum and composite materials, which provide a further barrier to cosmic radiation and a source of secondary radiation. Although they are not homogeneously distributed inside the spacecraft, the structures can be modeled as two extra layers called "Out-fitting". This thickness is derived from the total areal mass of devices and their structure. In particular, the Out-fitting was modeled as a layer of aluminum 2.8 cm thick covered by a layer of Kevlar-Epoxy 2.9 cm thick (see Table 5.1) [109]. Based on specifications shown in Table 5.1, we fabricated in our laboratory a sample of the multi-layers Columbus shield (see Figure 5.1) using aluminum alloy 2219 (density 2.84 g cm^{-3}), 3M Nextel® 312 AF-62 (density 2.7 g cm^{-3}), DuPont™ Kevlar® Ht T129 and Weicon Epoxy Casting Resin MS 1000 (density 1.28 g cm^{-3}). However, we recognize there might be uncertainties in adopting one single particular aluminium alloy to model the aluminium layer in the

Out-fitting due to the variety of structures and devices found inside the Columbus. Hence, we can assume that the aluminium density can vary in an acceptable range for aluminium alloys (2.64 - 2.84 g cm^{-3}) to satisfy the areal density requirements as main quantity chosen for comparison of materials.

Table 5.1. Reproduced from (M. Silvestri et al., 2011) [109]: multilayers structure of the Columbus shielding wall.

Layer's number	Material	Thickness (cm)	Areal density (g/cm^2)	Configuration
1	Al2219	0.25	0.7	
2	Nextel®	0.55	0.4	
3	Kevlar®-Epoxy	0.8	0.9	Columbus shell
-	MLI	0.13	0.2	
4	Al2219	0.48	1.3	
	Total	**2.2**	**3.5**	
5	Al2219	2.8	7.4	Columbus shell
6	Kevlar®-Epoxy	2.9	3.8	+ Out-fitting
	Total	**7.9**	**14.7**	

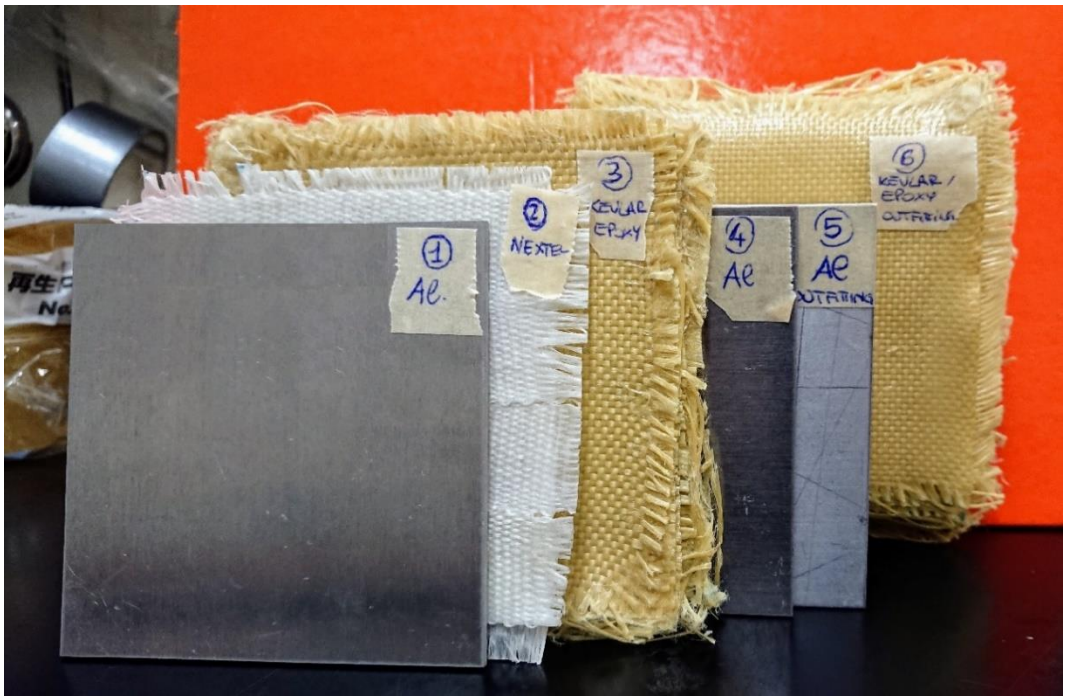

Figure 5.1. Sample of the Columbus shielding wall fabricated following specifications listed in the Table 5.1.

In the study discussed in Chapter 4 showed that aluminum, particularly the thick Out-fitting layer, could cause a higher production of secondary particles when energetic 500 MeV/u ^{56}Fe ions were used. Hence, this case represents a hazard to astronauts inside the Columbus when the high-energy iron ions were attenuated and the LET of the secondary particles was increased [102]. It is well known that the secondary neutrons production through nuclear interactions between the primary cosmic radiation and aluminum is not negligible. Neutrons can cause higher biological damage than photons and protons, and the cumulative neutron dose contribution could be significant during future long-term space travel. Compared to aluminum, hydrogenated materials such as polymers have better radiation protection properties, but their lack of mechanical strength prevents them from being used as sole building structures in aerospace vehicles [119]. Several studies suggest combining them with high mechanical strength materials such as carbon fiber (CF), carbon nanotubes (CNT) or graphene, although availability in bulk samples is limited [120].

For these reasons, we selected materials to be included in this study as Polymethyl-methacrylate (PMMA, density 1.18 g cm^{-3}), carbon fiber (CF, density 1.6 g cm^{-3}) to represent graphene, and Polyoxymethylene (POM, density of 1.41 g cm^{-3}) to compare the radiation environment behind a shield of different materials to the field generated behind an equivalent mass of aluminum. Based on areal density, the thickness of each material was evaluated and used in the shield instead of the aluminum layer (see Table 5.2). In particular, the pressurized shell of Columbus includes two layers of aluminum whose total area density is 2 g cm^{-2} and the aluminum Out-fitting of the Columbus corresponds to 7.4 g cm^{-2} [109]. Due to material availability, it was not possible to replace the Out-fitting aluminum layer with an equivalent mass of CF. Additionally, due to the available samples of Polyoxymethylene blocks used for the range shifter in carbon ion therapy, we used this material to characterize shielding properties. Although the areal density of this material was not exactly equivalent to those of the aluminum layers we still conducted some measurements to study the quality of the fragmented field of radiation generated behind the wall configurations. In particular, the areal density

for the shell POM layer was 2.8 g cm^{-2} (42% more than Al, 2 g cm^{-2}), and for the Out-fitting, the POM layer was 11.4 g cm^{-2} (54% more than Al, 7.4 g cm^{-2}).

Table 5.2. Thicknesses and areal densities of materials mass-equivalent to aluminum in Out-fitting and shell, except for the POM.

	Out-fitting		Shell	
Material	Thickness	Areal density	Thickness	Areal density
Aluminum	28 mm	7.4 g cm^{-2}	7.3 mm	2 g cm^{-2}
PMMA	62.7 mm	7.4 g cm^{-2}	16.9 mm	2 g cm^{-2}
CF	-	-	12.5 mm	2 g cm^{-2}
POM	*80 mm*	*11.4 g cm^{-2}*	*20 mm*	*2.8 g cm^{-2}*

5.2.2 Configurations of the shielding wall adopted during the irradiation

Irradiations were carried out at HIMAC in Japan using different heavy ions typical of GCRs in space such as 290 MeV/u ^{12}C, 400 MeV/u ^{20}Ne, and 180 MeV/u, 230MeV/u and 490 MeV/u ^{28}Si. Details of the beamline at HIMAC used for these experiments can be found in the previous chapter (section 4.1.1), together with information about energy losses before reaching the set-up isocenter [104, 105].

For irradiation with 400 MeV/u ^{20}Ne and 490 MeV/u ^{28}Si ions, the SOI "Mushroom" microdosimeter with a sensitive volume of 5 µm thick was used. During irradiation with 290 MeV/u ^{12}C ions, 180 and 230 MeV/u ^{28}Si ions, the SOI "Mushroom" microdosimeter with a sensitive volume of 10 µm thick was used. The SOI microdosimeter was connected to the low noise electronics MicroPlus probe and was placed in a free air geometry along the central axis of the beam behind the spacecraft shield samples. A 10mm thick PMMA piece was put in front of the detector to mimic 10 mm depth in a human body (Figure 5.2).

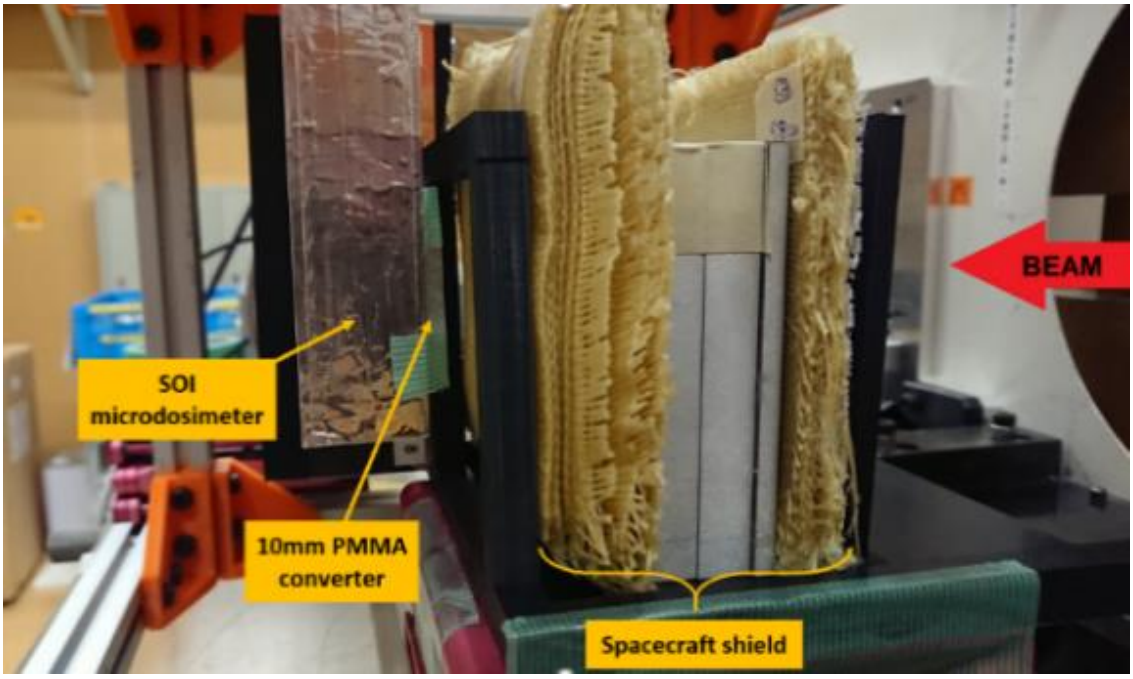

Figure 5.2. Experimental setup inside the irradiation room at HIMAC with SOI microdosimeter connected to the MicroPlus, behind the spacecraft shield sample.

Several layer configurations of the spacecraft's shield were studied and for each of them the microdosimetric spectrum was obtained. The quality factor $\bar{Q}$ and the personal dose equivalent $Hp(10)$ were evaluated, as described in [102]. Firstly, sequential measurements of the original structure of the Columbus shield were performed starting from the first outer layer of aluminum (2.5 mm thick) followed by five layers as shown in Table 5.1. This configuration was called "Al Full wall". Secondly, a configuration called "Swapped Al Full wall" was studied which was related to the Out-fittings arrangement. In the "Al full wall" configuration, 28 mm Al of the Out-fitting layer was followed by 29 mm a Kevlar-Epoxy layer (see Table 5.1). However, this layer order does not reflect the real scenario at each position of astronauts inside Columbus due to the inhomogeneous distribution of devices and structures. For this reason, in some configurations the order of layers relative to the direction of the incident heavy ions was changed or swapped, for instance, the aluminum layer was the last layer where the heavy ions passed through before reaching the astronaut body. In other configurations, either only Aluminum (layer 5) or Kevlar Epoxy (layer 6) of Out-fitting was present to provide shielding and we

called this “Truncated Aluminum” and “Truncated Kevlar-Epoxy” configurations respectively. In the last configuration, the thicker Out-fitting aluminum layer was replaced with an equivalent mass of PMMA, according to the original structure of the Columbus module wall (see Table 5.3). In Table 5.3, the first layer immediately downstream of the incoming beam was layer 1 and the SOI microdosimeter was placed after the last layer of the Out-fitting.

Table 5.3. Full wall configurations studied and corresponding sequential order of layers of modified out-fitting, as listed in Table 5.1.

Configuration	Shell layers	Out-fitting layers
“Al Full wall”	1-2-3-4	5-6
“Swapped Al Full wall”	1-2-3-4	6-5
“Truncated Aluminum”	1-2-3-4	5
“Truncated Kevlar-Epoxy”	1-2-3-4	6
“PMMA Full wall”	1-2-3-4	5(PMMA)-6
“POM Full wall”	*1-2-3-4*	*5(POM)-6*

Despite the pressurized shell being the main structural part that constitutes the Columbus module and guarantees mechanical strength, it includes aluminum that causes the production of secondary charged particles. Thus, we wanted to compare the production of secondary particles when replacing two thin layers of aluminum of 7.3 mm thick in total with PMMA and CF layers of equivalent areal density (see Table 5.2). In Table 5.4 it can be seen that all configurations studied for the pressurized shell are listed starting from the “Al Shell” currently used for the Columbus module, followed by configurations where the aluminum layers were substituted with an equivalent mass of different materials (e.g. “CF Shell” and “PMMA Shell”) while Nextel and Kevlar layers are placed in behind, without change. For simplified configurations with only two layers of Al (7.3 mm Al), replacement of Al with an equivalent layer of CF was studied to compare the effect of radiation shielding, keeping in mind the possible use of graphene in composite materials for the shell. In Table 5.4, the first layer immediately downstream of the incoming beam was layer 1 and the SOI microdosimeter was placed after the last layer of the pressurized shell.

Table 5.4. Pressurized shell configurations studied with different materials equivalent to aluminum, except for those ones implying the use of POM. Layer 2 and 3 corresponds to Nextel and Kevlar-Epoxy as in Table 5.1.

Configurations	Layers
"7.3 mm Al"	1-4
"12.5 mm CF"	1-4
"20 mm POM"	1-4
"Al Shell"	1(Al)-2-3-4(Al)
"CF Shell"	(1-4 CF)-2-3
"PMMA Shell"	(1-4 PMMA)-2-3
"POM Shell"	*(1-4 POM)*-2-3

5.2.3 GEANT4 simulation of the residual energy of primary ions behind the shielding wall

For a deep understanding of the shielding properties of the above-mentioned configurations, GEANT4 simulations were performed to evaluate the residual energy of primary ions exiting the shielding wall. When the residual energy was zero, the primary ions was considered to be fully stopped by the shielding wall. The LET in tissue-equivalent was calculated for comparison with the value of lineal energy measured at the peak of the microdosimetric spectrum by the SOI microdosimeter.

The simulated geometry reproduced the HIMAC beamline described in Figure 4.2 and the experimental set up adopted for each configuration. A monoenergetic beam was used to irradiate the SOI "Mushroom" microdosimeter behind the shielding wall configuration of interest.

The physics lists adopted to model the interaction of particles with matters are the same used for the simulation study discussed in Chapter 2.

5.3 Results and Discussion

In Figure 5.3, there are the curves of relative energy deposition normalized to 1 in correspondence of the Bragg peak measured by the ionization chambers. The ranges of ions in water are shown in Table 5.5. As explained in section 4.2.1, all values of dose equivalent detected by the SOI microdosimeter during experiments will be normalized by the dose at the Bragg peak in water.

Table 5.5. Ranges of ions in water obtained from measurement of the Bragg curve by using an ionization chamber.

Ion	Energy (MeV/u)	Range in water (mm)
^{28}Si	180	17.91
^{28}Si	230	33.07
^{28}Si	490	136.34
^{20}Ne	400	143.84
^{12}C	290	148.84

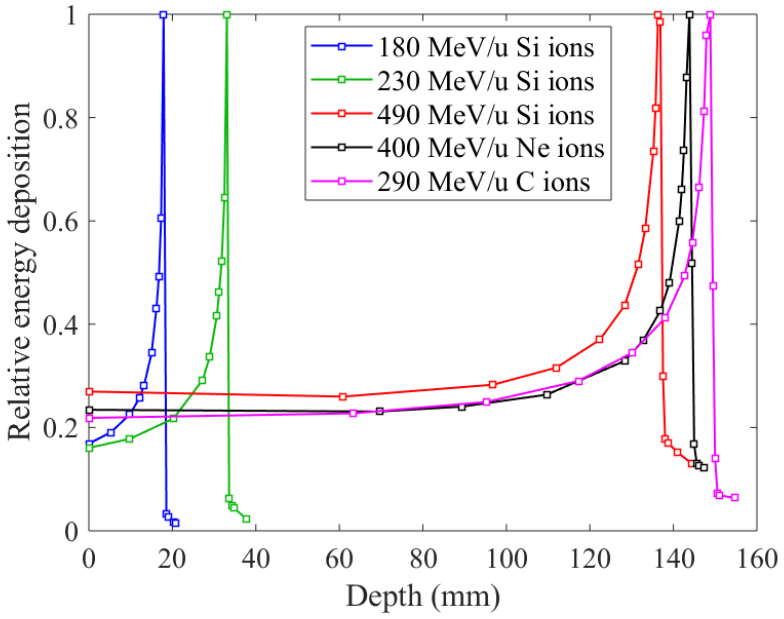

Figure 5.3. Relative energy deposition in water for 180, 230 and 490 MeV/u ^{28}Si ions, 400 MeV/u ^{20}Ne ions and 290 MeV/u ^{12}C ions, preliminarily measured at the HIMAC BIO exposure room. The

Bragg Peak was observed to be at 73.04 mm depth for iron ions and 186.1 mm depth for oxygen ions.

5.3.1 Irradiation of the full wall configurations

Figure 5.4 shows the microdosimetric spectra for a 490MeV/u ^{28}Si irradiation, adding sequentially layers until we reached the "Al Full wall". It can be seen that the first aluminum Out-fitting layer resulted in the production of secondary particles and fragmentation and it was confirmed by the shift of the peak at higher lineal energies and corresponded to an increase of the $\bar{Q}$ to a value of 23.78, from 17.76 of the previous layer of the shell (see Table 5.6). We observed that Kevlar and Nextel resulted in the least amount of fragmentation production. Overall, the dose equivalent after the last layer of the shield (i.e. Out-fitting) was double the dose equivalent encountered outside the spacecraft ("No wall" configuration).

Moreover, as discussed previously, the concept of Out-fitting does not guarantee a homogeneous distribution of aluminum and Kevlar all around inside of the spacecraft. When the Out-fitting layer order is reversed in the "Swapped Al Full wall" configuration, the radiation field detected inside the Columbus was the same (see Figure 5.5). In the absence of aluminum-based instrumentation packaging, the only layer of Kevlar-Epoxy in the "Truncated Kevlar-Epoxy" resulted in $Hp(10)$ of 2.72 Sv/Gy, which was approximately half of the value obtained with the "Al Full wall" at 5 Sv/Gy (see Table 5.6).

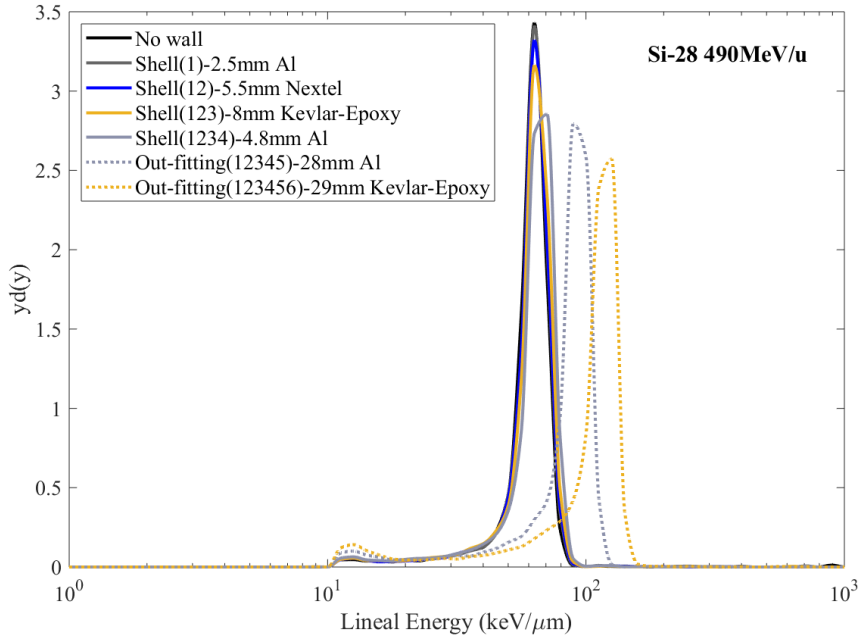

Figure 5.4. Microdosimetric spectra obtained by adding one layer at a time of the Columbus Standard wall configuration measured at 10mm depth of PMMA. In the legend, the thickness indicates the last layer added to the previous configuration.

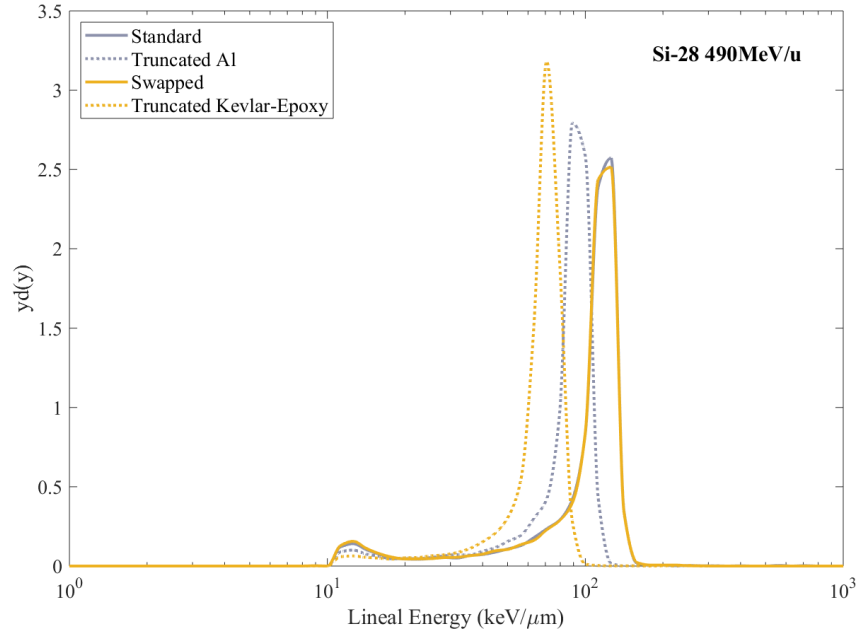

Figure 5.5. Comparison between microdosimetric spectra for "Al Full wall" and "Swapped Al Full wall" configurations (solid lines), and "Truncated Aluminum" and "Truncated Kevlar-Epoxy" (dashed lines).

Table 5.6. Dose equivalent and quality factors calculated based on microdosimetric spectra for silicon and neon ions. Errors were within a range of $\pm$ 2%.

	490 MeV/u ^{28}Si		**400 MeV/u ^{20}Ne**	
	$\bar{Q}$	$Hp(10)$ (Sv/Gy)	$\bar{Q}$	$Hp(10)$ (Sv/Gy)
"No wall"	16.95	2.55	9.29	1.26
"Shell(1)"	17.15	2.53	9.41	1.28
"Shell(12)"	17.16	2.54	9.45	1.26
"Shell(123)"	17.31	2.57	9.51	1.29
"Shell(1234)"	17.76	2.66	9.80	1.33
"Out-fitting(12345)"	23.78	4.10	13.34	2.02
"Out-fitting(123456)"	24.08	5.00	16.22	2.71
"Al Full wall"	24.08	5.00	16.22	2.71
"Swapped Al Full wall"	23.95	4.93	16.20	2.76
"Truncated Al"	23.78	4.10	13.84	2.02
"Truncated Kevlar"	18.72	2.72	10.40	1.36

The same irradiations were performed with 400 MeV/u ^{20}Ne ions and a similar trend was seen in comparison with ^{28}Si ions. The values for dose equivalent and quality factor are listed in Table 5.6. The introduction of the Out-fitting leads to a to a doubling of the dose due to the presence of the aluminum (28 mm). This infers that devices and structures inside the habitat do not provide a further barrier for astronauts against GCRs. The extra materials leads to more interactions of heavy ions with the aluminum, producing fragmentation and generating a cascade of scattered particles with lower energy but higher LET. The energy of primary ions is degraded leading to an increase in the LET, which could lead to a more harmful environment for humans in space (see Figure 5.6 and Figure 5.7).

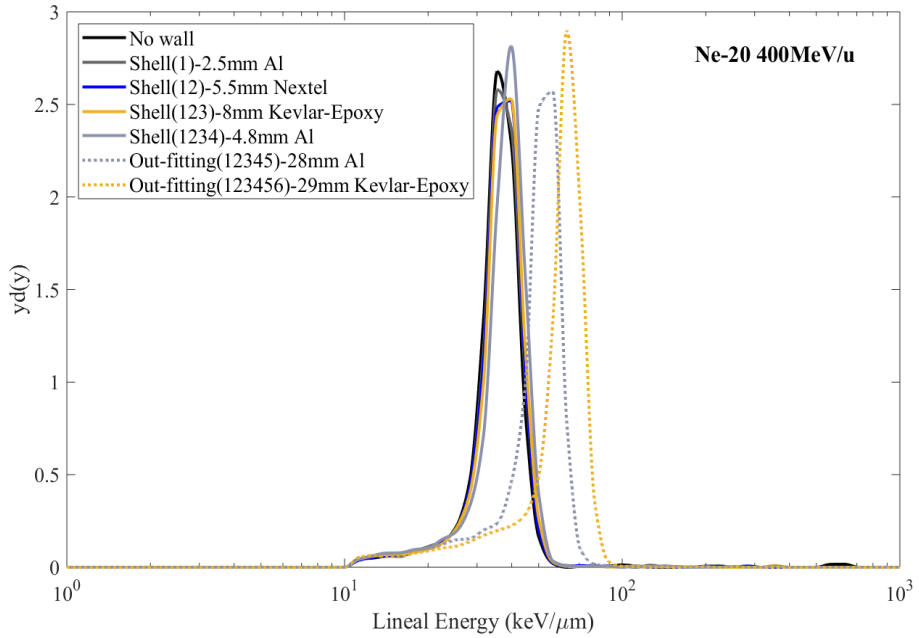

Figure 5.6. Microdosimetric spectra obtained by adding one layer at a time of the Columbus Standard wall configuration irradiated with Neon ions. In the legend, the thickness indicates the last layer added to the previous configuration.

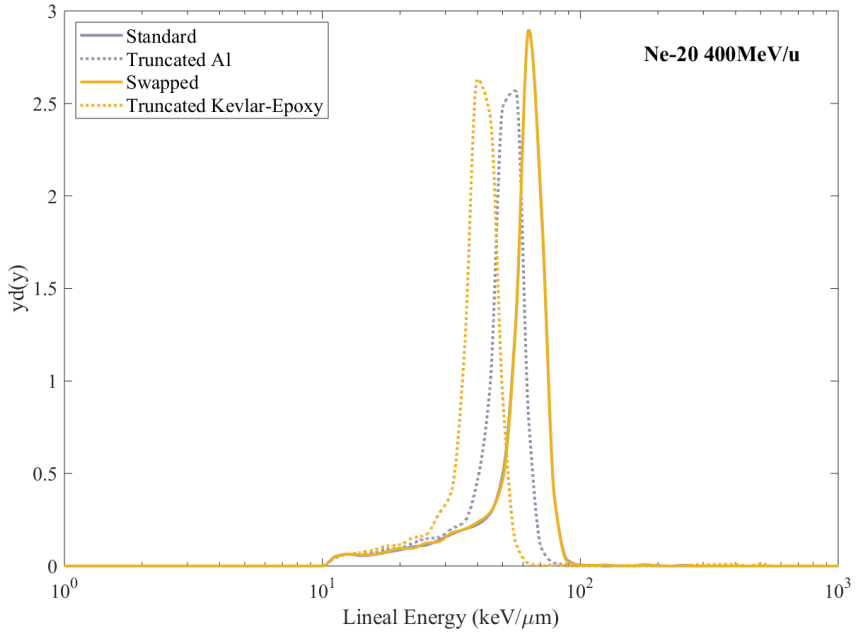

Figure 5.7. Comparison between microdosimetric spectra for "Al Full wall" and "Swapped Al Full wall" configurations (solid lines), and "Truncated Aluminum" and "Truncated Kevlar-Epoxy" (dashed lines) when irradiated with Neon ions.

As a first investigation of alternate material efficacy for radiation shielding, the Out-fitting aluminum layer was replaced with 62.7 mm of PMMA in the "Al Full wall" configuration and irradiation was performed with 400 MeV/u ^{20}Ne and 490 MeV/u ^{28}Si ions. Figure 5.8 shows that for both ions the microdosimetric spectra shifted to higher lineal energy when PMMA was present instead of aluminum. GEANT4 simulations showed that the energy of the primary ions exiting the last layer of the spacecraft's wall in the case of "PMMA Full wall" configuration was 16 and 80.5 MeV/u for ^{28}Si and ^{20}Ne ions respectively. These energies were lower than those obtained in the case of "Al Full wall" configuration: 99.8 MeV/u for silicon and 120.1 MeV/u for neon ions. Due to the lower exit energy of the primary ions in the case of PMMA, the microdosimetry spectra shifted to higher values of y, keeping its peaking shape confirming the nature of the particles as primary ions. However, $\bar{Q}$ and $Hp(10)$ are determined by the whole microdosimetric spectra including lower y events in the tail due to recoil protons, neutrons, and fragments. The more detailed analysis demonstrated that when PMMA was used to replace aluminum, the production of neutrons increased by 2% for ^{28}Si primary ions, while it decreased by 17% for ^{20}Ne primary ions, i.e. the partial contribution of low lineal energy tail decreased. Additionally, fragmentation spectra were different for Si and Ne. The combination of the fragmentation and direct ion contributions lead to the changes observed in $\bar{Q}$ and absorbed dose. In particular, the shift of the microdosimetric spectrum in the case of silicon ions to the region of LET which was higher than 150 keV/µm lead to an overkilling effect. This means that an over-clustering of ionization in one individual ion track happened but did not further increase the biological effect. To reflect this, the value of Q(LET) decreases for LET>150 keV/µm, making the product $\bar{Q} * D$ describe the biological effect as constant even with an increase of the absorbed dose D. Thus, for silicon ions, in the "PMMA Full wall" configuration, the $\bar{Q}$ decreased by 10% with absorbed dose increasing as a result of higher LET with a similar fluence. This finally results in almost the same dose equivalent $Hp(10)$ (see Table 5.7). For neon ions, the microdosimetric spectrum shifted to higher y values but was still below 100 keV/µm. This resulted in an increase of 18% in $\bar{Q}$ and an increase of 28% in the $Hp(10)$ due to the increase in the absorbed dose (see Table 5.7).

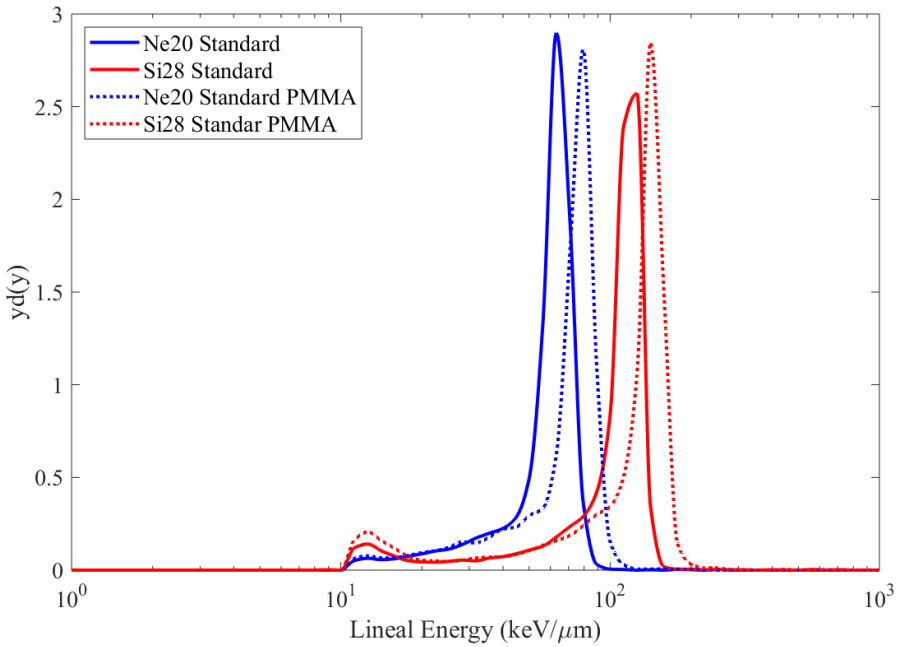

Figure 5.8. Microdosimetric spectra obtained from irradiations carried out with 490 MeV/u ^{28}Si, 400 MeV/u ^{20}Ne ions, considering "Al Full wall" and "PMMA Full wall" configurations.

Another example in Figure 5.9 shows the shielding efficiency of different configurations of the original Columbus module, when irradiated with 290 MeV/u ^{12}C ions. Starting from a scenario without a wall, meaning astronauts are outside the spacecraft, we sequentially added layers to eventually compare it with the "Al Full wall" configuration. Carbon ions are not stopped by any of the configurations, and in particular the 7.3 mm Al and the shell did not influence either the $\bar{Q}$, nor $Hp(10)$, which remained almost the same. However, the full wall configuration induced a shift to higher lineal energy, because of the lower energy possessed by primary carbon ions, 94.2 MeV/u, which exit the last layer. As a result, the average quality factor is almost doubled and the dose equivalent reaches a value of 2.5 times higher (see Table 5.7).

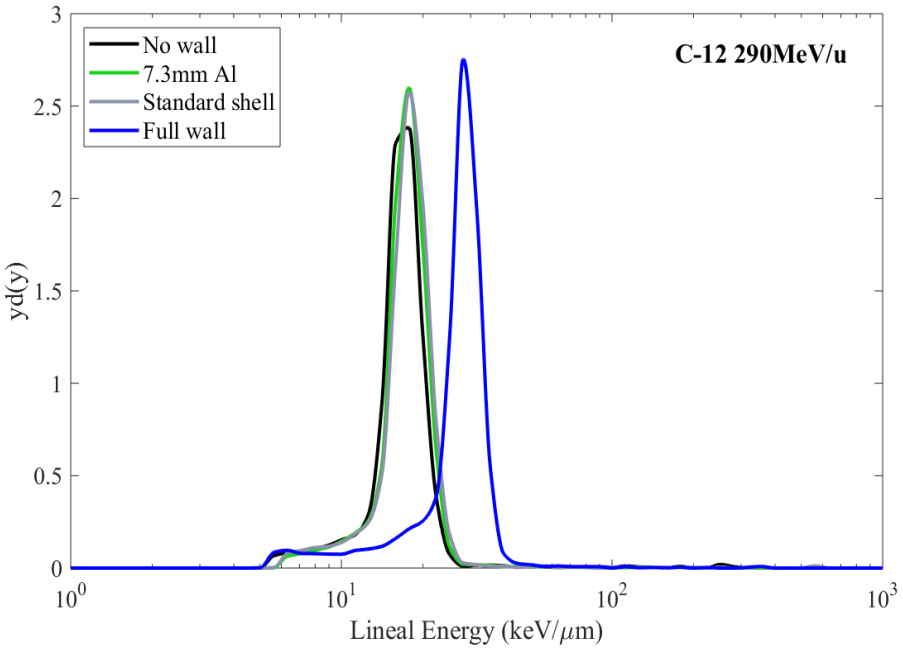

Figure 5.9. Microdosimetric spectra from irradiations carried out with 290 MeV/u ^{12}C, considering different configurations of the original Columbus module structure.

5.3.2 Irradiation of the pressurized shell configurations

The main structural part of the shielding wall is represented by the pressurized shell, which also includes two thin layers of aluminum. The shielding efficiency of CF and PMMA against aluminum in the shell has been investigated and results are shown in Figure 5.10. The microdosimetric spectra are characterized by the same peak at 20 keV/µm and almost unchanged values of $\bar{Q}$ and $Hp(10)$, as listed in Table 5.7. This confirms the feasibility in using CF as a strengthening component in hydrogenated materials such as polyethylene, which has been demonstrated to reduce the dose by 35%, when used as a replacement of aluminum [45]. Unfortunately, PMMA does not present better efficiency than aluminum, as already observed during irradiation with silicon and neon ions, for the specific kinetic energies considered. This leads to the conclusion that this material needs to be tested with a larger variety of ions and energies to confirm its shielding efficiency.

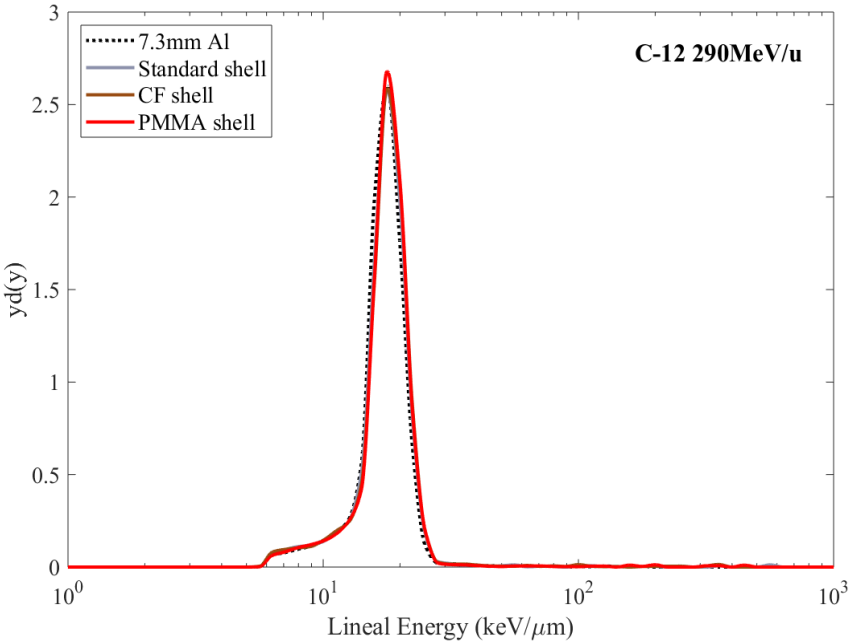

Figure 5.10. Microdosimetric spectra from irradiations carried out with 290 MeV/u ^{12}C, considering all different material configuration of the pressurized shell.

Table 5.7. Dose equivalent and quality factor for all configurations investigated with neon, silicon and carbon ions. Error range of ± 2%.

	490 MeV/u ^{28}Si		**400 MeV/u ^{20}Ne**	
Configuration	$\bar{Q}$	$Hp(10)$ *(Sv/Gy)*	$\bar{Q}$	$Hp(10)$ *(Sv/Gy)*
"No wall"	16.95	2.55	9.29	1.26
"Al Full wall"	24.08	5.00	16.22	2.71
"PMMA Full wall"	21.94	4.96	19.22	3.48
	290 MeV/u ^{12}C			
Configuration	$\bar{Q}$	$Hp(10)$ *(Sv/Gy)*		
"No wall"	3.30	0.18		
"7.3 mm Al"	3.41	0.18		
"Al Shell"	3.55	0.19		
"Al Full wall"	6.42	0.46		
"CF Shell"	3.63	0.19		
"PMMA Shell"	3.61	0.20		

Results from irradiation performed with 180 and 230 MeV/u ^{28}Si ions are compared in Figure 5.11. As graphene seems to be a promising alternative to aluminum for spacecraft shell's design, but still hardly available on the market, we decided to use a thin CF block of 12.5 mm thick to replace the two layers of aluminum 7.3 mm thick in the shell (without considering Nextel and Kevlar-Epoxy layers).

Observing the microdosimetric spectra obtained with 230 MeV/u ^{28}Si ions irradiation, it is clear that silicon ions were not stopped by 7.3 mm aluminum due to the presence of a sharp peak at approximately 200 keV/µm corresponding to primary silicon ions detected by the microdosimeter. The events at lower lineal energy are associated to secondary particles generated during interaction of Si ions with the shielding materials. When 12.5 mm CF block was used instead of 7.3 mm Al, the exit energy of Si ion is decreased from 139 MeV/u (when Al is used) to 126 MeV/u (when CF is used) decreasing $\bar{Q}$ almost by half. This is explained again by overkilling effect as microdosimetry peak shifted to 280 keV/um where Q(y) is decreasing but $Hp(10)$ value increased almost 20% from 1.43 in case of Al to 1.71 in case of CF used, due to an increase of the absorbed dose (see Table 5.8). Whereas, 180 MeV/u ^{28}Si ions, due to their lower energy, are completely stopped by both aluminum and CF (see dash lines Figure 5.11). However, in this case CF seems to bring benefits in terms of dose reduction by 40%.

Secondly, the "Al Shell" and "CF Shell" including Nextel and Kevlar-Epoxy layers were irradiated with 230 MeV/u ^{28}Si ions (see Figure 5.12). In this case, primary ions are stopped by both configurations. In particular, the microdosimetric spectrum obtained when irradiating the aluminum shell is characterized by downstream events reflecting the presence of high-LET heavier fragments generated by the interaction of primary silicon ions within the wall and the silicon of the detector. When comparing the "Al Shell" configuration to the "7.3 mm Al" only configuration, $\bar{Q}$ decreased by 2.7 times due to the overkilling effect (from 16.80 for the "7.3 mm Al" only to 6.25 for the "Al shell"). The $Hp(10)$ increased more than twice from 1.43 Sv/Gy ("7.3 mm Al") to 3.04 Sv/Gy ('Al shell"). On the contrary, when comparing the "CF Shell" configuration with the "12.5 mm CF", the $\bar{Q}$ slightly increased by 5% (from 9.37 for the "12.5 mm CF" only, to 9.78 for the "CF

Shell"). The $Hp(10)$ of the "CF Shell" sharply decreased to 0.13 Sv/Gy, being markedly lower than the dose equivalent observed in the "12.5 mm CF" configuration, 1.71 Sv/Gy (see Table 5.8). These results demonstrate that the mass equivalent layers "7.3 mm Al" and "12.5 mm CF" have different efficiencies in slowing down the primary silicon ions without completely stopping them, and consequently they generate fragments of a different nature i.e: type of particles, energy, LET. Particularly, CF reduced the energy of the primary ions by 17% following interaction of 12.5 mm CF layer with energy of 65.5 MeV/u. This is compared to the 78.9 MeV/u primary ions exiting the 7.3 mm Al layer. As a confirmation, the peak in the spectrum for the "12.5 mm CF" configuration shifted to higher y in Figure 5.11. Consequently, the reduced-energy primary ions and fragments are stopped differently when the additional layers of Nextel and Kevlar-Epoxy are added in the shell configurations, after either the single aluminum layer or the CF layer.

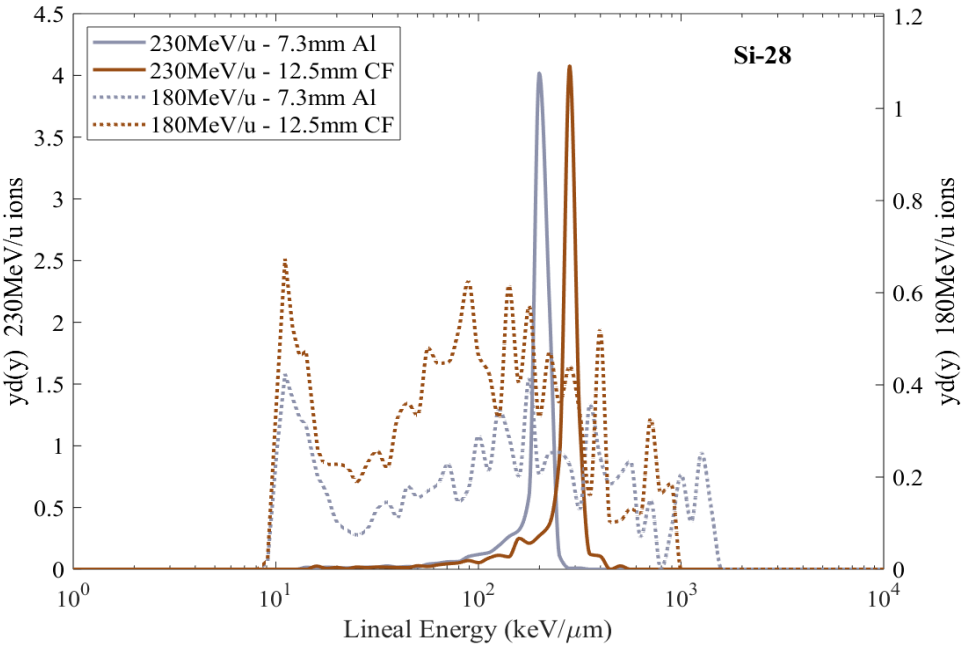

Figure 5.11. Comparison of microdosimetric spectra obtained irradiating 12.5 mm CF mass-equivalent to the 7.3mm aluminum layers in the pressurized shell, with 230 and 180 MeV/u ^{28}Si ions.

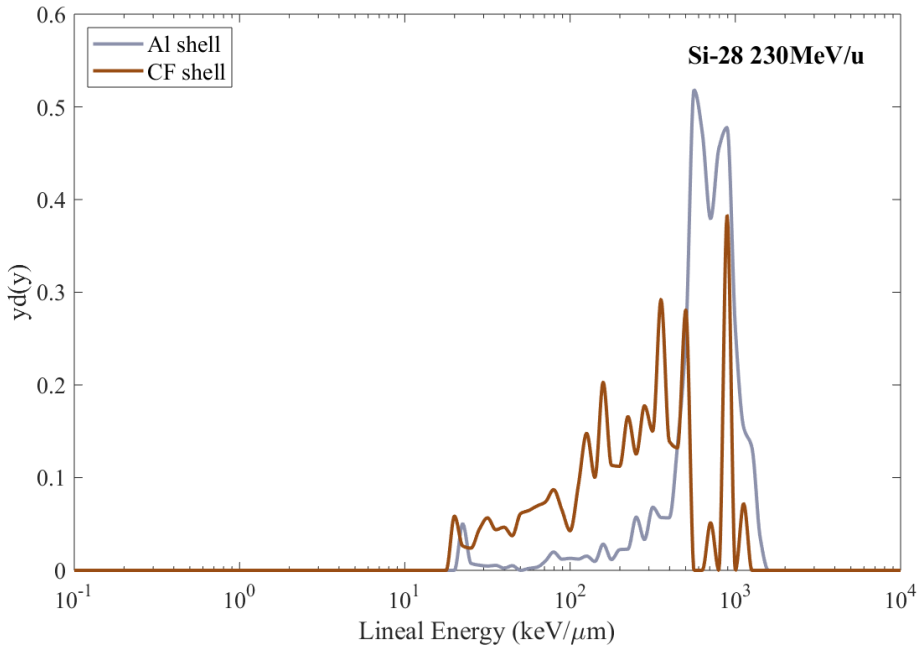

Figure 5.12. Comparison of microdosimetric spectra obtained irradiating the Al shell and the CF shell with 230 MeV/u ^{28}Si ions. Error range of ± 3%.

Table 5.8. Dose equivalent and quality factor for configurations investigated with silicon ions.

	230 MeV/u ^{28}Si		**180 MeV/u ^{28}Si**	
Configuration	$\bar{Q}$	$Hp(10)$ *(Sv/Gy)*	$\bar{Q}$	$Hp(10)$ *(Sv/Gy)*
"7.3 mm Al"	16.80	1.43	11.14	0.05
"12.5 mm CF"	9.37	1.71	12.01	0.03
"Al Shell"	6.25	3.04	-	-
"CF Shell"	9.78	0.13	10.82	0.01

5.3.3 Irradiation of the configurations adopting POM

Finally, in Table 5.9 we report results obtained when irradiating optional configurations where POM was used instead of aluminum for the corresponding spectra shown in Figure 5.13. Even though the areal density of POM configurations was around 50% higher than the aluminum ones, the reduction of the dose is observed to be more significant. For example, when "POM Full wall" was irradiated

with 290 MeV/u ^{12}C ions, primary ions were stopped and fragmentation was produced, resulting in a significant decrease in the dose equivalent by 78% compared to the dose observed with the "Al Full wall" configuration. A similar result was observed for 230 MeV/u ^{28}Si ions in that the doses equivalent obtained in the "20 mm POM" and "POM Shell" configurations are 94% and 95% lower than those obtained in"7.3 mm Al" and "Al Shell" configurations, respectively. Additionally, a reduction of 80% of the dose equivalent was seen while using POM instead of aluminum in the shell irradiated with 180 MeV/u ^{28}Si ions.

These results show the benefit of using POM as an alternative to aluminum: in fact, the dose reduction was not linearly dependent on the increase of areal density used, but higher than expected. This shows the high radiation shielding efficiency of POM and its potential application as a composite material with graphene for mechanical rigidity improvement.

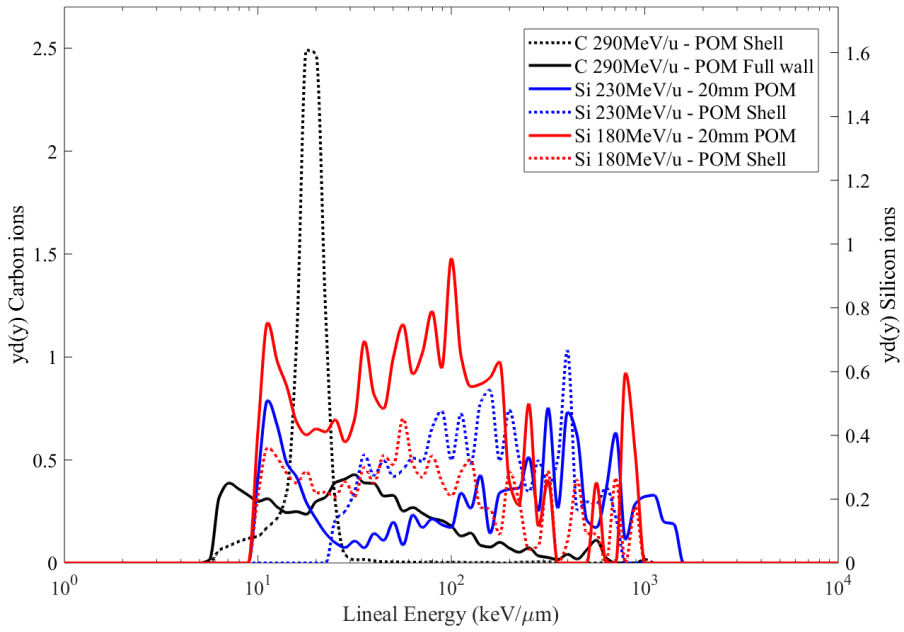

Figure 5.13. Microdosimetric spectra obtained while irradiating POM configurations with different ions.

Table 5.9. Comparison of dose equivalent and quality factor for POM configurations against aluminum ones. Error range of ± 2%.

290 MeV/u ^{12}C					
Configuration	$\bar{Q}$	$Hp(10)$ (Sv/Gy)	Areal Density (g cm^{-2})	Difference Areal Density POM/AL	Difference $Hp(10)$ POM/AL
"Al Shell"	3.55	0.19	3.3		
"POM Shell"	3.77	0.20	4.1	+42%	+5%
"Al Full wall"	6.42	0.46	7.4		
"POM Full wall"	9.69	0.10	11.4	+54%	-78%
230 MeV/u ^{28}Si					
Configuration	$\bar{Q}$	$Hp(10)$ (Sv/Gy)	Areal Density (g cm^{-2})	Difference Areal Density POM/AL	Difference $Hp(10)$ POM/AL
"7.3 mm Al"	16.8	1.43	2.0		
"20 mm POM"	10.25	0.09	2.8	+42%	-94%
"Al Shell"	6.25	3.04	3.3		
"POM Shell"	9.62	0.14	4.1	+42%	-95%
180 MeV/u ^{28}Si					
Configuration	$\bar{Q}$	$Hp(10)$ (Sv/Gy)	Areal Density (g cm^{-2})	Difference Areal Density POM/AL	Difference $Hp(10)$ POM/AL
"7.3 mm Al"	11.14	0.05	2.0		
"20 mm POM"	11.75	0.01	2.8	+42%	-80%
"Al Shell"	-	-	3.3		
"POM Shell"	11.85	0.02	4.1	+42%	

5.4 Conclusions

We investigated shielding properties of the ISS/Columbus wall against selected ions representative of the GCR environment. Particular attention was made on aluminum layers according to the first study conducted with oxygen and iron ions, discussed in Chapter 4. Aluminum has been demonstrated to considerably

influence the production of secondary particles reaching the inside habitat of the spacecraft. In the energy range and for the ions under study, the Out-fitting modeled layers which represent the great number of devices inside the habitat, did not provide a further barrier to radiation, indeed they enhanced the fragmentation of primary ions into secondary ions whose higher LET values imply major radiobiological issues for astronaut radiation protection. As a first approach, different orders of layers were implemented in the full wall configuration without shielding efficiency improvement. The only improvement in terms of dose equivalent reduction was obtained when the 28 mm aluminium layer of the Out-fitting was removed.

The second approach implied the use of promising materials with low Z/A ratio in replacement of aluminum, such as Poly(methyl-methacrylate) (PMMA), Polyoxymethylene (POM), and Carbon Fiber (CF) as a representation of graphene suggested in the literature. Unfortunately, it was observed that the shielding efficiency depended on the energy and type of ion, underlining the complexity of making decisions for a future shielded habitat, and the need of further investigation with additional energies and types of ions.

Regarding the type of ions and available energies at the time of the experiements which were investigated in this study, PMMA does not seem to be beneficial for radiation protection purposes, since there is no dose reduction when it was chosen instead of aluminum in all wall configurations. However, a final judgment regarding the benefit of this particular material is impossible based on the single energy and ion type used in this study.

In the literature, an alternative to aluminum is confirmed to be polyethylene. However, it is well known that its strength and structural properties do not fit requirements for space application, thus carbon fiber, carbon nanotubes and graphene are an option to be incorporated into polyethylene shields. Despite carbon fiber being included in the study, our results cannot confirm that carbon fiber always brings benefits in terms of radiation shielding. Usually, the microdosimetric spectra showed a shift to higher lineal energies when CF was used to replace aluminum, due to primary ions exiting the spacecraft's wall with reduced energy, as well as fragmentation. Hence, depending on the primary energy of ions, their type, and the

configuration selected, the dose equivalent $Hp(10)$ might be lower or higher. This demonstrates the complexity in predicting a unique dependence between the quality factor and the dose equivalent in a mixed charged particles field, leading to the need for portable microdosimetry instrumentation in the habitat and for astronauts to wear.

Additionally, the highly hydrogenated polymer POM demonstrated a high radiation shielding efficiency suggesting its application as a composite material with the above-discussed carbon fiber or nanotubes, to achieve a reduction in the dose equivalent.

In conclusion, the SOI "Mushroom" microdosimeter was demonstrated to be a powerful device to investigate the quality of a radiation field behind any desirable shielding material and configuration for optimization of spacecraft design. The shielding efficiency was investigated also through the evaluation of the dose equivalent giving information for personal monitoring of astronauts. In our study, the normalization of the dose equivalent $Hp(10)$ to the absorbed dose in water in a Bragg Peak delivered during the irradiation gives a conversion factor (Sv/Gy) that characterized the field generated by a particular type of ion, ion energy and shielding properties. Due to possible significant variation of the radiation field at different locations of the habitant within the spacecraft a network of such microdosimeters may be useful as a personal monitor. Currently used dosimeters for absorbed dose monitoring (e.g. TLD) when attached closely to SOI microdosimeter will provide synergy and redundancy in absorbed dosimetry while providing $\bar{Q}$ derived from microdosimetry. Shortcomings of these studies are in a limited number of ions and energies used for experiments, but still enrich the understanding of the nature of the mixed charged particles radiation field inside the spacecraft, allowing for a more complete investigation of shielding materials for future craft and habitat designs.

In the next chapters, the SOI "Mushroom" microdosimeter's response will be investigated against the other great component of the cosmic radiation environment: the proton field. The simulation results from the GEANT4 model discussed in Chapter 2 will be used to model the spectral fluence of proton in space to be delivered by using a treatment planning system of a clinical accelerator in a proton therapy centre.

Chapter 6

Modelling of protons spectra encountered in space using the clinical accelerator of PSI

In this chapter, results obtained from experiments done at Paul Scherrer Institute (PSI) are presented and were discussed at the 2020 Virtual IEEE Nuclear Science Symposium & Medical Imaging Conference.

These results have been included in the article "S. Peracchi et al., Modelling of protons spectra encountered in space using medical accelerator and its microdosimetric characterization", Advance in Space Research journal, available online Advances in Space Research, available online 2021/02/11/, 2021. *As first author of the paper, I have been allowed to include it in this thesis by the journal itself.*

The study introduces a procedure where a proton fluence spectra of interest for space radiation protection, previously generated by Monte Carlo simulations was delivered using a clinical proton therapy accelerator. Particularly, it reports first results of modelling a proton radiation field in space in the energy range from 70 to 230 MeV during a single experimental session by programming a treatment planning system (TPS) to deliver required proton irradiation energies. Moreover, the angular distribution of the proton irradiation field has been varied to reproduce the isotropic exposure experienced by humans in space. The obtained proton radiation field was characterized using the 3D sensitive volume SOI "Mushroom" microdosimeter, which was used previously for characterization of the heavy ions field in space.

6.1 Introduction

The main portion of radiation is related to high-energy protons originating from different sources in a very wide energy spectrum, up to hundreds of GeV as discussed in 1.1.1.

Knowledge of the particles types, their energies and spectral fluence is extremely important for the prediction of biological effects on astronauts' health. Currently, several Monte Carlo-based and other codes such as HZETRN, API, together with the published space weather data, [121-124] are used to simulate proton fluxes in space and to predict particles transport and interaction with spacecraft to assess dose and dose equivalent and consequently radiobiological effects on humans [63]. In order to validate the simulated results, benchmarking experiments must be carried out. There are only a few radiation facilities in the world which can partially reproduce the radiation environment in space using high energy ion accelerators. Most of them only provide monoenergetic and unidirectional protons beams, which are not enough to mimic the real scenario in space [125-130]. Moreover, space exploration is aiming to send humans to the Moon and to Mars for a longer period of time. The paramount need of knowing the effects related to astronauts' health deriving from such new and more dangerous radiation environments beforehand can be achieved only through ground-based radiation tests performed with whole energy spectra of protons to complement and validate the simulations. In fact, "In preparation for sending astronauts on long duration missions into space, it is necessary to simulate the same overall environment in ground-based facilities" [131].

For many years, ground-based facilities approach the problem of reproducing the complex radiation scenario encountered in space. Some studies with multiple ion energies and angles have been successfully performed. Thanks to the enhancement of the technology at the NASA Space Radiation Laboratory, it is nowadays possible to switch beam energy and ion type in an order of 2 minutes to achieve a more realistic energy spectrum generated by the GCR simulator [131, 132]. The Northeast Proton Therapy Center also offers radiation testing services using

proton beams which are degraded to reduce the energy beam to any value between 230 and 70 MeV [133, 134]. Additionally, the isotropic nature of the radiation environment in space must be reproduced in a ground-based campaign, considering large angle irradiation as partially done in the experimental campaign performed at the Loma Linda University Proton Therapy Centre [129]. However, it was repeatedly affirmed that the uncertainty associated with representing the GCR spectrum with discrete ion and energy beams, due also to constraints of current facilities, does influence the accuracy in evaluating the dose to astronauts [106, 135]. Many of these shortcomings in a current ground radiation testing facilities for modeling of space radiation effects are continuously discussed at Workshops on Radiation Monitoring on the ISS (http://www.wrmiss.org/) and IEEE NSREC conferences (http://nsrec.com).

In this chapter, we aim to introduce a methodology to the scientific community that tries to cojnfront the cited-above constraints, by describing how to program and use a treatment planning system (TPS) of clinical accelerator to deliver a modulated fluence based on the intensity of a realistic energy spectrum in the range 70 -230 MeV, previously simulated with GEANT4 [63]. This proposed methodology can potentially overcome the limit of conducting tests with several mono-energetic beams delivered one at a time.

Particularly, in this work the methodology was applied to a portion of the proton field typical of Low Earth Orbit (LEO) environement in the available energy range from 70 to 230 MeV achievable with the clinical proton therapy accelerator at the Paul Scherrer Institute. Hence, results of microdosimetric characterization of proton fields with spectral properties typical of GCR, SPE, and Van Allen Belts protons delivered in a single experimental session with the clinical proton accelerator at PSI, controlled by a specially programmed TPS, are reported.

6.1.1 Proton facility at PSI

In the ‘90s, the Paul Scherrer Institute (PSI) was the first one in the world to develop a scanning gantry for proton therapy. Later PSI developed a second-

generation Gantry 2, taking advantage of the experience gained from Gantry 1. It implements advanced magnetic scanning modes, which allow a significant reduction of the treatment time. This, it is possible to repeatedly irradiate a target with a one-side rotation form -30° to +180° (see Figure 6.1).

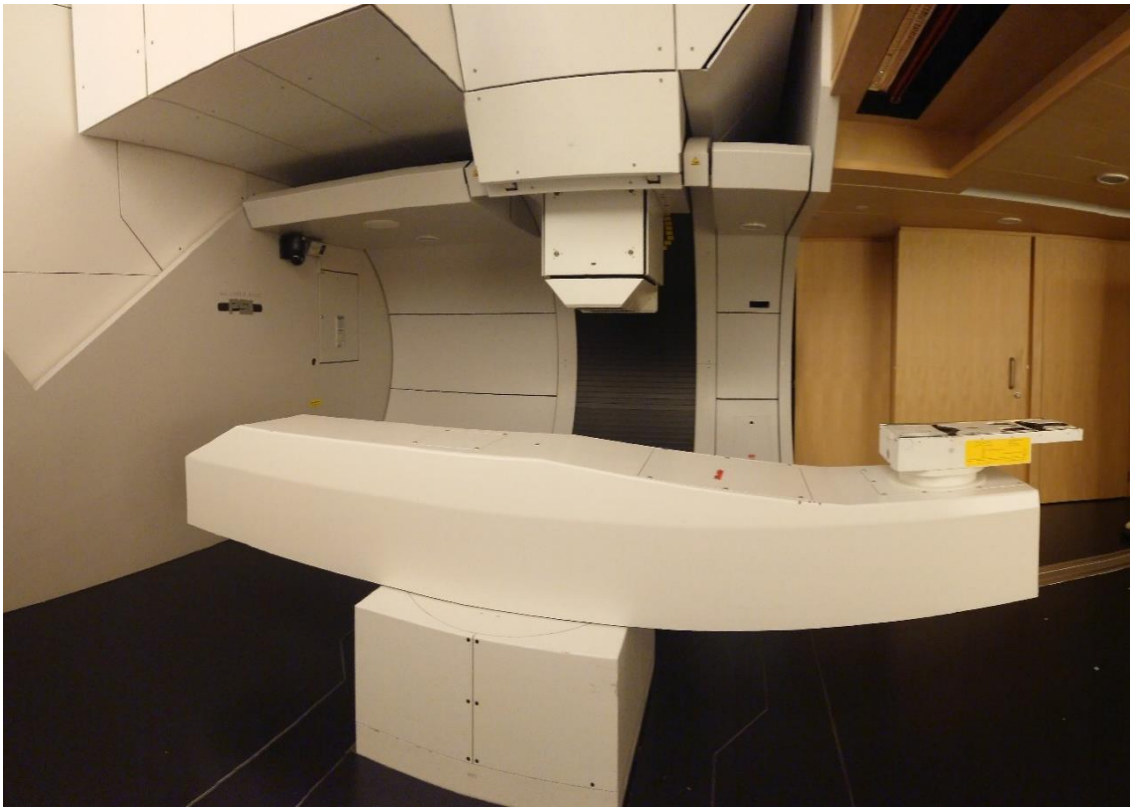

Figure 6.1. Photo of the irradiation room with the new Gantry2 taken at the PSI during experiments.

The accelerator used at PSI is a 250 MeV superconducting cyclotron, generating protons with a beam current extracted in a range from 0.05 to 800 nA, which can be varied smoothly. An energy degrader, consisting in two sets of carbon wedges, moved mechanically very quickly in and out of the beam, allows changing the energy of the protons in a range of 70 to 230 MeV, within approximately 80 ms [136]. During experiments carried out at PSI and discussed in here, the adopted beam current was in a range of 5 to 1 nA, much lower than the typical current used for patients' treatments (200 – 400 nA) with a pencil beam scanning (PBS).

The vacuum of the beamline extends to the end of the nozzle reducing the distance in air from the vacuum window to isocenter down to 90 cm. The nozzle of the gantry, i.e. the proton beam exit foil, has a minimum required thickness to minimize the broadening of the protons pencil beam due to scattering effects and prevent neutron contamination of the beam. Figure 6.2 shows all the materials inside the nozzle and how the beam size changes adding one by one each of these elements of the nozzle. The blue line represents the final radius σ of the Gaussian pencil beam achieved during the irradiation. For three main energies of interest considered for experiments in this thesis, the sigma of the pencil beam width was: 5, 2.75, and 2.15 mm for 70, 150, 230 MeV, respectively, with a stable penumbral uncertainty of ± 0.35 mm [136].

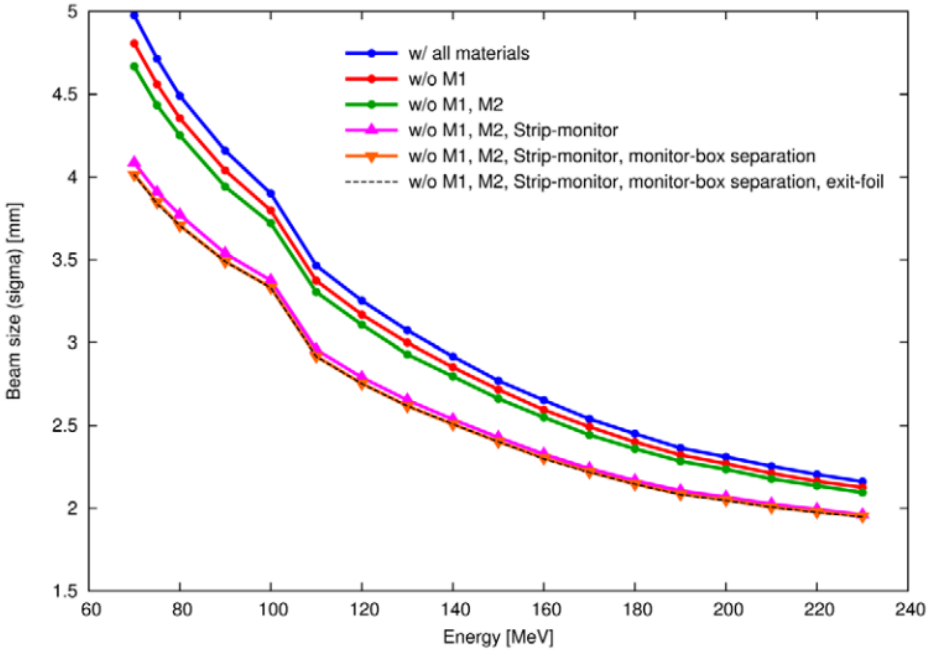

Figure 6.2. Image courtesy of (E. Pedroni et al., 2011) [136]: measured pencil beam size σ (FWHM/2.355) at the isocenter as a function of the beam energy, delivered by Gantry 2 at PSI. The curves show the effect of removing in sequence the two transmission monitors (MT), the strip-monitor, the sheet that separates the monitor-box and the foil of the exit of the nozzle.

Within the nozzle, two plane-parallel ionization chambers measure the instantaneous intensity of the pencil beam, calibrated to the number of delivered

protons per single delivered spot. Moreover for the following studies, we selected a particular field size of 5 x 5 cm^2, and a spot spacing of 0.4 cm at the isocenter to deliver a uniform irradiation field, the number of spots per single layer can be calculated and consequently, the total number of protons delivered by the machine. Thus, the distribution of the protons density for each layer is expected to be homogeneous (see Figure 6.3).

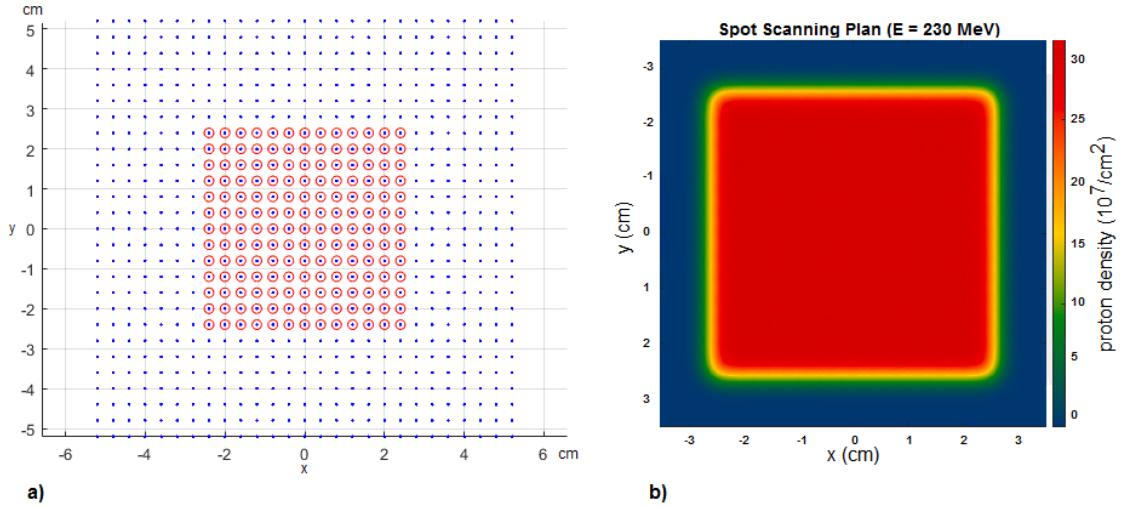

Figure 6.3. a) Example of the pencil beam pattern for the field size of 5 x 5cm^2 adopted during the experiments, b) and corresponding homogeneous proton fluence distribution delivered with of 5x10^7 protons/spot of Gaussian intensity distribution at 230 MeV.

6.2 Materials and Methods

In this study, the 3D SOI "Mushroom" microdosimeter was used, with cylindrical SVs with dimensions of 18 µm diameter and 10 µm height. The SOI microdosimeter was connected to the MicroPlus probe, which has been tested successfully multiple times in heavy ions beams mimicking heavy ions component of GCRs as discussed in Chapter 4 and Chapter 5 and in former publications [101, 102].

With respect of the principles of microdosimetry discussed in section 1.3.1, the mean chord of the SV adopted in this study was equal to the SV thickness (10 µm) of the SOI microdosimeter. In fact, the mean average chord of the cylindrical SV with aspect ratio 2:1 is equal to the height of the SV that is approximately the case for the "Mushroom" SV with a diameter 18 µm and height 10 µm [137]. The microdosimetric measurements allow the evaluation of the average quality factor $\overline{Q}$ of the radiation field, and the dose equivalent $Hp(10)$ for astronauts' individual monitoring, as explained in section 1.3.1.

6.2.1 Experimental set-up

The SOI microdosimeter is placed at the center of a PMMA cylindrical tube of inner diameter 44 mm with a wall thickness of 10 mm to mimic isotropic conditions for any angle of the beam incidence. The PMMA cylinder has been chosen as an approximation of the human tissue to obtain the individual dose equivalent at 10 mm depth in the body ($Hp(10)$). Finally, a 75 µm aluminum foil was used to cover the PMMA phantom as a faraday cage in order to avoid the detection of radiofrequency noise in the detection electronics (Figure 6.4b). The MicroPlus was installed in a freestanding position to allow a 180° rotation of the gantry around the SOI microdosimeter without interfering with the couch. The microdosimeter was placed at the isocenter of the gantry system (see Figure 6.4a). The gantry was programmed to deliver the same proton spectral field with 10° interval. In this paper, the response of the microdosimeter measured for gantry angles 0°, 90°, and 180° is presented.

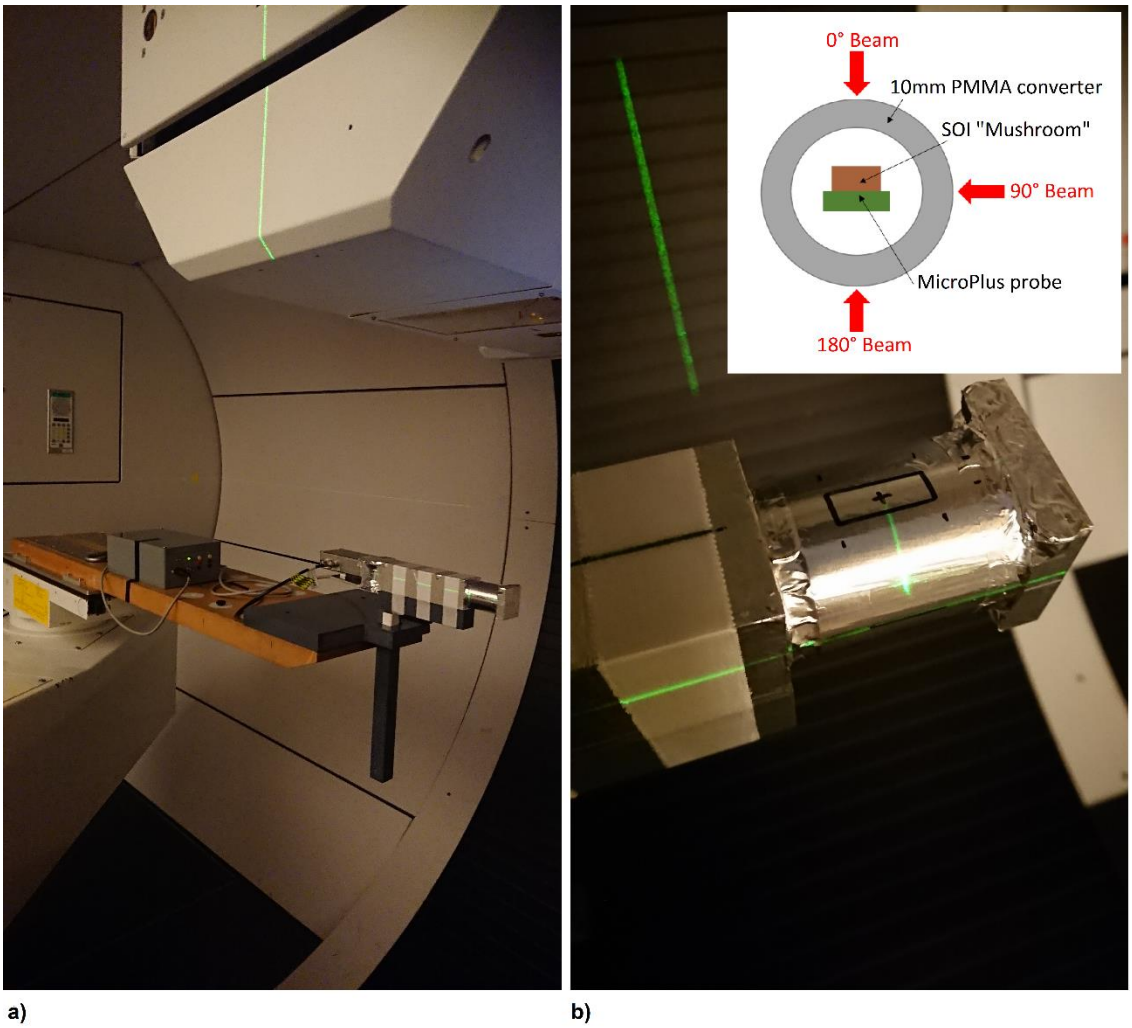

Figure 6.4. a) Photos taken inside the Gantry2 room of the experimental set up; b) 10 mm PMMA cylindrical converter covered with aluminum foil hosting the SOI microdosimeter at the isocenter ("black cross" mark is where the SOI microdosimeter is located).

6.2.2 Fluence modeling

The GCR, SPE, and Van Allen protons spectra encountered at the ISS's altitude were partially reproduced using a custom treatment planning system at PSI and then delivered by the PSI clinical proton therapy control system (TCS). The PSI integrated Elekta's XiO® treatment planning system and MOSAIQ® OIS (https://www.elekta.com/) into its centre to manage the flow of data between treatment simulation, planning and delivery. Since the protons per spot for each

proton energy is an input to the TCS, it was possible to deliver the proton fluence of particular energies normalized to the corresponding spectrum of space radiation of interest. The proton fluence spectra of GCR, SPE, and Van Allen protons outside and inside the ISS Columbus for the LEO environment used in this study were previously simulated and discussed in details in Chapter 2 [63]. Along the full energy simulated spectrum up to GeV, only the proton fluence outside and inside the Columbus habitat in the range 70 – 230 MeV with a 1 MeV energy step were taken as input of the TPS. This range of energy represented the largest available and achievable with the used medical accelerator. Even though it represents a narrowed part of the full spectrum, referring to Figure 6.5 for example, this energy range represents the 9, 52, and 63% of the entire inside spectra of GCR, SPE, and Van Allen Belts protons, respectively.

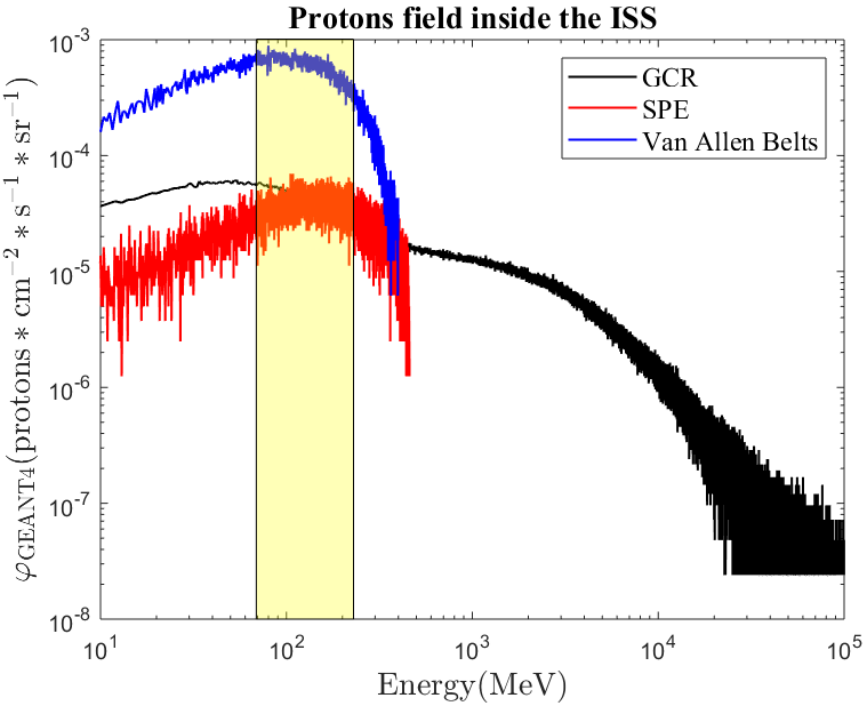

Figure 6.5. Example of protons fluences inside the ISS simulated with GEANT4 in previous work [63]; fluxes include both primary and secondary protons generated by nuclear interaction with shielding wall. The yellow area highlights the range of energy (70 to 230 MeV) used in this study.

Next, the protons fluence for each bin along the spectrum was calculated by referring to the planned fluence of 70 MeV protons and scaled to the space proton fluence.

The TPS associates a minimum value of protons per spot delivered $(\#p/s)_{min}$ at the energy layer with the lowest simulated fluence to guarantee a minimum acceptable statistic and consequently rescales the value $(\#p/s)_i$ for all remaining bin energies E_i. Additionally, to avoid pileup, the current is lowered to the level the system could withstand. This value is the one expected to be delivered at the isocenter in free air geometry, where the SOI microdosimeter was placed. Knowing the field size A of 5x5cm^2, equivalent to the area of a single-energy layer i, and the total number of spots in one layer $(\#s)$, 13x13 spots, the fluence expected to be delivered by the TPS φ_{TPS-i} (protons cm^{-2}) for each energy layer i was calculated as follows:

$$\varphi_{TPS-i} = \frac{(\#p/s)_i * \#s}{A} \tag{6.1}$$

to then obtain the spectral fluence expected to be delivered by the TPS $(\varphi_{TPS-expected})$.

Finally, for each irradiation, the two ionization chambers in the nozzle record the actual number of protons delivered per spot to account for any uncertainties in the beam current delivered. Such uncertainties are larger at the low currents used in this experiment, while are almost negligible at the higher currents used clinically. By using the formula in Equation (6.1), the actual fluence delivered by the TPS at the isocenter and measured by the ionization chambers $(\varphi_{TPS-delivered})$ was calculated for each irradiation and angle.

6.2.3 Dose evaluation

Additionally, as mentioned in the previous section, the SOI microdosimeter set-up was implemented to evaluate the dose equivalent $Hp(10)$ at 10mm depth in the body of an astronaut. The theoretical absorbed dose D_{TPS-i} (Gy), at the isocenter planned by the TPS and delivered for protons with energy E_i, was calculated as at the entrance of a hypothetical water phantom by the following formula:

$$D_{TPS-i} = \frac{\varphi_{TPS-i} * LET_i}{\rho} \tag{6.2}$$

where $\rho = 1$ g cm^{-3} is the density of water and the LET_i for protons in water was calculated with SRIM for each energy value E_i from 70 MeV to 230 MeV.

The total entrance absorbed dose in water delivered in any particular irradiation is a sum of contributions for each energy in a full spectrum:

$$D_{TPS} = \sum_{i=70MeV}^{230MeV} D_{TPS-i} \tag{6.3}$$

As repeatedly discussed through chapters and in section 1.3.1, the calculation of the average quality factor $\bar{Q}$ of the protons field is performed, providing the equation stated by the ICRP Publication 60 and reproduced in Table 1.3 [21]. Therefore, the value of $Hp(10)$ is calculated based on the equation (1.17) with tissue-equivalent conversion factor equal to 0.8, obtained as the average of proton mass stopping power ratio silicon to water in a proton energy range 70 to 230 MeV.

Finally, the $Hp(10)$ measured by the SOI microdosimeter is normalized by the corresponding value of entrance-absorbed dose delivered in water by the gantry for each irradiation. Even though the dose equivalent is not a protection quantity

adopted for radiation protection in space, it is still considered as important supplementary information, providing an additional quantity that can be useful to quantify biologically relevant hazard of the reference field [129, 135, 138].

6.3 Results and Discussion

6.3.1 Modeling of the fluence and dose

Figure 6.6 shows the comparison of expected spectral fluence for GCR, SPE, and Van Allen Belts (or trapped) protons outside and inside the ISS obtained with GEANT4 [63] with the reproduced proton spectra obtained using the custom TPS and delivered at gantry angle 0°, considering a minimum number of protons per spot $(\#p/s)_{min} = 10^5$. It can be seen that they match reasonably well. The TPS planed and delivered spectral fluences match the expected modeled with GEANT4 fluence with a relative standard deviation σ between 3 % and 5 %. The uncertainty in fluence delivery correlates with the beam current entering the gantry: particularly, the lower the current, the higher the difference from delivered fluence and planned by TPS. Consistent results were obtained also for the 90° and 180° irradiations.

Figure 6.7 shows spectral absorbed doses for each energy at a depth of 10 mm water retrieved from the simulated fluence by GEANT4, modeled and delivered by the TPS at the isocenter in both scenarios, outside and inside the ISS. As expected, the absorbed dose is characterized by the same uncertainty associated with the corresponding fluence in Figure 6.6, particularly σ is in a range of 3 to 5 %. The same uncertainty was observed for 90° and 180° irradiations.

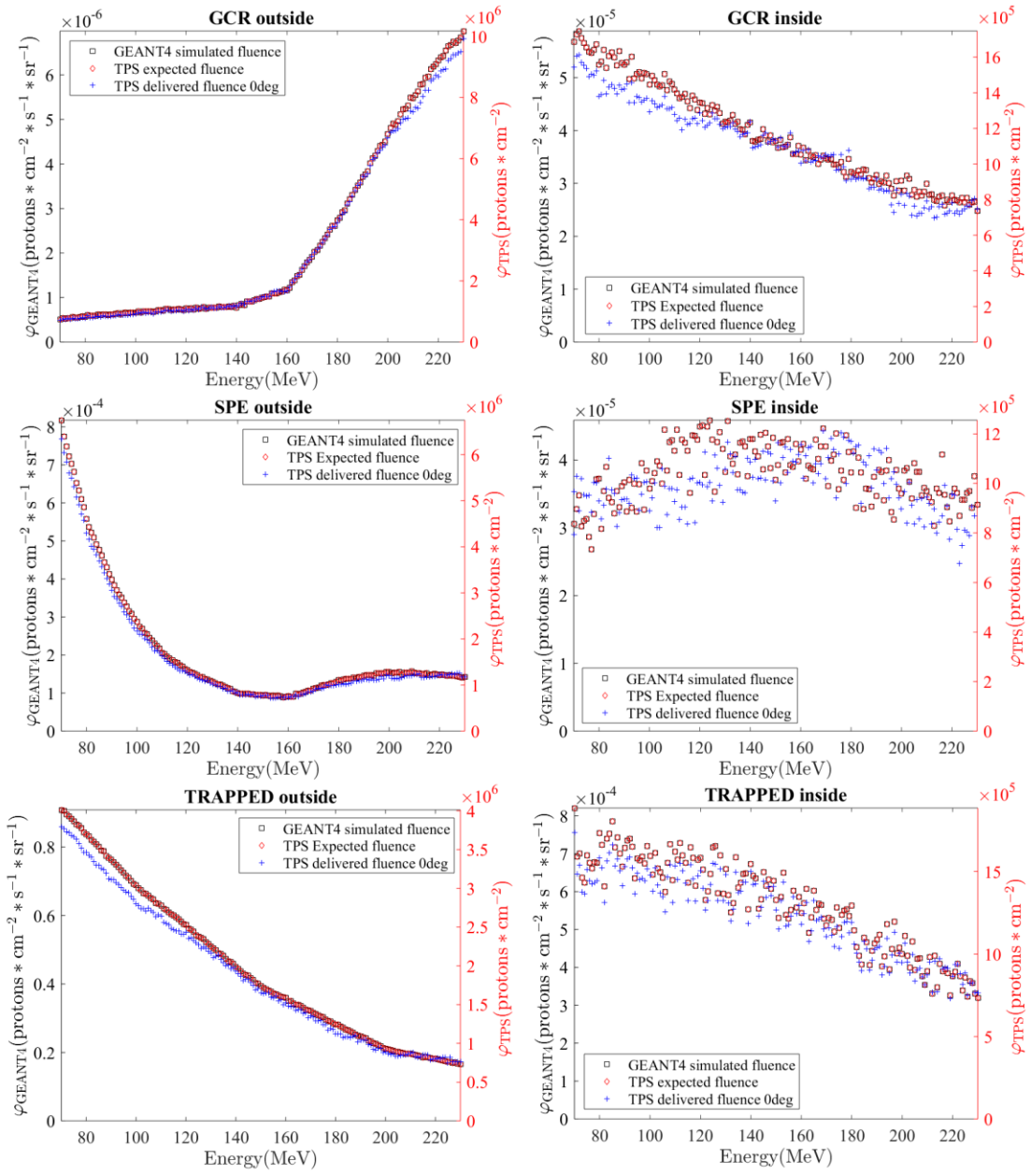

Figure 6.6. GCR, SPE, and trapped protons spectral fluence delivered by the gantry at the isocenter (blue +), compared with the fluence modelled with the TPS (red ◊) and GEANT4 (black □) simulation. The TPS red lines and GEANT4 black lines match perfectly as expected. Two scenarios were considered: spectra outside the ISS/Columbus module and inside it after protons propagating through the shielding of the spacecraft.

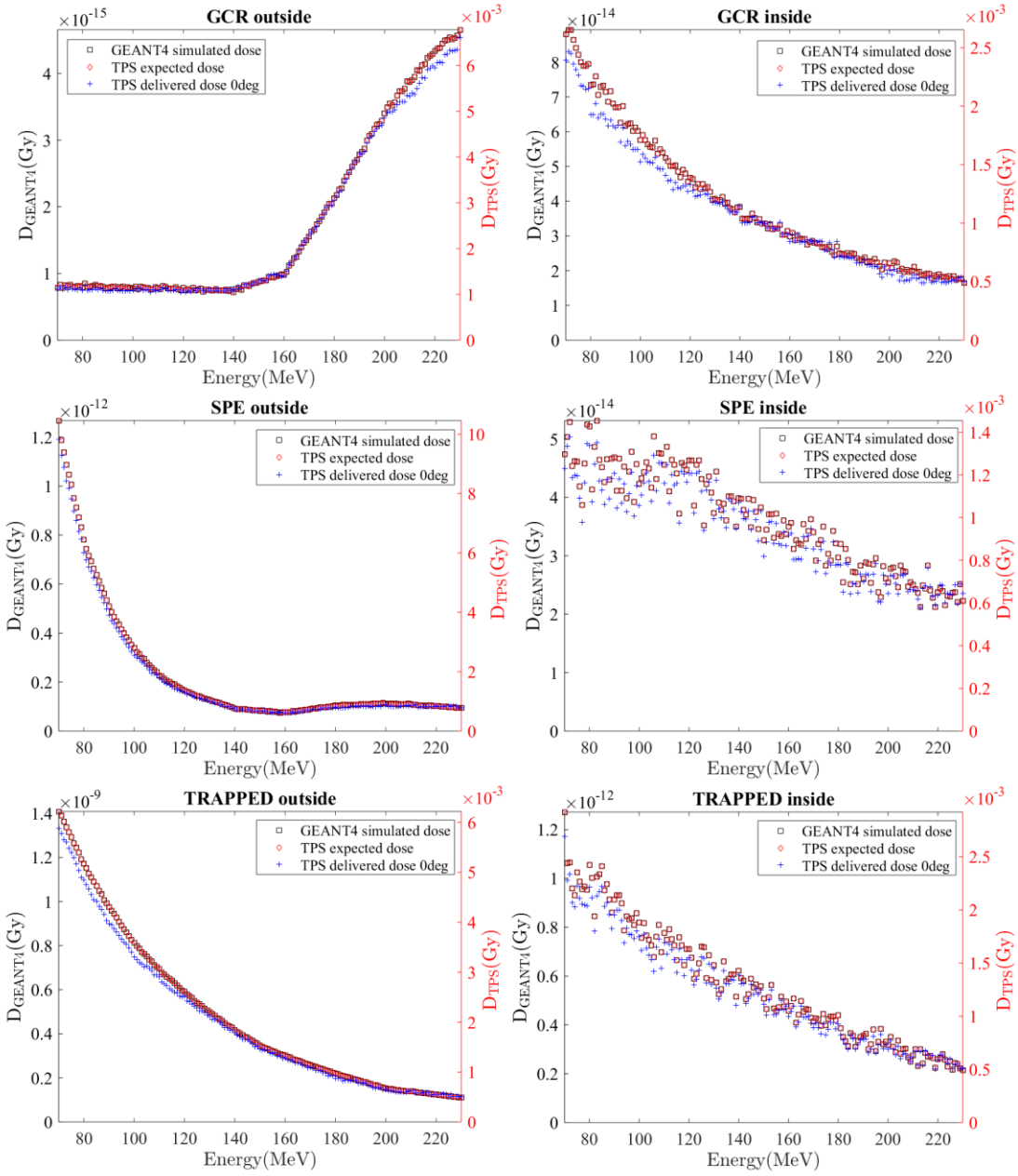

Figure 6.7. Spectral absorbed dose delivered by the gantry at the entrance to water at isocenter (blue +), compared with the absorbed dose modeled with the TPS (red ◊) based on GEANT4 (black □) simulation, for GCR, SPE, and trapped protons beams, outside and inside the ISS/Columbus module.

6.3.2 Measurement of the microdosimetric spectra

Figure 6.8 shows microdosimetric spectra measured by the SOI "Mushroom" microdosimeter during the delivery of GCR, SPE, and trapped proton spectral fluences discussed in the previous section, by a medical accelerator. Figure 6.8a shows the microdosimetric spectra obtained at 0°, 90°, and 180º for the proton radiation field partially modelling GCR, SPE, and trapped protons outside and inside the ISS. In case of GCR and SPE proton spectral fluences, the microdosimetric spectra for proton beam incident at 0° and 180º have essential partial contribution events with lineal energies below 10 keV/μm (all presented lineal energies are related to tissue). For 90° beam incidence, the microdosimetric spectrum is shifted to higher lineal energies above 10 keV/μm in both cases due to charge deposited in two or more "Mushroom" SVs which are read out as a single event.

For GCR outside the ISS, no essential difference between microdosimetric spectra measured at 0° and 180° is observed. It is due to the fact that the majority of these protons have energy above 160 MeV and not modified essentially by transmission through 2 mm thick plastic of the DIL package. Inside the ISS, the proton spectrum is with descending partial contribution of higher energy protons that leads to a slightly higher proportion of lower lineal energy events for 0° beam incidence in comparison to outside ISS microdosimetric spectra. It is caused by fewer events in a higher lineal energy tail due to inelastic reactions occurring in silicon and PMMA induced by high energy protons (e.g. Si(p, γ), Si(p, p)) generating alpha particles and recoil Si atoms. Even the single events with y>100 keV/μm will lead to a visible change of the lower y component of microdosimetric spectra. For 180° beam incidence, this effect is more pronounced because of the additional absorption of high LET particles (generated in PMMA) by DIL package. Also, low energy protons (70 MeV) that lose energy while propagating through the 10 mm PMMA degrade their energy propagating through the DIL package too. Because of both mentioned reasons, the contribution of events with y<10 keV/μm in the microdosimetric spectra is higher. The effect of softening of the proton spectra inside the ISS is also reflected in a slight shift of microdosimetric spectra to higher y for

90° beam incidence in comparison with corresponding microdosimetric spectra outside ISS.

For SPE spectrum outside the ISS, the essential partial contribution of lower energy protons makes the microdosimetric spectrum wider and skewed to higher lineal energies in comparison to GCR microdosimetry spectra for both 0° and180°. The identity of both microdosimetric spectra is explained with absence of single high lineal energy events due to much lower partial contribution of higher energy protons in SPE spectrum outside the ISS. The inside proton spectrum is much more uniformly distributed with equal partial contribution of lower and higher energy protons that is reflected in higher partial contribution of lower lineal energy events for 0° incidence angle in comparison to microdosimetric spectra outside the ISS (see explanation above). It is also confirmed by a shift of 90° microdosimetric spectra to lower lineal energies in comparison with corresponding microdosimetric spectra outside the ISS.

For trapped protons, the microdosimetric spectra for 0° and 90° beam incidence are identical for the inside and outside ISS scenarios due to similar proton spectral fluence (see Figure 6.6).

For all three protons spectra at 90º, the microdosimetric spectra shifted to higher lineal energy due to enhanced energy deposition by protons passing multiple SVs in the detector that is electrically connected to the same readout bus. In fact, values of $Hp(10)$ calculated at 90º are at least a factor 2 higher than doses measured at 0° and 180°, considering the same dose delivered by the clinical machine (see Table 6.1). However, the probability of such events in the cosmic isotropic field is extremely low due to the small size of the "Mushroom" SV and is associated to that acceptance solid angle for such events. To mitigate such events, the "Mushroom" design has odd and even linear arrays of SVs connected to different readout preamplifiers.

Table 6.1 shows the average values for the quality factors $\bar{Q}$ derived based on convolution of measured microdosimetric spectra and ICRU 60 recommended $Q(LET)$ [21]. Measured $\bar{Q}$ values of this study were compared with predicted values based on GEANT4 modelling of the SOI "Mushroom"

microdosimeter's response inside the ISS for proton spectral fluence extended up to 10^5 MeV as discussed in Chapter 2. GEANT4 predicted values 1.30, 1.31 and 1.41 for GCR, SPE and trapped protons respectively and discussed in section 2.3.2, are slightly lower than values measured by the SOI in this study, but still considered close to the interval error. Particularly values obtained for SPE (1.67) and trapped protons (1.48) and GCR scenario (1.48 - 1.89) can be explained essentially by the fact that the proton spectral fluence considered in this study is just limited to an energy range of 70 ÷ 230 MeV. For SPE and trapped most of proton spectral fluence is below 230 MeV protons and partially reflected in our experiment, but still the contribution of protons with energy outside this range is not considered. Similar for GCR protons up to 100 GeV: the high energy proton component, while with low LET, provides high energy delta electrons that produce a not negligible contribution to absorbed dose and microdosimetric spectra for y<0.4 keV/ m, which is not counted in present experiments. The convolution of the low lineal energy tail of microdosimetric spectra with $Q(LET)$ will lead to a reduction of $\bar{Q}$ which explains the observed difference.

In Figure 6.8b, another series of results is presented, by means of the microdosimetric spectra resulting from an approximated isotropic irradiation over 180°. The total spectra were obtained by merging the original MCA files for the same delivered fluence from the three irradiations at 0°, 90°, and 180° and performing the usual analysis as explained above. These results show a realistic approximation of how the microdosimetric spectra would look like in case of isotropic irradiation over 180°. Unfortunately, irradiations at 180° with SPE and trapped inside spectra and 180° trapped outside spectrum were not available, hence the missing inside microdosimetric spectra at 180° were assumed to be equal to the inside microdosimetric spectra obtained at 0°. Similarly, the missing trapped protons microdosimetric spectrum at 180° outside was considered as the same as the one measured at 0° outside the ISS. The assumption was made based on the similarity observable in Figure 6.8a, confirmed by the values of $\bar{Q}$ and $Hp(10)$ in Table 6.1.

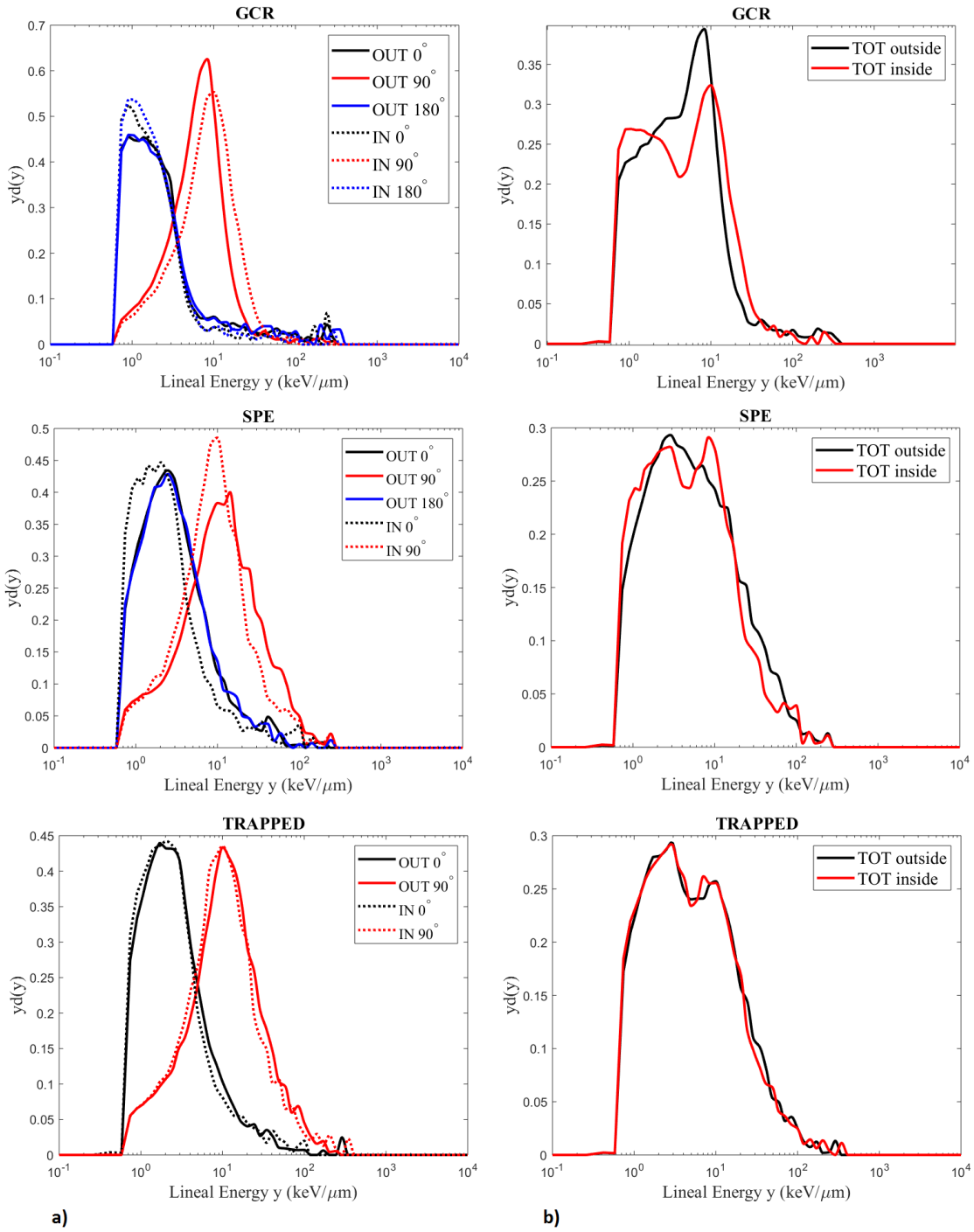

Figure 6.8. a) Microdosimetric spectra measured by the SOI microdosimeter during 0°, 90°, and 180° irradiations, modeling the proton fluence outside the ISS/Columbus (solid lines) and inside it (dashed lines).b) Microdosimetric spectra resulting from an isotropic irradiation over 180°.

Table 6.1. Values of dose calculated based on microdosimetric spectra analysis compared to dose delivered by TPS.

Beam	Angle	$\bar{Q}$	D_{TPS} (Gy)	Hp(10) (Sv/Gy)
GCR out	0°	2.02 ± 0.16	0.40	0.33 ± 0.01
	90°	1.73 ± 0.06	0.40	0.83 ± 0.01
	180°	2.12 ± 0.17	0.39	0.36 ± 0.01
GCR in	0°	1.89 ± 0.22	0.18	0.40 ± 0.01
	90°	2.04 ± 0.06	0.18	1.07 ± 0.01
	180°	1.48 ± 0.13	0.18	0.32 ± 0.01
SPE out	0°	1.59 ± 0.08	0.29	0.45 ± 0.01
	90°	4.25 ± 0.15	0.29	1.82 ± 0.02
	180°	1.50 ± 0.08	0.29	0.36 ± 0.01
SPE in	0°	1.67 ± 0.14	0.15	0.43 ± 0.01
	90°	3.16 ± 0.15	0.15	1.68 ± 0.02
Trap out	0°	1.46 ± 0.08	0.32	0.43 ± 0.01
	90°	3.91 ± 0.12	0.32	1.98 ± 0.02
Trap in	0°	1.48 ± 0.09	0.20	0.41 ± 0.01
	90°	3.61 ± 0.15	0.20	1.90 ± 0.02
GCR out	TOT	1.87 ± 0.06	1.19	0.50 ± 0.02
GCR in		1.88 ± 0.07	0.54	0.59 ± 0.01
SPE out		2.77 ± 0.07	0.88	0.88 ± 0.02
SPE in		2.43 ± 0.09	0.45	0.85 ± 0.01
Trap out		2.60 ± 0.06	0.97	0.94 ± 0.02
Trap in		2.53 ± 0.08	0.59	0.91 ± 0.01

6.4 Conclusions

This paper introduces a methodology to model the proton spectral fluence typically encountered in space using a programmed treatment planning system of a proton therapy accelerator. The study was conducted at the proton therapy centre Paul Scherrer Institue, where the fractional proton spectra of GCR, SPE, and Van Allen Belts in an energy range from 70 to 230 MeV were delivered by a pencil

scanning beam. These spectra used as an example of input were obtained by ad-hoc GEANT4 simulations of the radiation environment at the ISS's altitude [63].

The number of protons per each spot and energy was provided by the TPS to replicate the particular proton spectral fluence. A 5x5 cm^2 field of uniform proton fluence was delivered at the isocenter, where the microdosimeter was placed. Two ionization chambers placed at the window exit of the nozzle detected and controlled the actual fluence delivered to guarantee the best match with what expected from the TPS. This new methodology allows also the irradiation of electronic components or biological objects with a LET programed proton spectra that is important for SEU studies and radiobiological models verification. The advantage of delivering a modulated fluence based on the intensity of a realistic spectrum allows to skip the constant change in the beam set up to switch energy, gaining time and reducing the uncertainty.

It is the first time that the SOI "Mushroom" microdosimeter was irradiated in a cylindrical PMMA phantom with a realistic space partial proton spectral fluence isotropic field and the microdosimetric spectra were obtained. The quality factor $\bar{Q}$ and the personal dose equivalent $Hp(10)$ per unit of absorbed proton dose in water at the isocenter were evaluated for radiation protection purposes, in two scenarios: astronauts outside and inside the ISS/Columbus.

Results are consistent with previous simulated results for this microdosimeter using GEANT4 in the same proton spectral fields [63] confirming the accuracy of the implemented methodology to deliver any spectrum of interest simulated with Monte Carlo model. This study with spectral proton fluence and previous study with heavier ions in [102] demonstrated that SOI microdosimeter can accurately measure LET(Si) in a wide range 0.5-5000 keV/μm and can be useful for SEU prediction additionally to astronauts radiation protection.

In conclusion, after the characterization of the heavy ions field in space by usignt the SOI "Mushroom" microdosimeter discussed in Chapter 4 and Chapter 5 this study aimed to investigate the other main component of the cosmic radiation environement in space, i.e. the proton field. The successful progress of this study in the characterization of the field is the ability to model a spectral fluence

previously simulated with GEANT4. The approach and gained experience with proton medical accelerator for momicking the proton space field will be then translated to HIMAC (Japan) for modeling of GCR ion spectral fluence of He, C, O and Fe following the progress in the development of multi-ion therapy delivery [139].

Chapter 7
Characterization of the shielding efficiency of proposed materials against the proton field

This chapter shows results concerning the study of the angular dependence of the MicroPlus probe in an isotropic proton irradiation, modelling partially the ISS space environment as shown in Chapter 6. For the same radiation field, different shielding configurations of the Columbus module's wall were investigated. As well as against monoenergetic beams of 70, 150 and 230 MeV.

These results belong to the same experimental campaign performed at the Paul Scherrer Institute (PSI), whose methodology to model the spectral fluence by using the treatment planning system has been discussed in Chapter 6.

7.1 Introduction

In Chapter 6, a methodology to model the fluence of the GCR, SPE and Van Allen proton spectra encountered at the ISS altitude by using a clinical accelerator was presented. To mimic the isotropic exposure in space, the SOI "Mushroom" microdosimeter was placed at the isocenter to measure the microdosimetric spectra for each irradiation angle from 0° to 180°. Based on the microdosimetric spectra, the effect of angular dependence on the quality factor and the dose equivalent angular can be evaluated. The motivation of this work relies on the possibility that the current packaging of the SOI microdosimeter in dual-in-line (DIL) package could be a source of angular dependence especially for low energy ions, thus the MicroPlus probe was irradiated at multiple angles to investigate a variation of the dose mean lineal energy $\overline{y_D}$.

Additionally, in this chapter, we discuss results obtained during irradiations of different shielding configurations of the Columbus module of the ISS, by using the same methodology discussed previously in Chapter 6. In this case, both monoenergetic beams of 70, 150 and 230 MeV and the spectral fluences of GCR, SPE and Van Allen protons previously simulated with GEANT4 (see section 6.3.1) were used as radiation fields.

7.2 Materials and methods

The microdosimeter used in this study is the 3D SOI "Mushroom" model used also for experiments discussed in Chapter 6. More details about the microdosimeter can be found in section 6.2.

7.2.1 Angular dependence

When compared to the gold standard TEPC, the SOI "Mushroom" microdosimeter has the disadvantage of having cylindrical silicon SVs, as opposed

to a tissue-equivalent, spherical SV in the case of the TEPC. This means that the silicon microdosimeter has an inherent angular dependence. A useful way to study the angular dependence of the silicon microdosimeter under study is to measure the dose mean lineal energy, $\overline{y_D}$ as explained in Equation (1.8) in section 1.3.1, when irradiated with a radiation field with different angles of incidence.

In this work, the microdosimeter was set at the isocenter of the proton beam line of PSI and the microdosimetric spectra were measured while rotating the gantry around the isocenter, between angles 0° to 180° at 10° increments for spot beams.

The MicroPlus probe was inserted into a PMMA hollow cylinder with an inner diameter of 24 mm and a 10 mm outer wall thickness, ensuring that the beam passes through 10 mm of PMMA at any angle of incidence. This allows the evaluation of the operational quantity $Hp(10)$ dose equivalent at 10 mm depth in the body for astronauts individual monitoring. Together with the measurement of the microdosimetric spectra, the average quality factor $\bar{Q}$ was calculated and the proton field was characterized at each angle.

For a deep understanding of the influence that the irradiation angle can have on the dose equivalent and the quality factor, GEANT4 simulations were performed to evaluate the path length distribution for protons of 70, 150 and 230 MeV, at various angles.. All three energies used in the experiment were simulated, with the 70, 150 and 230 MeV beams having energy distributions of 0.7, 0.6 and 0.2% sigma, respectively, based on details from [140]. After passing through the nozzle, the beam then traverses air, with the distance from the nozzle to the detector being 40 cm. The detector was accurately modelled in GEANT4, with overlayers and contacts included. The detector was modeled on a DIL package on top of a PCB, in an open PMMA cylinder with an outer wall thickness of 10 mm and inner diameter of 24 mm. Finally, surrounding the PMMA cylinder is 75 µm of aluminum foil.

GEANT4 version 10.06 was used. The following physics lists components were used: for elastic and inelastic hadronic interactions the *G4HadronElasticPhysicsHP* and *G4HadronPhysicsQGSP_BIC_HP* were adopted, respectively, with neutron interactions up to 20 MeV described with neutron high precision (HP) model. Electromagnetic interactions were described with the standard EM option 4 model.

7.2.2 Shielding configurations

In Chapter 2, it was discussed the GEANT4 simulation of the proton environment at the LEO altitude and particularly how the particles fluxes change while propagating through the spacecraft wall of the Columbus module of the ISS. The microdosimetric response was studied and the field of mixed charged particles was characterized by means of evaluation of the quality factor and the dose equivalent. However, it is wellknown that ground-based experimental campaign must be performed complementary to simulation to validate results and prediction for future manned missions.

In this section, we present results where the SOI "Mushroom" microdosimeter was irradiated with 70, 150 and 230 MeV monoenergetic beam as well as with the GCR, SPE and Trapped protons spectral fluences from 70 to 230 MeV shown in Figure 7.1, behind a realistic sample of the Columbus shielding wall.

The fluences used in this experimental study are those one simulated with GEANT4 outside the ISS that were consequently modelled by using the TPS of the medical accelerator of PSI, discussed in details in Chapter 6.

The structure of the sample was reproduced based on specification found in the literature (see Table 5.1 and Figure 5.1), which have been explained in detail earlier in Chapter 5. The same materials used for the heavy ion irradiations at HIMAC were used for this experiment with proton beams. To briefly remind, the "Full wall" of the Columbus consists in 6 layers: the first 4 layers belongs to the pressurized shell, i.e the main structural part of the module, which are in sequence 2.5 mm aluminum alloy 2219, 5.5 mm Nextel, 8.0 mm Kevlar-Epoxy and 4.8 mm aluminum alloy 2219. Then, due to the great amount of devices and structure inside the Columbus habitat, such has instrumentation used by astronauts, two extra layers are modelled to take into account the extra shielding from radiation that they provide. These extra layers called "Out-fitting" are in sequence 28 mm aluminum alloy 2219 and 29 mm Kevlar-Epoxy (see Table 5.1 and Figure 5.1).

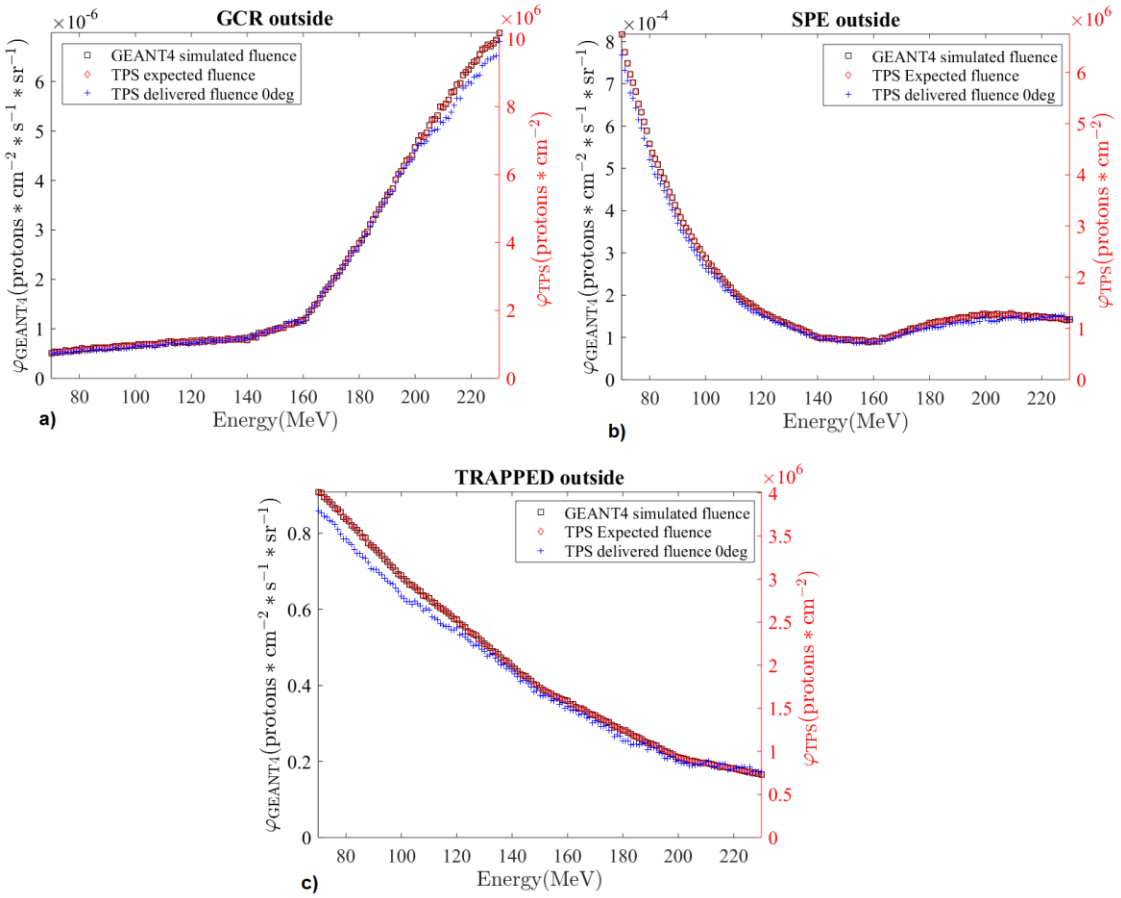

Figure 7.1. GCR, SPE and Trapped protons spectral fluences encountered outside the ISS in the energy range from 70 to 230 MeV used for the irradiation of all shielding configurations of the Columbus module.

We investigated the shielding efficiency of the "Full wall" configuration against 150, 230 MeV proton beam and against GCR, SPE and Trapped protons spectra (from 70 to 230 MeV) as a representation of the scenario of an astronaut inside the spacecraft (see Figure 7.2). We then compared the microdosimetric spectra obtained with the "No wall" configuration representing the scenario of an astronaut performing an extra vehicular activity (EVA). Finally, the "Full wall" and the "Inside spectrum-no wall" configurations were compared. This second configuration does not include the use of any sample of the shielding wall, but during the irradiation, it was used a spectrum simulated with GEANT4 representative of the protons fluence inside the Columbus. The interest in such irradiation is to compare the microdosimetric spectrum with the one obtained for the "Full wall"

configuration where the physical sample of the Columbus is present in front of the microdosimeter. The comparison allows the evaluation of the accuracy in modelling the Columbus wall with GEANT4 and the physical sample used during the experiments. The simulation takes into account the characteristics of the shielding materials used in the Columbus sample, subject of the experiments at Chapter 2, and considers all the interactions of primary protons coming from the outside, propagating through the wall, slowing down in energy and changing the initial fluence spectrum. The comparison of the simulation and experimental measurements will quantify the accuracy of the simulation results and will contribute to evaluate the reliability of GEANT4 for radiation protection in space human missions.

Figure 7.2. a) The "Full wall" sample is hold in place, while b) the probe hosting the SOI microdosimeter is placed immediately behind the wall sample. The wall sample is perpendicularly irradiated with a pencil beam exiting the gantry.

The pressurized shell was investigated separately as the main structural component of the shielding wall of the Columbus. The aluminum layers have been demonstrated to be the responsible of the highest production of secondary particles and fragments, such as neutrons from recoil protons, in the incident proton energy considered (70 – 230 MeV). As already discussed in Chapter 4 and Chapter 5, when heavy ion irradiations were performed at HIMAC, alternative materials to aluminum were used to test configurations that might have had better radioprotection properties. Hydrogenated materials as poly-methyl-methacrylate

(PMMA, density 1.18 g cm^{-3}), high-density poly-ethylene (HDPE, density 0.94 g cm^{-3}) are suitable to reduce the dose but they lack of strength. Thus, composite materials seem to be a solution for both structure and shield against radiation: thus carbon fiber (CF, density 1.6 g cm^{-3}) to represent graphene was used in this study. Several configurations of the shell (Al shell, PMMA shell, CF shell) were studied, replacing the two layers of aluminum (7.3 mm thick). The requirement for replacement was to keep the original areal density of the aluminum layers in the Columbus shell (2 g cm^{-2}) to avoid any increment in the structure mass. In fact, the weight of the space module is a fundamental parameter for its design, which has economical and structural impact in the mission's planning. The thicknesses of the mass-equivalent materials were calculated accordingly to their densities and illustrated in Table 7.1. Shells were irradiated with both monoenergetic beam (70, 150 and 230 MeV) and full spectrum of GCR, SPE and Trapped protons in the energy range 70-230 MeV.

Unfortunately, due to unavailable correct thickness of the HDPE slab to replace aluminum in the pressurized shell, the areal density occurred not to be the same as aluminum. The available HDPE sample had a thickness of 120 mm, meaning an areal density of 11.28 g cm^{-2}. Nevertheless, it was considered useful to study the influence that a small amount of carbon fiber causes when a hydrogenated material is irradiated with protons, whether improves or compromises the shielding properties. Two configurations were irradiated with 150 and 230 MeV mono-energetic beams: the "120 mm HDPE", and the "120 mm HDPE + 1 mm CF" configurations, which can be seen in Figure 7.3.

Table 7.1. Thicknesses and corresponding areal densities of materials corresponding to layers 1 and 4 in the pressurized shell.

Material	Thickness (mm)	Areal density (g cm^{-2})
Aluminum	7.3	2
PMMA	17	2
CF	12.5	2
HDPE	*120*	*11.28*
HDPE + CF	*120 + 1*	*12.88*

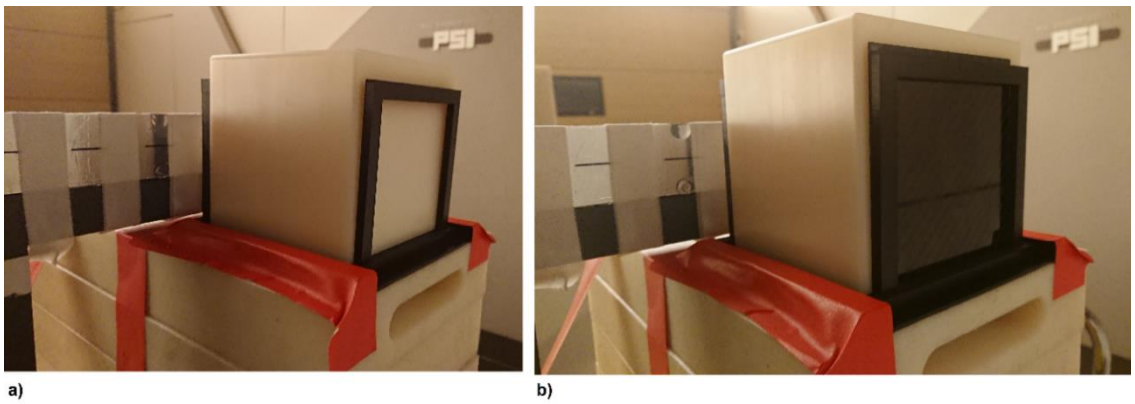

Figure 7.3. Example of the "120 mm HDPE" configuration (a) and the "120 mm HDPE + 1 mm CF" configuration (b).

For completeness, in Table 7.2 we report all configurations cited above with the corresponding sequence of layers (layer 1 is the one downstream) irradiated with different pencil beams.

Table 7.2. All different configurations investigated in this study irradiated with different pencil beams energies and fluences.

Configuration	Layers	Beam
"No wall"	-	150, 230 MeV – GCR, SPE, Trapped spectrum
"Full wall"	1-2-3-4-5-6	150, 230 MeV – GCR, SPE, Trapped spectrum
"Inside spectrum – no wall"	-	GCR, SPE, TRAPPED spectrum
"Al shell"	1-2-3-4	70, 150, 230 MeV – GCR, SPE, Trapped spectrum
"CF shell"	1-2-3-4	70, 150, 230 MeV – GCR, SPE, Trapped spectrum
"PMMA shell"	1-2-3-4	70, 150, 230 MeV – GCR, SPE, Trapped spectrum
"7.3 mm Al"	1-4	SPE, Trapped spectrum
"12.5 mm CF"	1-4	SPE, Trapped spectrum
"120 mm HDPE"	1-4	150, 230 MeV
"120 mm HDPE + 1 mm CF"	1-4	150, 230 MeV

7.3 Results and Discussions

7.3.1 Angular dependency study

Figure 7.5 shows the microdosimetric spectra obtained at various angles for protons spot beam of three energies of interest, 70, 150 and 230 MeV. It can be seen that that the microdosimetric spectra obtained at 90° are characterized by microdosimetric spectra, which are shifted to higher lineal energy compared to all the other angles. This is due to the incoming beam hits the microdosimeter SVs laterally and deposited energy into multiple SVs coincidently. When protons traverse multiple SVs connected in parallel at 90°, the energy deposition multiplies and it is counted as part of a single event. This is confirmed for 70 MeV protons in Figure 7.5c where the average quality factor and the dose equivalent trends are shown. Moreover, when protons pass through the edge of the DIL package before reaching the SVs, the interaction reduces the energy of protons and increases their LET. The interaction is more pronounced for protons with low energy such as 70 MeV which resulted much more broad with a wide low peak above 10 keV/µm, compared to cases of 150 and 230 MeV.

At 90°, the value of $\bar{Q}$ for 70 MeV is 3.34, meaning more than twice higher compared to the values of around 1.2 for all other angles. According to the ICRP definition of the quality factor depending on LET and/or y [21], for y>10keV/µm the Q increases, which is the case observed for 70 MeV protons and not for 150 and 230 MeV. Consequently, the energy deposition is enhanced at 90° resulting in a higher dose equivalent of 0.57 Sv/Gy compared to doses at other angles around 0.15 Sv/Gy (see Table 7.3).

The dose mean lineal energy $\overline{y_D}$ is also characterized by a sharp increase at 90° where the value jump from a range of 2 – 5 keV/µm to (15.69 ±0.39) keV/µm, as can be seen in Figure 7.6c.

The propagation of high-energy protons such as 150 and 230 MeV is not affected that much compared to 70 MeV protons. The quality factor and the dose equivalent at 90° are essentially the same as for other angles with the lineal energy ranging from 5 – 10 keV/µm. For high-energy proton beams the $\overline{y_D}$ fluctuate around an average value of approximately 6 keV/µm, without considerable variation occurring at 90° (see Table 7.3).

Regarding all other irradiation angles between 0° and 70° and 110° and 180°, the microdosimetric spectra are characterized by a symmetrical behavior without being affected by the presence of the DIL package (see Figure 7.5). The incident angle does not allow the crossing of multiple SVs, hence the path length of particles inside the SVs does not vary, and neither the dose nor the quality factor.

The negligible change in the path length for the two angle ranges (0° – 70°) and (110° – 180°) is confirmed by GEANT4 simulations. In Figure 7.4, the simulated path length of primary protons at various angles of incidence is presented. It can be seen that the mean path length varies slightly between 9.2 to 11.4 µm for angles between 0 to 70° and from 110 to 180°. Between 80° to 100°, the mean path length increases significantly due to protons passing multiple SVs and being scored as a single event.

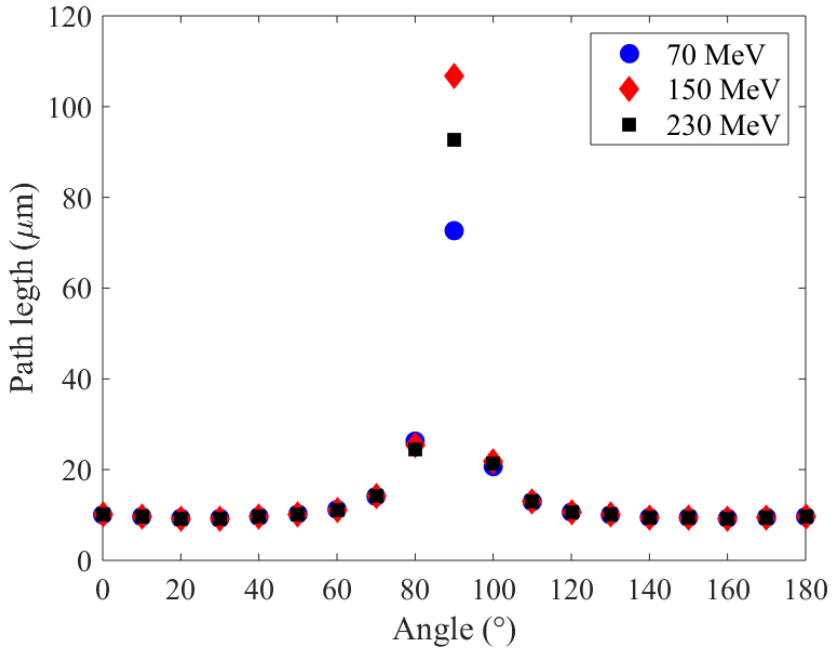

Figure 7.4. Path length distribution calculated by GEANT4 for 70, 150 and 230 MeV protons at various angles of incidence.

In summary, the 90° exposure of protons in an isotropic field is affected by the DIL package of the SOI, measuring a higher value of dose which however does not represent the incident proton field for low energies. Nevertheless, it is important to remind that in space the probability of events occurring at 90° is much lower compared to the totality of events occurring at all other irradiation angles, hence the contribution of the dose at 90° should not distort significantly the veridicity of the whole dose estimation.

The angular dependence of the dose mean lineal energy was demonstrated experimentally and also confirmed by GEANT4 simulation, especially for low energy protons. Therefore, it is important to consider an optimization of the design of the microdosimeter's package to hold the sensor instead of DIL package. For example, a thin layer of kapton with built in contacts could be investigated as possible solution. To totally avoid particles hitting multiple SVs at 90° angle of incidence, individual readout from each SV should be implemented such as pixelated detectors, however the fabrication process will be considerably more complicated due to needing ASIC readout electronics.

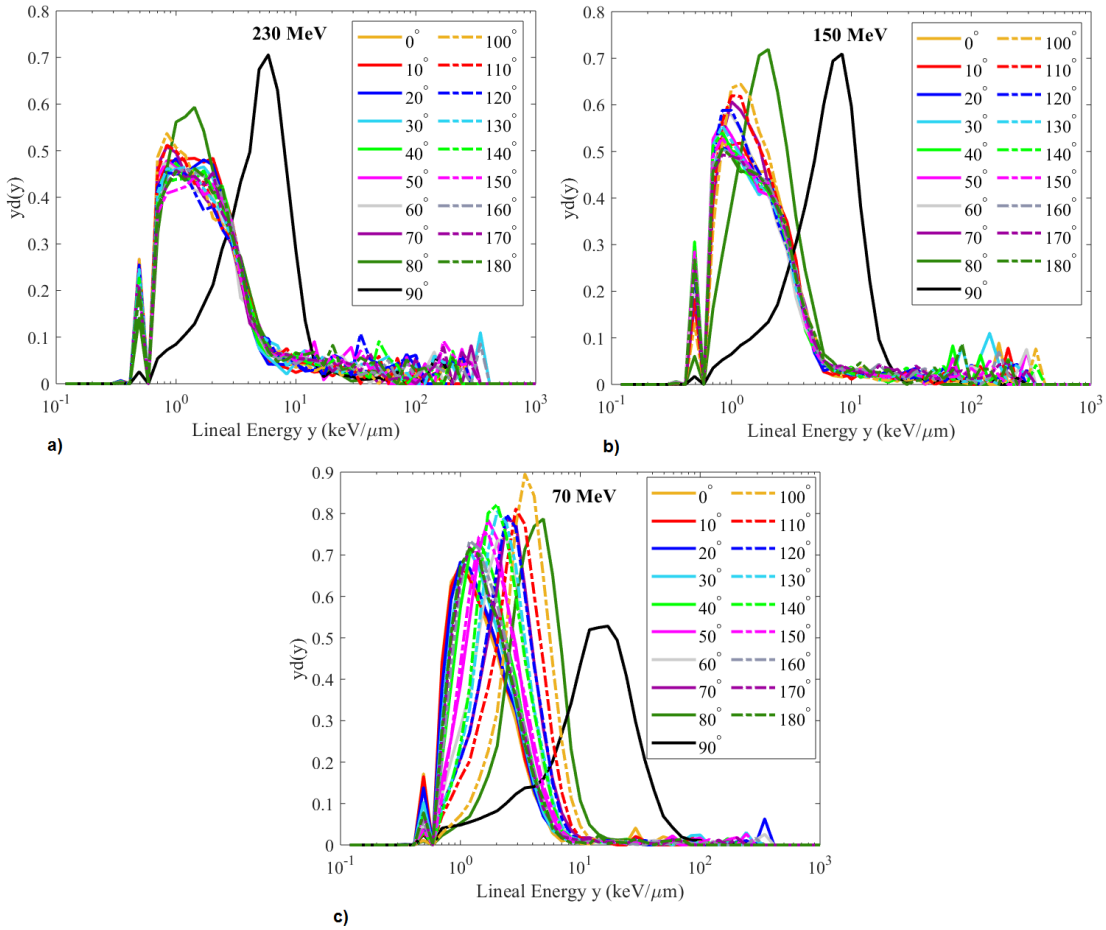

Figure 7.5. Experimental microdosimetric spectra obtained at different angles for a) 230 MeV, b) 150 MeV, and c) 70 MeV proton beams. The gantry was rotated around the SOI microdosimeter from 0° (normal incident to the surface of the microdosimeter) to 180° (normal incident from the back of the microdosimeter) with an angular increment of 10°.

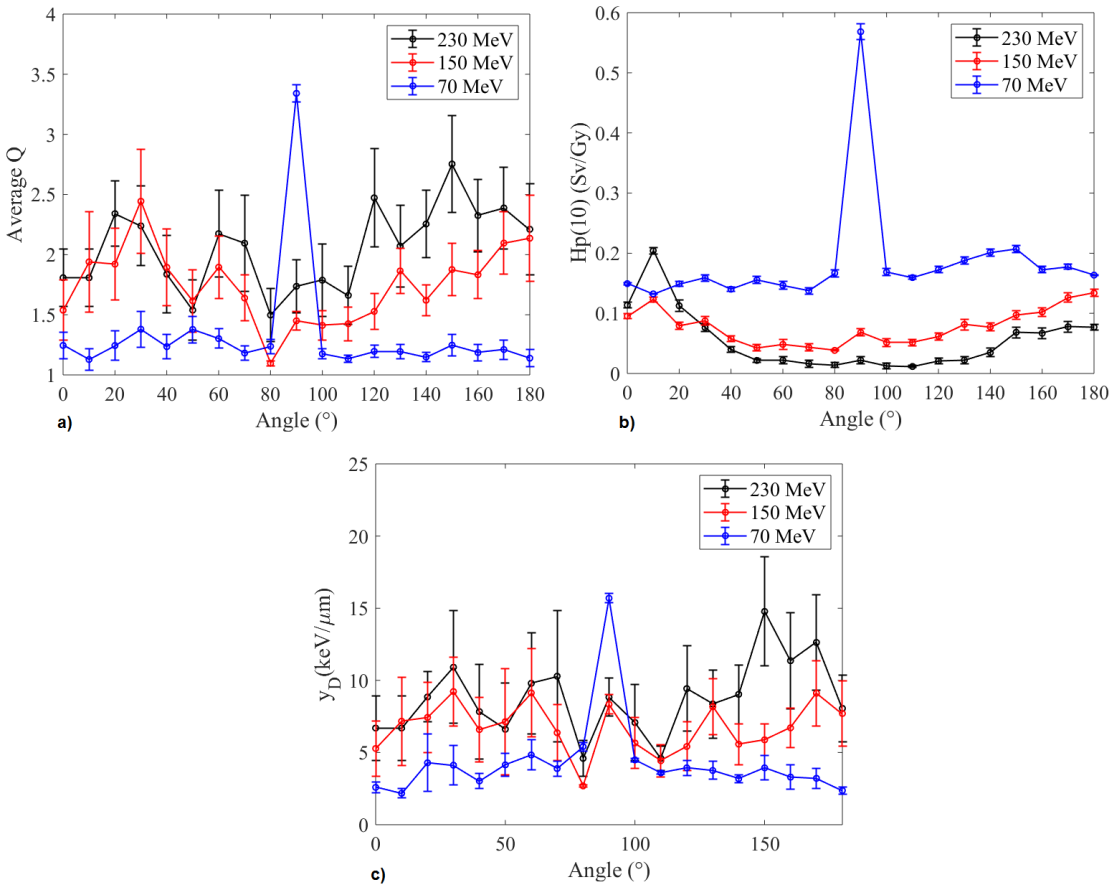

Figure 7.6. a) Trend of the quality average $\bar{Q}$, b) the corresponding dose equivalent $Hp(10)$, c) and the dose mean lineal energy $\overline{y_D}$, for irradiations from 0° to 180° performed with single spot beam at energy of 70, 150 and 230 MeV. The experimental error is show for each irradiations.

Table 7.3. Values of the average quality factor $\bar{Q}$, the dose equivalent $Hp(10)$, and the dose mean lineal energy $\overline{y_D}$ for irradiations performed with 70, 150 and 230 MeV pencil spot beam at various angles. Error range of ± 2%.

	$\bar{Q}$			$Hp(10)\ (Sv/Gy)$			$\overline{y_D}\ (keV/\mu m)$		
Angle (°)	70MeV	150MeV	230MeV	70MeV	150MeV	230MeV	70MeV	150MeV	230MeV
0	1.24	1.54	1.81	0.15	0.10	0.11	2.59	5.28	6.70
10	1.13	1.94	1.81	0.13	0.12	0.17	2.18	7.17	6.70
20	1.24	1.92	2.34	0.15	0.08	0.11	4.29	7.43	8.85
30	1.38	2.44	2.24	0.16	0.09	0.08	4.12	9.23	10.91
40	1.24	1.89	1.84	0.14	0.06	0.04	3.03	6.59	7.83
50	1.38	1.62	1.54	0.16	0.04	0.02	4.15	7.14	6.61
60	1.30	1.90	2.17	0.15	0.05	0.02	4.83	9.13	9.79
70	1.18	1.64	2.10	0.14	0.04	0.02	3.89	6.37	10.29
80	1.24	1.10	1.50	0.17	0.04	0.01	5.41	2.69	4.60
90	**3.34**	**1.45**	**1.74**	**0.57**	**0.07**	**0.02**	**15.69**	**8.34**	**8.83**
100	1.18	1.41	1.79	0.17	0.05	0.01	4.49	5.66	7.08
110	1.13	1.43	1.66	0.16	0.05	0.01	3.59	4.43	4.60
120	1.20	1.53	2.47	0.17	0.06	0.02	3.94	5.42	9.43
130	1.19	1.86	2.07	0.19	0.08	0.02	3.76	8.17	8.36
140	1.15	1.62	2.25	0.20	0.08	0.03	3.18	5.58	9.03
150	1.25	1.88	2.75	0.21	0.10	0.07	3.94	5.88	14.77
160	1.19	1.83	2.33	0.17	0.10	0.07	3.30	6.71	11.36
170	1.21	2.10	2.39	0.18	0.13	0.08	3.21	9.11	12.63
180	1.14	2.14	2.21	0.16	0.13	0.08	2.37	7.70	8.06

7.3.2 Shielding wall configurations study

Figure 7.7 shows the first comparison in terms of experimental microdosimetric spectra, between the two scenarios: outside the Columbus represented by the "No

wall" configuration and inside the Columbus represented by the "Full wall" one. Spectra obtained with a 150 MeV monoenergetic protons beam irradiation show that the presence of the full wall induced a considerable production of secondary particles with lineal energy less than 10 keV/µm, as neutrons, almost tripling the amplitude of the peak compared to the "No wall" peak. This obviously implied a reduction of the average quality factor $\bar{Q}$ but still a larger energy deposited, thus absorbed dose, which reflects in a increase of 11% in the dose equivalent. On the contrary, 230 MeV energetic protons interact with the wall inducing scattering of heavier fragments from the wall, which contribute more to the higher LET region in the spectrum above 10 keV/µm resulting in a higher value of the average quality factor $\bar{Q}$.

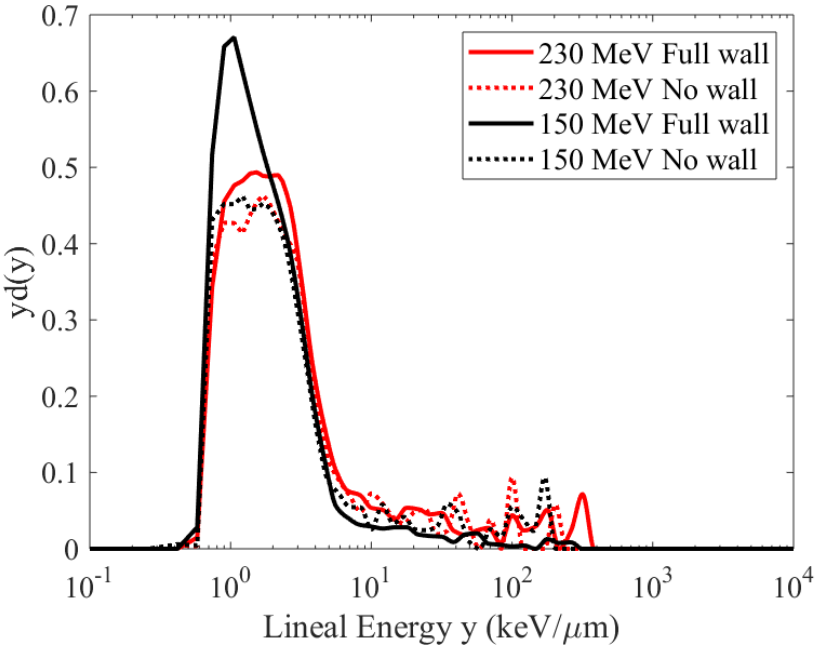

Figure 7.7. Experimental microdosimetric spectra from irradiations with 230 and 150 MeV proton monoenergetic beam, with and without the full Columbus wall.

Similarly, in Figure 7.8 it can be seen the comparison between the "No wall" and the "Full wall" configurations irradiated with the spectral fluence of GCR, SPE

and Trapped protons in a range from 70 to 230 MeV (see Figure 7.1), in one single irradiations.

GCR spectra with and without the wall have a predominant peak at lineal energies below 10 keV/µm, the $\bar{Q}$ is lower but the dose almost unvaried. Spectra derived from irradiation with SPE and Trapped protons in Figure 7.8b-c are very similar to each other due to the same trend of fluence. The presence of high-LET secondary particles generated by protons propagating through the wall causes a slightly increase of the quality factor (see Table 7.4). Since the fluence of SPE and Trapped protons is characterized by a greater abundance of particle of energies closer to the lower edge of the range (70 MeV), the majority of them do not produce high-LET fragments interacting with the shielding wall thus the dose for this configuration is reduced by 60% and 33% for SPE and Trapped protons respectively.

Additionally, in Figure 7.8 the experimental microdosimetric spectra for the "Inside spectrum – no wall" are presented. In this case irradiations were performed using the spectral fluence simulated inside the spacecraft. These spectra are the output of a GEANT4 simulation where the Columbus wall was modeled in its standard full structure, meaning all 6 layers. Details about these simulated spectra can be found in section 6.3.1: their fluence include all primary protons propagating through the Columbus wall and secondary protons produced by the interaction within the shielding materials. Therefore, the experimental set-up for these irradiations does not include the physical sample of the Columbus wall, but sees the SOI microdosimeter directly exposed to the pencil beam. The experimental errors reported in Table 7.4 confirm that values of $\bar{Q}$ and $Hp(10)$ comparable for experiment and simulation results. It has confirmed that the GEANT4 model of the spectral fluence behind the shielding well represent the field of protons generated by the physical shielding sample, thus the resulting microdosimetric spectra are in good agreement.

This result is of important interest because it shows that the experimental irradiations can be performed without a physical sample of the shielding material under study, at the condition that a preliminary simulation of the field behind such shielding is performed and the output spectral fluence is used as input spectrum to be delivered by the treatment planning system.

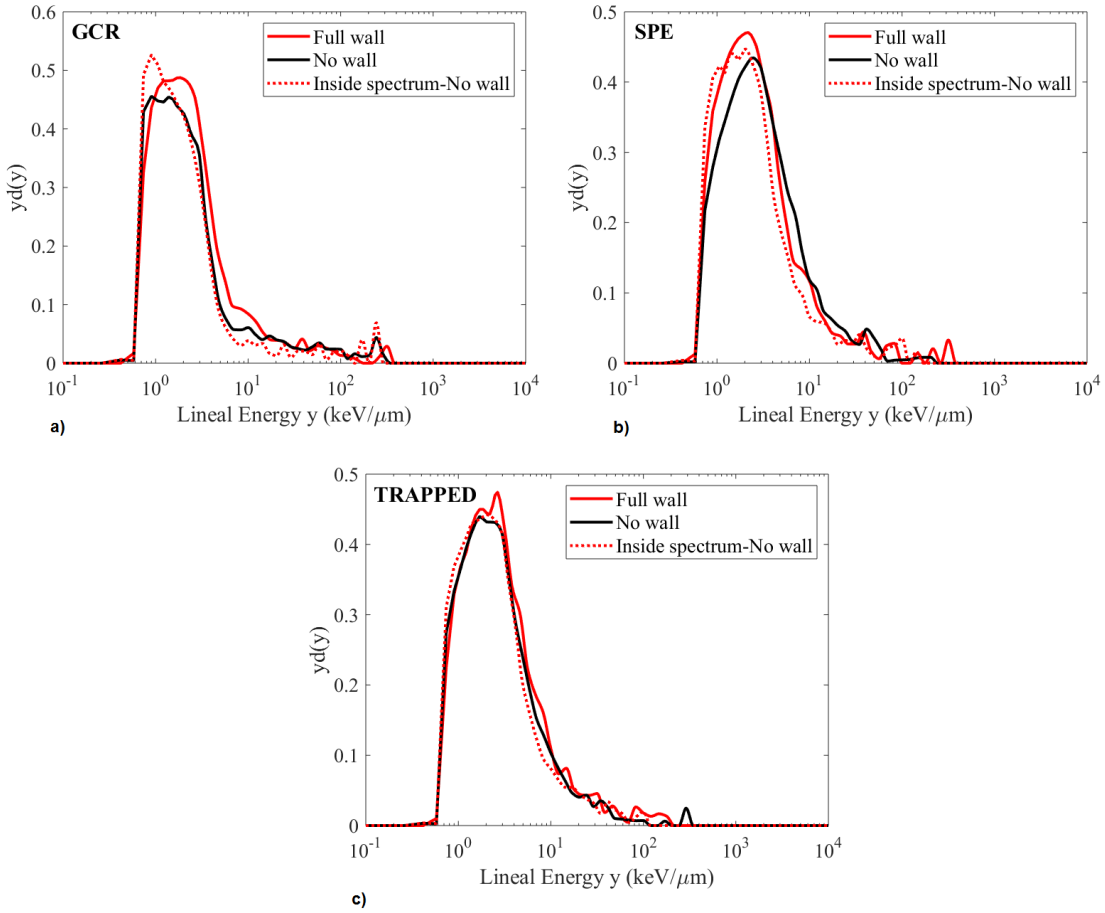

Figure 7.8. Experimental microdosimetric spectra from irradiations with a) GCR, b) SPE and c) Trapped proton spectra in an energy range from 70 to 230 MeV, with and without the Columbus wall. Dots lines represent the microdosimetric spectra obtained delivering the proton fluence spectra typically encountered inside the Columbus, simulated with GEANT4, but without using any kind of shielding sample during experiments.

Table 7.4. Quality factor and dose equivalent values obtained irradiating three configurations ("No wall", "Full wall" and "Inside spectrum – no wall") with 150 and 230 MeV monoenergetic pencil beam and full GCR, SPE and Trapped spectra beams.

	150 MeV		**230 MeV**	
	$\bar{Q}$	$Hp(10)$ (Sv/Gy)	$\bar{Q}$	$Hp(10)$ (Sv/Gy)
"No wall"	2.40	0.55	2.14	0.42
"Full wall"	1.39	0.61	2.49	0.50

	GCR		**SPE**		**Trapped**	
	$\bar{Q}$	$Hp(10)$ (Sv/Gy)	$\bar{Q}$	$Hp(10)$ (Sv/Gy)	$\bar{Q}$	$Hp(10)$ (Sv/Gy)
"No wall"	2.02	0.33	1.59	0.45	1.46	0.43
"Full wall"	1.83±0.13	0.34±0.09	1.76±0.20	0.18±0.06	1.77±0.13	0.29±0.07
"Inside spectrum – no wall"	1.89±0.22	0.40±0.11	1.67±0.14	0.43±0.07	1.48±0.09	0.40±0.07

The microdosimetric spectra obtained from irradiations of different pressurized shell configurations are shown in the following Figure 7.9 and Figure 7.10. Irradiations with 150 and 230 MeV monoenergetic beam are characterized by a similar shape of the microdosimetric spectra. High-energy protons produce neutrons during inelastic collisions with the spacecraft shell materials together with secondary particle as helium nuclei ejected by the shielding materials. These fragmentation events can be seen in the tail region of the spectra (lineal energy from 20 to 380 keV/µm). Additionally, neutrons generate recoil protons via interaction with PMMA converter that lead to have a wide peak at lineal energies below 10 keV/µm. While comparing different shell configurations, the "PMMA shell" configuration confirms its better properties for radiation protection as the dose equivalent is reduced to 50% and 36% of the dose in case of "Al shell" configuration, for 150 and 230 MeV protons respectively (see Table 7.5). Meanwhile for monoenergetic beams, particularly 70 and 150 MeV, the "CF shell" configuration is characterized by a dose equivalent around 30% higher than the one resulted from the irradiation of the "Al shell" configuration, whereas the use of CF reduced the dose of 30% for higher energy proton beam of 230 MeV.

When compared to a 150 MeV proton irradiation, the microdosimetric spectra obtained from 70 MeV protons happen to have a more defined peak, typical of primary particles traversing the shell without undergoing many inelastic reactions.

The “CF shell” configuration shows just a limited variation in terms of energy spectrum compared to the “Al shell” configuration: the peak shifted slightly to higher LET but not enough to have a consistent contribution of events above 10 keV/µm that will lead to an higher average quality factor, according to the ICRP Publication 60 definition [21]. The “PMMA shell” configuration is more efficient in slowing down the incoming protons: the downstream tail of the peak crosses the threshold of 10 keV/µm falling in the case where even a small increment of the quality factor (10%) still doubles the value of the dose equivalent (see Table 7.5Table 7.5). A few events can be seen in the region of LET above 100 keV/µm, and can be identified as the main responsible of the dose equivalent increase.

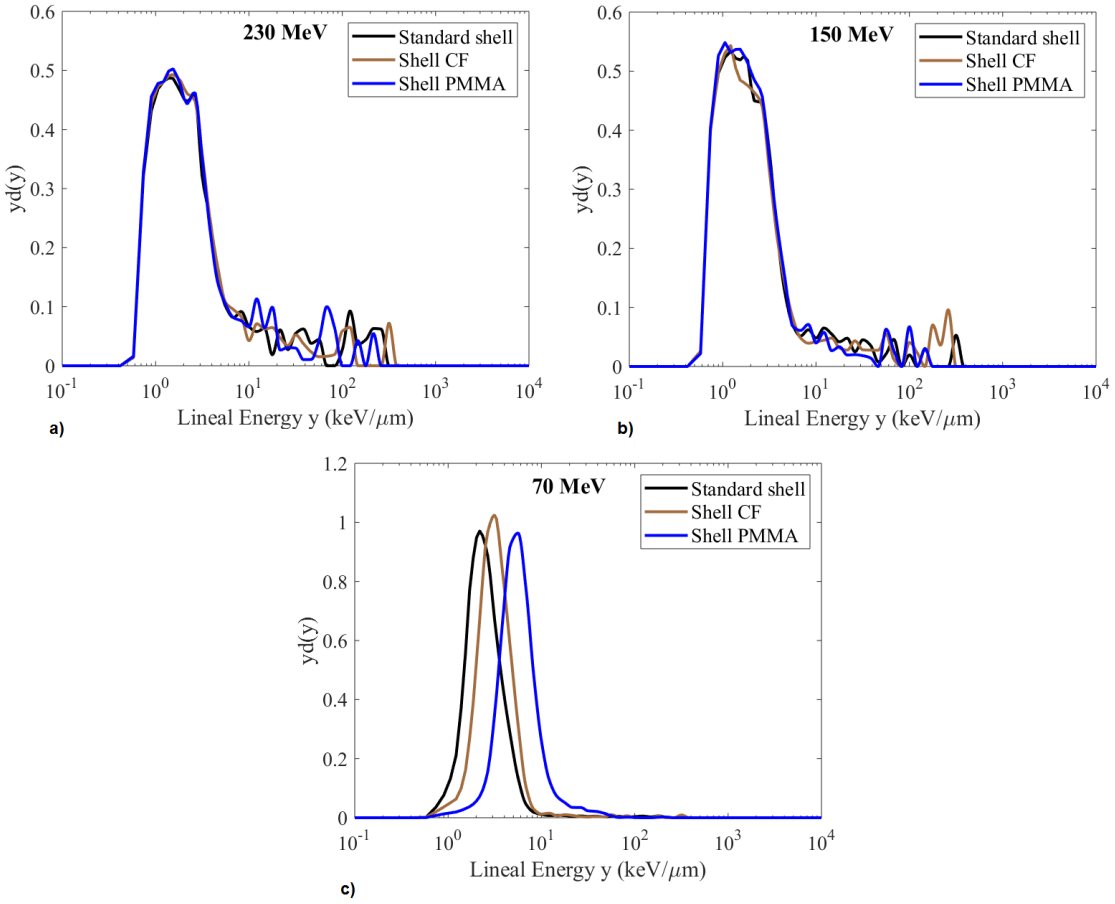

Figure 7.9. Microdosimetric spectra obtained from irradiations of different shell configurations with a) 230, b) 150 and c) 70 MeV mono-energetic proton beams.

Figure 7.10 shows the microdosimetric spectra obtained while irradiating different configurations of the pressurized shell with the GCR, SPE and Trapped protons spectra in the energy range 70 - 230 MeV. GCRs fluence is characterized by a considerably sharp increase in contribution of protons with kinetic energy above 150 MeV as represented in Figure 7.1a, thus the microdosimetric spectra in this case have similar shape to the microdosimetric spectra obtained with 150 and 230 MeV monoenergetic beams. The broad peak below 10 keV/µm results from the recoil protons produced by neutrons coming from inelastic interactions with the materials of the pressurized shell. Higher LET fragments produce the high lineal energy tail, up to hundreds keV/µm. The average quality factor $\bar{Q}$ resulting from GCR is in a range of 1.88 – 2.14, which agrees with the quality factor values found for monoenergetic beams of 150 MeV ($\bar{Q}$:1.86-2.55) and 230 MeV ($\bar{Q}$: 2.37-2.95). Obviously, in the case of GCR multi-energies spectrum, the average value of $\bar{Q}$ is also affected by the contribution of protons whose energies are below 150 MeV.

The fluences of SPE and Trapped protons have a different trend than the fluence of GCR. Trapped protons' fluence has almost linear descending trend along the energy spectrum and SPE fluence exponentially descends until 150 MeV, followed by a slow logarithmic ascension (see Figure 7.1). In both cases, the maximum value of the fluence is observed at 70 MeV, and as a consequence of the integral of the spectrum, we can observe that more than half of protons in the spectrum have energy below 150 MeV. Comparing the microdosimetric spectra obtained from irradiations with SPE and Trapped protons in Figure 7.10b-c with the microdosimetric spectra obtained with a monoenergetic beam of 70 MeV (see Figure 7.9c), we can identify a clearer Gaussian shape in the peak of the spectrum with less fragments at higher lineal energies. In this case, the majority of hadronic interactions are elastic scattering without emission of fragments from the pressurized shell's materials. This reflects in the quality factor being lower for SPE and Trapped protons, in a range of 1.39 – 1.45, and 1.47 – 1.75 respectively, and closer to the values of $\bar{Q}$ 1.16 - 1.28 obtained for 70 MeV beam (see Table 7.5).

Looking at the effects of using different materials such as CF and PMMA instead of aluminum in the pressurized shell, it can be concluded that for a spectrum between 70 and 230 MeV, of GCR, SPE and trapped protons, nor CF nor PMMA

bring substantial benefit, as the does equivalent did not vary essentially and still be in the experimental error range ±0.1 Sv/Gy.

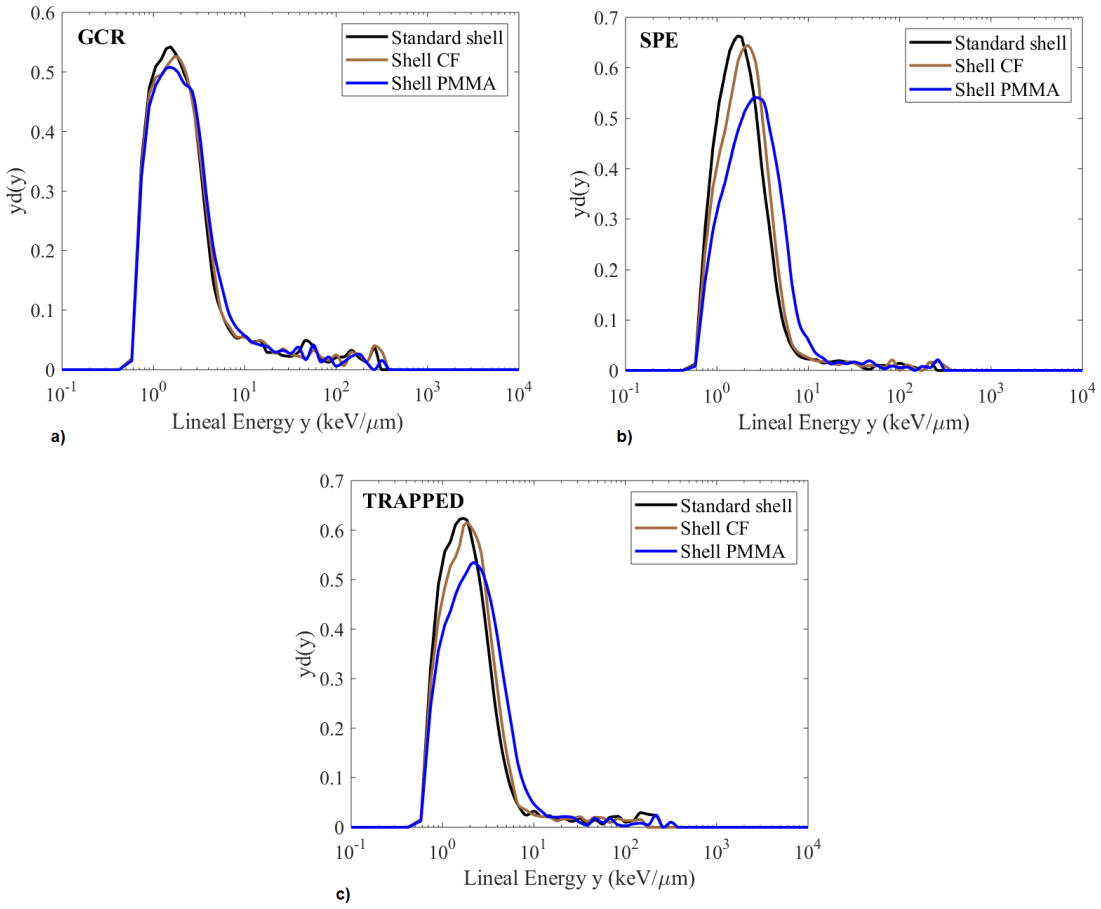

Figure 7.10. Experimental microdosimetric spectra obtained from irradiations of different pressurized shell configurations with a) GCR, b) SPE and c) Trapped proton spectra in an energy range from 70 to 230 MeV.

Table 7.5. Quality factor and dose equivalent obtained irradiating three configurations ("Al shell", "CF shell" and "PMMA shell") with 70, 150 and 230 MeV monoenergetic pencil beams and full GCR, SPE and Trapped spectra beams. Error range of $\pm$ 1%.

	70 MeV		**150 MeV**		**230 MeV**	
	$\bar{Q}$	$Hp(10)$ (Sv/Gy)	$\bar{Q}$	$Hp(10)$ (Sv/Gy)	$\bar{Q}$	$Hp(10)$ (Sv/Gy)
"Al shell"	1.17	1.13	1.89	0.77	2.95	1.27
"CF shell"	1.16	1.46	2.55	1.07	2.38	0.89
"PMMA shell"	1.28	2.69	1.86	0.39	2.37	0.46
	GCR		**SPE**		**Trapped**	
	$\bar{Q}$	$Hp(10)$ (Sv/Gy)	$\bar{Q}$	$Hp(10)$ (Sv/Gy)	$\bar{Q}$	$Hp(10)$ (Sv/Gy)
"Al shell"	2.12	0.35	1.39	0.46	1.75	0.50
"CF shell"	2.14	0.37	1.45	0.55	1.51	0.48
"PMMA shell"	1.88	0.34	1.40	0.63	1.47	0.53

As already mention in section 7.2, the unavailable correct thickness of the HDPE block with mass equivalent to the aluminum mass in the pressurized shell, did not allow the irradiation of the "HDPE shell" configuration. However, a thicker block of 120 mm HDPE was irradiated with monoenergetic proton beams and compared with the same block with an additional 1mm thick CF layer. In Figure 7.11 we observe two different outcomes of the irradiations of HDPE: the broad microdosimetric spectra from 230 MeV protons show again the high lineal energy tails of fragments, whereas the microdosimetric spectra from 150 MeV protons have a clearer Gaussian shape typical of primary particles propagating through the materials and reaching the SOI microdosimeter slowing down in energy, without producing a significant number of high LET fragments.

It is interesting to notice that for an incident 150 MeV proton beam, the addition of 1 mm thick of CF in front of the 120 mm HDPE block led to a shift of the peak in the spectrum to higher lineal energy and consequently to an increase of the $\bar{Q}$ and 21% of the $Hp(10)$ (see Table 7.6). Ideally, the addition of CF should not lead to an increase in the dose, because CF is considered a material to be used to strengthen hydrogenated materials with better properties against radiation. Unfortunately, the positive results obtained with 230 MeV is not achieved with 150

MeV, and we can predict that for protons with lower energy than 150 MeV, the dose will experience an increase until protons will be fully stopped by the shield.

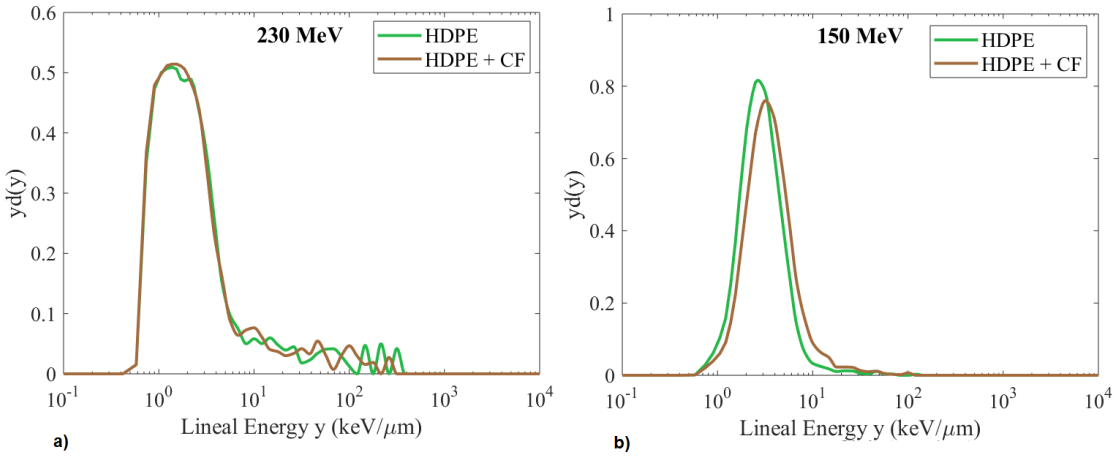

Figure 7.11. Experimental microdosimetric spectra from irradiations of 20 mm thick slab of HDPE and same slab with 1 mm thick sheet of CF downstream the incoming beam, using a) 230 and b) 150 MeV mono-energetic beam.

Similarly, we wanted to compare the shielding efficiency of the single CF layer mass-equivalent to the amount of aluminum in the shell of the Columbus. In Figure 7.12 the comparison is shown in case of irradiation with SPE and Trapped protons spectra. In both cases, the spectra from the "12.5 mm CF" configuration have a peak's amplitude lower than to the one obtained for "7.3 mm Al" configuration. This is due to the normalization to the area of the spectrum to 1 and a higher statistics of events at high lineal energy reduce the amplitude of the peak at lower lineal energies. Thus CF incurred in more fragmentation when irradiated

with protons, which consequently, due to the higher LET increase the value of the avegare quality factor and of the dose equivalent as can been seen in Table 7.6.

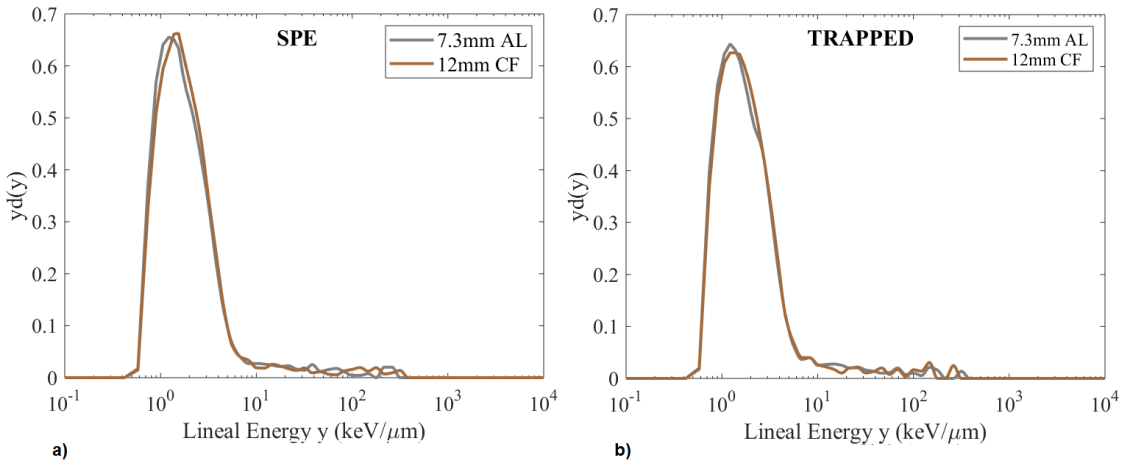

Figure 7.12. Experimental microdosimetric spectra from irradiations of 7.3 mm Al and 12 mm CF with a) SPE and b) Trapped proton spectra in an energy range from 70 to 230 MeV.

Table 7.6. Quality factor and dose equivalent obtained irradiating four configurations ("7.3 mm Al", "12.5 mm CF", "120 mm HDPE" and "120 mm HDPE + 1 mm CF") with 150 and 230 MeV monoenergetic pencil beams and full SPE and Trapped spectra beams. Error range of ± 1%.

	SPE		**Trapped**	
	$\bar{Q}$	$Hp(10)$ (Sv/Gy)	$\bar{Q}$	$Hp(10)$ (Sv/Gy)
"7.3 mm Al"	1.53	0.42	1.55	0.37
"12.5 mm CF"	1.64	0.49	1.61	0.42
	150 MeV		**230 MeV**	
	$\bar{Q}$	$Hp(10)$ (Sv/Gy)	$\bar{Q}$	$Hp(10)$ (Sv/Gy)
"120 mm HDPE"	1.11	1.82	2.26	0.96
"120 mm HDPE + 1mm CF"	1.20	2.31	2.24	0.95

7.4 Conclusions

This study investigated the shielding properties of the Columbus shielding wall against proton field, and the angular dependence of the microdosimeter response for

irradiation from 0° to 180°, as a representation of the isotropy of the proton field in space. The irradiations were performed with monoenergetic pencil scanning beam of 70, 150 and 230 MeV and also with spectral fluence of GCR, SPE and Van Allen belts protons encountered at the ISS altitude, with energy range between 70 MeV and 230 MeV.

The microdosimeter was placed at the isocenter in a free standing position and was encapsulated by a cylindrical PMMA sheath 10 mm thickness and irradiated at different angle by the rotating gantry to allow the evaluation of the dose eqivalent $Hp(10)$ for protons incident at different angles.

To mimic the isotropic exposure in space the microdosimeter was irradiate at angles from 0° to 180° with 10° increment, initially with mono-energetic beam of 70, 150 and 230 MeV. The angular dependence study showed that the response of the μ^+ probe in a proton scanning beam is reasonably uniform for most angles between 0º and 70º and 110º to 180º. Near 90º, an overestimation of lineal energy and $\overline{y_D}$ were observed due to protons hitting multiple SVs and the quantities calculated with a constant chord length. This was confirmed by the mean path length of primary particles in the field calculated by the GEANT4 simulation. The effect is observed predominantly for low energy proton of 70 MeV, whereas for 150 and 230 MeV, the quality factor, the dose equivalent and the dose mean lineal energy slightly fluctuate.

Concerning the characterization of the proton field behind different shielding configuration of the Columnbus, the spectral fluences of GCR, SPE and Van Alle belts were modeled following the methodology discussed in the previous chapter, by programming the Treatment Planning System of the proton therapy accelerator at PSI. For completeness and comparison, irradiations with monoenergetic scanning beams of 70, 150 and 230 MeV were performed. Alternative materials with expected better shielding radiation properties were considered for replacement of the aluminum present in the Columbus shield design. Carbon fiber, Perspex and high density Polyethylene were selected.

For each configuration of interest the quality factor $\bar{Q}$ and the personal dose equivalent $Hp(10)$ per unit of absorbed proton dose in water at the isocenter were evaluated for radiation protection purposes.

Results are interesting in terms of characterization of the field of mixed charged particles generated by primary protons. Some materials happen to incurr into more fragmentation than others, depending also on the enrgy of the incident protons. Hence, the variety of results, controversial time to time, do not lead to take a final certain decision regarding the use of such materials instead of the currently used aluminum. The full energy range of the GCR, SPE and trapped protons should be considered to draw any conclusion in terms of shielding. In addition, also cosmic alpha particles and HZE ions should be modelled as well. Thus, further experiments will be carried out in the future, but not included in this thesis because of limited time.

This study demonstrated for the first time that irradiations with a wide spectral fluence should be considered instead of monoenergetic beams, to mimic a more realist scenario encountered in space. SOI microdosimeters are powerful devices to perfom such test and provide qualitative and quantitative informations for radiation protection of humans in space.

Finally, the methodology discussed in Chapter 6 and used in this one, the modelling of cosmic radiation by means of medical hadrontherapy beam lines, can be considered as a first, convenient, ready to use, step to model at least partially radiation environments which are not nowadays physically accessible, like the Lunar and the Martian ones. The The synergy of Monte Carlo simulation tools and the capability to model at least partially radiation environements in particle accelerators faclities, can be very effective to investigate future spacecraft and habitat's designs will be extremely helpful for the planning of future human space missions.

Chapter 8

Conclusions

This thesis presented a study concerning radiation protection in space and aviation by using microdosimetric approach and last generation SOI microdosimeters, developed at the Centre for Medical Radiation Physics, University of Wollongong. Particular attention was devoted to the latest designs of the 3D SOI "Mushroom" microdosimeter, characterized by a large array of 3D free-standing cylindrical sensitive volumes (SVs), suitable for low-flux rate environments like the space and aviation ones. The performances of the SOI microdosimeters were investigated by simulation and experiments against heavy ions and protons fields.

Initially, a GEANT4 model was implemented to simulate the radiation environment at the Low Earth Orbit, were the International Space Station (ISS) hosts astronauts. The particle fluxes of the main sources of cosmic radiation (GCR protons and alpha particles, SPE protons and protons and electrons trapped in the Van Allen Belts) were simulated outside and inside the ISS. In particular, the Columbus module geometry was simulated according to specifications regarding the materials that constitute the shielding wall that we found in the literature. Clearly, primary particles with energy above 100 MeV/u were not fully stopped by the shielding wall, instead they propagated through, reaching the inside of the habitat. The secondary particle field produced by the incident radiation while propagating through the Columbus shielding materials was characterized in terms of particle type, energy and fluence. Neutrons and alpha particles were the main radiation components produced in spallation reactions by incident ions and protons with energies of hundreds of MeV/u. Several heavier ions and their isotopes such as carbon, oxygen, aluminum emerged from the Columbus structure as well.

The “Mushroom” microdosimeter’s response was evaluated by placing it inside the Columbus module of the ISS. The radiation field was characterized in terms of quality factor, and the dose equivalent to an astronaut was calculated for a 1-day mission. Simulated results showed a good agreement with experimental data obtained from measurements performed onboard the ISS, confirming the validity of the GEANT4 model.

By using the IBIC technique at the ANSTO heavy ion microprobe facility, the charge collection efficiency (CCE) of two latest designs of the 3D “Mushroom” microdosimeter, 5 and 10 µm thick, were studied against a 5.5 MeV He^{2+} ions scanning beam. GEANT4 simulations were used to evaluate the energy deposited by the ions in the detector geometry. The CCE resulted to be approximately 98% when a bias of 10V was applied. Moreover, the charge appeared to be uniformly collected and the well-defined volume shape of the SV was visualized, demonstrating that the microdosimeter was ready to be tested in irradiation facilities.

Therefore, the response of a SOI “Mushroom” microdosimeter was investigated first with heavy ions at HIMAC (Chiba, Japan). Two types of ions were selected as representative of the medium and high LET component of GCRs, 400 MeV/u ^{16}O ions and 500 MeV/u ^{56}Fe ions, respectively. Measurements were performed in a free air geometry and in a water phantom with and without the presence of two aluminum slabs (7.3 and 35.95 mm thick) representing only the pressurized shell and the full amount of aluminum including the out-fitting of the Columbus module. Concerning the free-air geometry measurements, the microdosimeter was covered by PMMA converters 0.07 and 10 mm thick as representation of the body of an astronaut that should be considered for the evaluation of dose equivalent. The dose equivalent at skin level, 0.07 mm deep in the body $Hp(0.07)$, and the dose equivalent at 10 mm depth in the body $Hp(10)$ were the two operational quantities used for personal monitoring studies.

The results showed that 400 MeV/u ^{16}O ions are not fully stopped by none of the aluminum slabs: the primary ions slowed down in energy and the LET increased, leading to an increase of the mean quality factor $\bar{Q}$. As results of the convolution with the absorbed dose, the dose equivalent increased as well.

On the contrary, 500 MeV/u ^{56}Fe ions were stopped by the 35.95 mm thick slab, and produced a not negligible amount of fragments in a broad spectrum of LET, that averagely led to a reduction of the $\bar{Q}$ and thus of the dose equivalent.

The average quality factor and the dose equivalent at different depths in the body of an astronaut inside and outside the spacecraft were calculated by performing measurements in a water phantom. For both irradiations with oxygen and iron ions, the scenario inside the spacecraft is characterized by a higher dose equivalent at more shallow depths in the body. The presence of a thin slab of aluminum caused a shift of the Brag peak in correspondence to organs which are located more superficially below the skin. These results gave an initial idea of how the same organ in the astronaut body will receive a different dose equivalent exposure if the astronaut was inside or outside the spacecraft (i.e. during an Extra-Vehicular Activity). For example, the dose equivalent observed for 500 MeV/u ^{56}Fe ions exposure of tissues at 4 cm depth is 2 times higher when the astronauts is inside the Columbus rather that outside. It should be noted that these conclusions depend on the energy spectra and type of ions, thus is difficult to predict accurately the outcome for other ions and energies, which are present in space. Monte Carlo simulations should be performed in the next stage of this research to investigate the dose equivalent due to the space radiation environment, which can't be reproduced with current accelerator technology on Earth.

As part of this experimental campaign, out-of-field measurements were carried out in water phantom to evaluate the exposure to nearby tissues. From the analysis of the microdosimetric spectra obtained at 2.5, 3.5 and 5.5 cm away from the beam central axis, it can be observe the abundance of low lineal energy secondary particles scattered away. The dose equivalent measured at the entrance of the water phantom was similar in and out of the field, whereas approaching the Bragg peak depth the dose equivalent out-of-field decreased. The difference is due to the tail of high LET secondary particles that are more pronounced at the entrance of the phantom.

Even though the aluminum is considered as the main responsible of production of fragments and other secondaries particles while incident cosmic rays propagate through it, it is important to consider the full shielding structure of a spacecraft. For this reason, a more detailed study of the multi-layer structure of the shielding

wall of the Columbus module was done at HIMAC. The Columbus wall consists in two main parts: the pressurized shell that represents the real supporting structure, and an ad-hoc extra block of materials called the Out-fitting. The Out-fitting represents the payload of all structures and devices inside the habitat of the Columbus that do not contribute to bring strength and mechanical properties to the structure of the module, but they can provide an extra barrier against incoming radiation. The Columbus wall was irradiated with the following ions: 180, 230 and 490 MeV/u ^{28}Si, 400 MeV/u ^{20}Ne, and 290 MeV/u ^{12}C. The Out-fitting resulted to be source of secondary particles that induced a doubling of the dose equivalent inside the Columbus compared to the dose that an astronaut would have received outside during an EVA.

It was decided to use alternative materials with low Z/A ratio in replacement of aluminum such as Poly(methyl-methacrylate) (PMMA), Polyoxymethylene (POM), and Carbon Fiber (CF) as a representation of graphene suggested in the literature. Configurations of the full shielding wall, and the pressurized shell only, were iradiated with layers of such innovative materials, keeping the same mass as aluminum. It was observed that the shielding effciency not always improved, depending on the type of ion and energy. This motivates to continue the study of materials with several ions that can cover a biggest portions of the full spectrum of GCR in space.

In particular, when PMMA was used as replacement of aluminum in the full wall configurations, the dose equivalent increased when irradiated with 490 MeV/u ^{28}Si, 400 MeV/u ^{20}Ne and 290 MeV/u ^{12}C. However, a similar polymer to PMMA, the high density polyethylene was confirmed to be the best suggested alternative to aluminum found in the literature, in terms of radiation shielding. Its lack of mechanical strength must be compensated by incorporating carbon nanotubes and graphene. The radiation shielding properties of carbon fiber were then studied and results showed benefits in terms of dose equivalent reduction only in some configurations when the pressurized shell was irradiated with 180 and 230 MeV/u ^{28}Si, but not when irradiated with 290 MeV/u ^{12}C. Another hydrogenated polymer POM was irradiated and confirmed its high capability of reducing dose equivalent suggesting its use in composite materials to strength it.

Hence, the variety of results does not allow judging definitively the shielding performances of these innovative materials. It is needed to perform simulation in the space radiation environment where the entire spectrum of ions and energies will be use to investigate the properties of carbon fiber and hydrogenated polymers.

The experiments at HIMAC demonstrated that the SOI "Mushroom" microdosimeter has a powerful ability to be used during test in ground-based facilities to promptly investigate the quality of a radiation field behind any desirable shielding material and configuration for the optimization of spacecraft design.

As the main component of radiation in space is represented by high-energy protons, the 3D "Mushroom" microdosimeter was tested with a proton field with energy range between 70 and 230 MeV. The studies were conducted at the proton thrapy centre PSI in Switzerland, where the medical accelerator was used to deliver a scanning beam. Two important costraints encountered while performing tests in ground-based facilities were investigated: the limitation of using mon-energetic beams and the mono-directional irradiation.

Firslty, to mimic the isoptropic exposure typical of space, the gantry inside the irradiation room rotated around the microdosimeter that was placed at the isocenter. The angular dependence of its repsonse was studied from 0° to 180° with 10° increment, with mono-energetic proton beams of 70, 150 and 230 MeV. Results showed a reasonably uniform response in terms of dose-mean lineal energy $\overline{y_D}$ for all angles except for 90°. At 90° an overestimation of the $\overline{y_D}$ occurred due to protons passing through multiple consecutive SVs that deposited more energy in many steps but they are counted as one. A GEANT4 simulation confirmed the results as the path length of particles was a factor 2 or 3 higher at 90° compared to other angles. Another confirmation came from the microdosimetric spectra for the 70, 150 and 230 MeV proton beam irradiations at all angles between 0° and 180° that happended to have a similar braod peak at low lineal energies. Instead, for the 90°, the spectra shifted to higher lineal energies due to the higher energy deposited in multiple SVs. A solution to avoid the overestimation of the dose equivalent associated to events hitting the microdosimter at 90° would be to implement individual readout from each SV similarly to the case of pixelated detectors. However, the fabrication process

will considerably become more complicated due to the ASIC readout electronics needed.

To represent the poly-energetic radiation environment, it was introduced a methodology to program the treatment planning system (TPS) of the clinical accelerator to deliver a beam modulated on the spectral fluence typically encountered in space. The partial proton spectra of GCR, SPE, and Van Allen Belts in the energy range of 70 – 230 MeV that were simulated with GEANT4 inside and outside the ISS, were used as input of the clinical Treatment Planning System. The dose delivered at the isocenter was modulated on those spectra according to the LET of protons. The microdosimeter was irradiated by a continuous scanning beam that covers the entire range of energy 70 – 230 MeV, in one single irradiation. Irradiations with the spectral fluence were done at three angles of interest (0°, 90° and 180°). The proton field inside and outside the ISS was characterized in terms of $\bar{Q}$ and the personal dose equivalent $Hp(10)$ thanks to the 10 mm thick cylindrical PMMA sheath surrounding the microdosimeter.

As similarly done with heavy ions at HIMAC, the Columbus shielding structure was investigated against the proton field modelled as described just above. The irradiations were performed with both monoenergetic beams (70, 150 and 230 MeV) and spectral fluence of GCR, SPE and trapped protons ranging from 70 to 230 MeV. Other than the original multilayer structure of the Columbus, several configurations including carbon fiber, PMMA and high density polyethylene were selected for comparison with the standard aluminum configurations. The variety of results didn't allow to make a final decision on the intrinsic shielding efficiency of such materials, as already said, because it was observed a strong depencency on type of ion and energy.

To conclude, the work presented in this thesis shows how SOI microdosimeters are powerful devices to perfom a wide range of tests and provide qualitative and quantitative information for radiation protection of humans in space and aviation.

The latest designs of the 3D SOI "Mushroom" microdosimeter demonstrated to be capable of characterizing the space radiation environment. They can be used as a tool for studying the shielding efficiency of innovative materials for future

missions' spacecraft an habitat designs. Finally, they can be used on-board spacecraft for real-time monitoring of the dose to be able to alert astronauts of unacceptable levels of exposure due for instance to unpredictable Solar Particle Events.

Future plans include GEANT4 simulation of the shielding efficiency of the studied materials in this thesis by using the entire spectrum of ions and energies encountered in space. Also, simulation should be used to validate extra experimental results obtainable with additional type of heavy ions and energies.

Appendix A

Statement of Contribution of Others

This statement clearly summarises the contribution to the intellectual input from all co-authors for the chapters based on journal articles.

Chapter 2: as first author, I received contribution to the article "*S. Peracchi et al., Modelling of the Silicon-On-Insulator microdosimeter response within 1 the International Space Station for astronauts' radiation protection," Radiation Measurements, vol. 128, 2019"* from J. Vohradsky, S. Guatelli, D. Bolst, L. T. Tran, D. A. Prokopovich, and A. B. Rosenfeld.

Chapter 4: as first author, I received contribution to the article "*S. Peracchi et al., A solid-state microdosimeter for dose and radiation quality monitoring for astronauts in space, IEEE Trans. Nucl. Sci., vol. 67, no. 1, pp. 169-174, January 2020"* from L. T. Tran, B. James, D. Bolst, D. A. Prokopovich, J. A. Davis, S. Guatelli, M. Petasecca, M. L. F. Lerch, N. Matsufuji, A. Kok, M. Povoli, M. Jackson, and A. B. Rosenfeld.

Chapter 5: as first author, I received contribution to the article "*S. Peracchi et al., Radiation shielding evaluation of spacecraft walls against heavy ions using microdosimetry, IEEE Trans. Nucl. Sci., 2020*" from B. James, F. Pagani, V. Pan, J. Vohradsky, D. Bolst, D. A. Prokopovich, S. Guatelli, M. Petasecca, M. L. F.

Lerch, S. H. Lee, T. Inaniwa, N. Matsufuji, M. Povoli, A. Kok, M. Jackson, T. Squire, A. B. Rosenfeld, and L. T. Tran,

Chapter 6: as first author, I received contribution to the article "*S. Peracchi et al., Modelling of protons spectra encountered in space using medical accelerator and its microdosimetric characterization, Advance in Space Research"* from B. James, S. Psoroulas, M. Grossmann, D. Meer, D. Bolst, Z. Pastuovic, J. Vohradsky, S. Guatelli, D. A. Prokopovich, M. Petasecca, M. L. F. Lerch, M. Povoli, A. Kok, M. Jackson, A. B. Rosenfeld, and L. T. Tran.

Appendix B

Permission for including published articles

I, Stefania Peracchi, declare that undertaking a thesis based on articles published on peer-review journals, I obtained the publishers' permission to include the published work in the thesis.

Here below, I attached the copy of the permission given for each published article included in this thesis.

Modelling of the Silicon-On-Insulator microdosimeter response within the International Space Station for astronauts' radiation protection

Author: S. Peracchi,J. Vohradsky,S. Guatelli,D. Bolst,L.T. Tran,D.A. Prokopovich,A.B. Rosenfeld

Publication: Radiation Measurements

Publisher: Elsevier

Date: September 2019

IEEE Requesting permission to reuse content from an IEEE publication

A Solid-State Microdosimeter for Dose and Radiation Quality Monitoring for Astronauts in Space

Author: S. Peracchi
Publication: IEEE Transactions on Nuclear Science
Publisher: IEEE
Date: Jan. 2020

Thesis / Dissertation Reuse

The IEEE does not require individuals working on a thesis to obtain a formal reuse license, however, you may print out this statement to be used as a permission grant:

Requirements to be followed when using any portion (e.g., figure, graph, table, or textual material) of an IEEE copyrighted paper in a thesis:

1) In the case of textual material (e.g., using short quotes or referring to the work within these papers) users must give full credit to the original source (author, paper, publication) followed by the IEEE copyright line © 2011 IEEE.
2) In the case of illustrations or tabular material, we require that the copyright line © [Year of original publication] IEEE appear prominently with each reprinted figure and/or table.
3) If a substantial portion of the original paper is to be used, and if you are not the senior author, also obtain the senior author's approval.

Requirements to be followed when using an entire IEEE copyrighted paper in a thesis:

1) The following IEEE copyright/ credit notice should be placed prominently in the references: © [year of original publication] IEEE. Reprinted, with permission, from [author names, paper title, IEEE publication title, and month/year of publication]
2) Only the accepted version of an IEEE copyrighted paper can be used when posting the paper or your thesis on-line.
3) In placing the thesis on the author's university website, please display the following message in a prominent place on the website: In reference to IEEE copyrighted material which is used with permission in this thesis, the IEEE does not endorse any of [university/educational entity's name goes here]'s products or services. Internal or personal use of this material is permitted. If interested in reprinting/republishing IEEE copyrighted material for advertising or promotional purposes or for creating new collective works for resale or redistribution, please go to http://www.ieee.org/publications_standards/publications/rights/rights_link.html to learn how to obtain a License from RightsLink.

If applicable, University Microfilms and/or ProQuest Library, or the Archives of Canada may supply single copies of the dissertation.

BACK CLOSE WINDOW

Modelling of protons spectra encountered in space using medical accelerator and its microdosimetric characterization

Author:
S. Peracchi,B. James,S. Psoroulas,M. Grossmann,D. Meer,D. Bolst,Z. Pastuovic,J. Vohradsky,S. Guatelli,D.A. Prokopovich,M. Petasecca,M. L.F. Lerch,M. Povoli,A. Kok,M. Jackson,A.B. Rosenfeld,L.T. Tran

Publication: Advances in Space Research

Publisher: Elsevier

Date: Available online 11 February 2021

Bibliography

[1] R. C. Carrington, "Description of a Singular Appearance seen in the Sun on September 1, 1859," *Monthly Notices of the Royal Astronomical Society,* vol. 20, pp. 13-15, 1859.

[2] A. M. Hillas, *Cosmic Rays* (Selected readings in physics). Oxford, New york: Pergamon Press, 1972.

[3] R. A. Millikan and G. H. Cameron, "The Origin of the Cosmic Rays," *Physical Review,* vol. 32, no. 4, pp. 533-557, 10/01/ 1928.

[4] E. R. Benton and E. V. Benton, "Space radiation dosimetry in low-Earth orbit and beyond," *Nucl Instrum Methods Phys Res B,* vol. 184, no. 1-2, pp. 255-94, Sep 2001.

[5] G. Horneck, "HZE particle effects in space," *Acta Astronautica,* vol. 32, no. 11, pp. 749-755, 1994.

[6] E. R. Benton and E. V. Benton, "Space radiation dosimetry in LEO and beyond," *Nuclear Instruments and Methods in Physics Research B,* vol. 184, no. 1-2, pp. 255-294, 2001.

[7] D. V. Reames, "The Two Sources of Solar Energetic Particles," *Space Science Reviews,* vol. 175, no. 1, pp. 53-92, 2013/06/01 2013.

[8] D. L. Williams, "Measurements of the Isotopic composition of Solar Energetic Particles with the MAST Instrument aboard the SAMPEX Spacecraft," 1998.

[9] T. Ersmark, P. Carlson, E. Daly, C. Fuglesang, I. Gudowska, B. Lund-Jensen, P. Nieminen, M. Pearce, and G. Santin, "Geant4 Monte Carlo Simulations of the Belt Proton Radiation Environment On Board the International Space Station/Columbus," *IEEE Trans. Nucl. Sci.,* vol. 54, no. 4, pp. 1444-1453, 2007.

[10] S. Peracchi, "Cosmic radiation dosimetry: detectors calibration during an on-board experience at commercial flight altitudes and improvement of dose assessment for aircrew members," MSc., Nuclear Engineering, Politecnico of Milan, 2016.

[11] M. B. McElroy, *Ionosphere and magnetosphere*. Encyclopædia Britannica, 2012.

[12] P. Goldhagen, "Overview Of Aircraft Radiation Exposure And Recent Er-2 Measurements," *Health physics,* vol. 79, pp. 526-44, 12/01 2000.

[13] M. Bagshaw and F. Cucinotta, *Cosmic Radiation* (Fundamentals of aeropsace medicine).

[14] P. H. Blard, "Cosmogenic 3He and 10Be in mafic phenocrysts: analytical improvements, calibration and new applications," 06/30 2006.

[15] M. A. Shea and D. F. Smart, "Worldwide trajectory-derived vertical cutoff rigidities and their application to experimental measurements," *Journal of Geophysical Research (1896-1977),* vol. 72, no. 7, pp. 2021-2027, 1967.

[16] D. F. Smart and M. A. Shea, "World Grid of Calculated Cosmic Ray Vertical Cutoff Rigidities for Epoch 2000.0," presented at the 30th International Cosmic Ray Conference, Mexico, 2007.

[17] T. Yeeram, "A study of galactic cosmic ray modulation in the negative solar magnetic cycles: solar cycles 21/22 and 23/24," 2018, vol. 42, pp. D1.3-40-18.

[18] C. Mertens, J. Wilson, S. Blattnig, B. Kress, J. Norbury, M. Wiltberger, S. Solomon, and W. K. Tobiska, "Influence of Space Weather on Aircraft Ionizing Radiation Exposure," *46th AIAA Aerospace Sciences Meeting and Exhibit,* 01/07 2008.

[19] National Research Council, *The Sun to the Earth and Beyond: A Decadal Research Strategy in Solar and Space Physics*. The National Academies Press, 2003.

[20] N. A. Schwadron, A. J. Boyd, K. Kozarev, M. Golightly, H. Spence, L. W. Townsend, and M. Owens, "Galactic cosmic ray radiation hazard in the unusual extended solar minimum between solar cycles 23 and 24," *Space Weather,* vol. 8, no. 5, pp. n/a-n/a, 2010.

[21] International Commission on Radiological Protection, "ICRP Publication 60: 1990 Recommendations of the International Commission on Radiological Protection," in "Annual of the ICRP," 1991, vol. 21.

[22] United Nations Scientific Committee on the Effects of Atomic Radiation, "Sources and Effects of Ionizing Radiation," 2008, vol. 1.

[23] International Commission on Radiological Protection, "ICRP Publication 132: Radiological Protection from Cosmic Radiation in Aviation," in "Annals of the ICRP," 2016, vol. 45.

[24] P. Beck, M. Latocha, S. Rollet, and G. Stehno, "TEPC reference measurements at aircraft altitudes during a solar storm," *Advances in Space Research,* vol. 36, no. 9, pp. 1627-1633, 2005.

[25] M. Latocha, M. Autischer, P. Beck, J. F. Bottolier-Depois, S. Rollet, and F. Trompier, "The results of cosmic radiation in-flight TEPC measurements during the CAATER flight campaign and comparison with simulation," *Radiat Prot Dosimetry,* vol. 125, no. 1-4, pp. 412-5, 2007.

[26] C. A. Federico, O. L. Gonçalez, L. V. E. Caldas, M. T. Pazianotto, C. Dyer, M. Caresana, and A. Hands, "Radiation measurements onboard aircraft in the South Atlantic region," *Radiation Measurements,* vol. 82, pp. 14-20, 2015.

[27] L. Tommasino, R. K. Jain, D. O'Sullivan, A. V. Prokofiev, N. L. Singh, A. N. Smirnov, S. P. Tripathy, and P. Viola, "Cosmic-ray neutron spectrometry by solid state detectors," *Radiation Measurements,* vol. 36, no. 1-6, pp. 307-311, 2003.

[28] J. F. Bottollier-Depois, F. Trompier, I. Clairand, F. Spurny, D. Bartlett, P. Beck, B. Lewis, L. Lindborg, D. O'Sullivan, H. Roos, and L. Tommasino, "Exposure of aircraft crew to cosmic radiation: on-board intercomparison of various dosemeters," *Radiat Prot Dosimetry,* vol. 110, no. 1-4, pp. 411-5, 2004.

[29] J. Hwang, J. Lee, K. S. Cho, H. S. Choi, S. R. Rho, and I. H. Cho, "Space Radiation Measurement on the Polar Route onboard the Korean Commercial Flights," *Journal of Astronomy and Space Sciences,,* vol. 27, no. 1, pp. 43-54, 2010.

[30] M. Hajek, T. Berger, W. Schoner, L. Summerer, and N. Vana, "Dose assessment of aircrew using passive detectors," *Radiat Prot Dosimetry,* vol. 100, no. 1-4, pp. 511-4, 2002.

[31] F. Spurný and T. Dachev, "On-board aircrew dosimetry using a semiconductor spectrometer," *Radiation protection dosimetry,* vol. 100, pp. 525-8, 02/01 2002.

[32] B. J. Lewis, P. Tume, L. G. I. Bennett, M. Pierre, A. R. Green, B. T. Cousins, E. Hoffarth, T. A. Jones, and J. R. Brisson, "Cosmic radiation exposure on canadian-based commercial airline routes," *Radiation Protection Dosimetry,* vol. 86, no. 1, pp. 7-24, 1999.

[33] A. Mitaroff and M. Silari, "The CERN-EU High-energy Reference Field (CERF) Facility for Dosimetry at Commercial Flight Altitudes and in Space," *Radiation Protection Dosimetry,* vol. 102, no. 1, pp. 7-22, 2002.

[34] M. Caresana, M. Ferrarini, A. Parravicini, and A. Sashala Naik, "Dose measurements with CR-39 detectors at the CERF reference facility at CERN," *Radiation Measurements,* vol. 71, pp. 502-504, 2014.

[35] S. Rollet, M. Autischer, P. Beck, and M. Latocha, "Measurement and simulation of lineal energy distribution at the CERN high energy facility with a tissue equivalent proportional counter," *Radiat Prot Dosimetry,* vol. 125, no. 1-4, pp. 425-8, 2007.

[36] D. O'Sullivan, D. Zhou, W. Heinrich, S. Roesler, J. Donnelly, R. Keegan, E. Flood, and L. Tommasino, "Cosmic rays and dosimetry at aviation altitudes," *Radiation Measurements,* vol. 31, no. 1, pp. 579-584, 1999/06/01/ 1999.

[37] Civil Aerospace Medical Institute Federal Aviation Administration, "MIRA 2017: A CARI-7 Based Solar Radiation Alert System," 2018.

[38] V. Mares and H. Yasuda, "Aviation route doses calculated with EPCARD.Net and JISCARD EX," *Radiation Measurements,* vol. 45, no. 10, pp. 1553-1556, 2010.

[39] H. Yasuda, T. Sato, and M. Terakado, "A Personal Use Program for Calculation of Aviation Route Doses," 01/01 2008.

[40] B. J. Lewis, L. G. Bennett, A. R. Green, A. Butler, M. Desormeaux, F. Kitching, M. J. McCall, B. Ellaschuk, and M. Pierre, "Aircrew dosimetry using the Predictive Code for Aircrew Radiation Exposure (PCAIRE)," *Radiat Prot Dosimetry,* vol. 116, no. 1-4 Pt 2, pp. 320-6, 2005.

[41] I. Clairand, N. Fuller, J.-F. Bottollier-Depois, and F. Trompier, "The SIEVERT system for aircrew dosimetry," *Radiation Protection Dosimetry,* vol. 136, no. 4, pp. 282-285, 2009.

[42] J. F. Bottollier-Depois, P. Beck, M. Latocha, V. Mares, D. Matthiä, W. Rühm, and F. Wissmann, "Comparison of codes assessing radiation exposure of aircraft crew due to galactic cosmic radiation," in "Radiation Protection," 2012, vol. 173.

[43] International Commission on Radiation Units & Measurements, "ICRP Publication 123: Assessment of Radiation Exposure of Astronauts in Space," in "Annals of the ICRP," 2013, vol. 42.

[44] Y. F. Ali, F. A. Cucinotta, L. Ning-Ang, and G. Zhou, "Cancer Risk of Low Dose Ionizing Radiation," *Frontiers in Physics,* vol. 8, 2020.

[45] F. A. Cucinotta and M. Durante, "Cancer risk from exposure to galactic cosmic rays: implications for space exploration by human beings," *The Lancet Oncology,* vol. 7, no. 5, pp. 431-435, May 2006.

[46] F. A. Cucinotta, "Radiation Risk Acceptability and Limitations," 2010.

[47] A. Bhardwaj, F. Ferrari, M. Panasyuk, A. K. Lal, Y. Li, A. Nagamatsu, V. Petrov, G. Reitz, L. Pinsky, S. Shukor, A. Singhvi, U. Straube, L. Tomi, and L. Townsend, "Feasibility study of astronaut standardized career dose limits in LEO and the outlook for BLEO," *Acta Astronautica,* vol. 104, 01/01 2014.

[48] F. A. Cucinotta and M. Durante, "Risk of Radiation Carcinogenesis," NASA Johnson Space Center & GSI Germany,2019.

[49] F. Cucinotta, M. Y. Kim, and L. Chappell, "Space radiation cancer risk projections and uncertainties," *NASA TP,* pp. 2011-216155, 01/01 2011.

[50] H. H. Rossi and M. Zaider, Springer, Ed. *Microdosimetry and Its Applications*. 1996.

[51] International Commission on Radiation Units and Measurements, "ICRU Report 36: Microdosimetry," 1983.

[52] International Commission on Radiation Units & Measurements, "ICRU Report 40: The Quality Factor in Radiation Protection," 1986.

[53] A. M. Kellerer and K. Hahn, "Consideration on a revision of the Quality Factor," *Radiation Research,* vol. 114, 1988.

[54] Prokopovich D. A., "Silicon On Insulator Microdosimetry For Radiation Protection In Mixed Radiation Fields For Aviation And Space Dosimetry," Doctor of Philosophy, Department of Engineering Physics, University of Wollongong, 3253, 2010.

[55] D. Srdoč, "Experimental Technique of Measurement of Microscopic Energy Distribution in Irradiated Matter Using Rossi Counters," *Radiation Research,* vol. 43, no. 2, pp. 302-319, 1970.

[56] S. E. Rademacher, T. B. Borak, C. Zeitlin, L. Heilbronn, and J. Miller, "Wall Effects Observed in Tissue-Equivalent Proportional Counters from 1.05 GeV/nucleon Iron-56 Particles," *Radiation Research,* vol. 149, no. 4, pp. 387-395, 1998.

[57] A. Rosenfeld, "Novel Detectors For Silicon Based Microdosimetry, Their Concepts And Applications," *Nuclear Instruments and Methods in Physics Research Section A: Accelerators, Spectrometers, Detectors and Associated Equipment,* vol. 809, pp. 156-170, 2016.

[58] P. Bradley, A. Rosenfeld, and M. Zaider, "Solid state microdosimetry," *Nuclear Instruments and Methods in Physics Research B,* vol. 184, pp. 135-157, 2001.

[59] S. Guatelli, M. I. Reinhard, B. Mascialino, D. A. Prokopovich, A. S. Dzurak, M. Zaider, and A. B. Rosenfeld, "Tissue Equivalence Correction in Silicon Microdosimetry for Protons Characteristic of the LEO Space Environment," *IEEE Trans. Nucl. Sci.,* vol. 55, no. 6, pp. 3407-3413, 2008.

[60] A. Wroe, A. Rosenfeld, M. Reinhard, V. Pisacane, J. Ziegler, M. Nelson, F. Cucinotta, M. Zaider, and J. Dicello, "Solid State Microdosimetry With Heavy Ions for Space Applications," *IEEE Trans. Nucl. Sci.,* vol. 54, no. 6, pp. 2264-2271, 2007.

[61] L. T. Tran, L. Chartier, D. A. Prokopovich, D. Bolst, M. Povoli, A. Summanwar, A. Kok, A. Pogossov, M. Petasecca, S. Guatelli, M. I. Reinhard, M. Lerch, M. Nancarrow, N. Matsufuji, M. Jackson, and A. B. Rosenfeld, "Thin Silicon Microdosimeter Utilizing 3-D MEMS Fabrication Technology: Charge Collection Study and Its Application in Mixed Radiation Fields," *IEEE Trans. Nucl. Sci.,* vol. 65, no. 1, pp. 467-472, October 2018.

[62] L. Chartier, L. T. Tran, D. Bolst, A. Pogossov, S. Guatelli, M. Petasecca, M. Lerch, D. Prokopovich, M. Reinhard, V. Perevertaylo, M. Jackson, N. Matsufuji, and A. B. Rosenfeld, "New silicon microdosimetry probes for RBE and biological dose studies using stationary and movable targets in12C ion therapy," *Journal of Physics: Conference Series,* vol. 777, no. 1, pp. 1-4, 2017, Art. no. 012019.

[63] S. Peracchi, J. Vohradsky, S. Guatelli, D. Bolst, L. T. Tran, D. A. Prokopovich, and A. B. Rosenfeld, "Modelling of the Silicon-On-Insulator microdosimeter response within the International Space Station for astronauts' radiation protection," *Radiation Measurements,* vol. 128, September 2019, Art. no. 106182.

[64] A. Wroe, I. Cornelius, A. Rosenfeld, V. Pisacane, J. Ziegler, M. Nelson, F. Cucinotta, M. Zaider, and J. Dicello, "Microdosimetry simulations of solar protons within a spacecraft," *IEEE Trans. Nucl. Sci.,* vol. 52, no. 6, pp. 2591-2596, 2005.

[65] F. A. Cucinotta and E. Cacao, "Non-Targeted Effects Models Predict Significantly Higher Mars Mission Cancer Risk than Targeted Effects Models," *Scientific Reports,* vol. 7, no. 1, p. 1832, May 12 2017.

[66] D. Heynderickx, B. Quaghebeur, J. Wera, E. J. Daly, and H. D. R. Evans, "New radiation environment and effects models in the European Space

Agency's Space Environment Information System (SPENVIS)," *Space Weather,* vol. 2, no. 10, pp. n/a-n/a, 2004.

[67] D. F. Smart and M. A. Shea, "A review of geomagnetic cutoff rigidities for earth-orbiting spacecraft," *Advances in Space Research,* vol. 36, no. 10, pp. 2012-2020, 2005.

[68] *Space environment (natural and artificial) — Galactic cosmic ray model*, 2004.

[69] R. A. Nymmik, M. I. Panasyuk, T. I. Pervaja, and A. A. Suslov, "A model of galactic cosmic ray fluxes," *International Journal of Radiation Applications and Instrumentation,* vol. 220, no. 3, pp. 427-429, 1992.

[70] L.I. Miroshnichenko, *Radiation Hazard in space* (Astrophysics and Space Science Library). Springer Science & Business Media, 2013.

[71] J. Feynman, G. Spitale, J. Wang, and S. Gabriel, "Interplanetary proton fluence model: JPL 1991," *Journal of Geophysical Research: Space Physics,* vol. 98, no. A8, pp. 13281-13294, 1993.

[72] L. Rosenqvist, A. Hilgers, H. Evans, and E. Daly, "Toolkit for Updating Interplanetary Proton-Cumulated Fluence Models," *Journal of Spacecraft and Rockets,* vol. 42, no. 6, pp. 1077-1090, 2005.

[73] M. Shea, D. F. Smart, J. H. Adams, D. Chenette, and J. Feynman, "Toward a descriptive model of solar particles in the heliosphere," 04/15 1988.

[74] M. A. Xapsos, J. L. Barth, E. G. Stassinopoulos, E. A. Burke, and G. B. Gee, "Space environment effects : model for emission of solar protons (ESP) - cumulative and worst-case event fluences," NASA,1999.

[75] J. N. Kapur and H. K. Kesavan, *Entropy Optimization Principles and Their Applications*. 1992, pp. 3-20.

[76] J. I. Vette, "The NASA/National Space Science Data Center Trapped Radiation Environment Model Program 1964-1991," 1991, no. NSSDC/WDC-A-R&S 91-29.

[77] J. D. Meffert and M. S. Gussenhoven, "CRRESPRO documentation," Phillips Laboratory,1994, vol. 1158.

[78] D. H. Brautigam and J. T. Bell, "CRRESELE Documentation," in "Environmental Research Papers," Phillips Laboratory,1995, vol. 1178.

[79] D. Heynderickx, M. Kruglanski, V. Pierrard, J. Lemaire, M. D. Looper, and J. B. Blake, "A low altitude trapped proton model for solar minimum conditions based on SAMPEX/PET data," *IEEE Trans. Nucl. Sci.,* vol. 46, no. 6, pp. 1475-1480, 1999.

[80] D. M. Boscher, S. A. Bourdarie, R. H. W. Friedel, and R. D. Belian, "Model for the geostationary electron environment: POLE," *IEEE Trans. Nucl. Sci.,* vol. 50, no. 6, pp. 2278-2283, 2003.

[81] A. Sicard-Piet, S. Bourdarie, D. Boscher, R. H. W. Friedel, M. Thomsen, T. Goka, H. Matsumoto, and H. Koshiishi, "A new international geostationary electron model: IGE-2006, from 1 keV to 5.2 MeV," *Space Weather,* vol. 6, no. 7, 2008.

[82] S. Agostinelli, J. Allison, K. Amako, J. Apostolakis, H. Araujo, P. Arce, M. Asai, D. Axen, S. Banerjee, G. Barrand, F. Behner, L. Bellagamba, J. Boudreau, L. Broglia, A. Brunengo, H. Burkhardt, S. Chauvie, J. Chuma, R. Chytracek, G. Cooperman, G. Cosmo, P. Degtyarenko, A. Dell'Acqua, G. Depaola, D. Dietrich, R. Enami, A. Feliciello, C. Ferguson, H. Fesefeldt, G. Folger, F. Foppiano, A. Forti, S. Garelli, S. Giani, R. Giannitrapani, D. Gibin, J. J. Gómez Cadenas, I. González, G. Gracia Abril, G. Greeniaus, W. Greiner, V. Grichine, A. Grossheim, S. Guatelli, P. Gumplinger, R. Hamatsu, K. Hashimoto, H. Hasui, A. Heikkinen, A. Howard, V. Ivanchenko, A. Johnson, F. W. Jones, J. Kallenbach, N. Kanaya, M. Kawabata, Y. Kawabata, M. Kawaguti, S. Kelner, P. Kent, A. Kimura, T. Kodama, R. Kokoulin, M. Kossov, H. Kurashige, E. Lamanna, T. Lampén, V. Lara, V. Lefebure, F. Lei, M. Liendl, W. Lockman, F. Longo, S. Magni, M. Maire, E. Medernach, K. Minamimoto, P. Mora de Freitas, Y. Morita, K. Murakami, M. Nagamatu, R. Nartallo, P. Nieminen, T. Nishimura, K. Ohtsubo, M. Okamura, S. O'Neale, Y. Oohata, K. Paech, J. Perl, A. Pfeiffer, M. G. Pia, F. Ranjard, A. Rybin, S. Sadilov, E. Di Salvo, G. Santin, T. Sasaki, N. Savvas, Y. Sawada, S. Scherer, S. Sei, V. Sirotenko, D. Smith, N. Starkov, H. Stoecker, J. Sulkimo, M. Takahata, S. Tanaka, E. Tcherniaev, E. Safai Tehrani, M. Tropeano, P. Truscott, H. Uno, L. Urban, P. Urban, M. Verderi, A. Walkden, W. Wander, H. Weber, J. P. Wellisch, T. Wenaus, D. C. Williams, D. Wright, T. Yamada, H. Yoshida and D. Zschiesche, "Geant4 - a simulation toolkit," *Nuclear Instruments and Methods in Physics Research Section A: Accelerators, Spectrometers, Detectors and Associated Equipment,* vol. 506, no. 3, pp. 250-303, 2003.

[83] GEANT4 Collaboration, *Book For Application Developers*. 2020.

[84] GEANT4 Collaboration, "Physics Reference Manual," 2020.

[85] ESA. *Space Environment Information System (SPENVIS).* Available: https://www.spenvis.oma.be/

[86] G. D. BADHWAR and A. KONRADI, "Conversion of omnidirectional proton fluxes into a pitch angle distribution," *Journal of Spacecraft and Rockets,* vol. 27, no. 3, pp. 350-352, 1990.

[87] D.M. Hassler, C. Zeitlin, R.F. Wimmer-Schweingruber, S. Böttcher, C. Martin, J. Andrews, E. Böhm, D.E. Brinza, M.A. Bullock, S. Burmeister, B. Ehresmann, M. Epperly, D. Grinspoon, J. Köhler, O. Kortmann, K. Neal, J. Peterson, A. Posner, S. Rafkin, L. Seimetz, K.D. Smith, Y. Tyler, G. Weigle, G. Reitz, and F.A. Cucinotta, "The Radiation Assessment Detector (RAD) Investigation," *Space Science Reviews,* 2012.

[88] R. Destefanis, E. Amerio, M. Briccarello, M. Belluco, M. Faraud, E. Tracino, and C. Lobascio, "Space environment characterisation of Kevlar®: good for bullets, debris and radiation too," in *SPACEEC*, 2014, pp. 80-113: Thales Alenia Space Italia S.p.A and Sofiter System Engineering.

[89] G. Santin, "Normalisation modelling sources," in "Geant4 tutorial," ESA/ESTEC2007.

[90] L. T. Tran, S. Guatelli, D. A. Prokopovich, M. Petasecca, M. L. F. Lerch, M. I. Reinhard, J. F. Ziegler, M. Zaider, and A. B. Rosenfeld, "A Novel Silicon Microdosimeter Using 3D Sensitive Volumes: Modeling the Response in Neutron Fields Typical of Aviation," *IEEE Trans. Nucl. Sci.,* vol. 61, no. 4, pp. 1552-1557, 2014.

[91] L. T. Tran, L. Chartier, D. A. Prokopovich, M. I. Reinhard, M. Petasecca, S. Guatelli, M. L. F. Lerch, V. L. Perevertaylo, M. Zaider, N. Matsufuji, M. Jackson, M. Nancarrow, and A. B. Rosenfeld, "3D-mesa 'bridge' silicon microdosimeter: charge collection study and application to RBE studies in 12C radiation therapy," *IEEE Trans. Nucl. Sci.,* vol. 62, no. 2, 2015.

[92] B. James, L. T. Tran, J. Vohradsky, D. Bolst, V. Pan, M. Carr, S. Guatelli, A. Pogossov, M. Petasecca, M. Lerch, D. A. Prokopovich, M. I. Reinhard, M. Povoli, A. Kok, D. Hinde, M. Dasgupta, A. Stuchbery, V. Perevertaylo, and A. B. Rosenfeld, "SOI Thin Microdosimeter Detectors for Low Energy Ions and Radiation Damage Studies," *IEEE Trans. Nucl. Sci.,* vol. 66, no. 1, pp. 320-326, 2018.

[93] D. Bolst, L. T. Tran, L. Chartier, D. A. Prokopovich, A. Pogossov, S. Guatelli, M. I. Reinhard, M. Petasecca, M. L. F. Lerch, N. Matsufuji, V. L. Perevertaylo, C. Fleta, G. Pellegrini, M. Jackson, and A. B. Rosenfeld, "RBE study using solid state microdosimetry in heavy ion therapy," *Radiation Measurements,* vol. 106, pp. 512-518, 2017.

[94] S. Lembit and T. Berger, "The DOSIS and DOSIS 3D project on-board the ISS - Current status and scientific overview," presented at the IEEE Aerospace Conference, 2016, 2017.

[95] T. Dachev, N. G. Bankov, B. T. Tomov, Y. N. Matviichuk, P. G. Dimitrov, D. P. Häder, and G. Horneck, "Overview of the ISS Radiation Environment Observed during the ESA EXPOSE-R2 Mission in 2014-2016," *Space Weather,* vol. 15, no. 11, pp. 1475-1489, 2017.

[96] Z. Pastuovic, D. Button, D. Cohen, D. Fink, D. Garton, M. Hotchkis, M. Ionescu, S. Long, V. Levchenko, M. Mann, R. Siegele, A. Smith, and K. Wilcken, "SIRIUS – A new 6 MV accelerator system for IBA and AMS at ANSTO," *Nuclear Instruments and Methods in Physics Research Section B: Beam Interactions with Materials and Atoms,* vol. 371, pp. 142-147, 2016.

[97] E. Vittone, "Semiconductor Characterization by Scanning Ion Beam Induced Charge (IBIC) Microscopy," *ISRN Materials Science,* vol. 2013, pp. 1-17, 2013.

[98] L. T. Tran, D. A. Prokopovich, M. Petasecca, M. L. F. Lerch, A. Kok, A. Summanwar, T.-E. Hansen, C. D. Via, M. I. Reinhard, and A. B. Rosenfeld, "3D Radiation Detectors: Charge Collection Characterisation and Applicability of Technology for Microdosimetry," *IEEE Trans. Nucl. Sci.,* vol. 61, no. 4, pp. 1537-1543, 2014.

[99] L. T. Tran, D. A. Prokopovich, M. Petasecca, M. L. F. Lerch, C. Fleta, G. Pellegrini, C. Guardiola, M. I. Reinhard, and A. B. Rosenfeld, "Ultra-Thin 3-D Detector: Charge Collection Characterization and Application for Microdosimetry," *IEEE Trans. Nucl. Sci.,* vol. 61, no. 6, pp. 3472-3478, 2014.

[100] L. T. Tran, "Advanced Semiconductor Silicon Detector For Dosimetry And Microdosimetry In Radiation Protection And Hadron Therapy," Doctor of Philosophy, Centre for Medical Radiation Physics, University of Wollongong, 2014.

[101] B. James, L. T. Tran, D. Bolst, S. Peracchi, J. A. Davis, D. A. Prokopovich, S. Guatelli, M. Petasecca, M. Lerch, M. Povoli, A. Kok, M.-J. Goethem, M. Nancarrow, N. Matsufuji, M. Jackson, and A. B. Rosenfeld, "SOI Thin Microdosimeters for High LET Single-Event Upset Studies in Fe, O, Xe, and Cocktail Ion Beam Fields," *IEEE Transactions on Nuclear Science,* vol. 67, no. 1, pp. 146-153, 2020.

[102] S. Peracchi, L. T. Tran, B. James, D. Bolst, D. A. Prokopovich, J. A. Davis, S. Guatelli, M. Petasecca, M. L. F. Lerch, N. Matsufuji, A. Kok, M. Povoli, M. Jackson, and A. B. Rosenfeld, "A solid-state microdosimeter for dose and

radiation quality monitoring for astronauts in space," *IEEE Trans. Nucl. Sci.,* vol. 67, no. 1, pp. 169-174, January 2020.

[103] O. Mohamad, H. Makishima, and T. Kamada, "Evolution of Carbon Ion Radiotherapy at the National Institute of Radiological Sciences in Japan," *Cancers (Basel),* vol. 10, no. 3, Mar 6 2018.

[104] D. Bolst, L. T. Tran, S. Guatelli, N. Matsufuji, and A. B. Rosenfeld, "Modelling the Biological Beamline at HIMAC using Geant4," *Journal of Physics Conference Series,* vol. 1154, no. 1, pp. 1-6, 2019, Art. no. 012003.

[105] O. Ploc, T. Dachev, Y. Uchihori, H. Kitamura, and L. Sihver, "Fragmentation from heavy ion beams in HIMAC BIO room calculated with PHITS and measured with Liulin," in *2017 IEEE Aerospace Conference*, 2017, pp. 1-10.

[106] T. C. Slaba, X. Xu, S. R. Blattnig, and R. B. Norman, "GCR environmental models III: GCR model validation and propagated uncertainties in effective dose," *Space Weather,* vol. 12, no. 4, pp. 217-224, 2014.

[107] International Commission on Radiological Protection, "ICRP Publication 103: the 2007 Recommendations of the International Commission on Radiological Protection," 2007, vol. 37.

[108] D. Bolst, S. Guatelli, L. T. Tran, L. Chartier, M. L. Lerch, N. Matsufuji, and A. B. Rosenfeld, "Correction factors to convert microdosimetry measurements in silicon to tissue in (12)C ion therapy," *Phys Med Biol,* vol. 62, no. 6, pp. 2055-2069, Mar 21 2017.

[109] M. Silvestri, E. Tracino, M. Briccarello, M. Belluco, R. Destefanis, C. Lobascio, M. Durante, G. Santin, and R. D. Schrimpf, "Impact of Spacecraft-Shell Composition on 1 GeV/Nucleon 56Fe Ion-Fragmentation and Dose Reduction," *IEEE Trans. Nucl. Sci.,* vol. 58, no. 6, pp. 3126-3133, December 2011.

[110] B. Gersey, S. Aghara, R. Wilkins, J. Wedeking, and R. C. Dwivedi, "Comparison of a Tissue Equivalent and a Silicon Equivalent Proportional Counter Microdosimeter to High-Energy Proton and Neutron Fields," *IEEE Trans. Nucl. Sci.,* vol. 54, no. 6, pp. 2276-2281, 2007.

[111] L. Walsh, U. Schneider, A. Fogtman, C. Kausch, S. McKenna-Lawlor, L. Narici, J. Ngo-Anh, G. Reitz, L. Sabatier, G. Santin, L. Sihver, U. Straube, U. Weber, and M. Durante, "Research plans in Europe for radiation health hazard assessment in exploratory space missions," *Life Sci Space Res (Amst),* vol. 21, pp. 73-82, May 2019.

[112] C. Zeitlin, D. M. Hassler, F. A. Cucinotta, B. Ehresmann, R. F. Wimmer-Schweingruber, D. E. Brinza, S. Kang, G. Weigle, S. Bottcher, E. Bohm, S. Burmeister, J. Guo, J. Kohler, C. Martin, A. Posner, S. Rafkin, and G. Reitz, "Measurements of energetic particle radiation in transit to Mars on the Mars science laboratory," *Science,* vol. 340, no. 80, pp. 1080-1084, 2013.

[113] J. C. Chancellor, G. B. I. Scott, and J. P. Sutton, "Space Radiation: The Number One Risk to Astronaut Health beyond Low Earth Orbit," *Life,* vol. 4, pp. 491-510, 2014.

[114] S. Peracchi, B. James, F. Pagani, V. Pan, J. Vohradsky, D. Bolst, D. A. Prokopovich, S. Guatelli, M. Petasecca, M. L. F. Lerch, S. H. Lee, T. Inaniwa, N. Matsufuji, M. Povoli, A. Kok, M. Jackson, T. Squire, A. B. Rosenfeld, and L. T. Tran, "Radiation shielding evaluation of spacecraft walls against heavy ions using microdosimetry," *IEEE Transactions on Nuclear Science,* pp. 1-1, 2020.

[115] S. B. Guetersloh, C. Zeitlin, L. Heilbronn, J. Miller, T. Komiyama, A. Fukumura, Y. Iwata, T. Murakami, and M. Bhattacharya, "Polyethylene as a radiation shielding standard in simulated cosmic-ray environments," *Nuclear Instruments and Methods in Physics Research Section B: Beam Interactions with Materials and Atoms,* vol. 152, no. 2, pp. 319-332, October 2006.

[116] A. Lourenco, D. Shipley, N. Wellock, R. Thomas, H. Bouchard, A. Kacperek, F. Fracchiolla, S. Lorentini, M. Schwarz, N. MacDougall, G. Royle, and H. Palmans, "Evaluation of the water-equivalence of plastic materials in low- and high-energy clinical proton beams," *Phys Med Biol,* vol. 62, no. 10, pp. 3883-3901, April 2017.

[117] C. Lobascio, M. Briccarello, R. Destefanis, M. Faraud, G. Gialanella, G. Grossi, V. Guarnieri, L. Manti, M. Pugliese, A. Rusek, P. Scampoli, and M. Durante, "Accelerator-based tests of radiation shielding properties of materials used in human space infrastructures," *Health Physics,* vol. 94, no. 3, pp. 242-247, April 2008.

[118] R. Destefanis, M. Faraud, and M. Trucchi, "Columbus debris shielding experiments and ballistic limit curves," *International Journal of Impact Engineering,* vol. 23, no. 1, pp. 181-192, December 1999.

[119] M. Vuolo, G. Baiocco, S. Barbieri, L. Bocchini, M. Giraudo, T. Gheysens, C. Lobascio, and A. Ottolenghi, "Exploring innovative radiation shielding approaches in space: A material and design study for a wearable radiation

protection spacesuit," *Life Sci Space Res (Amst),* vol. 15, pp. 69-78, August 2017.

[120] Z. Li, S. Chen, S. Nambiar, and Y. Sun, "PMMA/MWCNT nanocomposite for proton radiation shielding applications," *Nanotechnology for Aerospace,* vol. 27, no. 23, April 2016, Art. no. 234001.

[121] J. W. Wilson, T. C. Slaba, F. F. Badavi, B. D. Reddell, and A. A. Bahadori, "3DHZETRN: Shielded ICRU spherical phantom," *Life Sci Space Res (Amst),* vol. 4, pp. 46-61, Jan 2015.

[122] J. W. Wilson, R. K. Tripathi, G. D. Qualls, F. A. Cucinotta, R. E. Prael, J. W. Norbury, J. H. Heinbockel, and J. Tweed, "A space radiation transport method development," *Adv Space Res,* vol. 34, no. 6, pp. 1319-27, 2004.

[123] L. Pinsky, F. Carminati, and A. Ferrari, "Simulation of Space Shuttle neutron measurements with FLUKA," *Radiation Measurements,* vol. 33, no. 3, pp. 335-339, 2001/06/01/ 2001.

[124] J. Wilson, F. Badavi, F. Cucinotta, J. Shinn, G. Badhwar, R. Silberberg, C. Tsao, L. Townsend, and R. Tripathi, "HZETRN: Description of a Free-Space Ion and Nucleon Transport and Shielding Computer Program," *NASA STI/Recon Technical Report N,* vol. 95, 07/16 1995.

[125] National Academies of Sciences Engineering and Medicine, "Testing at the Speed of Light: The State of U.S. Electronic Parts Space Radiation Testing Infrastructure," The National Academies Press, Ed., ed. Washington, 2018.

[126] A. Koziukov, I. Tuzhikova, Pellish J, P. Chubunov, P. Paillet, R. Ecoffet, V. Anashin, S. M. Barbero, S. K. Höffgen, G. Berger, and H. Guerrero, "Compendium of international irradiation test facilities," in *RADECS*, Moscow, Russia, 2015, vol. 2.

[127] J. Miller, "Proton and heavy ion acceleration facilities for space radiation research," *Gravitational and space biology bulletin: publication of the American Society for Gravitational and Space Biology,* vol. 16, no. 2, pp. 19-36, 2003.

[128] C. Zeitlin, L. Heilbronn, and J. Miller, *Radiation tests of the extravehicular mobility unit space suit for the international space station using energetic protons*. 2001.

[129] E. R. Benton, E. V. Benton, and A. L. Frank, "Characterization of the radiation shielding properties of U.S. and Russian EVA suits," Lawrence Berkeley National Laboratory,ERI-000501, 2001.

[130] M.-H. Y. Kim, A. Rusek, and F. A. Cucinotta, "Issues for Simulation of Galactic Cosmic Ray Exposures for Radiobiological Research at Ground-

Based Accelerators," (in English), *Frontiers in Oncology,* vol. 5, no. 122, 2015.

[131] J. W. Norbury, W. Schimmerling, T. C. Slaba, E. I. Azzam, F. F. Badavi, G. Baiocco, E. Benton, V. Bindi, E. A. Blakely, S. R. Blattnig, D. A. Boothman, T. B. Borak, R. A. Britten, S. Curtis, M. Dingfelder, M. Durante, W. S. Dynan, A. J. Eisch, S. Robin Elgart, D. T. Goodhead, P. M. Guida, L. H. Heilbronn, C. E. Hellweg, J. L. Huff, A. Kronenberg, C. La Tessa, D. I. Lowenstein, J. Miller, T. Morita, L. Narici, G. A. Nelson, R. B. Norman, A. Ottolenghi, Z. S. Patel, G. Reitz, A. Rusek, A. S. Schreurs, L. A. Scott-Carnell, E. Semones, J. W. Shay, V. A. Shurshakov, L. Sihver, L. C. Simonsen, M. D. Story, M. S. Turker, Y. Uchihori, J. Williams, and C. J. Zeitlin, "Galactic cosmic ray simulation at the NASA Space Radiation Laboratory," *Life Sci Space Res (Amst),* vol. 8, pp. 38-51, Feb 2016.

[132] L. C. Simonsen, T. C. Slaba, P. Guida, and A. Rusek, "NASA's first ground-based Galactic Cosmic Ray Simulator: Enabling a new era in space radiobiology research," *PLOS Biology,* vol. 18, no. 5, p. e3000669, 2020.

[133] E. W. Cascio, J. A. Sisterson, B. Gottschalk, and S. Sarkar, "Measurements of the energy spectrum of degraded proton beams at NPTC," in *IEEE Radiation Effects Data Workshop (IEEE Cat. No.04TH8774)*, 2004, pp. 151-155.

[134] J. M. Sisterson, J. B. Flanz, and J. E. Burns, "A new proton irradiation facility at the Northeast Proton Therapy Center," in *1999 IEEE Radiation Effects Data Workshop. Workshop Record. Held in conjunction with IEEE Nuclear and Space Radiation Effects Conference*, 1999, pp. 123-127.

[135] T. C. Slaba, S. R. Blattnig, J. W. Norbury, A. Rusek, and C. La Tessa, "Reference field specification and preliminary beam selection strategy for accelerator-based GCR simulation," *Life Sci Space Res (Amst),* vol. 8, pp. 52-67, Feb 2016.

[136] E. Pedroni, D. Meer, C. Bula, S. Safai, and S. Zenklusen, "Pencil beam characteristics of the next-generation proton scanning gantry of PSI: design issues and initial commissioning results," *The European Physical Journal Plus,* vol. 126, no. 66, pp. 1-27, 2011.

[137] D. Bolst, S. Guatelli, L. T. Tran, and A. B. Rosenfeld, "Optimisation of the design of SOI microdosimeters for hadron therapy quality assurance," (in eng), *Phys Med Biol,* vol. 63, no. 21, p. 215007, Oct 24 2018.

[138] Interantional Commission on Radiation Units and Measurements and Interantional Commission on Radiological Protection, "Operational Quantities for External Radiation Exposure," 2017.

[139] T. Inaniwa, M. Suzuki, S. Hyun Lee, K. Mizushima, Y. Iwata, N. Kanematsu, and T. Shirai, "Experimental validation of stochastic microdosimetric kinetic model for multi-ion therapy treatment planning with helium-, carbon-, oxygen-, and neon-ion beams," *Physics in Medicine & Biology,* vol. 65, no. 4, p. 045005, 2020/02/12 2020.

[140] C. Grassberger, A. Lomax, and H. Paganetti, "Characterizing a proton beam scanning system for Monte Carlo dose calculation in patients," (in eng), *Phys Med Biol,* vol. 60, no. 2, pp. 633-45, Jan 21 2015.

The End